

# Distributed Sensing for MIMO Radar Systems



**Christos V. Ilioudis**

Centre in Signal and Image Processing  
Department of Electronic and Electrical Engineering  
University of Strathclyde  
Glasgow

This dissertation is submitted for the degree of  
*Doctor of Philosophy*

2017

To my loving family and friends.

## **Declaration**

This thesis is the result of the author's original research. It has been composed by the author and has not been previously submitted for examination which has led to the award of a degree.

The copyright of this thesis belongs to the author under the terms of the United Kingdom Copyright Acts as qualified by University of Strathclyde Regulation 3.50. Due acknowledgement must always be made of the use of any material contained in, or derived from, this thesis.

Christos V. Ilioudis

2017

## Acknowledgements

This thesis has been conducted at the Department of Electronic and Electrical Engineering of Strathclyde University.

Completing my doctoral thesis, I would like to thank my supervisors Professor John J. Soraghan and Doctor Stephan Weiss for their excellent and invaluable guidance, encouragement and decisive contribution to the development and completion of this thesis. Under their supervision I was taught everything I need to be a great researcher including being creative, thinking deeply, and the skills for developing and presenting ideas.

I also would like to thank Doctor Carmine Clemente for the help he offered me when I needed it during my study and the preparation of my thesis, for his valuable comments and corrections as well as for his participation in the supervising committee.

Moreover, I would like to thank my colleagues and friends Domenico, Adriano, Alessio and Jianlin for all their support and collaboration throughout these years.

Finally, this project would have been impossible without the support of my sponsors, the University of Strathclyde and the MOD University Defence Research Collaboration in Signal Processing.

# Abstract

The research presented in this thesis deals with the concepts of distributed sensing for multiple-input multiple-output (MIMO) radar systems and important signal processing algorithms with regard to multiple sensing optimisations. These novel algorithms include an edge detection scheme based on the phase stretch transform (PST) for synthetic aperture radar (SAR) imaging systems, the application of the fractional Fourier transform (FrFT) in generating new waveform libraries and the synthesis of a generalised MIMO ambiguity function (AF) based on the Kullback-Leibler divergence (KLD).

In particular, a new edge detection algorithm for SAR images is proposed. This method is an enhanced scheme that is based on the phase stretch transform (PST). The high-accuracy of the presented edge detection method is tested and verified experimentally using two SAR image datasets. Experimental results show that thresholding and further morphological operation leads in excellent edge extraction despite the noise embedded into the image. Including PST into the structure of the edge detection algorithm is proved to be very advantageous, since the efficiency in edge determining could be improved by means of tuning the strength and wrap parameters of PST phase kernel. It is shown that the proposed method is very effective and capable to remove embedded noise and introduced artefacts even from image parts corresponding to the surface of the sea.

A novel waveform design scheme is proposed to create waveform libraries employing the FrFT. Additionally an efficient algorithm based on a modified Gerchberg-Saxton algorithm (MGSA) is developed to reconstruct the proposed fractional waveform libraries under constant envelope (CE) constrain. This efficient technique is capable of generating novel libraries of phase-coded waveforms through FrFT and optimise the signal retrieval, while the signal waveforms retain their constant modulus. Specifically, the reconstruction of sequences from the FrFT based waveforms is achieved by means of the error reduction algorithm (ERA). The performance of this new method is evaluated via simulation analysis, showing the good properties of the waveforms in terms of AF performance parameters and

in attaining high diversity between waveforms for both fractional and CE fractional libraries. In addition, the applicability of the derived fractional waveforms is experimentally validated, while their performance is evaluated through comparing with conventional techniques in a distributed MIMO radar scenario.

Moreover, a novel-multiplexing scheme also based on the FrFT is introduced enabling radar systems to operate in a message exchange mode via embedding the required information into fractional waveforms. The efficiency of the proposed waveform design is evaluated regarding the AF properties of the communicating radar (Co-Radar) waveform.

A new, generalised AF is presented based on the KLD and applied in a MIMO radar signal model. The proposed MIMO AF can be factorised into auto-correlation and cross-correlation signal matrices, and channel correlation matrices. Moreover, it is shown that the proposed MIMO AF maximally stretches between 0 and 1, while also being flexible for various geometrical and operating signal configurations. The relationship of the proposed MIMO AF with other definition is also examined, showing that it reduces to the traditional Woodward definition when the same signal model is assumed. In addition, the behaviour of the proposed MIMO AF is investigated for different target placements and operating waveforms highlighting the advantages of each configuration. Finally, the good performance of the AF is demonstrated in a simulated MIMO radar system.

# Table of contents

<b>List of figures</b>	<b>x</b>
<b>List of tables</b>	<b>xvi</b>
<b>Nomenclature</b>	<b>xvii</b>
<b>1 Introduction</b>	<b>1</b>
1.1 Preface . . . . .	1
1.2 Motivation . . . . .	3
1.3 Contribution . . . . .	4
1.4 Publications . . . . .	5
1.5 Thesis Organization . . . . .	6
<b>2 Radar Systems</b>	<b>9</b>
2.1 Introduction . . . . .	9
2.2 Basic and Advanced Techniques . . . . .	9
2.2.1 Basic Operation Principles . . . . .	10
2.2.2 Advanced Techniques of Radar Systems . . . . .	14
2.2.3 Waveforms Design and Pulse Compression . . . . .	17
2.3 Multisensor Systems . . . . .	26
2.3.1 Co-located Radar Systems . . . . .	27
2.3.2 Distributed Radar Systems . . . . .	30
2.3.3 Current Challenges in MIMO Radar . . . . .	32
2.4 Spectrum Sharing In Radar . . . . .	33
2.4.1 Waveform Diversity . . . . .	34
2.4.2 Joint Communication and Radar . . . . .	39
2.5 Radar Imaging and Edge Detection . . . . .	41
2.5.1 Synthetic Aperture Radar . . . . .	41
2.5.2 Speckle Noise . . . . .	43

2.5.3	Edge Detection . . . . .	45
2.6	Summary . . . . .	47
<b>3</b>	<b>Advanced Time-Frequency Transforms</b>	<b>48</b>
3.1	Introduction . . . . .	48
3.2	Time-Frequency Analysis . . . . .	48
3.2.1	Linear Transforms . . . . .	49
3.2.2	Quadratic transforms . . . . .	51
3.3	Ambiguity Function . . . . .	52
3.3.1	Canonical AF Definition . . . . .	53
3.3.2	AF Cuts and Properties . . . . .	53
3.3.3	Ideal and basic signal AF . . . . .	55
3.3.4	Kullback-Leibler Divergence based AF . . . . .	58
3.3.5	MIMO AF Definitions . . . . .	60
3.4	Fractional Fourier Transform . . . . .	62
3.4.1	FrFT Properties . . . . .	64
3.4.2	FrFT Implementations . . . . .	66
3.4.3	Applications of FrFT in Signal processing . . . . .	67
3.5	Phase Stretch Transform . . . . .	68
3.5.1	PST Based Edge Detection . . . . .	70
3.6	Summary . . . . .	72
<b>4</b>	<b>Edge Detection in SAR Images using Phase Stretch Transform</b>	<b>73</b>
4.1	Introduction . . . . .	73
4.2	Edge Detection Based on PST . . . . .	73
4.3	Experimental Results . . . . .	77
4.4	Summary . . . . .	79
<b>5</b>	<b>Novel Fractional Fourier Transform Based Radar Waveforms</b>	<b>80</b>
5.1	Introduction . . . . .	80
5.2	FrFT based Waveforms . . . . .	80
5.2.1	Fractional Waveforms Design and Libraries . . . . .	81
5.2.2	Constant Envelope Fractional Waveforms . . . . .	84
5.2.3	Diversity In Fractional Waveform Libraries . . . . .	91
5.2.4	Validation and Performance Analysis . . . . .	94
5.3	Information embedded Fractional Waveforms . . . . .	103
5.4	Summary . . . . .	108

<b>6</b>	<b>Generalised MIMO Ambiguity Function</b>	<b>109</b>
6.1	Introduction . . . . .	109
6.2	Signal Model . . . . .	109
6.3	Channel Correlation . . . . .	116
6.3.1	Distributed System . . . . .	120
6.3.2	Co-Located System . . . . .	121
6.4	MIMO Ambiguity Function Formulation . . . . .	123
6.5	Reduction to Woodward AF . . . . .	128
6.6	Example and Illustrations . . . . .	128
6.6.1	Normalised Channel Correlation Matrix . . . . .	129
6.6.2	Disrtibuted and Co-located System Performance . . . . .	130
6.7	Simulations and Comparison . . . . .	135
6.7.1	Modified AF . . . . .	135
6.7.2	Correlation matrix approximation . . . . .	136
6.7.3	Simulated results . . . . .	138
6.8	Summary . . . . .	143
<b>7</b>	<b>Conclusions and Future Works</b>	<b>145</b>
7.1	Conclusion . . . . .	145
7.2	Future Work . . . . .	147
	<b>Appendix A</b>	<b>149</b>
A.1	Further FrFT Properties . . . . .	149
A.2	FrFT and AF relationship Proof . . . . .	150
	<b>Appendix B</b>	<b>152</b>
B.1	Definition of Time Delay, Time Scale and Frequency Shift Matrix	152
B.2	Phase Integral and Sinc function Relation Proof . . . . .	153
B.3	Inverse Corelation Matix Proof . . . . .	153
B.4	Proof of Lower Limits . . . . .	154
	<b>References</b>	<b>157</b>

# List of figures

2.1	Basic radar operation schematic. . . . .	11
2.2	Pulse radar transmission and reception operations. . . . .	11
2.3	Illumination in different azimuth and elevation angles using a directional antenna. . . . .	12
2.4	Range resolution issue between targets in close proximity with each other. . . . .	13
2.5	Matched filter output of (a) an unmodulated square pulse and (b) a LFM pulse. . . . .	21
2.6	Waveform design categorisation. . . . .	21
2.7	Time-frequency profile of (a) linear and (b) non-linear FM waveforms. . . . .	22
2.8	Time-frequency profile of (a) LFM and (b) Costas 7 code. . . . .	24
2.9	Multisensor systems categorisation. . . . .	28
2.10	Example of phased array antenna beam-forming. . . . .	29
2.11	Example of time-frequency mapping in (a) DFCW-FF, (b) DFCW-LFM, and (c) Hybrid DFCW-LFM schemes . . . . .	37
2.12	SAR system geometry . . . . .	42
2.13	Example of two images before (left) and after introducing Gaussian (middle) and speckle (right) noise. . . . .	44
2.14	Example of edge detection in (a) an original using (b) a Sobel and (c) a Canny detector. . . . .	46
3.1	Illustration of the STFT of a LFM pulse and the projection of its real part in time domain and absolute value in frequency domain (spectrum). . . . .	50
3.2	Illustration of the (a) WVD and (b) STFT for two consequent LFM pulses. . . . .	52
3.3	Ambiguity function of an unmodulated square pulse. . . . .	56
3.4	Ambiguity function of a LFM with $TB = 20$ . . . . .	58

3.5	Graphical representation of the MIMO AF proposed in (San Antonio et al., 2007) as a function of range, Doppler shift and azimuth angle	61
3.6	FrFT as a rotation in the time-frequency plane. . . . .	64
3.7	Time-frequency representation using STFT of a Gaussian pulse after applying FrFT of different orders. . . . .	64
3.8	Wideband AF of a FFT-based signal (a) before and (b) after applying FrFT of $\vartheta = 30^\circ$ as presented in (Liu, 2009). . . . .	68
3.9	Phase derivative profiles comparison for four different kernels. . .	69
3.10	Edge detection method based on PST as it was proposed in (Asghari and Jalali, 2015). . . . .	70
3.11	Effect on detected edges of warp $W_{Ph}$ and the strength $S_{Ph}$ of phase applied to a sample image (Asghari and Jalali, 2015). . . . .	71
4.1	Block diagram of proposed edge detection method. . . . .	74
4.2	Example of (a) a grayscale image with extended “dark” areas (black color) and the PST output phase image with the intensity of red color representing the intensity of the phase (b) including artifacts and (c) after removing the artifacts. . . . .	75
4.3	Kernel used to determine the number of “dark” neighbours surrounding a “dark” pixel. . . . .	75
4.4	Edge detection performance of the proposed technique on a sample from the Coherent Change Detection Challenge data set, (a) Original sample, (b) Detected edges using the proposed method using the following parameters: $\Delta f = 1.8$ , $N = 12$ , $S_{Ph} = 5$ , $W_{Ph} = 14$ , $T_d = 3.3\%$ , $T_a = 16$ , $T_e = 0.2$ . . . . .	77
4.5	Edge detection performance on a sample from the Vancouver, BC dataset (a) Original sample, (b) Detected edges using the proposed method with parameters: $\Delta f = 0.12$ , $N = 14$ , $S_{Ph} = 0.7$ , $W_{Ph} = 10$ , $T_d = 3.3\%$ , $T_a = 16$ , $T_e = 0.0042$ , (c) Overlay edges in a part of the sample image using the following parameters: $\Delta f = 0.2$ , $N = 5$ , $S_{Ph} = 0.7$ , $W_{Ph} = 8$ , $T_d = 33\%$ , $T_a = 16$ , $T_e = 0.008$ . . . . .	78
5.1	Real (Re) and imaginary (Im) parts of (a) a Barker 13 code and (b) a fractional Barker 13 waveform generated using samples per bit rate $o = 50$ , and fractional order $a = 0.5$ . . . . .	82

5.2	Ambiguity function in logarithmic scale of (a) a Barker 13 code and (b) a fractional Barker 13 waveform generated using $o = 50$ , $a = 0.5$ . . . . .	83
5.3	Ambiguity function contour of (a) a LFM pulse with time-bandwidth product $TB = 2600$ and, (b) a fractional Barker 13 waveform generated using $o = 200$ , $a = 0.5$ . . . . .	83
5.4	Complex plane representation of a Barker 13 code modulated with FrFT using $a = 0.5$ and $o = 200$ before (a) and after reconstruction with CE constraint (b). . . . .	85
5.5	Spectrum and AC function of a fractional waveforms of different fractional Barker 13 waveform generated using $o = 200$ and $a = 0.5$ before ( $s_{0.5}$ ) and after ( $\tilde{s}_{0.5}$ ) dividing it by its modulus. . . . .	86
5.6	Block diagram of the Gerchberg-Saxton algorithm. . . . .	87
5.7	Peak-to-average power ratio (PARP) of CE and non-CE Barker 13 (a) and P4 25 (b) fractional waveforms of different fractional order using $r = 50$ and $r = 200$ . . . . .	88
5.8	Ratios of the AF quality parameter for fractional Barker 13 waveforms of different $a$ before and after applying CE constraints in terms of resolution (a), SLL (b) and interference (c) for $o = 50$ and resolution (d), SLL (e) and interference (f) for $o = 200$ . . . . .	89
5.9	Ratios of the AF quality parameter for fractional P4 25 waveforms of different $a$ before and after applying CE constraints in terms of resolution (a), SLL (b) and interference (c) for $o = 50$ and resolution (d), SLL (e) and interference (f) for $o = 200$ . . . . .	90
5.10	SLL-thresholded maxima of the cross-correlations between the waveforms generated using different $a$ and the same $\mathbf{c}$ for $o = 50$ . The cases above the thresholds are shown in black. . . . .	92
5.11	SLL-thresholded maxima of the cross-correlations between the waveforms generated using different $a$ and the same $\mathbf{c}$ for $o = 200$ . The cases above the thresholds are shown in black. . . . .	93
5.12	Reuse interval of CE fractional P4 25 waveforms of different $a$ for $o = 200$ and its overall and optimum maxima resulting for different interval of $a$ . . . . .	94
5.13	Matched filter outputs of the transmitted sequence $w_{tr}$ after applying the matched filter with (a) $s_1$ , (b) $s_2$ and (c) $s_3$ respectively. . . . .	96
5.14	Theoretical (a) and experimental (b) Zero Doppler cut of waveform's $s_1$ auto-AF and its cross-AF with waveform $s_2$ . . . . .	96

5.15	Sensors and targets geometry in a surveillance area . . . . .	98
5.16	Ambiguity Function Zero-Doppler cut for all three waveforms in (a) CE fractional, (b) LFM and (c) DSSS sets. . . . .	100
5.17	Occupied bandwidth for each waveform of (a) CE fractional, (b) LFM and (c) DSSS sets. . . . .	101
5.18	Mean error of center target's real and estimated location for differ- ent horizontal distances from the left target using three different waveform libraries. . . . .	102
5.19	Mean error of left target's real and estimated location for different horizontal distances from the center target using three different waveform libraries. . . . .	102
5.20	Range profile of the two targets with distance 2.5m to each other in the first transmitter-receiver pair (2,2) (north-west) using CE fractional, LFM and DSSS waveform sets. . . . .	103
5.21	Block diagram of the proposed multiplexing scheme. . . . .	105
5.22	Time-frequency representation though spectrogram a Co-radar waveform with (a) $N_c = 6$ and (b) $N_c = 20$ chirp sub-carriers. . .	105
5.23	Real ((a)) and approximated ((b)) AF of a Co-Radar waveform generated for $N_c = 6$ . . . . .	107
5.24	Real ((a)) and approximated ((b)) AF of a Co-Radar waveform generated for $N_c = 20$ . . . . .	108
6.1	System geometry assuming (a) distributed and (b) co-located sensor allocation. . . . .	120
6.2	Example of two transmitter-receiver pairs $(i, j)$ and $(i', j')$ and a target with dimensions $\Delta_x$ and $\Delta_y$ , with each sensor's line of sight (dashed line) having a different angle $\gamma$ with the positive x-axis . .	121
6.3	Sensors geometry in the surveillance area . . . . .	129
6.4	Normalized sum of non diagonal elements of the channel correlation matrix $\mathbf{\Omega}$ for target dimensions (a) $\Delta_x = \Delta_y = \lambda$ and (b) $\Delta_x = 1/2\lambda$ and $\Delta_y = 2\lambda$ ; transmitters and receivers are denoted by squares ( $\square$ ) and rhombi ( $\diamond$ ) respectively. . . . .	130
6.5	MIMO AF when the target's centre of gravity is positioned in (a) $\mathbf{x}_{0,\mathcal{Q}} = [0, 0]^T$ and (b) $\mathbf{x}_{0,\mathcal{Q}} = [-400, -400]^T$ , and orthogonal waveforms and constant energy parameter is considered; trans- mitters and receivers are denoted by squares ( $\square$ ) and rhombi ( $\diamond$ ) respectively. . . . .	131

6.6	Zoomed part of the MIMO AF when the target's centre of gravity is positioned in (a) $\mathbf{x}_{0,\mathcal{Q}} = [0, 0]^T$ and (b) $\mathbf{x}_{0,\mathcal{Q}} = [-400, -400]^T$ , and orthogonal waveforms and constant energy parameter is considered.	131
6.7	Values of $\text{SNR}_\theta$ in (a) random and (b) line sensor configuration, when orthogonal waveforms and constant energy parameter are considered; transmitters and receivers are denoted by squares ( $\square$ ) and rhombi ( $\diamond$ ) respectively.	132
6.8	MIMO AF when the target's centre of gravity is positioned in (a) $\mathbf{x}_{0,\mathcal{Q}} = [0, 0]^T$ and (b) $\mathbf{x}_{0,\mathcal{Q}} = [-400, -400]^T$ , and fully correlated waveforms and constant energy parameter is considered; transmitters and receivers are denoted by squares ( $\square$ ) and rhombi ( $\diamond$ ) respectively.	133
6.9	Zoomed part of the MIMO AF when the target's centre of gravity is positioned in (a) $\mathbf{x}_{0,\mathcal{Q}} = [0, 0]^T$ and (b) $\mathbf{x}_{0,\mathcal{Q}} = [-400, -400]^T$ , and fully correlated waveforms and constant energy parameter is considered.	134
6.10	Values of $\text{SNR}_\theta$ in (a) random and (b) line sensor configuration, when fully correlated waveforms and constant energy parameter are considered; transmitters and receivers are denoted by squares ( $\square$ ) and rhombi ( $\diamond$ ) respectively.	134
6.11	Euclidean distance between the theoretical and simulated channel correlation matrix for an approximated (a) distributed and (b) co-located system.	137
6.12	Sensor geometry for the simulated system in (a) distributed and (b) co-located configuration.	138
6.13	Illustration of (a) proposed and (b) traditional MIMO AF in a distributed system configuration using orthogonal waveforms.	139
6.14	Illustration of (a) proposed and (b) traditional MIMO AF in a distributed system configuration using correlated waveforms.	140
6.15	Illustration of (a) proposed and (b) traditional MIMO AF in a distributed system configuration using correlated waveforms. The red line marks the $-3\text{dB}$ contours of the MIMO AFs, while the white line marks the contour where the proposed MIMO AF is 50% lower than the canonical.	140
6.16	Illustration of (a) proposed and (b) traditional MIMO AF in a co-located system configuration using orthogonal waveforms.	141

- 
- 6.17 Illustration of (a) proposed and (b) traditional MIMO AF for area close to the target, in a co-located system configuration using orthogonal waveforms. The red line marks the  $-3\text{dB}$  contours of the MIMO AFs. . . . . 142
- 6.18 Illustration of (a) proposed and (b) traditional MIMO AF in a co-located system configuration using fully correlated waveforms. . . 142
- 6.19 Illustration of (a) proposed and (b) traditional MIMO AF for area close to the target, in a co-located system configuration using fully correlated waveforms. The red line marks the  $-3\text{dB}$  contours of the MIMO AFs, while the white line marks the  $10\text{dB}$  contour of  $\text{SNR}_\theta$ . 143

# List of tables

2.1	Known Barker Codes . . . . .	25
2.2	Spectrum Sharing for Radar and Communication systems . . . . .	35
2.3	Comparison Between Different Information-Embedding Techniques (Hassanien et al., 2016) . . . . .	40
4.1	Design Parameters of Edge Detection Algorithm . . . . .	76
5.1	Fractional order reuse interval for different values of $\alpha$ . . . . .	93
5.2	Time-Bandwidth Product . . . . .	99
6.1	Theoretical MIMO System Variables . . . . .	133
6.2	Simulated MIMO System Variables . . . . .	139

# Nomenclature

## Roman Symbols

$\mathbf{A}(\cdot)$	MIMO time delay, time scaling, and frequency shift transfer matrix
$A$	Arbitrary real positive constant
$a$	Order of FrFT
$\mathcal{A}_{\text{Ca}}(\cdot, \cdot)$	Canonical AF
$\mathcal{A}_{\text{Co}}(\cdot, \cdot)$	AF of Co-Radar waveform
$\mathcal{A}_{\text{Co,Cross}}(\cdot, \cdot)$	Cross-AF between different sub-carriers
$\mathcal{A}_{\text{Co,Orth}}(\cdot, \cdot)$	AF of Co-Radar waveform accounting orthogonal sub-carriers
$\mathbf{a}(\cdot)$	Time delay, time scaling, and frequency shift transfer matrix
$\mathcal{A}_{\text{MIMO}}(\cdot, \cdot)$	KLD based MIMO AF
$\hat{\mathcal{A}}_{\text{MIMO}}(\cdot, \cdot)$	Normalised KLD based MIMO AF
$B$	Bandwidth
$B_{\text{LFM}}$	Bandwidth of LFM waveform
$B_m$	Modulation bandwidth
$B_{s_i}$	Bandwidth of Co-Radar waveform
$B_{\text{Lo}}$	Localisation kernel bandwidth
$B_m$	Bandwidth of symbol sequences
$B_{s_i}$	Bandwidth of fractional waveform
$\mathbf{C}(\cdot)$	Covariance matrix of $\mathbf{H}(\cdot)$

---

$c$	Speed of light in vacuum $c \approx 3 \times 10^8$ m/s
$c_k$	Code bit
$\mathcal{CN}(\cdot, \cdot)$	Complex normal distribution
$\mathbf{c}$	Code vector
$d$	Spatial distance
$d_0$	Distance from radar to target
$\hat{d}$	Distance between targets
$\mathbf{D}$	Distance vector from scatter to transmitter/receiver
$\mathcal{F}$	Discrete Fourier transform transfer matrix
$\mathcal{F}_a$	Discrete fractional Fourier transform transfer matrix of order $a$
$\mathbf{E}(\cdot)$	MIMO signal energy matrix
$e$	Mathematical constant $e \simeq 2.71 \dots$
$E$	Energy of signal
$\hat{E}_{\mathcal{T}}$	Energy of the signal on transmitter
$\mathcal{E}\{\cdot\}$	Expected value
$f_c$	Carrier frequency
$f_{\text{cut}}$	Cut-off frequency of low-pass filter
$f_D$	Doppler frequency shift
$f_{Di}$	Doppler shift in $i$ -th transmitted pulse
$f_{D\text{max}}$	Maximum estimated Doppler frequency shift
$f_i$	Carrier frequency at the $i$ -th transmitter
$f_s$	Sampling frequency
FFT $\{\cdot\}$	Fast Fourier transform
STFT $\{\cdot\}$	Sort time Fourier transform

---

$\mathcal{F}\{\cdot\}$	Fourier transform
$\mathcal{F}^a\{\cdot\}$	Fractional Fourier transform of order $a$
$\mathcal{F}^{-1}\{\cdot\}$	Inverse Fourier transform
$g(\cdot)$	Emitted time signal from transmitter
$G$	Gain at transmitter/receiver
$G[\cdot]$	DFT of $g$ .
$g[\cdot]$	CE sequence approximating $s_a$
$\mathcal{G}$	Manifold of PDFs
$\mathbf{H}(\cdot)$	MIMO amplitude and phase shift matrix
$\mathbf{h}(\cdot)$	Amplitude and phase shift vector
$h$	Amplitude and Doppler shift of signal
$h(\cdot)$	Amplitude and phase shift of transmitted signal
$h_{\text{MF}}$	Matched filter impulse response
$\mathcal{H}$	Hypotheses of an event
$\mathcal{I}(\cdot, \cdot)$	KLD from a PDF to an other
$\mathcal{I}_{\text{ub}}(\cdot)$	Upper bound of $\mathcal{I}(\cdot, \cdot)$
IFFT $\{\cdot\}$	Inverse fast Fourier transform
$\mathbf{K}(\cdot)$	MIMO phase steering matrix
$K$	Length of code sequence
$\mathbf{k}(\cdot)$	Phase steering vector
$\mathbf{K}_a(\cdot, \cdot)$	FrFT of order $a$ kernel
$K_{\text{PST}}[\cdot, \cdot]$	PST phase kernel
$L$	Non free-space losses in transmitter-receiver path
$L_S$	Length of fractional waveform library $\mathbf{S}$

---

$m[\cdot]$	Symbol sequence
$n$	Discrete sample variable
$n(\cdot)$	Noise at the receiver
$\mathbf{n}$	Vector of noise at the receiver
$n_{\max}$	Discrete sample in which the SNR is maximum
$N_{\mathcal{T}/\mathcal{R}/\mathcal{Q}}$	Number of transmitters/receivers/scatterers
$N_c$	Number of sub-carriers
$N_m$	Number of symbol sequences
$N_s$	Number of orthogonal waveforms
$o$	Samples per code bit
$PD[\cdot, \cdot]$	PST kernel phase derivative
$R$	Range of sensors from the centre of the scene
$r(\cdot)$	Signal at the receiver
$\mathbf{r}(\cdot)$	Vector of received signal
$\mathbf{R}$	Correlation matrix of received signal
$\text{rect}\{\cdot\}$	Rectangular function
$\mathbf{S}$	MIMO transmitted signal matrix
$\mathbf{S}$	Waveform library composed by fractional waveforms
$s_a[\cdot]$	Fractional waveform of order $a$
$s(\cdot)$	Complex envelope of time signal in transmitter
$\mathbf{s}$	Vector of transmitted signal
$s_{\text{LFM}}$	Near-orthogonal LFM waveforms
$S_a[\cdot]$	DFT of $s_a$
$s_{i_{\text{OFDM}}}$	Sub-carrier of OFDM signal

---

$s_{i_{\text{OFDM-LFM}}}$	Sub-carrier of OFDM signal using LFM baseband waveforms
$s[\cdot]$	Waveform generated by a code sequence
$s_a[\cdot]$	Fractional waveform
$s_{\text{Co}}[\cdot]$	Co-Radar waveform
SNR	Signal to noise ratio
$S_{\text{Ph}}$	Strength of phase in PST
$T$	Pulse width
$t$	Time variable
$T_{\text{Ed}}$	Threshold applied on phase image for edge extraction
$\mathbf{U}$	Velocity vector from scatter to transmitter/receiver
$\mathbf{u}$	Transmitter/receiver/target/scatterer velocity in Cartesian plane
$w(\cdot)$	Sub-waveforms composing $w_{tr}$
$w_{tr}(\cdot)$	Transmitted waveform from vector signal generator
$W_{\text{Ph}}$	Wrap of phase in PST
$\text{WVD}(\cdot, \cdot)$	Wigner-Ville Distribution
$x$	Coordinate in $x$ -axis
$\mathbf{x}$	Transmitter/receiver/target/scatterer location in Cartesian plane
$\tilde{x}[\cdot]$	Arbitrary waveform with unitary envelope
$x[\cdot]$	Arbitrary discrete signal
$x(\cdot)$	Arbitrary time signal
$\mathbf{Y}(\cdot)$	MIMO time and frequency sifted baseband signal matrix
$y(\cdot, \cdot)$	Time and frequency sifted baseband time signal
$y$	Coordinate in $y$ -axis
$\mathbf{Z}$	MIMO scatters' complex reflectivity matrix

$\mathbf{z}$	Scatters' complex reflectivity vector
$\mathcal{Z}(\cdot, \cdot)$	Reflectivity of target in the Cartesian plane
$\tilde{\mathbf{Z}}$	Covariance matrix of $\mathbf{Z}$

### Greek Symbols

$\alpha$	Time scaling factor
$\delta(\cdot)$	Dirac delta function
$\Delta B$	Frequency bin of modulation code
$\Delta d$	Range resolution
$\Delta\phi$	Phase delay
$\Delta T$	Time bin of modulation code
$\Delta\tau$	Delay resolution
$\Delta_x$	Target x-axis dimension
$\Delta_y$	Target y-axis dimension
$\eta[\cdot]$	Phase of arbitrary complex waveform
$\lambda$	Wavelength of carrier signal
$\mathbf{\Omega}(\cdot)$	Channel correlation matrix
$\omega$	Angular frequency shift
$\hat{\Omega}(\cdot)$	Normalised channel correlation degree
$\mathbf{\Phi}(\cdot)$	Correlation matrix of $\mathbf{H}(\cdot)$
$\phi$	Phase shift
$\phi[\cdot]$	Phase of $G[\cdot]$
$\phi_{\text{PST}}[\cdot, \cdot]$	Phase of PST phase kernel
$\phi_{\text{PST,polar}}[\cdot]$	Phase of PST phase kernel with circular symmetry
$\pi$	Mathematical constant $\pi \simeq 3.14\dots$

$\Psi(\cdot, \cdot)$	Cross-correlation matrix of differently indexed $\mathbf{H}(\cdot)$
$\psi[\cdot]$	Phase of $g[\cdot]$
$\varrho_{\text{LFM}}$	Compression ratio of a LFM pulse
$\varrho_{\text{PC}}$	Compression ratio of a PC pulse
$\sigma_n^2$	Noise variance
$\sigma_0^2$	Target RCS variance
$\tau$	Time delay
$\tau_0$	Round trip time of a signal to propagate from the radar to the target
$\tilde{\tau}$	Signal delay expressed in Taylor series
$\tau_{\text{max}}$	Time instant in which the SNR is maximum
$\tau_{\text{null}}$	Delay of the first null in zero-Doppler AF cut
$\theta$	Location parameter
$\vartheta$	Rotation angle of FrFT
$\theta_{\text{be}}$	Bearing angle of sensor pairs
$\theta_{\text{st}}$	Steering direction of a phased array
$\zeta$	Complex reflectivity

### Superscripts

$\{\cdot\}^*$	Complex conjugate operator
$\{\cdot\}^\dagger$	Conjugate transpose operator
$\{\cdot\}^{(\cdot)}$	Scatter identifier
$\{\cdot\}^T$	Transpose operator

### Subscripts

$\{\cdot\}_\kappa$	Target notation
--------------------	-----------------

---

$\{\cdot\}_{\mathcal{Q}}$	Scatters notation
$\{\cdot\}_{\mathcal{R}}$	Receivers notation
$\{\cdot\}_{\mathcal{T}}$	Transmitters notation
$\{\cdot\}_{\theta}$	Resolution bin identifier

**Other Symbols**

$\angle\langle\cdot\rangle$	Angle operator
$\int$	Integration operator
$\Sigma$	Summation operator

**Acronyms / Abbreviations**

2-D	Two Dimensional
3-D	Three Dimensional
AC	Auto-Correlation
ADC	Analogue-to-Digital Converter
AF	Ambiguity Function
BC	Binary Coding
BLUE	Best Linear Unbiased Estimator
C/A	Coarse/Acquisition
CAF	Cross Ambiguity Function
CC	Cross-Correlation
CDFCW	Chaotic Discrete Frequency-Coding Waveform
CE	Constant Envelope
Co-Radar	Communicative Radar
CRB	Cramer-Rao Bound
CREW	Cognitive Radar Engineering Workspace

---

CW	Continuous Waveform
DC	Duty Circle
DEM	Digital Evaluation Maps
DFCW	Discrete Frequency-Coding Waveform
DFRC	Dual Function Radar Communication
DFrFT	Discrete Fractional Fourier Transform
DMRS	Distributed multistatic radar systems
DRS	Distributed Radar Systems
DSP	Digital Signal Processing
DSSS	Direct Sequence Spread Spectrum
ECM	Electronic Countermeasures
EM	Electromagnetic
EMI	Electromagnetic Interference
EPM	Electronic Protective Measures
FF	Fixed Frequency
FFrFT	Fast Fractional Fourier Transform
FIM	Fisher Information Matrix
FMCW	Frequency Modulated Continuous Wave
FM	Frequency Modulation
FrFT	Fractional Fourier Transform
FT	Fourier Transform
GSA	Gerchberg-Saxton Algorithm
IF	Intermediate Frequency
IFT	Inverse Fourier Transform

---

IOs	Illuminators of Opportunity
ITS	Intelligent Transportation Systems
KLD	Kullback Leibler Divergence
LFM	Linear Frequency Modulated
LPI	Low Probability of Intercept
MGSA	Modified Gerchberg-Saxton Algorithm
MIMO	Multiple-Input Multiple-Output
MPS	Minimum Peak Sidelobe
NLFM	Non-Linear Frequency Modulated
NRT	Noise Radar Technology
OFDM	Orthogonal Frequency Division Multiplexing
PAF	Periodic Ambiguity Function
PAPR	Peak-to-Average Power Ratio
PC	Phase-Coded
PCR	Pulse Compression Ratio
PDF	Probability Density Function
PM	Phase Modulation
PPI	Plan Position Indicator
PRF	Pulse Repetition Frequency
PRI	Pulse Repetition Interval
PSLL	Peak Side Lobe Level
PST	Phase Stretch Transform
RADAR	RAdio Detecting And Raging
RCS	Radar Cross-Section

---

RF	Radio Frequencies
ROA	Ratio Of Averages
SAR	Synthetic Aperture Radar
SDR	Software Defined Radio
SFCOS	Same Frequency Coding Orthogonal Signals
SISO	Single-Input Single-Output
SLL	Side Lobe Level
SNR	Signal-to-Noise Ratio
SS	Spectrum Sharing
STFT	Short Time Fourier Transform
SWAP	Size Weight And Power
T-F	Time-Frequency
TOA	Time Of Arrival
T/R	Transmit/Receive
WD	Waveform Diversity
WVD	Wigner-Ville Distribution

# Chapter 1

## Introduction

### 1.1 Preface

In recent years multiple-input and multiple-output (MIMO) radar systems have attracted the interest of the research community due to their capability to significantly increase their performance compared to traditional phased array radars. Generally, MIMO radar systems are classified into two main categories: co-located and distributed, depending on how the antennas of each system are spatially allocated (Haimovich et al., 2008; Li and Stoica, 2007). The co-located configuration is similar in geometry to the phased array systems with all the antennas placed in a close proximity, while in the distributed, also known as statistical, structure the antennas are widely extended in a large area. The co-located configuration offers superior parameter identification and flexibility of transmitted beam-pattern designs (Hassanien and Vorobyov, 2010; Nysaeter and Iwe, 2016), while the distributed configuration allows enhanced target localization and detection performance (Fishler et al., 2006; Godrich et al., 2010). In addition, MIMO radar systems generally have shown great potential supporting fading mitigation (Mao et al., 2015), and interference and jamming suppression (Bechter et al., 2017; Li et al., 2014a). The main distinctive characteristic between MIMO and other multisensor radar systems is that in MIMO each antenna unit can independently transmit an arbitrary waveform, while each receiving antenna can receive all the reflected signals. These echo signals can be re-assigned to each transmitter-receiver pair separately considering the diversity in the operating waveforms.

In MIMO radar applications, the use of optimised waveform designs is of primary importance allowing significant improvement in target detection performance, tracking and resolution (Li and Stoica, 2009; Yang and Blum, 2007;

Zhou et al., 2016). Several design methods based on fixed and adaptive radar waveforms have been extensively investigated providing waveforms suitable for different applications (Cui et al., 2014; Liu et al., 2014b; Mehany et al., 2015; Wang, 2015a; Wen-kun et al., 2016). In (Clemente et al., 2014b) a new approach was proposed to generate radar waveform libraries through applying the fractional Fourier Transform (FrFT) (Ozaktas et al., 2001) to sequences with good ambiguity function (AF) properties such as Barker 13 code. These novel libraries were shown to provide significant advantages considering delay resolution, interference and sidelobe level reduction. Furthermore, a reuse evaluation in (Clemente et al., 2014a) demonstrated that multiple low cross-correlation waveforms could be generated by applying a FrFT of different order to the same sequence and also changing its cardinality.

The AF is one of most common tools used to evaluate the performance of a radar system providing information regarding the resolution, estimation accuracy, probability of detection and false alarm etc. In the case of mono-static radar systems the AF is defined as the response of a filter matched to the transmitted signal for different time delays and Doppler shifts in the received signal (Levanon and Mozeson, 2004). However, the application of the same concept is not sufficient to evaluate a MIMO radar system since parameters such as the system's geometry and the degree of correlation between the operating waveforms play a significant role in the overall performance of the system. In recent years various formulations of the AF for multi-static radars have been proposed based on optimal detectors (Chen et al., 2012; Derham et al., 2010; Radmard et al., 2014; San Antonio et al., 2007). Using the concept of optimum detector, the MIMO AF can be obtained by summing the matched filtered result from each receiver (Derham et al., 2010; San Antonio et al., 2007). Following a different approach, an alternative AF definition could be based on the log-likelihood function and the concept of information theory (Chen et al., 2012; Li and Stoica, 2009; Radmard et al., 2014). A very similar definition approach of the AF based on the Kullback-Leibler divergence (KLD) was first introduced for a monostatic system configuration in (Rendas and Moura, 1998).

Synthetic aperture radar (SAR) refers to a particular form of imaging radar system, where a real aperture or antenna is moved through a series of sequential positions along the inspected area to implement a larger synthetic antenna. Applying a combination of signal processing techniques, the SAR returns can synthesise a fine resolution, photograph-like rendering of the illuminated scene (Richards et al., 2010). Edge detection in SAR images can provide valuable information

such as coastline, road and man-made target returns. While the same techniques from optical image processing can also be applied to SAR images, the later suffers from multiplicative noise, called speckle, and therefore often preprocessing is required. Through the last decades, several approaches for reducing speckle noise have been suggested (Lopes et al., 1990; Yu and Acton, 2002), while others focus directly on edge detection in its presence (Baselice et al., 2014; Jiang et al., 2015; Prasad et al., 2013; Touzi et al., 1988). In (Asghari and Jalali, 2014), a novel edge detection scheme based on the phase stretch transform (PST) is proposed. The good performance of the PST was demonstrated both in optical and biomedical images.

## 1.2 Motivation

One of the aims of this thesis is to investigate new signal processing algorithms in generating novel waveform libraries with good AF properties and reconstructing these waveforms under CE constraints. Intent of this waveform design scheme is to offer a large number of low cross-correlation waveforms suitable for MIMO radar systems, while also providing the basis to allow message exchange operations through embedding information into the radar waveforms. Moreover, this thesis targets to explore a generalised AF for facilitating both narrowband and wideband signals in a MIMO sensor system. In addition this thesis is aimed to investigate an enhanced algorithm for SAR image edge detection, which can effectively reduce the embedded noise and remove phase image artefacts.

The research objectives presented in this thesis are: the development of an effective technique to obtain radar waveform libraries applying FrFT on code sequences; the development of a low complexity and efficient algorithm to reconstruct FrFT based waveforms under CE constraints using a modified Gerchberg-Saxton algorithm (MGSA); a preliminary study regarding the information exchange between radar systems using FrFT based waveform design; the invention of the generalised signal model for MIMO radar systems and the corresponding MIMO AF utilizing the KLD and expressed by the channel and operating signal correlation matrices; the design and implementation of an enhanced algorithm for edge detection of SAR images exploiting the advantages of the PST; the study of algorithm parameter tuning for optimising the image edge detection. The applicability and the performance of the aforementioned signal processing techniques will be evaluated through simulations and experiments in various MIMO radar scenarios.

Moreover, the thesis will address the inventions, developments, enhancements and modifications required to accomplish the research, as to achieve enhanced resolution and target identification in MIMO environments and excellent quality in performing edge detection of SAR images.

## 1.3 Contribution

The research enclosed in this thesis includes original contributions in the field of MIMO radar networks, spectrum sharing and SAR image processing. The thesis contributions are as follows:

- A new method for edge detection in SAR images is developed, using an enhanced scheme based on the PST. The presented algorithm is shown to be capable of reducing speckle noise effects while also removing phase image artefacts introduced by the PST implementation. Experimental results based on two SAR image datasets demonstrate the high-accuracy edge extraction capabilities of the proposed scheme. In addition, the ability of the developed scheme to adjust for different tasks is shown.
- A novel waveform design scheme to generate waveform libraries based on the FrFT is introduced. In conjunction with the proposed design, an efficient algorithm based on the MGSA is employed in order to reconstruct the proposed waveforms libraries under constant envelope constraints. The suitability of the generated waveforms for monostatic and MIMO radar applications is demonstrated through simulation analysis. Furthermore, the applicability of the proposed scheme is experimentally validated, while its performance is evaluated and compared with conventional techniques in a distributed MIMO radar scenario. The research results highlight that the proposed design scheme is able to provide an efficient way of generating multiple near-orthogonal waveforms with good AF properties suitable for MIMO radar scenarios.
- A new modulation scheme is developed utilising the FrFT based waveform design for joint radar communication systems. The proposed technique allows information to be embedded into waveforms suitable for radar operations. The performance of the proposed waveform design is also examined based on its AF properties.

- A novel AF designed for MIMO radar systems is presented. The definition of the MIMO AF is based on the KLD and applied on a generalised MIMO signal model. The proposed approach offers a flexible definition composed by channel and signal correlation matrices, accounting for different geometry and operating waveforms configurations respectively. Moreover, the described MIMO AF maximally stretched between 0 and 1 while its relationship with other proposed definition is also examined. The behaviour of the proposed MIMO AF is investigated for different target and waveform configuration. Lastly the performance of the proposed MIMO AF is evaluated and compared with more conventional approaches in simulated MIMO systems.

## 1.4 Publications

### Journal Papers

- Persico, A. R., Clemente, C., Gaglione, D., Ilioudis, C., Cao, J., Pallotta, L., Maio, A. D., Proudler, I., and Soraghan, J. J. (2017). On Model, Algorithms and Experiment for Micro-Doppler based Recognition of Ballistic Targets. *IEEE Transactions on Aerospace and Electronic Systems*, PP(99):1–1

### Conference Papers

- Ilioudis, C. V., Clemente, C., Proudler, I., and Soraghan, J. (2016b). MIMO Radar Ambiguity Functions: A Case Study. In *11th IMA International Conference on Mathematics in Signal Processing*, pages 1–5
- Ilioudis, C. V., Clemente, C., Proudler, I., and Soraghan, J. (2016a). Ambiguity function for distributed MIMO radar systems. In *2016 IEEE Radar Conference (RadarConf)*, pages 1–6
- Gaglione, D., Clemente, C., Persico, A. R., Ilioudis, C. V., Proudler, I. K., and Soraghan, J. J. (2016b). Fractional Fourier Transform Based Co-Radar Waveform: Experimental Validation. In *2016 Sensor Signal Processing for Defence (SSPD)*, pages 1–5
- Gaglione, D., Clemente, C., Ilioudis, C. V., Persico, A. R., Proudler, I. K., and Soraghan, J. J. (2016a). Fractional fourier based waveform for a joint radar-communication system. In *2016 IEEE Radar Conference (RadarConf)*, pages 1–6

- Ilioudis, C. V., Clemente, C., Asghari, M. H., Jalali, B., and Soraghan, J. J. (2015a). Edge detection in SAR images using Phase Stretch Transform. In *2nd IET International Conference on Intelligent Signal Processing 2015 (ISP)*, pages 1–5
- Persico, A. R., Clemente, C., Ilioudis, C., Gaglione, D., Cao, J., and Soraghan, J. (2015). Micro-Doppler Based Recognition of Ballistic Targets Using 2D Gabor Filters. In *2015 Sensor Signal Processing for Defence (SSPD)*, pages 1–5
- Clemente, C., Parry, T., Galston, G., Hammond, P., Berry, C., Ilioudis, C., Gaglione, D., and Soraghan, J. J. (2015). GNSS based passive bistatic radar for micro-Doppler based classification of helicopters: Experimental validation. In *2015 IEEE Radar Conference (RadarCon)*, pages 1104–1108
- Ilioudis, C. V., Clemente, C., Proudler, I., and Soraghan, J. J. (2015b). Performance analysis of fractional waveform libraries in MIMO radar scenario. In *2015 IEEE Radar Conference (RadarCon)*, pages 1119–1124
- Ilioudis, C., Clemente, C., Proudler, I., and Soraghan, J. (2014). Constant Envelope Fractional Fourier Transform based Radar Waveforms Detection and Localization Performance in DMRS. In *Sensor Signal Processing for Defence Conference 2014 (SSPD 2014), Edinburgh, UK*, pages 1–6
- Clemente, C., Ilioudis, C., Gaglione, D., Thompson, K., Weiss, S., Proudler, I., and Soraghan, J. (2014a). Reuse of Fractional Waveform Libraries for MIMO Radar and Electronic Countermeasures. In *6th International Symposium on Communications, Control, and Signal Processing (ISCCSP 2014), Athens, Greece*

## 1.5 Thesis Organization

The remainder of the thesis is divided into six chapters organised as follows: Chapter 2 introduces the key concepts of radar systems including basic operations and advanced systems. The basic principles of pulse compression is also discussed along with the most common techniques in waveform design. Later, the notion of multisensor systems and their categorisation in connection with their operating waveforms and spatial geometry. The topical issue of spectrum sharing is also investigated along with the most recent advances in waveform diversity and joint

communication radar systems. Finally, the basic principles of SAR and the current issues in radar image processing are described.

Chapter 3 is dedicated to advanced time-frequency transforms. First the concept of time-frequency analysis is introduced with commonly time-frequency signal representations being also discussed. Later, the concept of AF is introduced with the traditional, KLD based and other common definitions being also provided. Additionally, an extensive analysis in FrFT is presented. Specifically, the properties, implementations and applications of FrFT in radar systems are discussed in more detail. Finally, the PST is presented with focus on its applications in image edge detection.

Chapter 4 introduces a new method to extract edge images based on the PST. The proposed method attempts to address issues associated with the presence of speckle noise in SAR images and the cancellation of the introduced artifacts in the edge images due to pre-processing stages. The performance of the proposed method is experimentally evaluated using real SAR images from two different datasets.

Chapter 5 is dedicated in the proposed design of fractional waveforms. The first section of the chapter introduces the concept of utilising the FrFT to generate waveforms suitable for MIMO radar applications and how constant envelope restriction can also be addressed. Validation of the proposed waveform generation scheme is later held using experimental results and simulations. Finally, a new method is introduced for achieving joint communication and radar functionality using information embedded waveforms based on the concept of the fractional waveforms.

Chapter 6 presents an in depth investigation concerning the concept of the AF applied on MIMO radar systems. First, the signal model of MIMO radar systems for extended targets is derived. Based in this signal model a framework is defined to approximate the degree of correlation between the different transmitter-receiver channels. Later the proposed MIMO AF is formulated based on the KLD with examples and illustration being provided. Moreover, Chapter 6 discusses the relation of the proposed and other AF definitions. Finally, simulations are carried out to explore the performance and efficiency of the proposed framework.

Chapter 7 presents a summary of the thesis conclusions in connection with the future direction of research.

The appendices provide a proof regarding the relationship of FrFT and the AF, the relation of phase integral and the sinc function, the inverse correlation

---

matrix of a MIMO radar signal, lower limits, and definition of matrices used in the thesis.

# Chapter 2

## Radar Systems

### 2.1 Introduction

In this chapter, a review of radar research concepts is discussed. Key areas, such as basic radar concepts, advanced radar techniques, radar waveform design and signal processing will be reviewed. Pulse compression techniques will be an area of focus, providing a short summary of the most commonly used waveform modulation algorithms and code sequences, while the current challenges of research in waveform design field are also introduced. Additionally, different categories of multisensing are discussed and an overview in most challenging research area is presented combining basic operation principles and advanced multiple-input multiple-output (MIMO) radar techniques. Various aspects of the spectrum overcrowding are also discussed with focus on their effects in radar systems. More specifically, recent advances regarding spectrum sharing (SS) techniques such as waveform diversity (WD) in MIMO radar systems and dual-function radar communication (DFRC) systems are discussed in order to identify the introduced assets and trade-offs. Finally, the advanced concepts in synthetic aperture radar (SAR) are presented including SAR imaging, speckle noise reduction and edge detection.

### 2.2 Basic and Advanced Techniques

Radar is a highly multidisciplinary field with researchers focusing among other subjects on phenomenology, antenna technology, waveform design, detection, tracking and target identification, multi-sensor fusion and concepts of operation (Gini et al., 2012; Levanon and Mozeson, 2004; Richards, 2005; Richards et al., 2010). Modern

radar are highly complex sensing systems, employing the latest advances in technology and relying on sophisticated algorithms and signal processing techniques to accomplish accurate results. Over the last decades many researchers have made great efforts to develop new techniques of advanced target identification and parameter estimation for various types of applications. More specifically, there have been numerous publications focused on modern radar systems improving significantly the parameter identifiability, applicability of adaptive MIMO arrays for target detection, parameter estimation, and design flexibility for transmitted beampattern (Godrich et al., 2010, 2011; Li et al., 2007; Maio and Lops, 2007; Yang and Blum, 2007).

Basic principles and advanced techniques of modern radar systems are critical to the performance of current and future radar systems. Basic techniques of modern radar include principal radar concepts, i.e. fundamental radar principles and functions, radar signal characteristics, external factors affecting target tracking, radar subsystems and key aspects of radar signal processing (Richards et al., 2010). Advanced techniques cover the most recent developments in the radar research community including advanced signal processing methods essential to current and future implementations of radar systems, such as enhanced waveform schemes, SAR imaging, speckle reduction, edge detection and MIMO ambiguity function design (Levanon and Mozeson, 2004; Melvin and Scheer, 2014; Richards, 2005; Richards et al., 2010). Particularly, applications of advanced techniques may require specific hardware configurations or radar topologies, as discussed later herein.

### 2.2.1 Basic Operation Principles

As implied by their acronym (RADIO Detecting And Raging), radar systems are used to detect the presence of an object and determine its location by measuring the object's distance or range and specifying its direction. The main principle on which radar operation is based is the property of an electromagnetic (EM) wave to be reflected or *echoed* back if it is emitted in the direction of an object or a target (Melvin and Scheer, 2014; Nathanson et al., 1991; Richards et al., 2010).

Briefly, the operating principle of a radar can be described in three steps. First the radar antenna transmits an EM wave and it switches to *listening* or receiving mode. Then if a target is present and illuminated by the transmitted wave, an echo is reflected. This echo is then propagated back to the radar and picked up by a receiving device. Supposing that the speed of EM wave  $c$  is known, the distance

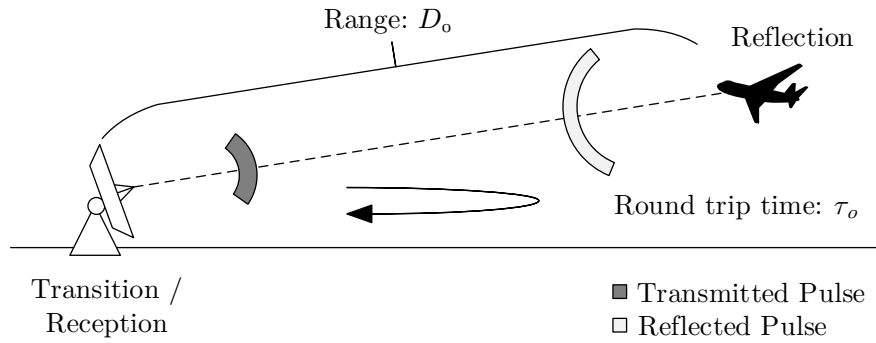


Fig. 2.1 Basic radar operation schematic.

$d_0$  of the object can be estimated using the time  $\tau_0$  required for an echo of the transmitted pulse to return. Since the total distance the EM wave has to travel towards and back from the target, the basic range radar equation is written as:

$$d_0 = \frac{c\tau_0}{2} \quad (2.1)$$

The aforementioned steps are actually describing the operating principles of what is called a *pulse radar*. In a different operating configuration, a radar may have dedicated transmitter and receiver systems allowing it to continuously emit EM waves while listening in parallel. This configuration is called continuous wave (CW) radar. A schematic of a pulse radar operation is illustrated in Fig. 2.1. The time difference between consequent transmissions in a pulse radar is called pulse repetition interval (PRI). A graphical illustration of how PRI is defined is given in Fig.2.2. Another usual term is the pulse repetition frequency (PRF) which is given as  $\text{PRF} = 1/\text{PRI}$ . Moreover, the ratio between the pulse's duration, or width,  $T$  and the PRI is defined as the duty cycle (DC) of the radar, i.e.  $\text{DC} = T/\text{PRI}$ .

Modern radar systems are composed of a number of smaller subsystems. Although these subsystems can vary depending on the particular radar system,

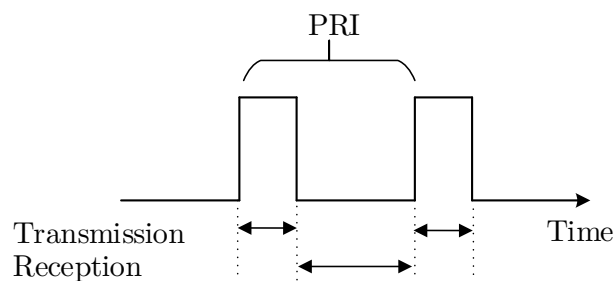


Fig. 2.2 Pulse radar transmission and reception operations.

they almost always include a transmitter, an antenna, a receiver, and a signal processor. In a typical radar system, the transmitter subsystem generates the EM waves which the antenna subsystem takes as input and introduces them into the propagation medium. The incident EM waves induce currents on the target causing retransmission of the resulting EM waves into the environment. In reception, the antenna system first captures and amplifies the received signal before it is passed to the receiver subsystem. The RF signal is then down-converted to an intermediate frequency (IF), and subsequently applied to an analog-to-digital converter (ADC) before passed to the signal processor. In pulse radar the transmitter and receiver are connected to the antenna through a transmit/receive (T/R) device, which is usually a circulator or a switch. The T/R device has the function of providing a connection point so that the transmitter and the receiver can both be attached to the same antenna simultaneously while providing isolation between the transmitter and receiver protecting the sensitive receiver components from the high-powered transmit signal (Richards et al., 2010). Finally, the processed radar signals are displayed on the traditional plan position indicator (PPI) or other more advanced radar display systems showing a map-like picture of the area scanned by the radar beam (Melvin and Scheer, 2014; Nathanson et al., 1991).

The target's direction is determined by the directivity of the antenna, sometimes known as the directive gain, which represents the ability of the antenna to transmit the energy in a particular direction. An antenna characterised by high directivity is also called directive antenna. Both the target's *azimuth* and *elevation* angles referred to radar, can be determined by measuring the direction in which the antenna is pointing when the echo signal is received. In Fig.2.3 it is graphically illustrated how directive antennas can be used to illuminate different azimuth and elevation angle.

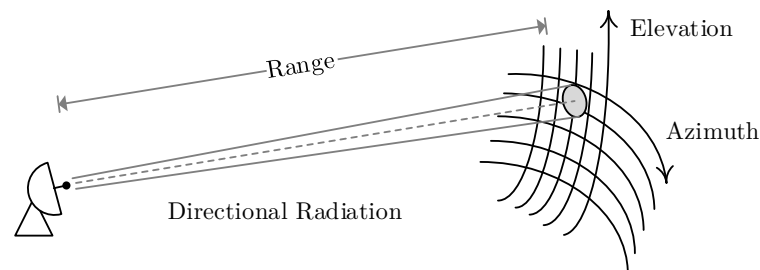


Fig. 2.3 Illumination in different azimuth and elevation angles using a directional antenna.

In radar systems the term *accuracy* is used to express the degree of convergence between the estimated and real position and/or the velocity of a target at a given time. Usually a statistical measure of error represents the accuracy performance of the system. The *resolution* of radar is its ability to distinguish between targets that are in a very close proximity and it is different from accuracy. Radar spatial resolution is usually divided into two categories; range resolution and angular or bearing resolution. In Fig. 2.4 an example of the resolution being able to resolve (a) both and (b) only one of the two present targets is illustrated. Weapons-control radars, which require great precision, should be able to distinguish between targets that are only meters apart. On the other hand, search radar are usually less precise and are required to only distinguish between targets that are hundreds of meters or even kilometres apart.

Normally, the transmitted signal is echoed in a wide number of directions. The term *backscatter* is referred to the reflections in the opposite direction to the incident electromagnetic waves. While a powerful transmitter is used to generate the radar signal, only a small portion of the reflected energy is captured on a highly sensitive receiver. The degree of that return energy is highly dependent from what is called radar cross-section (RCS) of the target. In a general sense, RCS is a measure of how detectable an object is to a radar and is expressed in units of area (e.g.,  $\text{m}^2$ ). The RCS of a target is not static but varies depending on the viewing angle of the target relative to the radar, the operating frequency and the polarization of the EM wave. Moreover, signal echoes occur not only from the desired target but also from other surfaces on the ground and in the atmosphere. These unintentional and unwanted signals are called *clutter*.

Propagation effects of the atmosphere and earth on the waves may also alter the strength of the EM waves both at the target and at the receive antenna. Echo

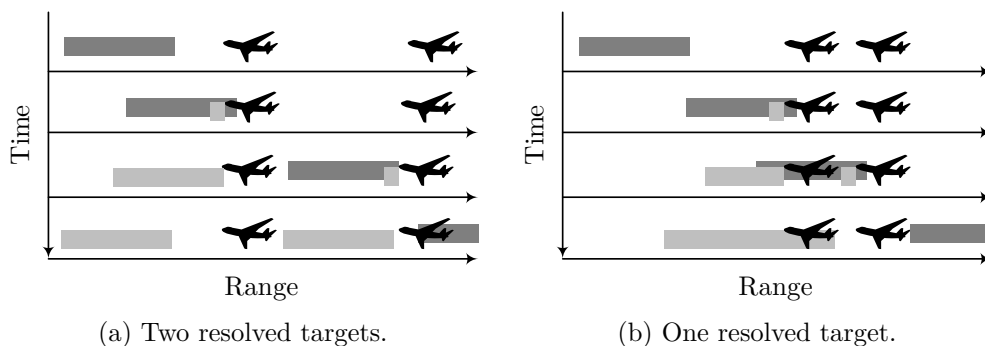


Fig. 2.4 Range resolution issue between targets in close proximity with each other.

signals from targets are received in the presence of interference, which is due to the following four different causes: a) internal and external electronic noise, b) reflection from unrelated objects, clutter, c) unintentional EM waves created by other human activities, i.e. electromagnetic interference (EMI) and d) intentional *jamming* from an electronic countermeasures (ECM) system in the form of noise or false target information. A primary function of a signal processor is the extraction of target information in the presence of clutter, and EMI and ECM noise. Noise coming from electric motors or engine ignition is considered as EMI noise, while jamming signals can appear as much like internal receiver thermal noise or false targets (Richards et al., 2010).

### 2.2.2 Advanced Techniques of Radar Systems

Advanced techniques for modern radar systems are addressing the most important aspects of current and critical research topics (Levanon and Mozeson, 2004; Melvin and Scheer, 2014; Skolnik, 1970). In the following paragraphs the most important current advanced techniques are discussed.

**Waveform design:** In radar systems waveform design comprises advanced pulse compression techniques to provide high resolution and adjust compressed waveform impulse response. Jointly optimised or adapted transmit waveforms with complementary processing is a challenging research subject employing the advances in waveform generation and multiple antenna array technologies (Melvin and Scheer, 2014; Richards, 2006). The topic of waveform design will be extensively discussed in Section 2.2.3.

**Ambiguity function (AF):** The radar AF is a significant analytical tool for waveform design and analysis, which describes much clearly the behaviour of a waveform paired with its matched filter. For a given waveform the AF is useful in examining resolution, sidelobe behaviour, and ambiguities concerning range and Doppler, as well as phenomena such as range-Doppler coupling (Levanon and Mozeson, 2004; Melvin and Scheer, 2014). More details in the canonical definition, KLD based definition and other definitions of AF are presented in Section 3.3.

**Multi-input, multi-output (MIMO):** In a broader definition, MIMO radar could be considered as a multi sensor system that employs antenna arrays to advance target identification via sophisticated signal processing algorithms. In

addition to the tremendous advances in computing technology, a trend in modern radar is to move the digitisation advances closer and closer to the antenna element. This places great emphasis on the importance of the collection approach, sensor topology, and the particular algorithms and techniques applied to the incoming data to provide a superior performance.

It has been recently shown that the MIMO systems are advantageous over single antenna systems, since they have the potential to greatly improve the overall communication performance. Unlike beamforming, where high correlation is presumed between transmitted or received signals from an antenna array, the MIMO radar concept exploits the independence between transmitted/received signals from array elements (Melvin and Scheer, 2014; Skolnik, 1970). An extensive discussion of MIMO radar systems and their configuration is held in Section 2.3. Moreover studying deterministic waveforms with ideally low cross-correlation functions, allows exploiting the benefits of the additional phase diversity on transmit, which has the potential to enhance the radar system capabilities to resolve targets in angle (Li and Stoica, 2009; Melvin and Scheer, 2014; Skolnik, 1970). A discussion on waveform diversity (WD) and waveform design suitable for MIMO radar is held in Section 2.2.3. In addition, extending the radar AF to the MIMO radar systems allows not only the range and Doppler resolution but also the angular resolution to be improved through proper choice of radar waveform. A proposed definition on MIMO AF is extensively presented in Chapter 6.

**Synthetic aperture radar (SAR):** In an abstract definition, a SAR system can be defined as a combination of a radar and moving platform system that can exploit the relative motion and signal processing techniques to generate a photograph-like rendering of the scene of interest (Richards et al., 2010). Some of the main advantages of SAR are their potential of very fine resolution, ability to penetrate the foliage and ground to expose targets beneath tree covering and buried objects respectively, and ability to provide information regarding the type of the illuminated surface and ground vehicle identification (Richards et al., 2010). A discussion in SAR imaging principles and the current challenges in the field is held in Section 2.5.

**Passive radar:** A passive radar utilises signals emitted from a non-cooperative illuminator to perform radar operation such as target detection and tracking (Baker et al., 2005; Griffiths and Baker, 2005). Examples of these illuminators of opportunity (IOs) include but are not limited to radio, television, cellular,

and satellite signals. The main distinctive characteristic of passive radar systems compared to active is that it does not emit EM waves. This introduces advantages associated with lower power requirements, high tolerance in ECM, and no need of dedicated spectrum for its operation. Moreover by utilising multiple IOs, passive radar systems can easily operate in multistatic configuration (He and Blum, 2014).

**Cognitive radar:** Cognition in radar is a recently introduced concept with very high potentials on surveillance applications in fast altering environments. In a general definition cognitive radar are intelligent systems aware of their environment, that can adjust to adopt in real time statistical variation of their environment (Abad et al., 2016). While having many similarities with adaptive radar, cognitive radar distinguish themselves in three different aspects (Haykin, 2006):

- The radar system progressively acquires knowledge of its operating environment through interactions from its transmitter, while constantly updating the receiver with relevant information.
- The transmitter takes into account information from the environment, such as target range and size, in order to adjust its operation in an effective, efficient, and reliable manner.
- The entire system's architecture is characterised by a dynamic closed feedback loop between the transmitter, environment, and receiver.

Cognitive radar have various applications in advanced operations such as target detection and tracing (Bell et al., 2015a,b; Wang et al., 2016b). In (Smith et al., 2016) the authors presented experimental results on the Cognitive Radar Engineering Workspace (CREW) system. The results demonstrated the superior performance that cognitive approaches have when compared with traditional fixed parameter approaches.

**Compressive sensing (CS):** Despite of the common conception in data acquisition, CS is a novel sensing/sampling method that allows the recovery of certain signals from significantly fewer samples or measurements than conventional methods require (e.g. Shannon theorem based on the so-called Nyquist rate). Compressive sensing could attain this based on two principles: sparsity and incoherence. Sparsity is associated with the signals of interest, while incoherence is associated with the detection modality (Candès and Wakin, 2008). In (Baraniuk and Steeghs, 2007) the authors investigated the application of CS in radar

system proposing two potential improvements regarding the elimination of the matched filter at the radar receiver and reduction of the required ADC sampling rate. Moreover, the application of CS in SAR imaging to acquire high-quality images by using undersampling in a novel collection scheme was investigated in (Patel et al., 2010). In (Berger et al., 2010) the potential benefits of applying CS techniques for underwater communication channels were demonstrated using numerical simulations and field result.

In addition to the aforementioned advanced techniques applied in modern radar, the space-time coded apertures are also significant for mission-tailored beam patterns. In remote sensing MIMO SAR can provide potential solutions to resolving the disadvantages of conventional SAR in high-resolution wide-swath (HRWS). Also electronic protection is a critical issue enabling the radar system to resist electronic attacks due to hostile denial or manipulation of the electromagnetic spectrum. Additionally post-processing techniques, such as the application of polarimetry, enhance the radar performance in automatic target recognition, and multitarget tracking (Melvin and Scheer, 2014).

### 2.2.3 Waveforms Design and Pulse Compression

Following, the basic aspects of waveform design are discussed including range resolution, pulse compression concept and related techniques, such as frequency and phase modulation. The peak side lobe level (SLL) phenomenon and its effects in pulse compression are also presented.

Waveform design attempts to find an appropriate solution that best fits to the relevant application. In a simple pulsed radar applications the average radiation power and pulse length restrict the range sensitivity and resolution respectively. Therefore the design of any radar system always should involve a compromise between these two constraints. Using of optimised waveform designs allows significant improvement in target detection performance, tracking and resolution (Levanon and Mozeson, 2004; Melvin and Scheer, 2014; Nathanson et al., 1991; Richards et al., 2010; Skolnik, 1970). Additionally many different aspects have been considered aiming to achieve higher signal-to-noise ratio (SNR) at the receiver through waveform optimization. As modern radar systems are increasingly being required to operate in fast changing and electromagnetically overcrowded environments, their effective operation may be significantly degraded due to interference, frequency occupancy and performance constraint.

### Matched Filter

In radar theory, the probability of detection is highly related to the SNR rather than to the exact received signal. As a consequence, there is a need to maximise the SNR rather than maintain the shape of received waveform. To achieve this in radar applications, the knowledge of the transmitted signal is utilised to design a linear filter that maximises the SNR. In the presence of additive white Gaussian noise, the impulse response of the optimum filter, in terms of SNR, is a time reversed version of the transmitted signal or simply a filter “matched” to the transmitted pulse.

For a better understanding, first let us consider an arbitrary continuous signal  $x(t)$ . The matched filter of  $x(t)$  will have an impulse response given as (Richards et al., 2010):

$$h_{\text{MF}}(t) = kx^*(\tau_{\text{max}} - t) \quad (2.2)$$

where  $k$  is a constant,  $\{\cdot\}^*$  denotes the complex conjugate operation and  $\tau_{\text{max}}$  is the time instant in which the SNR is maximised (Richards, 2005). If the signal  $x(t)$  is of a finite length  $T$ , then  $\tau_{\text{max}} \leq T$  for causality and the response  $h_{\text{MF}}(t)$  will be finite. On the other hand,  $h_{\text{MF}}(t)$  will be infinite only if the signal  $x(t)$  that it is matched to is infinite in duration. Examining (2.2) it can be derived that filtering a signal with its matched filter corresponds in computing its autocorrelation (AC) function. This can be better illustrated by deriving the convolution of  $x(t)$  and  $h_{\text{MF}}(t)$ :

$$\begin{aligned} y(t) &= \int_{-\infty}^{\infty} h_{\text{MF}}(u)x(t-u)du \\ &= \int_{-\infty}^{\infty} x^*(\tau_{\text{max}} - u)x(t-u)du \\ &= \int_{-\infty}^{\infty} x^*(u)x(u + \tau_{\text{max}} - t)du \\ &= R_{xx}(t - \tau_{\text{max}}) \end{aligned} \quad (2.3)$$

where  $R_{xx}(t)$  denotes the AC of the signal  $x(t)$ . As it can be seen the last step of (2.3) return the AC of  $x(t)$  at a lag equal to  $t - \tau_{\text{max}}$ . Moreover it can be easily derived that (2.3) will have maximum at  $y(\tau_{\text{max}}) = E_x$  where  $E_x$  is the total energy of the signal  $x(t)$ . Finally, in the presence of additive white Gaussian noise with a distribution  $\mathcal{CN}(0, \sigma_n^2)$ , the peak SNR is given as:

$$\text{SNR}_{\text{max}} = \frac{E_x}{\sigma_n^2} \quad (2.4)$$

Similar to the continuous or analog matched filter definition in (2.2), the discrete-time matched filter is given as:

$$h_{\text{MF}}[n] = kx^*[n_{\text{max}} - n] \quad (2.5)$$

where  $n_{\text{max}}$  is the sample lag giving the maximum SNR. Moreover, the discrete equivalent of (2.3) is given as:

$$\begin{aligned} y[n] &= \sum_{m=-\infty}^{\infty} h[m]x[n - m] \\ &= \sum_{m=-\infty}^{\infty} x[m]x^*[m + n_{\text{max}} - n] \\ &= R_{xx}[n - n_{\text{max}}] \end{aligned} \quad (2.6)$$

In both continuous and discrete definition the matched filter exhibits the same properties as they will be discussed in the next paragraphs.

### Pulse compression

Normally a radar system should be able to distinguish individual targets separated in a distance of a tens of meters to tens of millimetres of each other depending on the application (Melvin and Scheer, 2014). If only the received power is considered as a detection criterion, then a radar system should be capable to generate and radiate the total transmit energy in just a few  $\mu\text{s}$  or even ns to avoid overlapping between echoes from different targets (see Fig. 2.4). However, high-power transmitters based on semiconductors cannot produce such pulses due to their limited dielectric strength and operating temperature. Therefore the transmitted radar pulse must last much longer to radiate the same energy to avoid technical limitations for the peak power, i.e. maximum high voltage or power at the output stage (Levanon and Mozeson, 2004; Melvin and Scheer, 2014; Skolnik, 1970).

Pulse compression came from the necessity to amplify the transmitted pulse through time compression. In general the pulse compression term describes a wave shaping process that allows radar to use long waveforms in order to obtain high energy and simultaneously achieve the resolution of a short pulse by internal modulation. In this methodology the high energy of a long pulse width and the high resolution of a short pulse width can be combined together.

Having relatively large transmitting pulse duration, the pulse is modulated internally in order to improve range resolution of radar. Since each part of the pulse has unique frequency, the returns from the target can be completely separated and integrated into a shorter single output pulse. In addition, the pulse compression filter contribute greatly to the noise level reduction and moreover the pulse compression methodology can succeed in an output signal even when the noise level is larger than the input signal (Melvin and Scheer, 2014).

By definition, range resolution represents the ability to detect and distinguish targets that are located in close proximity to each other (see Section 2.2.1). The resolution in the range domain  $\Delta d$  corresponds to the resolution in the time domain  $\Delta\tau$  and is ultimately governed by the shape and width of the mainlobe in the matched filter response. In the literature two more common metrics are used to define resolution (Richards et al., 2010):

1. The width between the mainlobe peak and the first null (*Rayleigh criterion*).
2. The width of the mainlobe at specific point below the peak, most commonly half drop or  $-3\text{dB}$  point.

Following, the second definition at the  $-3\text{dB}$  point will be used. In compressed pulses the resolution is associated to the signal's bandwidth according to the relation:

$$\Delta d = \frac{c\Delta\tau}{2} \approx \frac{c}{2B} \quad (2.7)$$

Increasing the bandwidth of the waveform can therefore improve range resolution without the need of decreasing the pulsewidth (Levanon and Mozeson, 2004; Skolnik, 1970). Essentially, the pulse compression permits a decoupling between range resolution and waveform energy allowing higher range resolution and better detection probability at the same time. In Fig.2.5 the amplitude of the matched filter output of (a) an unmodulated square pulse and (b) a compressed pulse of the same duration in which linear frequency modulation (LFM) has been applied are illustrated. As it can be seen the LFM pulse, i.e. the compressed pulse, exhibits a much narrower mainlobe width leading to finer range resolution compared to the unmodulated pulse. On the other hand, applying pulse compression has also introduced secondary lobes, also called *sidelobes* alongside the mainlobe while the unmodulated pulse exhibits only a mainlobe.

Sidelobes are undesired side effects of applying matched filter in compressed or modulated signals. In real radar measurements, sidelobes associated with targets of high RCS may be equal or even higher in amplitude than the mainlobe

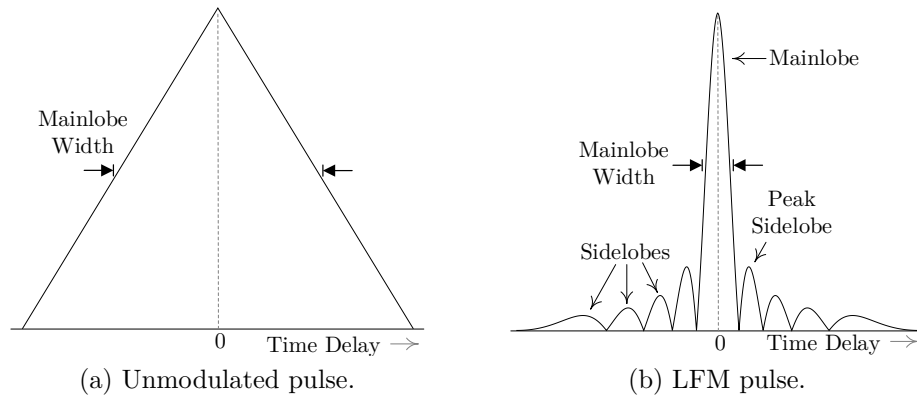


Fig. 2.5 Matched filter output of (a) an unmodulated square pulse and (b) a LFM pulse.

corresponding to a weaker target. It is therefore possible for high RCS targets to mask smaller targets even if they are well resolved in range in terms of resolution. One of the most important property of modulated pulses is the ratio between the mainlobe peak and maximum sidelobe peak. This ratio is most commonly referred as sidelobe level (SLL) and is usually expressed in dBs.

Following, the most common pulse compression techniques are discussed. A summary of the categorisation between different waveform designs is illustrated in Fig.2.6. As it can be seen, two main categories are identified depending on if the design is based on the frequency or the phase of the waveform. Those two main categories are also partitioned in their respective sub-categories according to their respective characteristics.

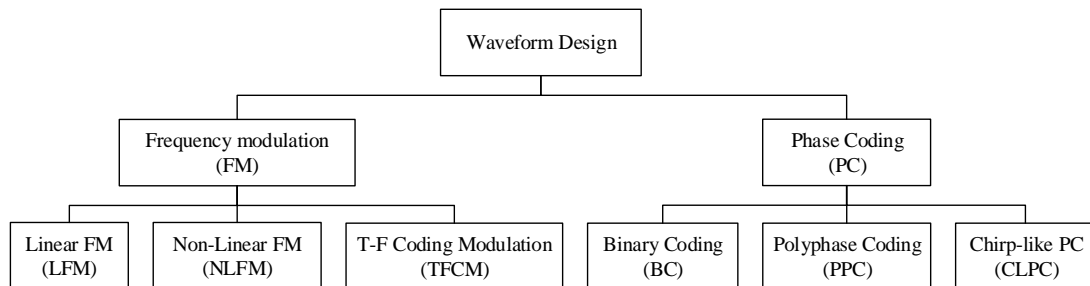


Fig. 2.6 Waveform design categorisation.

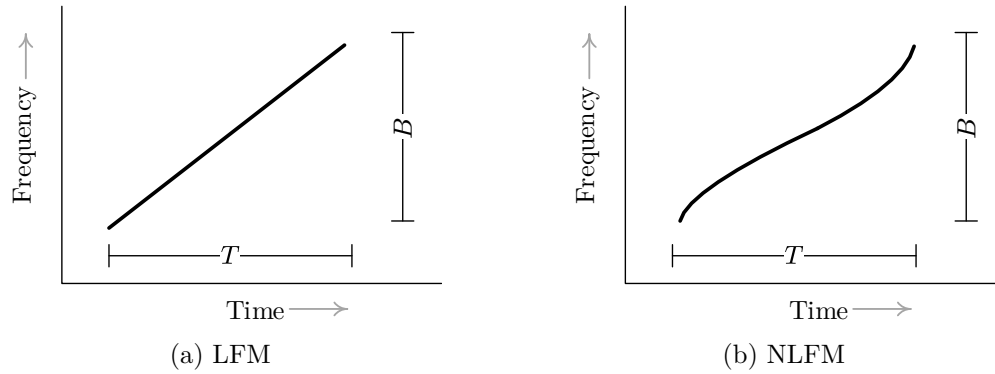


Fig. 2.7 Time-frequency profile of (a) linear and (b) non-linear FM waveforms.

### Frequency Modulation

In the frequency modulated (FM) waveforms the applied modulation or coding can be linear FM (LFM or Chirp), non-linear frequency modulation (NLFM) or time-frequency coded modulation (e.g. Costas code) of the transmitted waveform.

**Linear Frequency Modulation:** Linear FM waveform is a very popular choice in modern radar systems because it can achieve high range resolution holding the advantage that the hardware implementation can relatively be kept simple. The complex envelope of a LFM pulse with increasing instantaneous frequency and amplitude equal to 1 is expressed as:

$$x(t) = e^{j\pi(B/T)t^2}, \quad 0 \leq t \leq T \quad (2.8)$$

where  $B$  and  $T$  are the bandwidth and duration of the pulse respectively. A graphical representation of the LFM time-frequency profile is illustrated in Fig. 2.7a. Other advantages of LFM include its insensitivity to Doppler shifts and the good hardware availability to form and process it. However, due to their ease of generation LFM pulses are very susceptible to jamming. Moreover when the bandwidth is on the order of hundreds of MHz, or even GHz, it becomes difficult to perform matched filtering or pulse compression, because high-quality ADC are hard to operate at such data rates (Levanon and Mozeson, 2004; Melvin and Scheer, 2014; Richards et al., 2010). Also the range-Doppler cross coupling is among the disadvantages resulting in measurement errors unless one of the coordinates (range or Doppler) is determined. Another drawback is that the range sidelobes are high compared with non-linear FM and phase-coded waveforms. Weighting, also known as *windowing*, is usually required for reducing the SLLs,

resulting to a 1 – 2 dB loss in SNR while also degrading the spatial resolution (Richards, 2006; Skolnik, 1970).

**Non-Linear Frequency Modulation:** The non-linear FM waveforms have several distinct advantages compared to their LFM counterparts. In NLFM low sidelobe levels of the compressed pulse can be achieved without requiring the use of special weighting for their suppression. Hence NLFM has no signal-to-noise ratio losses, as in the LFM. On the other hand, NLFM is more sensitive to Doppler frequency shifts. In addition this pulse modulation technique is more complex and the development of waveform generation is limited (Richards, 2006; Richards et al., 2010; Skolnik, 1970). In Fig. 2.7b, a graphical representation of the NLFM time-frequency profile is presented.

**Time-Frequency Coded Modulation:** In time-frequency (T-F) coded modulated waveforms a relatively long pulse of length  $T$  is divided into  $N_c$  sub-pulses in time bins with duration  $\Delta T = T/N_c$ , with each sub-pulse allocated in different frequency bin  $\Delta B = B/N_c$ , where  $B$  is the total bandwidth. Those sub-pulses are usually referred as *chips*. Generally, the time and frequencies are equally spaced and the pulses are of the same amplitude but may also vary. As a special case, if the frequencies are monotonically increasing or decreasing, the waveform is simply a stepped approximation of LFM (see Fig. 2.8a).

Costas codes, originally introduced by (Costas, 1984), compose one of the most important classes of frequency-coded waveforms. The uniqueness of Costas codes is that the number of overlapping sub-pulses of an original and a time-frequency shifted Costas code cannot be larger than one for all but the zero-shift case (Cohen, 1991; Levanon and Mozeson, 2004). The time-frequency coding of a Costas 7 code is illustrated in Fig. 2.8b.

### Phase Coding

Phase-coded (PC) waveforms differ from LFM and NLFM waveforms in that a long pulse is sub-divided into a number of shorter sub-pulses of equal duration. Each sub-pulse has a particular phase, which is selected in accordance with a specified phase code or code sequence. In general each sub-pulse corresponds with a range bin. Binary coding (BC) is the most widely used type of phase coding. Among the common advantageous characteristic of phase-coded waveforms are their lower range sidelobes compared with LFM waveforms and their robustness

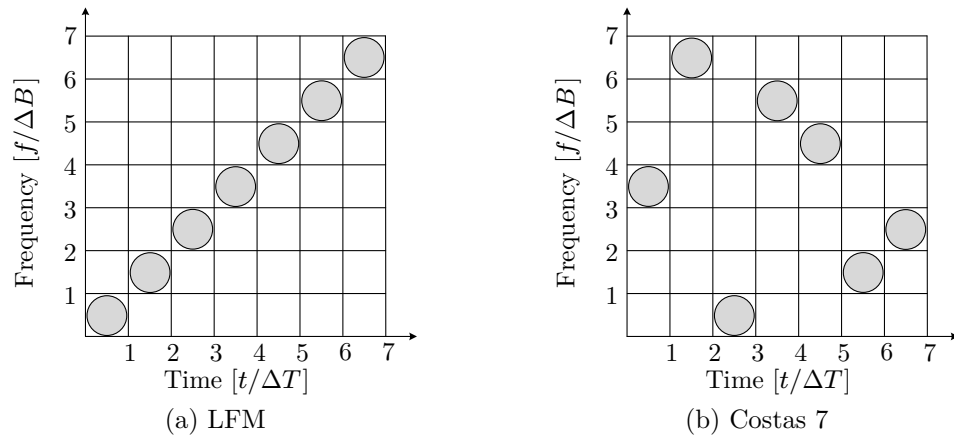


Fig. 2.8 Time-frequency profile of (a) LFM and (b) Costas 7 code.

in jamming conditions, since coding of the transmitted signal offers additional protection against ECM. However the resolution performance of PC waveforms can be rather poor in a dense target environment or in presence of distributed clutter (Nathanson et al., 1991; Richards, 2006; Skolnik, 1970).

**Binary coding:** Binary coding is the most widely used phase coded waveform. In this coding method, the binary code of pulse compression consists of a sequence of either  $+1$  or  $-1$  associated with the set of phases to be selected. First a long pulse of duration  $T$  is divided in time equally into  $N_c$  sub-pulses of width  $\Delta T$ . The phase of each sub-pulse then is chosen to be either  $0$  or  $\pi$  radians corresponding to a code bit of  $+1$  or  $-1$  respectively. The transmitted signal alternates between  $0$  and  $\pi$  radians in accordance with the sequence of elements permitting an increment of pulse bandwidth by means of changing appropriately the phase of each sub-pulse. Since the transmitted frequency is usually not a multiple of the reciprocal of the sub-pulse width, the coded signal is generally discontinuous at the phase-reversal points (Levanon and Mozeson, 2004; Nathanson et al., 1991; Skolnik, 1970).

The matched filter output could be similar to a spike of width  $\Delta T$ . The pulse compression ratio (PCR) is thus given as  $\rho_{PC} = T/\Delta T \approx BT$ , where  $B \approx 1/\Delta T$  represents the bandwidth of a sub-pulse<sup>1</sup>. Also the output waveform extends a time distance of  $T$  to either side of the peak response (or central spike) having waveform segments other than spike, which are called time or range sidelobes. After receiving the echo signal the compression filter readjusts the relative phases

<sup>1</sup>The pulse compression ratio can be expressed as the ratio of the range resolution of an unmodulated pulse of length  $T$  to that of the modulated pulse of the same length and bandwidth  $B$ .

Table 2.1 Known Barker Codes

Length	Codes	Sidelobe level ratio
2	+ -	++ -6 dB
3	+ + -	-9.5 dB
4	+ + - +	+ + + - -12 dB
5	+ + + - +	-14 dB
7	+ + + - - + -	-16.9 dB
11	+ + + - - - + - - + -	-20.8 dB
13	+ + + + + - - + + - + - +	-22.3 dB

of the frequency components so that a narrow or compressed pulse is reproduced or reconstructed. Targets with noise overlapping can be separated in the receiver using suitable processing algorithms (Levanon and Mozeson, 2004; Nathanson et al., 1991; Skolnik, 1970). As a matter of fact the selection of the so-called random  $0, \pi$  phases are very critical.

Optimum or Barker codes are a special class of binary codes, which are considered optimum in the sense that provide low sidelobes of equal magnitude in equal time. A limited number of these optimum codes exist, while a computer based study searching for Barker codes up to 6000 elements has obtained only 13 (see Table 2.1). Since there are no Barker codes greater than 13, the maximum compression ratio is 13 which is rather low. Setting  $N_c$  equal to code length, the main lobe to SLL peak ratio of Barker code is  $1/N_c$  giving a minimum of  $-22.3$  dB power ratio for  $N_c = 13$  (Skolnik, 1970). Binary codes that are characterised by minimum sidelobes but do not meet the  $1/N_c$  Barker criterion are often called minimum peak sidelobe (MPS) codes. These codes are found using exhaustive computation and have a peak SLL for each maximum code length  $N_c$ , i.e. peak SLL of 1 for  $N_c \leq 13$ , peak SLL of 2 for  $N_c \leq 28$ , peak SLL of 3 for  $N_c \leq 51$ , etc. (Levanon and Mozeson, 2004).

**Polyphase coding:** In *polyphase* coding the phase values are allowed to take any value, in comparison to binary which only values of 0 and 1 are permitted. This can lead to lower to SLL with however the mainlobe to peak SLL ratio being always bounded by the  $1/N_c$  limit (Levanon and Mozeson, 2004). The polyphase coded sequences with minimal main lobe to SLL peak ratio are called generalised Barker or polyphase Barker sequences and are usually derived using numerical methods that optimise the AC function sidelobes.

**Chirp-like phase coding:** The main drawback of binary and polyphase coding is that they aim to optimise only the AC of the signal and do not take into account the response of the matched filter if a Doppler shift is introduced due to the targets relative motion in radar applications. Chirp-like phase codes use phase coding to achieve responses similar to LFM pulses also called chirps. More precisely, the Frank codes are derived from the phase history of a linear frequency stepped pulses (Levanon and Mozeson, 2004) with the main drawback that the code sequence must be of a perfect square length, i.e.  $N_c = m^2$ . The P1, P2 and Px codes are modified version of the Frank codes with the dc or center frequency being moved in the middle of the pulse instead of the beginning, as in Frank. Although the mainlobe to SLL peak ratio in both Px and Frank codes is the same, the integrated sidelobe of the Px is lower. Unlike Frank and Px codes, Zadoff-Chu codes are chirp-like phase codes that can be generated for any desired length  $N_c$  given by  $\mathbf{c}_{ZC} = e^{j\phi_c}$ , where  $\phi_c$  is a  $N_c$  length vector with each of its elements calculated as:

$$\phi_c = \begin{cases} \frac{2\pi r(m-1)^2}{N_c} & \text{if } N_c \text{ is even} \\ \frac{2\pi r(m-1)}{N_c} & \text{if } N_c \text{ is odd} \end{cases} \quad (2.9)$$

where  $1 \leq m \leq N_c$ , and  $r$  is any integer relatively prime to  $N_c$ , i.e.  $r$  and  $N_c$  are commonly divisible by only 1. Other chirp-like phase codes include the P3, P4 and Golomb polyphase codes which are cyclically shifted and decimated versions of the Zadoff-Chu codes.

It should be mentioned that while other, more advanced pulse compression waveform modulations, such as stepped chirp waveforms and adaptive waveform designs (Melvin and Scheer, 2014), are widely used in radar applications they are not in the scope of this thesis and hence will not be examined.

## 2.3 Multisensor Systems

Nowadays many tracking and surveillance systems are arranged as multisensor configurations, which are used to enhance the breadth of measurement and increase the capability of the system to overcome the failure of any individual sensor. Multisensor radar systems are a promising technology, which has received significant attention for both military and non-military applications. These multiple sensing systems are characterized by utilizing a large variety of sensors to detect, to classify and track targets.

Currently, most of the multisensor system architectures depend on either a central processor unit for the implementation of global data fusion or a central communications medium for all message exchanges between individual sensors. By decentralising the information processing, detection, target estimation, and other high level products of local processing are communicated to a central processor. This pre-processing limits the amount of information that needs to be passed on to develop a final detection decision or estimation. The central processor takes advantage of the information provided by individual radars to improve detection/estimation performance (Blum, 1999; Blum et al., 1997; Chernyak, 1998; Viswanathan and Varshney, 1997).

Depending on the radar waveforms transmitted from each radar system, the multisensor radar systems are classified into two categories: Multistatic and MIMO radar systems (Haimovich et al., 2008). In multistatic radar system, each radar component transmits the same waveform that might shift in phase. Often multistatic radar is also referred to as ‘multisite’ or ‘netted’ radar. While in the literature MIMO radar has been oftenly viewed as a type of multistatic radar, in contrast to multistatic, MIMO radar is characterized by the distinction of waveforms attributed to each transmitter and the joint processing that MIMO is emphasised (Bliss and Forsythe, 2003; Haimovich et al., 2008). Due to the different waveforms that MIMO radar employ, the echo signals can be re-assigned to the single transmitter. Additionally the multiple arbitrary waveforms affect the range and Doppler resolution of the radar system, while the probability of target detection is also increased improving the SNR (Li and Stoica, 2007, 2009; Li et al., 2007). Furthermore, this type of sensor network can significantly improve target detection, parameter estimation, as well as target tracking and recognition performance (Lehmann et al., 2006; Li and Stoica, 2007; Li et al., 2007).

Multisensor systems can also be categorised by the way the nodes are allocated in the space. Generally, multisensor systems fall into two main spatial configurations: co-located and distributed characterising systems with sensors placed in close and wide proximity respectively (Haimovich et al., 2008). In Fig.2.9 an illustration of how multisensor systems can be categorised depending on their operating waveforms and spatial configurations is provided.

### 2.3.1 Co-located Radar Systems

Co-located arrays are a typical radar configuration, where the arrays of T/R antenna units are placed in a close proximity, such that their directions to the area

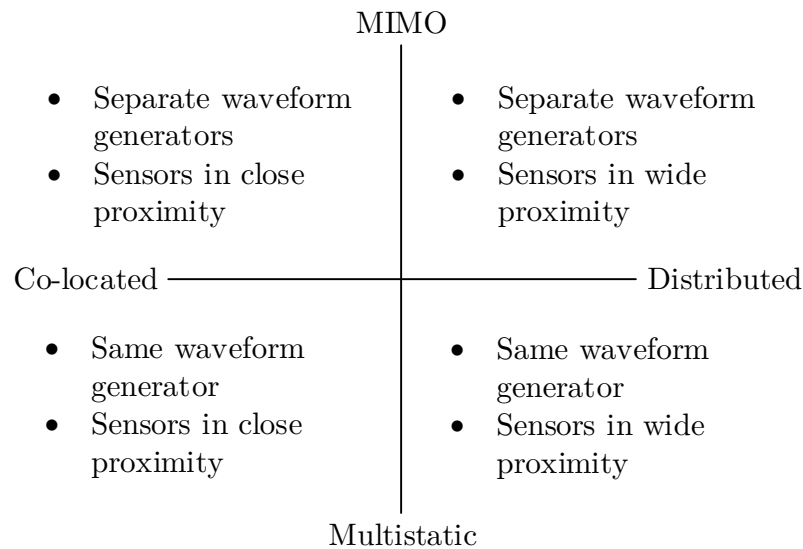


Fig. 2.9 Multisensor systems categorisation.

of interest is the same. Since both transmitters and receivers are in closely spaced arrays, the target bearings are the same with respect to both transmitting and receiving arrays. Considering this antenna configuration, the transmitting antennas are positioned closely enough such that the target RCS observed is identical for all transmitter-receiver pairs. Hence the target is approximated as a point like target similar to the traditional radar systems. This orientation offers superior parameter identification, direct applicability of adaptive non-parametric techniques for parameter estimation, enhanced performance of parametric algorithms and flexibility of transmitted beampattern designs (Li and Stoica, 2009).

### Phased Arrays Antenna

One of the most commonly used configuration of co-located radar systems in phased arrays antennas. In main principle, a thinned array of antennas with controllable phase are used to create a beam of radio waves that can be electronically steered to point in different directions, without moving the antennas (Balanis, 2016; Fishler et al., 2006; Milligan, 2005; Stutzman and Thiele, 2012). In a phased array antenna system, although each T/R unit has its own transceiver and ADC, it only transmits a copy of a transmission signal obtained from a central waveform generator, which is possibly time-shifted. The power from the transmitter is fed to the antennas through devices called phase shifters, controlled by a computer system, which can alter the phase electronically, thus steering the beam of radio waves to a different direction. Shifting the phase of the signal emitted from each

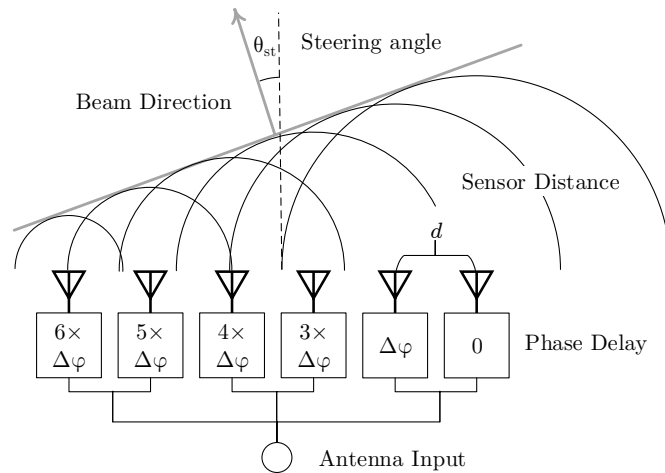


Fig. 2.10 Example of phased array antenna beam-forming.

radiating element, to provide constructive/destructive interference so as to steer the beams in the desired direction (Fishler et al., 2006; Milligan, 2005). In Fig 2.10 a graphical illustration of a phased array is given. As it can be seen the antenna elements are placed in a line with a distance  $d$  from each other. To control the beam angle the phase delay  $\Delta\phi$  is chosen as:

$$\Delta\phi = \frac{2\pi}{\lambda} d \sin \theta_{st} \quad (2.10)$$

where  $\lambda$  is the wavelength of the input signal and  $\theta_{st}$  is the steering direction. To avoid grating lobes and simplify the system usually half of a wavelength is chosen as the distance between the antenna elements, i.e.  $d = \lambda/2$  (Richards et al., 2010).

### Co-located MIMO

Although the configuration of co-located MIMO and phased array systems is very similar, on contrary to phase array scheme, in a co-located MIMO radar system each radiator has its own arbitrary waveform generator. This implies that each transmitter of co-located MIMO uses an individual waveform, which is the basis for the assignment of the echo signals to the corresponding source. The fundamental difference between co-located MIMO and phased array radar is that MIMO radar always transmits multiple probing signals via its antennas that may be correlated or uncorrelated with each other, whereas phased array radars transmit shifted versions of a single waveform, which are fully correlated. In literature phased array antenna system is often referred as single-input multiple-output (SIMO), if

it is compared with MIMO radar system (Li and Stoica, 2007, 2009; Melvin and Scheer, 2014).

In co-located systems, the receiver always knows the properties of the transmitted vector signal for a given array configuration. Similarly, parameters estimated at the receiver can be fed back to the transmitter as well. This is a major advantage of the co-located systems having the potentials to develop novel techniques that could adaptively optimise various transmitter characteristics, such as array geometry and waveform design, depending on the fed back parameters estimated at the receiver. Moreover, the co-located systems configuration has further practical advantages due to array geometry, since required processing tasks could be performed locally without wireless communication link to a central processor (Li and Stoica, 2009). Supposing that the T/R elements of a narrowband signal model are placed within relatively small area of a common phase origin, then known relative antenna displacements lead to predictable phase offsets of signal. This allows co-located array response vectors to be defined as a function of signal bearings and array properties (Lehmann et al., 2006; Li and Stoica, 2009).

### 2.3.2 Distributed Radar Systems

Recently the technology of distributed radar system (DRS) or also known as distributed radar networks received increasing attention providing an ability to survey an area of interest with multiple transmitters and receivers. In the distributed radar arrangements, the antennas are widely separated and the radar data processing is much more complex than in the co-located systems case. Using this configuration, a very large area is possible to be kept under surveillance by distributing the sensors accordingly. Normally the radar sensors are located in a random distribution over the entire area, while the number of devices comprising the network should be considered into analysis of such a radar system.

In contrast to co-located systems, distributed radar networks consist of several transmitter and receiver units spread over an extended area. It is obvious that a major difference between a distributed system and a co-located system is the need for communication between the individual nodes of the radar network. This implies that communication media, wavebands and paths, reliability in information traffic and speed, and security of performance should be involved into the desired surveillance scheme (Beide, 2001). The criterion regarding communication issues may be decided upon whether or not the link between the nodes and/or the central processing station will be wireless or wired. Wireless communication is preferable

solution for distributed radar referred to a long baseline scenario, since it can offer more flexibility in implementing particular radar system formation.

### **Distributed Multistatic**

Distributed multistatic radar systems (DMRS) also known as distributed aperture coherent radars, can exploit spatial diversity as they contain multiple spatially diverse monostatic or bistatic radar components covering an extensive area. Similarly to phased array systems, the DMRS are characterised by coherent transmitted signals often shifted in phase (Attia and Abend, 1991; Haimovich et al., 2008; Lin et al., 2016). Each of the radar sensors contains a transmitter and/or a receiver dedicated on radar operation and a communication link with the beam controller through networking cables, fibres or wireless (Attia and Abend, 1991; Li and Stoica, 2009). As described in (Lin et al., 2016) a DMRS of  $N$  sensors can achieve a  $N^3$  SNR gain if full coherency is achieved. Their main advantages include increase of target detection range, high accuracy of target localization, improved estimation of both target speed and acceleration, increased resistance in jamming and reduced clutter density. It should be noted that the real possibilities of taking certain advantages depend on the specific type of multistatic system (Chernyak, 1998). However there are several drawbacks as additional difficulties, which should be addressed when creating and operating a multistatic radar system. Among the main disadvantages are the necessity of centralised control and synchronization, the necessity of data transmission lines, additional requirements for phasing of stations, increased requirements for signal and data processing, the necessity of accurate station positioning and mutual alignment, need for lines-of-sight (not necessary straight) between stations and targets, system complexity and system cost (Chernyak, 1998).

### **Distributed MIMO**

As described in previous paragraphs, the distinctive difference between MIMO and multistatic radar is the diversity in the waveforms operated by the different sensors. One of the main advantage is that this diversity can offer the ability to improve radar performance by exploiting RCS diversity in radar systems with widely separated antennas. In (Fishler et al., 2006) the authors have provided a simplified method for modeling the signals received from complex targets, based in which the necessary sensor spacing conditions for a MIMO radar system to be able to categorised as distributed were derived. Moreover a comparison of phased-array

and distributed MIMO radar systems was presented in (He et al., 2010) in terms of detection performance on moving targets in homogeneous clutter. Results showed that distributed MIMO can better handle slow moving targets by exploiting Doppler estimates from multiple directions. The ability of distributed MIMO to support high resolution target localization was also discussed in (Haimovich et al., 2008) and (Lehmann et al., 2006). More precisely, in (Haimovich et al., 2008) it was shown that if phase synchronisation and coherent processing of the received signals is achieved, the spatial resolution of MIMO radar with widely separated antennas scales with the wavelength of the carrier frequency and therefore can greatly exceed the bandwidth resolution of the operating waveforms waveform.

### 2.3.3 Current Challenges in MIMO Radar

MIMO technologies have been intensively researched in recent years. New operational scenarios demand greater flexibility and higher capacity detection for radar systems. One of the most important current challenges in MIMO radar is the search for orthogonal waveforms, aim to remove interference problems between the antenna during both the transmission and matched filtering phases. Since the bandwidth of a radar pulse is highly related to its resolution in time (see Section 2.2.3), orthogonal waveforms for MIMO radar are desired to share the same bandwidth. This falls to the spectrum sharing (SS) and waveform diversity (WD) challenge which is more extensively discussed in Section 2.4.1.

Optimum sensor placement and power allocation are two very important considerations in both co-located and distributed MIMO systems which usually are expressed as a joint problem. In the literature many approaches addressing this complex issue have been proposed. In (Gorji et al., 2014) the optimal sensor placement problem is considered based on the Cramer-Rao lower bound (CRLB) accounting for co-located MIMO configurations. Simulation results indicated that superior localisation performance can be achieved when the proposed optimal antenna configuration is used.

Considering distributed configurations, in (Sun et al., 2002) an antenna placement analysis is held based on the Fisher information matrix (FIM) of the system accounting for both radar signal and SNR. Moreover, the optimum subset of the available sensors to be operating is derived based on the Fisher information distance and an exhaustive search method. Furthermore, in (Ma et al., 2014) the FIM and squared position error bound are used as metrics for a joint optimisation of a sensor subset selection and a power allocation problem. Additionally, in

(Chen et al., 2015a) the power allocation problem is investigated for range-only target tracking based on the Bayesian FIM examining different sensor geometries. From the above discussion it is concluded that different antenna-target geometries obtain variant information about the target location due to the fluctuation of the target's RCS in different observation angles. Moreover different metrics such as the Fisher information distance and the Kullback-Leibler divergence (KLD) (see Section 3.3.4) may yield different results when optimum sensor selection is considered. In addition, allocating the constrained available power into a small subset of sensors can significantly improve the localisation accuracy of the overall system, while use of more sensors leads to better tracking performance, regardless of the power allocation strategies and antenna geometries.

Finally, the optimisation of sensor allocation for MIMO radar system in multi-target scenarios has been investigated. In (Gao et al., 2014b) and (Gao et al., 2014a) an antenna only and an antenna-time allocation scheme were introduced based on the relative entropy and applied in distributed configurations. The derived analysis indicated that antenna allocation generally outperforms time allocation while the proposed antenna-time allocation scheme is able to achieve the best detection performance.

Concluding, it should be pointed out that most of the work in the reviewed literature has investigated the various optimisation approaches based on prior assumptions regarding either the operating waveform designs or the sensor-target geometries while also focusing on specific performance aspects of the MIMO radar system. In Section 3.3.5 the concept of the MIMO ambiguity function (AF) will be discussed in an attempt to define a more general performance evaluation tool for MIMO radar systems.

## 2.4 Spectrum Sharing In Radar

The vast rise of wireless technology through the last decades has allowed a dramatical growth on the number of users and services that operate in the range of radio frequencies (RF). Moreover, predictions indicate that the amount of active devices and data trafficking will continue to grow in the next years with much higher rates (Cisco, 2016). In addition due to their advantage to operate in any light and weather conditions, radar systems have been introduced in numerous military and civilian applications. As both wireless communication and radar devices need to operate in the same medium, spectrum management

and allocation have been very challenging issues attracting the interest of the research community. Here the definitions of spectrum sharing (SS) will be used for methods and techniques which allow simultaneous usage of a specific RF band in a specified spatial occupancy.

In general, SS can be employed between communication systems, radar systems, and between communication and radar systems. While the spectrum management between communication systems is a very topical subject in communication research community, it does not fall into the scope of this research and will not be further discussed in this section. Due to the nature of the transmitted signal, SS between radar systems can be better expressed by the term of waveform diversity (WD) (Gini et al., 2012; Wicks and Mokole, 2011). Main goals of WD is to address the issue of ever-growing competition for radar allocated spectrum and exploit the rapid advances in digital signal generation and processing (Blunt and Mokole, 2016). Further discussion regarding WD in modern radar systems will be given in Section 2.4.1.

During the last decade researchers have proposed various SS schemes allowing the simultaneous radar and communication operations. In (Hayvaci and Tavli, 2014) these techniques were categorised into three broad categories summarised in Table 2.2. The first category addresses scenarios in which the radar operation is prioritised and remains unaffected while the communication system needs to ensure the shared spectrum restrictions are satisfied. In the second category, systems are prioritising the communication operations and the interference is mitigated at the radar side. In (Aubry et al., 2016) an extensive review is presented on waveform designs allowing spectral coexistence with overlaid RF system while trading in radar performance features such as resolution and SLL. While the examined methods follow different approaches, their aim is to provide dynamic optimization of the spectrum usage only on the radar side. Finally, in the third category, more sophisticated schemes employ joint Radar-Communication designs to allow both the systems to co-operate to achieve better overall performance. Basic techniques and recent advances regarding joint Radar-Communication designs will be discussed in Section 2.4.2.

### 2.4.1 Waveform Diversity

As discussed in Section 2.3, MIMO radar is a rising technology with many advantages compared to their more traditional monostatic and multistatic counterparts. The main discriminative characteristic of MIMO radar is the diversity governing

Table 2.2 Spectrum Sharing for Radar and Communication systems

System category	Radar operation	Comms operation
Comms in presence of Radar	Not affected	Restricted
Radar in presence of Comms	Interfered	Not restricted
Joint Radar and Comms	Co-operation	Co-operation

the operating waveforms. One of the most general assumption made when the performance of MIMO radar schemes is assessed, is the full orthogonality of the operating waveforms i.e.:

$$R_{kl}(\tau) = \int_{-\infty}^{\infty} s_k(t)^* s_l(t - \tau) dt = 0, \quad \text{for all } k \neq l \quad (2.11)$$

where  $s_k(t)$  and  $s_l(t)$  denote the waveforms operating on the  $k$ -th and  $l$ -th transmitter respectively, and  $R_{kl}(\tau)$  is the cross-correlation function between  $s_k(t)$  and  $s_l(t)$ . A straight forward approach of a such WD design scheme is implementing orthogonal frequency division multiplexing (OFDM) to place the transmitted signals into different orthogonal sub-carriers i.e.:

$$s_{i_{\text{OFDM}}}(t) = m(t)e^{j2\pi f_i t} \quad (2.12)$$

where  $m(t)$  and  $f_i$  are the modulated signal and carrier frequency on the  $i$ -th transmitter respectively. To achieve full orthogonality the carrier frequencies must be chosen as:

$$f_i \geq f_0 + (i - 1)B_m \quad (2.13)$$

where  $f_0$  is the starting frequency, and  $B_m$  is the modulation bandwidth of the signal  $m(t)$ . Among others, the authors in (Wen-kun et al., 2016) adopted this signal model using linear frequency modulated (LFM) baseband waveforms. In this special but very widely used case the signal in (2.12) can be expressed as:

$$s_{i_{\text{OFDM-LFM}}}(t) = \frac{1}{\sqrt{T}} \text{rect}\left(\frac{t}{T}\right) e^{j2\pi f_i t + j\pi(B_{\text{LFM}}/T)t^2} \quad (2.14)$$

where  $B_{\text{LFM}}/T$  is the chirp rate and  $B_{\text{LFM}}$  is the modulation bandwidth of the LFM waveform.

While this so called OFMD scheme has the advantage of being easy to implement, it comes with two main drawbacks. The first is associated with the choice of  $f_i$  being restricted by the maximum Doppler shift  $f_{D_i}$  introduced on

each transmitted pulse. In cases of relative motion between the nodes in each transmitter-target-receiver signals will be moved to different harmonic sub-carriers  $\hat{f}_i = f_i + f_{Di}$  on the reception. This implies that for a proper orthogonality and complete decorrelation of the signals on the receiver side the sub-carrier frequencies in (2.13) shall be reformed as:

$$f_i \geq f_0 + (i - 1)(B_m + f_{D\max}) \quad (2.15)$$

where  $f_{D\max}$  is the maximum estimated frequency shift. In (Fang et al., 2008) an extended analysis on the effects of different frequency intervals  $f_i - f_{i-1}$  was investigated for the OFDM-LFM case showing how high sidelobes can be introduced on the matched filter output. The second drawback is associated with the SS problem. As it can be easily extracted from (2.12) and (2.13) the total occupied bandwidth of OFMD-WD scheme will be:

$$B \geq N_s B_m \quad (2.16)$$

where  $N_s$  is the total number of orthogonal waveforms. Since the bandwidth of a signal is highly associated with its time/range radar resolution; it can be easily seen from (2.16) that for a fixed bandwidth  $B$  there will be a trade-off between the number of orthogonal waveforms that can be generated and their radar range resolution. To address this SS problem, various WD techniques have been proposed in the literature. While the term “orthogonal signals” or “orthogonal waveforms” is widely used to describe such SS-WD designs, in reality the condition in (2.11) generally is not met in SS-WD designs. Here a more loose condition will be used to describe waveforms with low cross-correlation i.e.:

$$R_{kl}(\tau) = \int_{-\infty}^{\infty} s_k(t)^* s_l(t - \tau) dt \leq \epsilon \quad (2.17)$$

where  $\epsilon$  is a threshold parameter the value of which depends on the degree of orthogonality or how low the cross-correlation between the waveforms should be for a specific application. The next paragraphs will discuss WD schemes that generate low cross-correlation (CC) that can apply on MIMO radar applications.

### Discrete Frequency-Coding Waveform

The discrete frequency-coding waveforms (DFCW) has been commonly used in wideband radars, as they can allow high range resolution and improve detection

capability (Wehner, 1987). In the literature many authors have proposed variations of DFCM, as schemes for SS-WD designs. A technique based on frequency coding used to generate low CC waveforms for “super low cross-correlation noise” in MIMO SAR was presented in (Meng et al., 2013). The applied technique, also called “same frequency coding orthogonal signals” (SFCOS), uses series of consequent sub-pulses each of which has a constant randomly selected phase. Special cases of these waveforms include the traditional up and down chirps where the phase instead of being random is in an increasing or decreasing order respectively. In (Liu, 2009) the AC and CC properties of DFCW with basis of fixed frequency (FF) pulses (DFCW-FF) and LFM pulses (DFCW-LFM) were investigated. An illustration of the time-frequency profiles of a random DFCW-FF and DFCW-LFM waveform are presented in Fig.2.11a and Fig.2.11b respectively. As it can be seen while DFCW-FF uses monotonic sub-pulses, DFCW-LFM utilises LFM in a sub-pulse level to achieve higher diversity. In fact, as demonstrated in (Liu, 2009), DFCW-LFM can offer lower AC SLL as well as nullify the grating lobes compared to DFCW-FF. Moreover a relationship between the CC peak levels of DFCW-LFM generated waveforms and their time-bandwidth product was also presented. A numerically optimized method to generate low CC DFCW-LFM with good AC properties was proposed in (Reddy et al., 2012).

In (Wang, 2015b) the authors presented a hybrid LFM coding technique, also called “OFDM Chirp Basis Design”, to generate low CC waveforms. As it can be seen in Fig.2.11c, the proposed scheme utilises an extra degree of freedom compared to DFCW-LFM as it uses both up and down chirps allocated in different time-frequency bins based on a random mapping matrix. The good performance

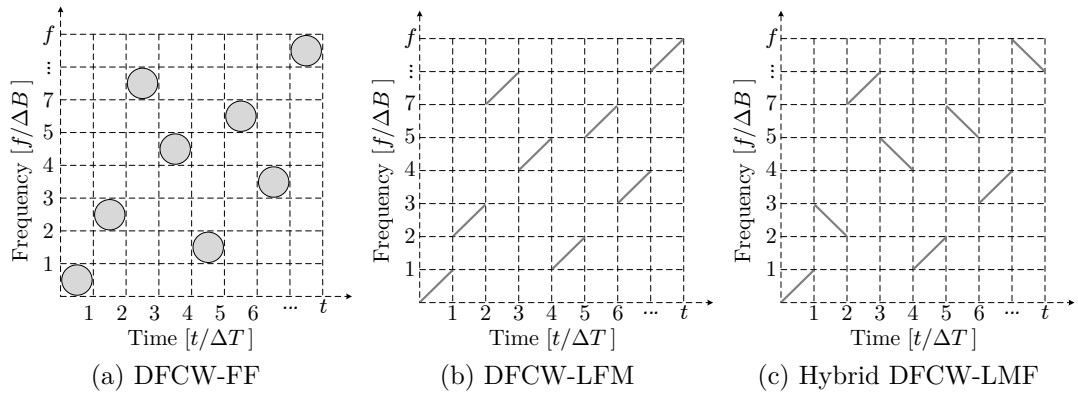


Fig. 2.11 Example of time-frequency mapping in (a) DFCW-FF, (b) DFCW-LFM, and (c) Hybrid DFCW-LMF schemes

of the waveforms was illustrated in terms of AF and cross-ambiguity function (CAF) properties and SAR imaging simulation. The authors in (Shen et al., 2014) proposed chaotic DFCW (CDFCW) designs, showing that Tent and Bernoulli DFCW outperform the design presented in (Liu, 2009). In (Yong-Hua et al., 2015) a discontinuous spectra DFCW design method for MIMO sky-wave radar was presented. The design showed to offer DFCW-FF and DFCW-LFM waveform sets with low CC but high AC SLL introduced by the spectra discontinuity. Authors in (Mehany et al., 2015) showed that by replacing LFM with modified LFM in a DFCM scheme the peak and integrated sidelobe ratios can be significantly reduced.

### Other techniques

While DFCW has been demonstrated to be an attractive scheme for MIMO radar waveform design, other techniques can be also applied to achieve WD with good spectrum utilisation. In particular, time division multiplexing (TDM) can be used to decorrelate waveforms in different time slots. Being a straight forward and easy to implement approach, TDM unfortunately is not applicable in all radar systems due to the requirement of good synchronisation and the range ambiguities that are introduced. For these reasons, TDM has been mostly proposed for co-located configurations system (see Section 2.3.1). Namely, in (Rambach and Yang, 2013) and (Rambach et al., 2014) an investigation on the performance of DOA estimation of moving targets in TDM MIMO radar was held, deriving also the conditions for optimal TDM schemes based on the Cramer-Rao bound (CRB). Moreover, a comparison of motion compensation methods for TDM continuous wave (FMCW) radar was demonstrated in (Guetlein-Holzer et al., 2014). Experimental results showed that both intertwined and triangular TDM schemes are able to deal with the presence of different velocities in the same scene.

In a different approach, a MIMO radar waveform design based on chirp rate diversity was presented in (Wang, 2015a). As shown the proposed scheme can generate a large number of low CC waveforms with large time-bandwidth product, constant envelope (CE), no range-Doppler coupling target response, and Doppler tolerance. Furthermore, chirp rate diversity was also utilised in (Li et al., 2017) where an OFDM chirp WD design was proposed. This modulation scheme shares the same principle with DFCW, with the sub-pulses composing the waveforms however having different time duration or different bandwidths, and constitutively different chirp rates with each other. As the authors demonstrate, this allows

for lower AC and CC SLL compared to the DFCW-LFM and DFCW-HLFM methods.

### 2.4.2 Joint Communication and Radar

Recent technological advancements have increased the number of applications in which both communication and radar operations are required simultaneously by the same system. Examples of this kind of scenarios include intelligent transportation systems (ITS) in which automotive vehicles must detect changes in their environment while also performing vehicle-to vehicle and/or vehicle-to-infrastructure communication in order to exchange information and alerts (Hartenstein and Laberteaux, 2008; Hubaux et al., 2004). Another example of such applications is distributed MIMO sensing networks in which the nodes must be able to perform radar operations while also being aware of the state and position of collaborating sensors.

The simplest and more straight-forward approach in joint communication and radar systems is to employ two separate sub-systems dedicated for each task. An obvious drawback of such an approach however is the need of separate hardware and spectrum resources which can be very significant for systems restricted by low size, weight and power (SWAP), and areas/bands with high spectrum occupancy respectively. To address these drawbacks, many researchers have adapted the concept of joint communication-radar designs also called dual-function radar communication (DFRC) systems (Hassanien et al., 2016). In (Blunt et al., 2010) the authors exploited WD to embed a communication signal into radar emissions using a bank of radar waveforms with each of which corresponding to a communication symbol. The proposed design allows the communication receiver to retrieve the correct transmitted symbol by matched filtering the received signal.

A different approach where time-modulated arrays are employed in order to transmit information in a certain spatial direction by controlling the SLL while also being able to perform radar operations though the main lobe was introduced in (Euzière et al., 2014) and further examined in (Euzière et al., 2015). Moreover, the authors in (Hassanien et al., 2015a) employ both WD and bi-level sidelobe control to transmit series of bits in each radar waveform emission while keeping the main lobe constant to perform radar operations. Lastly in (Hassanien et al., 2015b) the authors proposed a phase-modulation (PM) method which uses two orthogonal waveforms and a phase dictionary to map a phase symbol on the total transmitted waveform. By applying a phase detector the receiver can determine

Table 2.3 Comparison Between Different Information-Embedding Techniques (Hassanien et al., 2016)

	Waveform diversity	Sidelobe AM	Multiwaveform ASK	PM method
Number of waveforms	$2^{N_b}$	One	$N_b$	One pair
SSLs change from pulse to pulse	No	Yes	Yes	No
Communication via side/main lobe	Both	Sidelobe	Sidelobe	Both
Directivity in communication	Broadcasting	Directional	Directional	Either

the phase difference between the two waveforms and retrieve the transmitted symbol.

A comparison between the aforementioned DFRC schemes was presented in (Hassanien et al., 2016) with the result being summarised in Table 2.3. In general, all the discussed joint communication and radar strategies aim to share the available resources, such as hardware, power and bandwidth, to perform both operations simultaneously, prioritising however the radar function of the system. Nevertheless, inspecting Table 2.3 it can be seen that four discriminative characteristics are identified. Namely, the number of waveforms used by each respective method can significantly effect the memory requirements of the system. As it can be seen the WD method (Blunt et al., 2010) requires the larger number of waveforms among all the discussed techniques. Moreover, SSLs variation between pulse to pulse transmissions may significantly distort the clutter and signal dependent interference perceived by the radar system, consequently limiting its ability to compensate these components. As previously discussed, sidelobe AM (Euzière et al., 2015) and multiwaveform ASK (Hassanien et al., 2015a) schemes utilise these SSLs changes to embed information in their transmissions. Another consequence of employing the SSLs for communication operations, is that the system must support for digital beamforming, i.e. sensor array, while the communication receiver must also be located in specific directions. In this manner, the WD (Blunt et al., 2010) and PM (Hassanien et al., 2015b) methods can be considered more flexible as they do not require any specific antenna structure, with the former method however also not allowing for directivity in the communication.

## 2.5 Radar Imaging and Edge Detection

Synthetic aperture radar (SAR) refers to a particular implementation of an imaging radar system that utilizes the movement of the radar platform and specialized signal processing to generate high-resolution images. A SAR is principally an airborne or spaceborne coherent side-looking radar. This configuration takes advantage of the echoes history as the radar platform is moving forward to synthesise an antenna of larger aperture called syntetic aperture (Curlander and McDonough, 1991; Melvin and Scheer, 2014; Skolnik, 1970).

Since SAR is an active radar system, it can overcome some of the fundamental problems associated with conventional passive remote sensing, e.g. cloud cover, changes of solar illumination, etc. The structures in SAR images give important contextual information useful to the detection and the classification of entities, as vegetation, urban area, and industrial area. Although SAR is a very effective terrain and sea surface-mapping device, the provided images may be strongly affected by speckle noise (Goodman, 1976). Significant aspects such as SAR imaging principles, speckle noise reduction and edge detection are briefly discussed in next paragraphs.

### 2.5.1 Synthetic Aperture Radar

Synthetic aperture radar systems have a side-looking imaging geometry based on pulsed radar, which is installed on a forward moving platform. A graphical illustration of a typical SAR geometry is given in Fig. 2.12. The direction of the moving platform is commonly called *along-track* direction while perpendicular direction in which the radar antenna is pointing is called *cross-track* direction. As the radar moves continuously, high power pulses are transmitted from different of its individual positions. Each transmission period is followed by the echo window operation during which the radar captures the scattered echoes and stores the received signals in a system memory. The transmission and reception or listen procedure compose a complete T/R cycle repeated every PRI of time equal to the inverse of the PRF (see Section 2.2). After passing through the receiver, the return echoes are kept in the system memory. Therefore over the time, individual T/R cycles are completed with the data from each cycle being stored in a processing memory.

The SAR signal processing algorithms use both magnitude and phase of the received signals over successive pulses from the elements of a *synthetic aperture*.

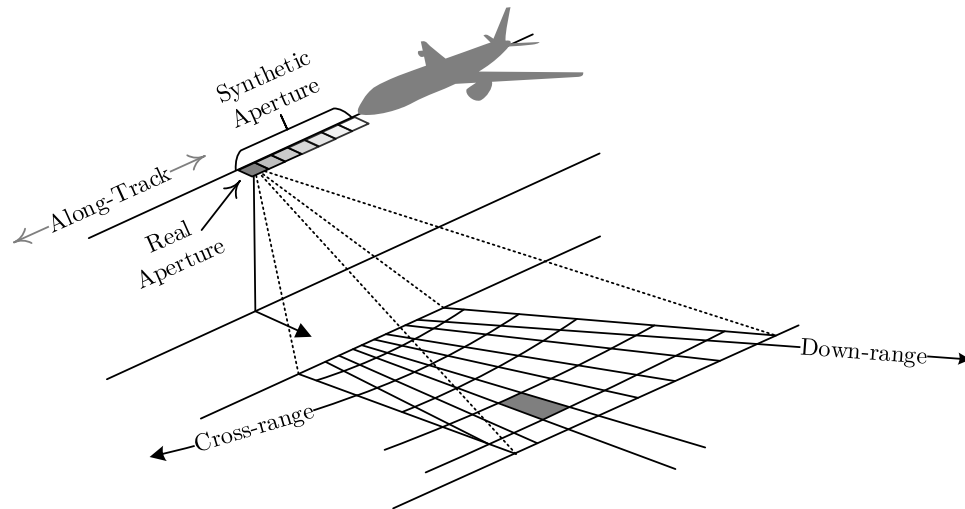


Fig. 2.12 SAR system geometry

The inherent Doppler effects is also taken into account for the different transmitter to target geometry in each succeeding cycle. Using these effects, targets can be separated in the along-track direction on the basis of their different Doppler frequencies. This technique was originally known as Doppler beam sharpening, but later became known as SAR (Curlander and McDonough, 1991; Melvin and Scheer, 2014). Using the different delays in cross-track and the different Doppler shifts in along-track direction the radar system can resolve the returns in *down-range* and *cross-range* respectively (see Fig. 2.12) synthesising a 2-D map or a SAR image of the illuminated area (Carrara et al., 1995).

The SAR operation is similar of a phased array (see Section 2.3.1), however SAR uses one antenna in time-multiplexing mode in contrary to the large number of the parallel antenna elements of a phased array. The range or down-range resolution of a SAR image is directly related to the bandwidth of the transmitted signal, while the azimuth or cross-range resolution improves as the length of the real antenna aperture reduces. Therefore, transmitting wide bandwidth waveforms allows to obtain fine down-range resolution, while high cross-range resolution is achieved through coherently processing the echoes from the various positions along flight path when emulating a large aperture (Elachi and Van Zyl, 2006; Massonnet and Souyris, 2008; Oliver and Quegan, 2004).

As discussed previously, each position of the radar platform is taken into account when adding the signals to integrate the energy for the along-track direction. As a result of the radar movement, the distance between the radar and the scatterer changes continuously with the minimum distance occurring when

the scatterer is directly broadside of the radar platform. The distance changing between the radar and the scatterer implies that after range compression, the phase of the signal will be different for the separate positions along the flight path (Melvin and Scheer, 2014). In practice, the phase of the return signal is affected by several factors, which together can make the absolute phase return in any SAR data collection essentially arbitrary, with no correlation from pixel to pixel. To get any useful information from the phase, some of these effects must be isolated and removed.

The most important factor affecting the phase is the interaction with the ground surface. Depending on the properties of the material, the phase of the wave may change on reflection. Therefore SAR system can measure target physical properties (roughness and dielectric constant). Also coherent phase measurements allow for digital elevation maps (DEM) and deformation mapping (Fetterer et al., 1994). Operation of SAR system requires a complex integrated array of on-board, navigational and control systems, with location accuracy provided by both Doppler and inertial navigation equipment. A stable, full-coherent transmitter, an efficient and powerful SAR-processor, and exact knowledge of the flight path and the velocity of the platform are the main requirements of SAR system (Cumming and Wong, 2005; Curlander and McDonough, 1991; Franceschetti and Lanari, 1999).

### 2.5.2 Speckle Noise

Electromagnetic waves emitted by active sensors travel in phase and interact minimally on their way to the target area. After interaction with the target, these waves are no longer in phase even though they are coherent in frequency. This is caused by several factors, such as the difference in distance the waves travel back from different targets, or the single versus multiple scattering due to the variance in surface roughness (Lee et al., 1994). Also it should be noted that the signals might go out of phase as the synthesized antenna moves (Hervet et al., 1998).

As a SAR image is formed by coherently processing the backscatter returns of successive radar pulses, out-of-phase waves are superimposed producing a resultant wave of greater, lower or the same amplitude. This interference effect causes a pixel-to-pixel variation in intensity, which appears as a granular pattern having bright and dark pixels called *speckle* noise. This irregularity of pixels result in a SAR image not to have a constant mean radiometric level in homogeneous areas. The coherent nature of the SAR imaging system inevitably leads to speckle noise (Bruniquel and Lopes, 1997; Goodman, 1976; Lee et al., 1994). In Fig. 2.13

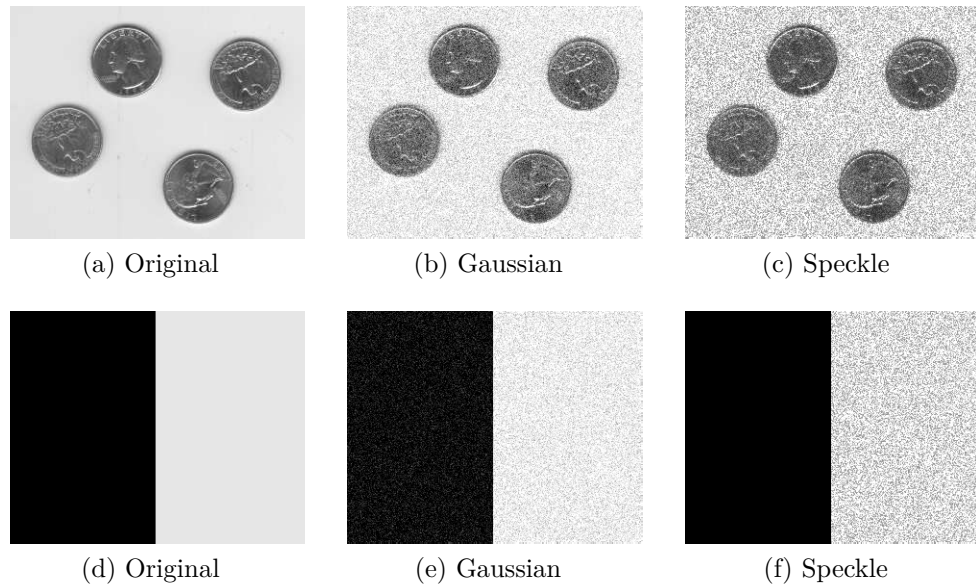


Fig. 2.13 Example of two images before (left) and after introducing Gaussian (middle) and speckle (right) noise.

examples in two images injected with artificial Gaussian and speckle noise are illustrated. The main difference between the two different kinds of noise is that Gaussian is an additional noise process while speckle noise is multiplicative (Singh and Shree, 2016). This can be better illustrating by comparing the black region in subfigures Fig. 2.13e and Fig. 2.13f. As it can be seen when speckle noise is introduced in completely black or zero value pixels the effect is suppressed.

The presence of speckle reduces the radiometric resolution of the image and the detectability of the image features. Speckle reduction is becoming a commonly used routine process, since it is desirable to reduce the speckle noise prior to image applications. In the literature various filtering approaches to reduce the speckle noise have been proposed (Mansourpour et al., 2006; Meenakshi and Punitham, 2011; Podder and Hasan, 2016). Namely, simple approaches such as mean, median and local region filters can be employed to mitigate the speckle intensity. Moreover, Gamma-MAP, Frost and Lee filter which take into consideration further statistical characteristics of the image usually have better performance (Mansourpour et al., 2006). In (Yu and Acton, 2002) a speckle reducing anisotropic diffusion method was proposed, demonstrating its superior performance compared to conventional techniques in preserving edges. Further speckle reduction techniques include, among others, wavelet based methods (Jagadesh and Rani, 2016; Liu et al., 2014a) and local polynomial regression (Sharabati and Xi, 2016). In (Mohan et al., 2016)

an approach based on Wiener filtering and adaptive wavelet thresholding, which outperforms the method proposed in (Liu et al., 2014a), was demonstrated.

### 2.5.3 Edge Detection

In radar applications, it is common to apply image processing techniques for target detection in SAR images. A fundamental step in image analysis is the image segmentation which consists of partitioning an image into homogeneous regions that share some common properties. There are two main strategies approaching the image segmentation problem: edge and region based. Edge-based segmentation looks for discontinuities in the intensity of an image, while region-based segmentation looks for uniformity within a sub-region based on a desired property, e.g. intensity, color, and texture. In gray-scale images, edges are associated with intensity changes and are efficient descriptors of the image structure. Results of the edge detection process are used in higher-level image analysis stages such as pattern recognition and three dimensional (3-D) image reconstruction (Le Moigne and Tilton, 1995; Marr and Hildreth, 1980; Wang, 1993).

Edge detection process plays a key role in image analysis. In images with no texture, an edge can be defined as the boundary between two regions with relatively distinct properties. Among the main criteria that should be satisfied by an edge detector are the low sensitivity to noise, the good edge localization and the avoidance of incorrect edge detection (Canny, 1983). Over the time many classical edge detectors have been developed including morphological edge detectors and differentiation-based edge detectors (Holyer and Peckinpaugh, 1989; Jensen, 1986; Lee et al., 1987; North and Yu, 2001; Shen and Castan, 1992). Some of them are mainly based on either detection of maxima of the gradient or zero crossings of the second derivatives. Since differential operators are sensitive to noise, a pre-processing smoothing is often required. Particularly in processing SAR images, operators of very low sensitivity to noise should be considered to efficiently detect edges. The usual gradient-based edge detectors, developed for optical images, compute the difference between the local mean values on opposite sides of considered pixel. Some of the well-known edge detection operators based on the first derivative of the image are Roberts, Prewitt, and Sobel, which are traditionally implemented by convolving the image with masks (Ulaby et al., 1981). In Fig.2.14 an example of edge extraction using (b) a Sobel and (c) a Canny detector is illustrated, using automatic threshold as implemented in (MathWorks,

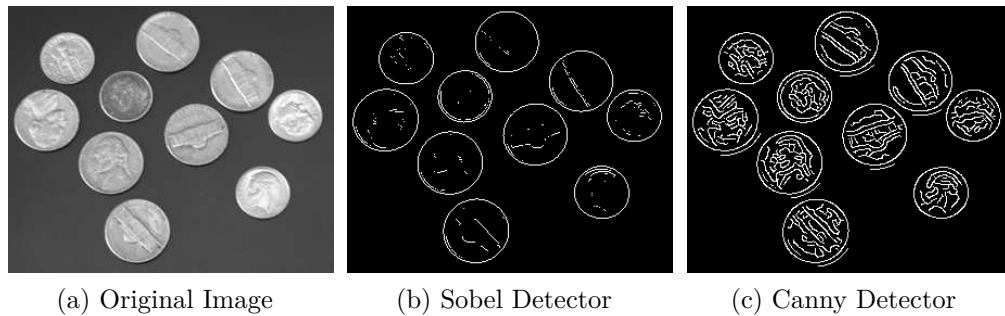


Fig. 2.14 Example of edge detection in (a) an original using (b) a Sobel and (c) a Canny detector.

2017a). As it can be seen the Canny detector is more sensitive to weak edges (see shapes inside the coins) compared to the Sobel detector. However, it should be mentioned that generally Sobel detectors are much simpler to implement than Canny detectors.

In the literature various edge detection techniques specialised for SAR images have been proposed. Namely, in (Touzi et al., 1988) an edge detector based on the ratio of averages (ROA) between pixel values has been developed. For better edge extraction, the detector operates along four directions over windows of increasing size while a geometrical operator is also applied to thin the retained edges. Following more recent studies, in (Wang et al., 2011) a method for detecting edges in SAR images based on edge localisation from their respective optical images is presented. While the obvious disadvantage of such technique is that both SAR and optical images are required for the same area, the proposed method demonstrated to outperform the ROA and Canny detectors. An edge detection technique using real and imaginary decomposition was proposed in (Baselice et al., 2014). As demonstrated, the proposed method is robust to phase offset artifacts while achieving good edge detection performance, in the cost however of high computational cost. In (Hazarika et al., 2015) an enhanced Lee filter based on the Lapped orthogonal transform was introduced to allow simultaneous speckle reduction and edge detection. Moreover, in (Wei et al., 2016) crater-shaped windows were employed to replace the more traditional square-shaped windows. Applied in combination with an edge compensation strategy, the proposed technique demonstrated its good edge detection performance in simulated and real images.

## 2.6 Summary

This chapter presented a critical research review in a number of very important aspects in radar systems. Basic and advanced radar techniques were discussed with more focus on radar waveform design and pulse compression techniques. The multisensor radar systems were also introduced exploring their categorisation depending on the operating signals and geometry. Later, the topical subject of spectrum sharing was discussed addressing recent advances regarding WD in MIMO radar and DFRC. Analytically, proposed WD schemes such as OFDM and DFCW that allow design of multiple waveforms with good AC properties and low CC peak levels were investigated. Moreover, recently proposed techniques that allow joint communication and radar operations were investigated. Namely schemes exploiting WD, sidelobe AM, multiwaveform ASK, and PM to allow communication transmission through radar emissions were discussed. Lastly, the concept of SAR was introduced with focus on the speckle reduction and edge detection challenges.

# Chapter 3

## Advanced Time-Frequency Transforms

### 3.1 Introduction

In this chapter the basic concepts of time-frequency (T-F) analysis are discussed in the context of radar signal processing. Commonly used T-F transforms and signal representations such as the short-time Fourier Transform (STFT) and Wigner-Ville distribution (WVD) are introduced in conjunction with their general radar applications. Moreover, the ambiguity function (AF) will be extensively discussed highlighting its importance as a performance evaluation tool for radar systems. In detail, the canonical or Woodward AF definition and its applications in waveform design are firstly discussed. A different, less common definition of the AF based on the Kullback-Leibler divergence (KLD) is also introduced, considering its more generic approach compared to the canonical definition. For completion, other common AF definitions are also provided concerning both monostatic and multisensor systems. Next, the fractional Fourier transform (FrFT) is introduced as a generalisation of the conventional Fourier transform (FT), while its various applications in radar signal processing are also discussed. Lastly, the phase stretch transform (PST) is presented in connection with its good performance in edge detection applications.

### 3.2 Time-Frequency Analysis

Signal analysis in both time and frequency domains is fundamental for almost all radar applications. As discussed in Chapter 2, in basic radar processing, time

and frequency measurements are directly converted, respectively, into the target's range and relative velocity from the radar sensor. As a result, the signal needs to be examined in either of these two domains to extract the desired parameters. Since the received signal is sampled in the time domain, to transfer it into the frequency domain the FT is commonly employed. While for basic radar processes the FT is sufficient, examining signals in more complex scenarios usually requires more sophisticated tools.

In signal processing, T-F analysis includes representations and processing techniques that allow the study of a signal in both time and frequency domains simultaneously. Essentially, in T-F analysis rather than examining a 1-dimensional signal as function of time or frequency separately, T-F transforms are employed to extract information of the signal as a function of both or even in between domains. Generally, the T-F transforms can be divided into two classes: linear and bi-linear or quadratic transforms corresponding to their dependence on the applied signal (Hlawatsch and Boudreaux-Bartels, 1992).

### 3.2.1 Linear Transforms

Linear transforms include operations which satisfy superposition and linearity principles, i.e.:

$$\mathcal{T}\{c_1x_1(t) + c_2x_2(t)\} = c_1\mathcal{T}_{x_1} + c_2\mathcal{T}_{x_2} \quad (3.1)$$

where  $\mathcal{T}\{\cdot\}$  is a T-F transform,  $x_1(t)$  and  $x_2(t)$  are two arbitrary functions,  $c_1$  and  $c_2$  are two arbitrary constants, and  $\mathcal{T}_{x_1}$  and  $\mathcal{T}_{x_2}$  are the transformed results of  $x_1(t)$  and  $x_2(t)$  respectively. A very important property that can be derived from (3.1), is that the output of a linear transform applied on the summation of different signals, depends only on their individual behaviour and not their in-between relationship. As a direct result, cross-interference between correlated signals can generally be avoided. Linear T-F transforms include among others the STFT and wavelet transform, with the former being extensively used for radar signal representations (Boultadakis et al., 2004).

#### Sort-Time Fourier Transform

The STFT of an arbitrary time signal  $x(t)$  is defined as:

$$\text{STFT}\{x(t)\}(t', f) = \int_{-\infty}^{\infty} x(t)w^*(t - t')e^{-j2\pi ft} dt \quad (3.2)$$

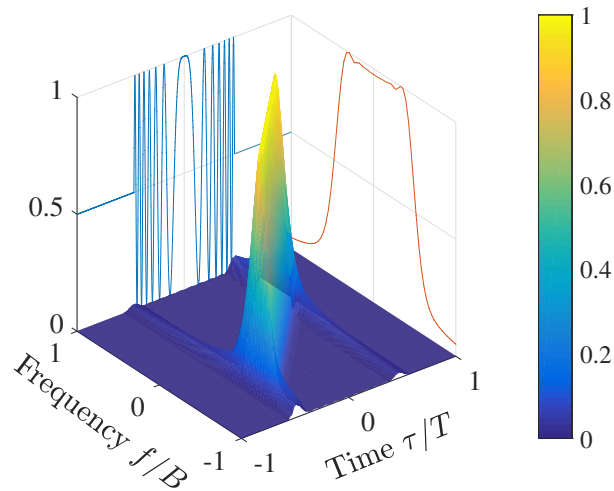


Fig. 3.1 Illustration of the STFT of a LFM pulse and the projection of its real part in time domain and absolute value in frequency domain (spectrum).

where  $w(t)$  is a window function, e.g. Hamming or Gaussian window, centred at zero delay (Heinzel et al., 2002). Examining (3.2) it can be easily derived that the STFT uses a window to divide a long non-stationary signal into shorter segments centred at  $t'$  and perform spectrum analysis in each segment separately using the FT. Similarly to FT, the STFT of a signal results to values in the complex plane. For this reason visual representation of its modulus, i.e.  $|\text{STFT}\{x(t)\}(t', f)|$ , is usually employed to provide an illustration of the signals intensity in different T-F resolution bins.

The STFT finds various applications in radar T-F analysis, with waveform design being a typical example. As discussed in Section 2.2.3, pulse compression is directly related to the T-F profile of the modulation scheme. In Fig. 3.1 the STFT of a LFM waveform is illustrated along with its real part and absolute value projections in time and frequency plane respectively. As it can be seen, while time and frequency representations can offer informations of the signal's characteristic on the respective domains, the STFT provides a complete profile of the signal in both domains simultaneously.

While using STFT is the most straight-forward approach for T-F analysis, its main drawback is that it always poses a trade-off between time and frequency resolution, depending on the size of the window. Particularly, larger window sizes lead to finer frequency resolution but also result into poorer time resolution (Allen and Mills, 2003). Window overlapping can mitigate this issue to a degree, however too high overlap can lead to the segments being strongly correlated and hence not providing more inform on the signal (Heinzel et al., 2002).

### 3.2.2 Quadratic transforms

In contrary to the linear, quadratic transforms satisfies the *quadratic superposition principle*:

$$\mathcal{J}\{c_1x_1(t) + c_2x_2(t)\} = |c_1|^2\mathcal{J}_{x_1} + |c_2|^2\mathcal{J}_{x_2} + c_1c_2^*\mathcal{J}_{x_1,x_2} + c_2c_1^*\mathcal{J}_{x_2,x_1} \quad (3.3)$$

where  $\mathcal{J}_{x_1,x_2}$  and  $\mathcal{J}_{x_2,x_1}$  are the results of the cross-transforms of  $x_1(t)$  with  $x_2(t)$  and  $x_2(t)$  with  $x_1(t)$  respectively. While the results of these cross terms, i.e.  $\mathcal{J}_{x_1,x_2}$  and  $\mathcal{J}_{x_2,x_1}$ , will vary depending on the applied transform and the correlation between the different components, i.e.  $x_1(t)$  and  $x_2(t)$ , they usually characterised as cross-term interference and are undesirable (Kadambe and Boudreaux-Bartels, 1992). In the literature, several techniques such as windowing, smoothing and scaling in T-F domain (Amirmazlaghani and Amindavar, 2009; Xing et al., 2009) have been proposed to reduce this effect. Commonly used quadratic transforms include among other the AF, WVD, pseudo Winger distribution and Choi–Williams transform (Allen and Mills, 2003; Hlawatsch et al., 1995; Levanon and Mozeson, 2004).

#### Wigner-Ville Distribution

The WVD of an arbitrary signal  $x(t)$  is defined as:

$$\text{WVD}\{x(t)\}(t, f) = \int_{-\infty}^{\infty} x(t + \frac{\tau}{2})x^*(t - \frac{\tau}{2})e^{-j2\pi f\tau}d\tau \quad (3.4)$$

Comparing (3.4) with the STFT definition in (3.2), it can be seen that instead of using a window  $w(t)$  to segment the examined signal  $x(t)$ , WVD correlates time and frequency shifted versions of  $x(t)$  with each other to generate a T-F representation of the signal. As a significant consequence, WVD does not exhibit the T-F resolution trade-off that STFT suffers from (Boashash, 2015). Being a quadratic transform however, WVD suffers from cross-term interference between correlated components. In Fig. 3.2 the (a) WVD and (b) STFT are illustrated for two consequent LFM pulses centred at  $t = -T/4$  and  $t = T/4$  respectively. As it can be seen while the WVD exhibits superior resolution compared to the STFT, it does suffer from interference terms centered at  $t = 0$ .

To cope with the undesired interference terms, smoothing can be applied in both time and frequency domains to provide the what is known as *smoothed-pseudo-WVD* (Hlawatsch and Boudreaux-Bartels, 1992). Unfortunately, while

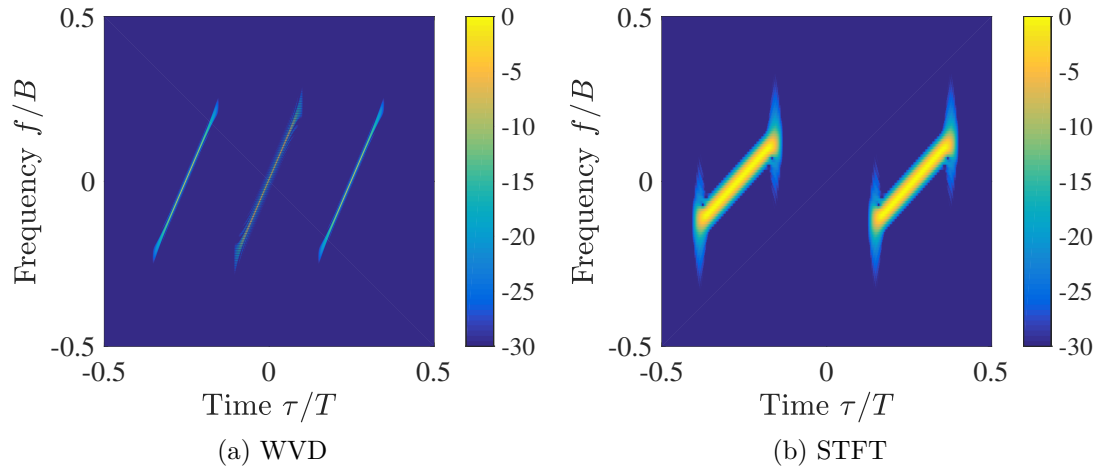


Fig. 3.2 Illustration of the (a) WVD and (b) STFT for two consequent LFM pulses.

smoothing can attenuate the interference terms, it generally causes a broadening of signal terms and hence degradation in resolution. In the literature various generalisations and modified versions of the WVD have been proposed to provide good resolution and free of interference signal analysis (Goncalves and Baraniuk, 1998; Pikula and Beneš, 2014; Ren et al., 2016; Stankovic, 1994).

### 3.3 Ambiguity Function

As discussed in Section 2.2.3, the matched filter is a fundamental tool in radar signal processing. While the matched filter output of a waveform can provide information regarding the expected resolution and sidelobes in time domain, it is not sufficient for predicting the performance of the system in cases that the return signal is miss-matched in the frequency domain due to Doppler shifts.

The AF is one of the most important tools in radar signal processing. Being a quadratic transform, usually expressed as a function of time and frequency shifts, the AF aims to provide a metric for the parameter estimation performance of a sensor system. Since its first conception for radar signals, the AF has been extensively applied in a variety of fields, such as sonar, communications and optics, many different definitions have been proposed in the literature. Following a review of the most common radar related AF definitions is held.

### 3.3.1 Canonical AF Definition

In 1967, Woodward P. introduced the general AF concept, aiming to characterize how well a system could identify the target's range and velocity parameters, based on the transmission of a known waveform (Woodward, 1953). The general definition of the AF is given as (Richards et al., 2010):

$$\mathcal{A}_{Ca}(\tau, f_D) = \int_{-\infty}^{+\infty} x(t)x^*(t - \tau)e^{j2\pi f_D t} dt \quad (3.5)$$

where  $\tau$  and  $f_D$  are time and frequency shifts respectively, and  $\{\cdot\}^*$  is the complex conjugate operator.

Comparing (3.5) with (3.4) it can be seen that there is a strong relationship between the AF and the WDV. In fact the AF of a signal can be expressed as the 2D FT of its WVD (Allen and Mills, 2003). It is worth noting that unlike the STFT and WVD which aim to provide a T/F profile of the examined signal  $x(t)$ , the AF describes the response of a filter matched to  $x(t)$  when the signal is received with a delay  $\tau$  and a Doppler shift  $f_D$  relative to the nominal values expected by the filter (Levanon and Mozeson, 2004). In the concept of radar systems positive values of time delay, i.e.  $\tau > 0$ , imply that the target is located away from the reference position  $\tau = 0$  while negative values, i.e.  $\tau < 0$ , indicate that the target is located closer. Moreover, positive and negative Doppler shift, i.e.  $f_D > 0$  and  $f_D < 0$ , indicate that the target is moving toward or in an opposite direction from the radar.

The AF is also used to describe the interference caused by the range and/or Doppler shift of a target when compared to a reference target of equal radar cross section (RCS) called nominal targets. Therefore the AF at nonzero points, i.e. all other points except the origin, represents returns from some range and Doppler different from those for the nominal target, while returns from nominal target are located at the origin of the AF (Richards, 2005).

### 3.3.2 AF Cuts and Properties

By its definition, the AF of an arbitrary signal returns complex values. It is therefore common in radar processing to use the modulus of the AF, i.e.  $|\mathcal{A}_{Ca}(\tau, f_D)|$  to describe performance characteristics of the examined signal (Levanon and Mozeson, 2004). Following the absolute value of the AF in (3.5) will be considered to review some of its major properties.

One-dimensional cuts of the AF are commonly used to provide very important properties associated with the expected resolution and ambiguities in the time and Doppler domain separately. First, consider the cut along the delay axis or the so called zero-Doppler cut. Setting  $f_D = 0$  the AF formula in 3.5 can be rewritten as follows:

$$|\mathcal{A}_{Ca}(\tau, 0)| = \left| \int_{-\infty}^{+\infty} x(t)x^*(t - \tau)dt \right| \quad (3.6)$$

As it can be easily seen in (3.6) the zero-Doppler cut is described by the AC of the signal  $x(t)$  which can also be expressed as the inverse Fourier transform (IFT) of the signal's power spectrum:

$$\int_{-\infty}^{+\infty} x(t)x^*(t - \tau)dt = \mathcal{F}^{-1}\{|\mathcal{F}\{x(t)\}|^2\} \quad (3.7)$$

where  $\mathcal{F}\{\cdot\}$  and  $\mathcal{F}^{-1}\{\cdot\}$  denote the FT and IFT respectively. It can therefore be derived that the zero-Doppler AF cut of a signal  $x(t)$  can be manipulated with proper design of its spectrum.

The second examined AF cut is along the Doppler frequency axis also called zero-delay cut. Setting  $\tau = 0$  the AF formula in 3.5 can be rewritten as follows:

$$|\mathcal{A}_{Ca}(0, f_D)| = \left| \int_{-\infty}^{+\infty} |x(t)|^2 e^{j2\pi f_D t} dt \right| \quad (3.8)$$

The formula in (3.8) implies that the zero-delay cut of the AF is a function only of the magnitude of the signal  $x(t)$  and is equal to the Fourier transform of its squared magnitude. In other words, this cut remains unchanged to any phase or frequency modulation in  $x(t)$  (Levanon and Mozeson, 2004). Some further properties of the AF are described as follows:

**Maximum Value:** The maximum value of the AF of any signal will be located at the origin of its axes:

$$|\mathcal{A}_{Ca}(\tau, f_D)| \leq |\mathcal{A}_{Ca}(0, 0)| = E \quad (3.9)$$

**Symmetry about the origin:** The AF of any signal will be symmetric at its origin:

$$|\mathcal{A}_{Ca}(\tau, f_D)| = |\mathcal{A}_{Ca}(-\tau, -f_D)| \quad (3.10)$$

**Volume invariance:** The AF of any signal with finite energy  $E$  will have a finite volume equal to  $E^2$ :

$$\int_{-\infty}^{+\infty} \int_{-\infty}^{+\infty} |\mathcal{A}_{Ca}(\tau, f_D)|^2 dt df_D = E^2 \quad (3.11)$$

### 3.3.3 Ideal and basic signal AF

Usually the ideal shape of the AF is described as a spike of infinitesimal width that peaks at the origin of time-Doppler axes,  $\tau = 0$  and  $f_D = 0$ , and is zero everywhere else, corresponding to an ideal resolution between neighbouring targets. This, usually described as “thumbtack”, AF shape however cannot physically exist, since such an AF should have finite peak value equal to  $E$  and a finite volume also equal to  $E^2$  at the same time (see AF properties in (3.9) and (3.11)). As a direct consequence of these limitations, reducing the “height” of the AF in certain regions, e.g. close to the centre to increase the resolution, will push the volume in other areas leading to secondary sidelobes in the delay-Doppler plain. Similar to the AC (see Section 2.2.3), sidelobes in the AF are undesired as any non-zero values other than its origin represents a potential range and Doppler shifts that could be mistaken for the correct one.

In general, AFs are analysed on a single pulse basis. Hence there is no error considering the AF analysis on CW radars, since the results apply equally well to CW radar waveforms. However, in CW radars there is an advantage referred to the concept of periodic ambiguity function (PAF), which is not shared by modulated pulsed radars. The concept of PAF allows attaining an AC function without sidelobes on the delay axis for certain class of phase-coded signals employed in CW radars (Levanon, 2010). Following the AF of two basic signals will be discussed.

#### Unmodulated Square Pulse

Consider the normalized rectangular  $x(t)$  pulse, i.e.  $\int_{-\infty}^{+\infty} |x(t)|^2 dt = 1$ , defined by:

$$x(t) = \frac{1}{\sqrt{T}} \text{rect} \left\{ \frac{t}{T} \right\} \quad (3.12)$$

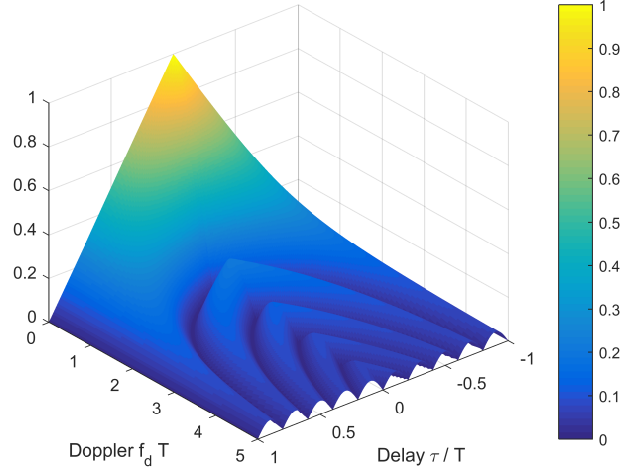


Fig. 3.3 Ambiguity function of an unmodulated square pulse.

where  $T$  is the duration of the pulse and  $\text{rect}\{\cdot\}$  is the rectangular function. Substituting (3.12) in (3.5) the AF of  $x(t)$  is given as:

$$|\mathcal{A}_{\text{Ca}}(\tau, f_D)| = \left| \left(1 - \frac{|\tau|}{T}\right) \frac{\sin\left(\pi f_D T \left(1 - \frac{|\tau|}{T}\right)\right)}{\pi f_D T \left(1 - \frac{|\tau|}{T}\right)} \right|, \quad |\tau| \leq T \quad (3.13)$$

From (3.13) the zero-Doppler AF cut can also be calculated as:

$$|\mathcal{A}_{\text{Ca}}(\tau, 0)| = \left| \left(1 - \frac{|\tau|}{T}\right) \right| \quad (3.14)$$

What should be pointed from (3.14) is that the first null of the zero-Doppler cut is located at  $\tau_{\text{null}} = T$ . This indicates that the width of the main lobe is proportional to the pulse width. Moreover the zero-delay cut is given as:

$$|\mathcal{A}_{\text{Ca}}(0, f_D)| = \left| \frac{\sin(\pi f_D T)}{\pi f_D T} \right| \quad (3.15)$$

As mentioned previously in this section, the zero-delay cut only depends on the modulus of the signal  $|x(t)|$ . As it can be seen in (3.15), any signal with a square modulus has a zero-delay cut described by a sinc function. In Fig. 3.3 a graphical representation of the AF of a square pulse is given.

### LFM Pulse

Consider the normalized LFM  $x(t)$  pulse defined by:

$$x(t) = \frac{1}{\sqrt{T}} \text{rect} \left\{ \frac{t}{T} \right\} e^{j\pi(B/T)t^2} \quad (3.16)$$

where  $B$  is the bandwidth of the pulse. Substituting (3.16) in (3.5) the AF of  $x(t)$  is given as:

$$|\mathcal{A}_{\text{Ca}}(\tau, f_D)| = \left| \left(1 - \frac{|\tau|}{T}\right) \frac{\sin \left( \pi T \left( f_D + \frac{B}{T} \tau \right) \left(1 - \frac{|\tau|}{T}\right) \right)}{\pi T \left( f_D + \frac{B}{T} \tau \right) \left(1 - \frac{|\tau|}{T}\right)} \right|, \quad |\tau| \leq T \quad (3.17)$$

From (3.13) the zero-Doppler AF cut can also be calculated as:

$$|\mathcal{A}_{\text{Ca}}(\tau, 0)| = \left| \left(1 - \frac{|\tau|}{T}\right) \frac{\sin \left( \pi B \tau \left(1 - \frac{|\tau|}{T}\right) \right)}{\pi B \tau \left(1 - \frac{|\tau|}{T}\right)} \right| \quad (3.18)$$

From (3.18) it can be extracted that if the time-bandwidth of the pulse is large enough, i.e.  $TB \gg 4$ , the first null of the zero-Doppler cut is located at  $\tau_{\text{null}} \approx 1/B$ .

Comparing with the results from the square pulse it can be seen that after applying LFM the main lobe of zero-Doppler depends on the bandwidth  $B$  instead of the pulse width  $T$ . This indicates that the choice of  $B$  can completely determine the compressed pulse width of the matched filter output. Consequently the LFM AF cut along the time delay axis is narrower than that of the unmodulated pulse by a factor of:

$$\varrho_{\text{LFM}} = \frac{T}{1/B} = TB \quad (3.19)$$

Here the factor  $\varrho_{\text{LFM}}$  is referred to as the compression ratio, also called time-bandwidth product or compression gain. All three names can be used interchangeably having the same meaning. Equation (3.19) simply indicates that the compression ratio is getting greater as the radar bandwidth is increased (Mahafza, 2002). Finally, since the modulus of the LFM pulse has the same shape with the modulated pulse, the zero-delay AF cut of an LFM pulse will be the one given in (3.15). In Fig.3.4 a graphical representation of the AF of a LFM pulse is given.

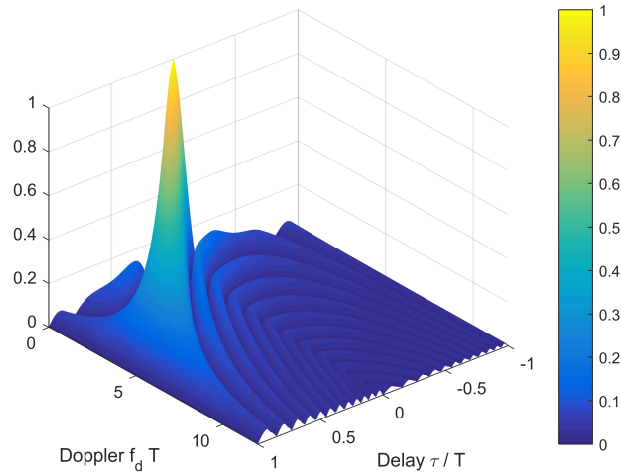


Fig. 3.4 Ambiguity function of a LFM with  $TB = 20$ .

### 3.3.4 Kullback-Leibler Divergence based AF

In probability and information theory, the KLD is considered as a measure of difference between two probability distributions  $p$  and  $q$  over a variable  $x$  (Kullback, 1968; Kullback and Leibler, 1951). Kullback S. and Leibler R. originally introduced the KLD in 1951 as the directed divergence between two distributions (Kullback, 1968). It is also closely related to relative entropy, information divergence, and information for discrimination. In applications,  $p$  typically represents the “true” distribution of data, observations, or a precisely calculated theoretical distribution, while  $q$  typically represents a theory, model, description, or approximation of  $p$ . The KLD is sometimes also called the information gain achieved if  $p$  distribution is used instead of  $q$  distribution.

The concept of KLD has been mainly used in the data mining literature and it was originated from probability theory and information theory. The mathematical representation of the KLD from  $q$  to  $p$  is denoted as:

$$\mathcal{I}(p : q) = \mathcal{E}_p \left\{ \ln \frac{p}{q} \right\} \quad (3.20)$$

where  $\mathcal{E}_p \{ \cdot \}$  is expectation with respect to the probability distribution  $p$ . More specifically it represents a measure of the information gained when revising from the prior probability distribution  $q$  to the posterior probability distribution  $p$ . In other words, it is the amount of information lost when  $q$  is used to approximate  $p$ . The KLD is also used to express a sort of distance between  $p$  and  $q$ . While

the KLD does not satisfy all the properties of a distance such as symmetry and triangular inequality, as seen from its definition in (3.20), it can be shown that (Kullback, 1968):

$$\mathcal{I}(p : q) \geq 0 \quad \text{and} \quad \mathcal{I}(p : q) = 0 \Leftrightarrow p = q \quad (3.21)$$

In a different aspect, the KLD also measures the expected number of extra bits required to code samples from  $p$  using a code optimised for  $q$  rather than the code optimised for  $p$  (Kullback and Leibler, 1951).

There is an increasing interest in the study of the detection and location of targets in inhomogeneous mediums, where many authors have considered the complex multipath structure. Besides the design of signal processing algorithms that can effectively deal with the peculiarities of multipath propagation, it is important to establish limits on the performance attainable in this situation. Two distinct methods of performance analysis are usually considered: local and global.

In a local performance analysis, the Cramér-Rao bound is determined for the location of sources propagating over multipath channels. In the context of target location problems, global performance analysis traditionally involves the computation of the AF. The typical AF has been defined only for very simple models and is not adequate to the global analysis of source location in inhomogeneous mediums. Moreover, it is not applicable in studying passive systems, since the signal correlation function is supposed to be known. In addition, radar resolution based on conventional AF considers only the waveform, regardless of the noise influence. The introduced noise can degrade the achievable resolution to a high degree affecting the target detection and tracking performance (Radmard et al., 2014).

A general definition of AF based on the KLD between probability densities can measure the difficulty in distinguishing any two points in the parameter space (Cochran et al., 2009). Introducing KLD concept in AF design, the distance between probability density functions (PDFs) of radar measurements can be efficiently specified. Thus the radar resolution could be greatly improved including the waveform effect and the SNR measurements (Chen et al., 2012; Radmard et al., 2014; Rendas and Moura, 1998).

In (Rendas and Moura, 1998) it was shown that in a localisation system, such as radar or sonar sensor systems, where the location parameter  $\theta$  is to be estimated from the received signal  $\mathbf{r}$ , the estimation problem can be completely defined by

the family of PDFs or manifold:

$$\mathcal{G}_\theta = \{p(\mathbf{r}|\theta), \theta \in \Theta\} \quad (3.22)$$

where  $p(\mathbf{r}|\theta)$  is the PDF of the observed data indexed by the vector  $\theta$ , and  $\theta$  takes values in the parameter space  $\Theta$ . Additionally by the definition given in (Rendas and Moura, 1998) the ambiguity provides an index on the ability to discriminate between different values of  $\theta$  in the model manifold  $\mathcal{G}_\theta$  and is solely dependent on the geometric properties of  $\mathcal{G}_\theta$ .

To evaluate the problem of estimating the real value  $\theta_0$  of an unknown parameter  $\theta$ , the following binary decision test can be employed:

$$\begin{aligned} \mathcal{H}_0 : \mathbf{r} &\rightarrow p_{\theta_0} = \{p(\mathbf{r}|\theta_0)\} \\ \mathcal{H}_1 : \mathbf{r} &\rightarrow p_\theta = \{p(\mathbf{r}|\theta)\} \end{aligned} \quad (3.23)$$

where hypotheses  $\mathcal{H}_0$  and  $\mathcal{H}_1$  are defined as events corresponding to the presence and absence of the target, respectively. The estimation of  $\theta_0$  can therefore be derived as the problem of distinguishing between the two PDFs  $p(\mathbf{r}|\theta_0)$  and  $p(\mathbf{r}|\theta)$  in the family  $\mathcal{G}_\theta$ . By denoting  $\mathcal{I}(\theta_0 : \theta) = \mathcal{I}(p(\mathbf{r}|\theta_0) : p(\mathbf{r}|\theta))$  a definition of the AF can be given as (Rendas and Moura, 1998):

$$\mathcal{A}_{\text{KLD}}(\theta_0, \theta) \triangleq 1 - \frac{\mathcal{I}(\theta_0 : \theta)}{\mathcal{I}_{\text{ub}}(\theta_0)} \quad (3.24)$$

where  $\mathcal{I}_{\text{ub}}(\theta_0)$  denotes the upper bound of  $\mathcal{I}(\theta_0 : \theta)$ . From (3.21) and (3.24) it can be easily derived that  $1 \geq \mathcal{A}_{\text{KLD}}(\theta_0, \theta) \geq 0$  with  $\mathcal{A}_{\text{KLD}}(\theta_0, \theta) = 1$  when  $\theta_0 = \theta$ .

### 3.3.5 MIMO AF Definitions

The traditional AF applies to monostatic narrowband applications. However, ever since it was firstly introduced various interpretations were adapted to suit different applications of interest. Namely a number of wideband AFs have been investigated in (Dawood and Narayanan, 2003; Lush and Hudson, 1991; Sibul and Titlebaum, 1981) while in (Urkowitz et al., 1962) an AF parametrised by azimuth, elevation, range and Doppler was introduced.

More recently and due to the promising tendency of radar technology to extend to multi-sensor/multi-platform configurations, various formulations of AFs for MIMO systems (see Section 2.3) have been proposed (Chen et al., 2012; Derham et al., 2010; Li and Stoica, 2009; Radmard et al., 2014; San Antonio et al., 2007). In

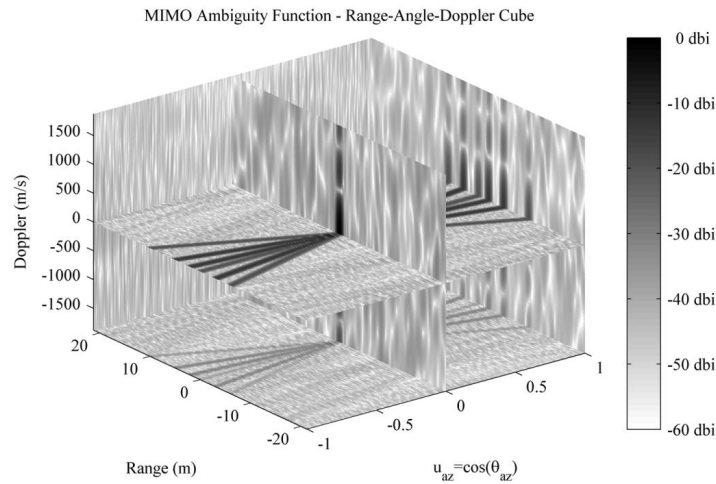


Fig. 3.5 Graphical representation of the MIMO AF proposed in (San Antonio et al., 2007) as a function of range, Doppler shift and azimuth angle

(San Antonio et al., 2007) and (Derham et al., 2010) the optimum detector concept is used and the MIMO AF is obtained by summing the matched filtered result from each receiver. A graphical illustration of the MIMO AF in a range-angle-Doppler cube is illustrated in Fig. 3.5. One obvious but very important observation is that the MIMO AF is represented in a higher dimension than the canonical AF discussed in Section 3.3.3. This is due to the extra spatial parameter, azimuth angle in this case, that has to be added to fully illustrate the performance of the system. In closer inspection it can be seen that Fig. 3.5 provides an intensity map in different cuts of the MIMO AF. Most importantly, examining the zero-Doppler cut it can be seen that the MIMO AF is composed by various ridges crossing the origin of the axes. As extensively discussed in (San Antonio et al., 2007), the number of these ridges is depended on the number of transmitter-receiver pairs and the correlation between the operating waveforms, while the placement of the ridges depends on the geometry of the system.

In (Li et al., 2014b) and (Li et al., 2015), a MIMO AF definition similar to the one proposed in (San Antonio et al., 2007), considering however arbitrary transmit power allocation, was proposed in order to examine MIMO radar with correlated waveforms. The performance improvement that a proper waveform correlation matrix design can introduce is also investigated in (Li et al., 2014b) and (Li et al., 2015) through a comparison with the AF metric defined in (Abramovich and Frazer, 2008) where spatially diverse waveforms are proposed. Lastly, the authors in (Khan et al., 2014) used the matched filter definition to derive an AF and its

properties, for a special case of MIMO radar, called phased-MIMO radar, in which waveform diversity is employed to divide an array into phased subarrays.

Under the similar concept of matched filter summation, a MIMO AF based on a general ultrawideband signal model is derived in (Yan et al., 2013). Here, the authors also propose a factorisation of three MIMO AF parameters, the transmitted signal, system topology, and relative motions, while an analysis is presented focusing on how each of these parameters affect the performance of the system without calculating the entire MIMO AF. Furthermore, in (Hussain, 2016) a MIMO AF based on the squared-sum of all matched filter responses was derived as an analytic tool for designing orthogonal ultrawideband impulse waveforms.

A different approach, based on the KLD AF definition in (Rendas and Moura, 1998) (see 3.3.4), is explored in (Li and Stoica, 2009) where the suggested MIMO AF definition is based on the log-likelihood function and the concept of information theory. Although this approach is very similar to the KLD, the proposed AF is not bounded in values between 0 and 1. Moreover, the authors derive a formulation composed by the transmitted signals' expected and actual matched filter outputs while a comparison of the proposed MIMO AF was also carried out under different transmitted waveforms scenarios. In (Chen et al., 2012) a log-likelihood based MIMO AF was derived based on bistatic MIMO radar systems. A similar log-likelihood based MIMO AF definition, was also applied on a widely distributed MIMO system signal model in (Radmard et al., 2014). Additionally, an optimisation of the MIMO AF (Radmard et al., 2014) through waveform design is presented in (Radmard et al., 2015). Later, in Chapter 6 a proposed definition of a generalised MIMO AF is analytically derived based on the KLD definition.

### 3.4 Fractional Fourier Transform

The fractional Fourier transform (FrFT) was firstly introduced in (Namias, 1980) as a technique to help in solving certain classes of ordinary and partial differential equations with applications in quantum mechanics. Later, it was rediscovered by (Alieva et al., 1994) and (Kutay et al., 1997; Mendlovic and Ozaktas, 1993; Ozaktas et al., 2001) for application in optic and by (Almeida, 1994) in signal processing. The FrFT is defined as a generalization of the canonical Fourier transform (FT) covering fractional orders, with the ordinary FT having an order of 1. Let  $x(u)$  be an arbitrary signal defined in the domain  $u$ , the  $a$ -th ordered

FrFT of  $x(u)$  is given by (Ozaktas et al., 2001):

$$x_a(u') = \mathcal{F}^a\{x(u)\} = \int K_a(u', u)x(u)du \quad (3.25)$$

where  $a$  is the fractional order,  $u'$  is the domain in which  $x_a(u')$  is defined and  $K_a(u', u)$  is the kernel of the transform defined as (Ozaktas et al., 2001):

$$K_a(u', u) = \begin{cases} \frac{e^{j\vartheta/2}}{\sqrt{j \sin \vartheta}} e^{j\pi(u'^2+u^2) \cot \vartheta - 2u'u \csc \vartheta} & \text{if } \vartheta \text{ is not a multiple of } \pi \\ \delta(u' - u) & \text{if } \vartheta \text{ is a multiple of } 2\pi \\ \delta(u' + u) & \text{if } \vartheta + \pi \text{ is a multiple of } 2\pi \end{cases} \quad (3.26)$$

where  $\vartheta = a\frac{\pi}{2}$  is the rotation angle associated with the fractional order  $a$ . As it can be seen from the kernel in (3.26), the FrFT can be parametrised by an angle  $\vartheta$  which is the rotation angle between the domain  $u$  and  $u'$  in the phase plane that the signal is defined. For a better understanding, consider the stationary time signal  $x(t)$ , with its phase plane being defined by the time and frequency axis. By applying the ordinary FT the one-dimensional signal  $x(t)$  is mapped from the time to frequency axis. In the case of FrFT the signal is mapped in an in-between axis along the time-frequency plane. Translating this mapping into rotation of the signal in the time-frequency plane, a time signal  $x(t)$  is rotated by the angle  $\vartheta$  when FrFT is applied with the special case of the canonical FT corresponding to a rotation of  $\vartheta = 90^\circ$ . In Fig. 3.6 a graphical illustration of this rotation is illustrated. Equation (3.26) shows that for angles that are not multiples of  $\pi$ , the computation of the FrFT can be described by the following steps:

1. A product by a chirp;
2. A FT scaled by  $\csc \vartheta$ ;
3. Another product by a chirp;
4. A product by a complex amplitude factor.

In summary, the FrFT is an invertible linear transform, continuous in the angle  $\vartheta$ , which satisfies the basic conditions for it to be meaningful as a rotation in the time-frequency plane. This rotation can be better illustrated in Fig. 3.7 where the STFT of a complex Gaussian pulse is illustrated after FrFT of different orders has been applied on the pulse.

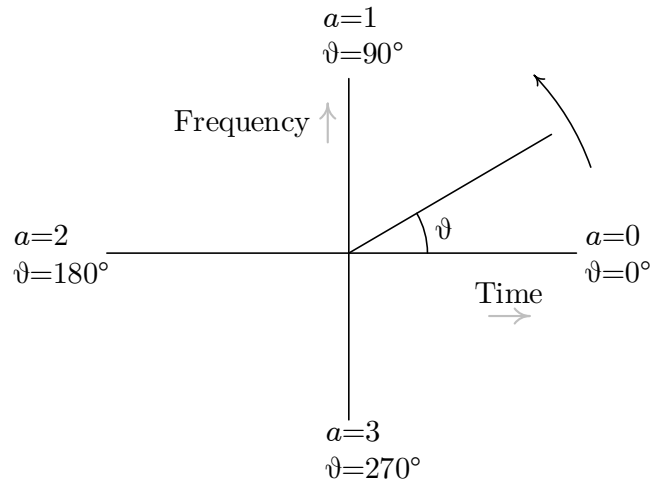


Fig. 3.6 FrFT as a rotation in the time-frequency plane.

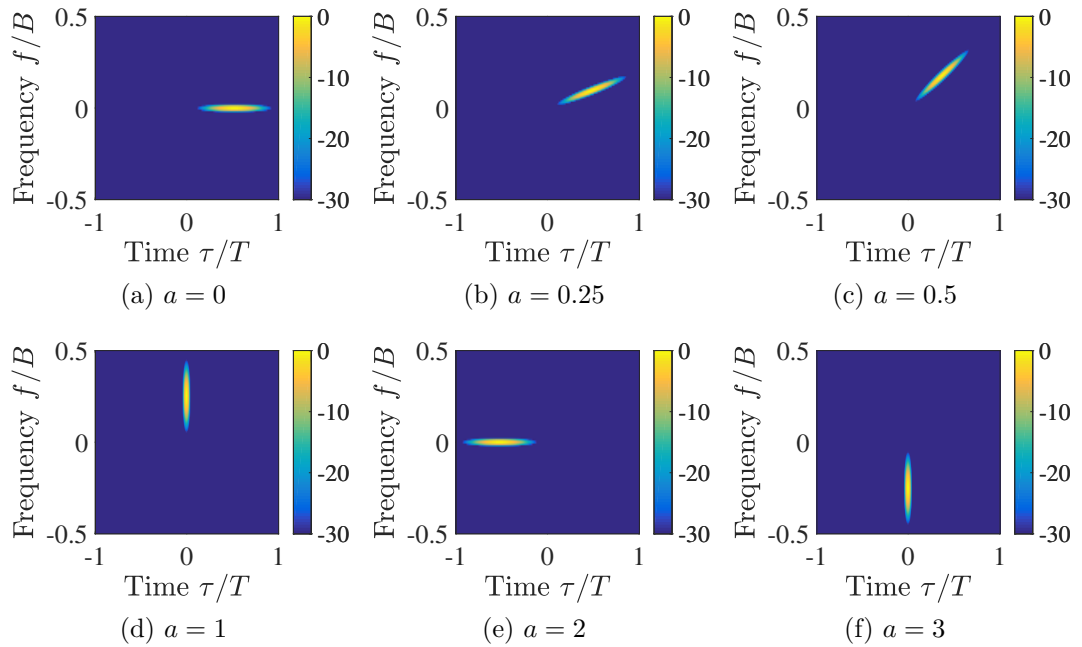


Fig. 3.7 Time-frequency representation using STFT of a Gaussian pulse after applying FrFT of different orders.

### 3.4.1 FrFT Properties

In the literature the various properties of FrFT have been investigated (Ozaktas et al., 2001; Poularikas, 2010). In the following paragraphs the most important properties of FrFT will be discussed. Moreover, some further properties of FrFT are also provided in Appendix A.

**Linearity:** Similar to the original FT, the FrFT is a linear transform i.e.:

$$\mathcal{F}^a \left\{ \sum_k h_k x_k(u) \right\} = \sum_k h_k \mathcal{F}^a x_k(u) \quad (3.27)$$

where  $h_k$  is a constant and  $x_k(u)$  is an arbitrary function.

**Integer Order:** The integer orders of FrFT return well-know functions as listed:

$$\mathcal{F}^4 = \mathcal{F}^0 = I \quad (\text{Identity Function}) \quad (3.28)$$

$$\mathcal{F}^1 = \mathcal{F} \quad (\text{Fourier Transform}) \quad (3.29)$$

$$\mathcal{F}^2 = \mathcal{P} \quad (\text{Parity Operator}) \quad (3.30)$$

$$\mathcal{F}^3 = \mathcal{F}^{-1} = (\mathcal{F})^{-1} \quad (\text{Inverse Fourier Transform}) \quad (3.31)$$

where the parity operation of an arbitrary signal  $x(t)$  is given by  $\mathcal{P}\{x(t)\} = x(-t)$ .

**Index additivity:** Sequential FrFTs are equivalent to a FrFT with an order equal to the summation of all the orders, i.e.:

$$\mathcal{F}^{a_1} \mathcal{F}^{a_2} = \mathcal{F}^{a_1+a_2} \quad (3.32)$$

**Repetition:** From (3.28) and (3.32) it can be easily derived that:

$$\mathcal{F}^{4m+a} = \mathcal{F}^a \quad \forall m \in \mathbb{Z} \quad (3.33)$$

**Inverse:** From (3.28) and (3.32) it also follows that the inverse of a FrFT of an order  $a$  is a FrFT of order  $-a$ , i.e.:

$$(\mathcal{F}^a)^{-1} = \mathcal{F}^{-a} \quad (3.34)$$

**Commutativity and Associativity:** Sequential FrFTs follow both the commutativity and associativity properties, i.e.:

$$(\mathcal{F}^{a_1} \mathcal{F}^{a_2}) \mathcal{F}^{a_3} = \mathcal{F}^{a_1} (\mathcal{F}^{a_3} \mathcal{F}^{a_2}) \quad (3.35)$$

**Parseval's Theorem:** Similar to FT, FrFT satisfies the Parseval's theorem which implies that a signal will contain the same energy before and after FrFT is applied, i.e.:

$$\int_{-\infty}^{\infty} x(t)y^*(t)du = \int_{-\infty}^{\infty} \mathcal{F}^a\{x(t)\} \mathcal{F}^a\{y^*(t)\}du \quad (3.36)$$

where  $x(t)$  and  $y(t)$  are arbitrary signals and  $u$  is the variable of fractional domain in which  $\mathcal{F}^a\{x(t)\}$  and  $\mathcal{F}^a\{y^*(t)\}$  are defined.

### 3.4.2 FrFT Implementations

The discussion on FrFT has only covered application on continuous signals as it can be also seen in the definition provided in (3.25). In the following paragraphs, the two mainly used approaches for implementation of FrFT in discrete signals will be discussed.

#### Discrete FrFT

Assume an arbitrary discrete signal described by the vector  $\mathbf{x}$ :

$$\mathbf{x} = [x[1], x[2], \dots, x[N]]^T \quad (3.37)$$

where  $\{\cdot\}^T$  is the transpose matrix operation. The discrete fractional Fourier transform (DFrFT) of  $\mathbf{x}$  is defined as the vector  $\mathbf{x}_a = \mathcal{F}_a \mathbf{x}$ , i.e., the vector populated as:

$$x_a[n] = \sum_{k=1}^N \mathcal{F}_a[n, k] x[k], \quad n = 0, \dots, N \quad (3.38)$$

where  $\mathcal{F}_a$  is the  $N \times N$  DFrFT matrix. Moreover the DFrFT matrix can be decomposed as:

$$\mathcal{F}_a = \mathbf{E} \mathbf{\Lambda}^a \mathbf{E}^T \quad (3.39)$$

where  $\mathbf{E}$  is the eigenvectors' matrix and  $\mathbf{\Lambda}$  is the diagonal eigenvalues' matrix of discrete FT (DFT), i.e.  $\mathcal{F} = \mathbf{E} \mathbf{\Lambda} \mathbf{E}^T$ . In general, the DFrFT can be employed as an approximation of the continuous FrFT if the value of  $N$  is large (Bultheel and Sulbaran, 2004). However, more direct and less complex methods have been proposed for the approximation of continuous FrFT as it will be discussed below.

#### Fast Approximation of FrFT

To define the fast approximation of FrFT we use the definition given in (Bultheel and Sulbaran, 2004). The algorithms discussed in (Bultheel and Sulbaran, 2004) are algorithms that approximate the continuous FrFT in the sense that they map samples of the signal to samples of the continuous FrFT. This comes to a difference with the fast FT (FFT), introduced in (Brigham and Brigham, 1974), which is a much lower in complexity technique of implementing the DFT. More particularly,

when the computation of the DFT of a vector  $\mathbf{x}$  with length  $N$  is applied using matrix multiplication, i.e.  $\mathcal{F}\{\mathbf{x}\} = \mathcal{F}\mathbf{x}$ , the technique will have a complexity of  $\mathcal{O}(N^2)$ . On the other hand, FFT offers a much lower complexity of  $\mathcal{O}(N \log(N))$  (Van Loan, 1992). While FFT and inverse FFT (IFFT) can be used to perform fast calculation of DFrFT of order  $a = 1$  and  $a = 3$  respectively, there is not a known genuine fast FrFT (FFrFT) that satisfies all the conditions in (3.27)-(3.36) (Bultheel and Sulbaran, 2004), (Singh and Saxena, 2013).

### 3.4.3 Applications of FrFT in Signal processing

Similar to the traditional FT, FrFT has many applications in digital signal processing (DSP) covering even larger field due to its higher degree of freedom which can allow further optimisation and thus achieving better performance. Application of FrFT in time-varying filtering on non-stationary processes was investigated in (Kutay et al., 1997) while a novel fractional adaptive filtering scheme was presented in (Durak and Aldirmaz, 2010) showcasing the advantages of non-adaptive filtering and adaptive filter in fractional domain compared to the time and frequency domain counterparts. Techniques implementing the FrFT for digital watermarking applications were studied in (Djurovic et al., 2001), (Yu et al., 2006) and (Cui, 2009) where 2-D FrFT is used to embed a large number of watermarks in images.

Communications is another area of application for FrFT with the authors in (Martone, 2001) proposing a multicarrier multiplexing scheme where FrFT is used instead of DFT significantly improving the performance in fast varying channels. Recent publications showed, among others, applications of FrFT also in fibre optic communications (Chandra and Sahu, 2015), underwater communications (Ashri et al., 2016), and security-coded multiplexing (Wang et al., 2016a). Application of FrFT for image compression was introduced in (Yetik et al., 2001) while modified and multiparameter interpretations of FrFT were used for cryptography applications in (Cusmario, 2004), (Pei and Hsue, 2006), (Youssef, 2008), (Ran et al., 2009) and (Bhatnagar and Wu, 2014).

The FrFT has also been extensively used in radar applications. Namely, FrFT based techniques for SAR images have been proposed in (Amein and Soraghan, 2005; Chen et al., 2015b; Pelich et al., 2015; Sun et al., 2002). Moreover, the authors in (Clemente and Soraghan, 2010a,b,c) showed how FrFT can be useful in performing high resolution SAR processing. In (Liu et al., 2014b) the authors proposed an optimisation of OFDM radar signals based on FrFT showing that the proposed design offers better wideband AF shape as well as higher range

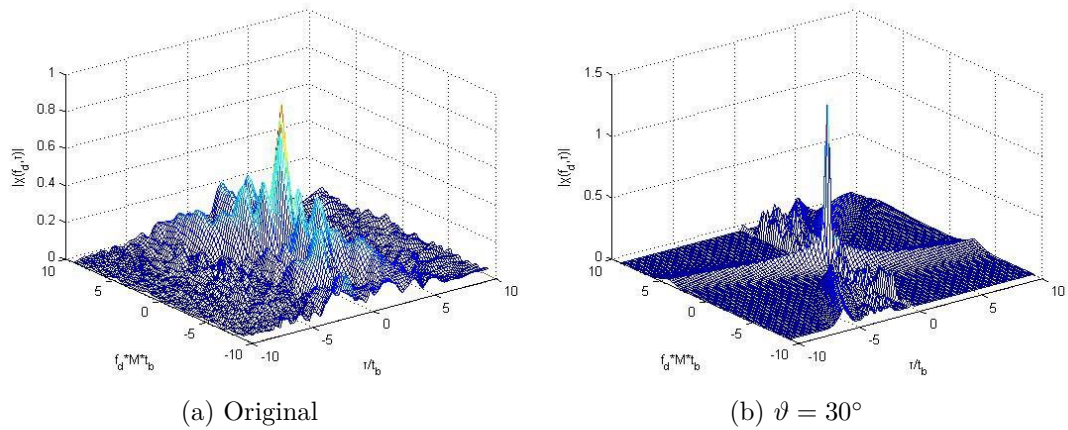


Fig. 3.8 Wideband AF of a FFT-based signal (a) before and (b) after applying FrFT of  $\vartheta = 30^\circ$  as presented in (Liu, 2009).

and velocity resolution compared to traditional OFDM, see Fig. 3.8. Moreover, in (Clemente et al., 2014b) a novel waveform design scheme based on FrFT was introduced showing that the generated waveforms are suitable for radar applications while in (Clemente et al., 2014a) the low cross-correlation properties of the designed waveforms were investigated. Recently the authors in (Zhang et al., 2016) proposed a FrFT based optimal waveform design in signal-dependent interference and additive channel noise. Simulation results showed that waveform design based on fractional domain can be more flexible and effective than one based on Fourier domain. Further discussion on waveform designs based on FrFT will be held in Chapter 5.

### 3.5 Phase Stretch Transform

The phase stretch transform (PST) is a physics-inspired transform that emulates propagation of an electromagnetic wave through a diffractive medium with a dielectric function that has a warped dispersive (frequency dependent) property (Asghari and Jalali, 2015). Originally introduced in (Asghari and Jalali, 2014) as a method applied for edge detection in natural images, PST has been recently used in biomedical applications for segmentation of optic disc (Firdausy and Oktoeberza, 2016) and a diagnostic tool for pneumothorax (Suthar et al., 2016). It is worth mentioning that in previous work a similar approach has been employed for signal and SAR image compression in (Asghari et al., 2014) and (Asghari and Jalali, 2013) respectively.

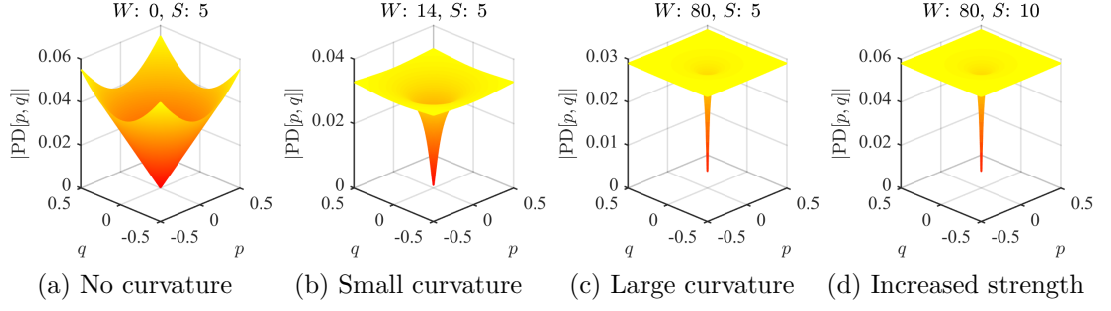


Fig. 3.9 Phase derivative profiles comparison for four different kernels.

The PST of a 2-D array  $\mathbf{B}$  is defined as:

$$\mathbf{A} = \text{PST}\{\mathbf{B}\} = \angle\langle \text{IFFT2}\{\mathbf{K}_{\text{PST}} \cdot \text{FFT2}\{\mathbf{B}\}\} \rangle \quad (3.40)$$

where  $\mathbf{A}$  is the output phase image,  $\angle\langle \cdot \rangle$  is the angle operator, FFT2 and IFFT2 are the 2-D Fast Fourier Transform and its inverse operation respectively, and  $\mathbf{K}_{\text{PST}}$  is the phase kernel described by a frequency dependent phase  $\phi_{\text{PST}}$  as follows:

$$\mathbf{K}_{\text{PST}}[p, q] = e^{j\phi_{\text{PST}}[p, q]} \quad (3.41)$$

where  $p$  and  $q$  are the two dimensional frequency variables. In the case of circular symmetry, the phase  $\phi_{\text{PST}}[p, q]$  can also be expressed as:

$$\phi_{\text{PST}}[p, q] = \phi_{\text{PST,polar}}[r, \vartheta] = \phi_{\text{PST,polar}}[r] \quad (3.42)$$

where  $r = \sqrt{p^2 + q^2}$  and  $\vartheta = \tan^{-1}(q/p)$ . Although there is no restriction on the applied phase kernel  $\mathbf{K}_{\text{PST}}[p, q]$ , it is desirable to use kernels of which the phase derivative  $\text{PD}[p, q]$  is a linear or sublinear function of the frequency variables. As shown in (Asghari and Jalali, 2015) the inverse tangent can be used as a simple example of such phase derivative profiles leading to the PST kernel defined as:

$$\phi_{\text{PST,polar}}[r] = S_{\text{Ph}} \frac{W_{\text{Ph}} r \tan^{-1}(W_{\text{Ph}} r) - \frac{1}{2} \ln(1 + (W_{\text{Ph}} r)^2)}{W_{\text{Ph}} r_{\text{max}} \tan^{-1}(W_{\text{Ph}} r_{\text{max}}) - \frac{1}{2} \ln(1 + (W_{\text{Ph}} r_{\text{max}})^2)} \quad (3.43)$$

where  $r_{\text{max}}$  is the maximum value of  $r$ . The variables  $S_{\text{Ph}}$  and  $W_{\text{Ph}}$  in (3.43) are real numbers related to the strength and wrap of the phase profile applied to the image. Those values determine the phase derivative of the kernel and therefore the amount of phase applied to each frequency.

In Fig. 3.9 four representative derivative profiles are illustrated along with

their respective  $S_{Ph}$  and  $W_{Ph}$  values. As it can be seen in Fig. 3.9a choosing near zero value for  $W_{Ph}$  returns a linear phase derivative profile. Increasing the value of  $W_{Ph}$  will produce a small curvature on the kernel, while for very high values of  $W_{Ph}$  the curvature increases even more as it can be seen in Fig. 3.9b and Fig. 3.9c respectively. Finally the value of  $S_{Ph}$  scales the total phase derivative profile as it can be seen comparing Fig. 3.9c and Fig. 3.9d.

### 3.5.1 PST Based Edge Detection

In (Asghari and Jalali, 2014) and (Asghari and Jalali, 2015) the authors discussed the good properties of PST as a tool to extract edges from natural images. The block diagram of the algorithm proposed in (Asghari and Jalali, 2015) is illustrated in Fig. 3.10. As it can be seen, the process is composed by four main steps: First the original image is passed through a localisation filter with a certain bandwidth  $B_{Lo}$ . In (Asghari and Jalali, 2015) a Gaussian filter was proposed. On the resulting image a PST of certain  $S_{Ph}$  and  $W_{Ph}$  is applied to extract the phase image. The amount of phase that will be applied on each pixel of the image is frequency dependent meaning that for higher frequencies a higher amount of phase will be applied. Since edges are mostly contained in higher frequencies, PST will emphasise them by applying more phase to higher frequencies (Asghari and Jalali, 2015). On the resulting phase image a threshold  $T_{Ed}$  is applied that will determine the desired sensitivity in edges. In the last step, the thresholded image is post-processed by morphological operations to generate the detected edges. As it was discussed in (Asghari and Jalali, 2015), the proposed method offers a trade-off between spatial resolution and edge detection. In general, a large phase strength  $S_{Ph}$  results in edges with less noise but it lowers the spatial resolution. On the other hand larger wrap  $W_{Ph}$  offers sharper edges increasing however the edge noise.

A demonstration on how the different values of  $W_{Ph}$  and  $S_{Ph}$  affect the detected edges is presented in Fig. 3.11. The test image is the well known “Barbara” from

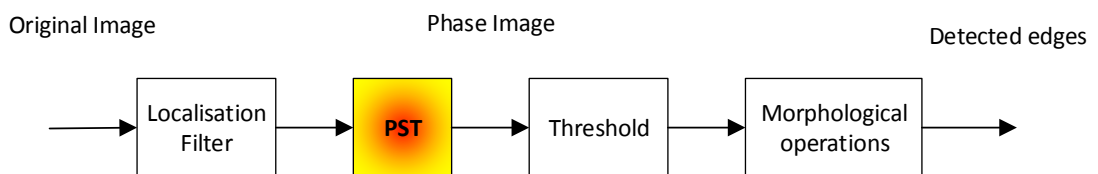


Fig. 3.10 Edge detection method based on PST as it was proposed in (Asghari and Jalali, 2015).

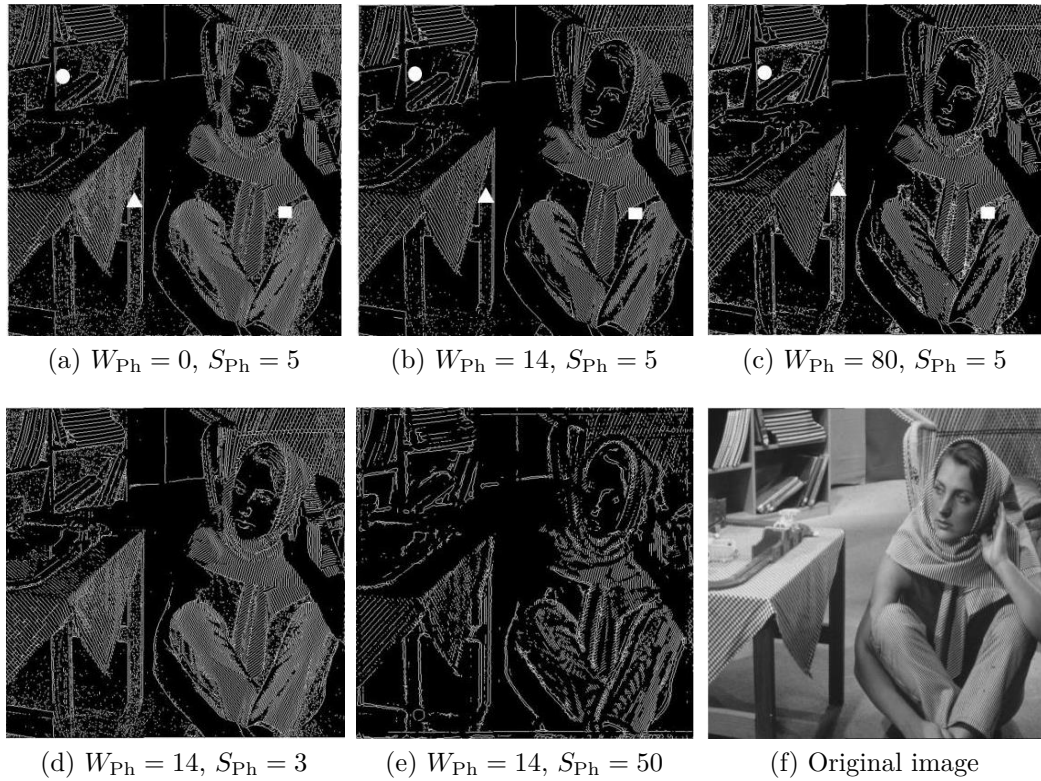


Fig. 3.11 Effect on detected edges of warp  $W_{Ph}$  and the strength  $S_{Ph}$  of phase applied to a sample image (Asghari and Jalali, 2015).

Marco Schmidt's standard test images database. In all cases the bandwidth of the localisation kernel is  $B_{Lo} = 2$ , the threshold is set as  $T_{Ed} = 0.047$  and morphological operations are used (Asghari and Jalali, 2015). First a comparison between edge images resulted by the same  $S_{Ph} = 5$  and different  $W_{Ph}$  is held in figures Fig. 3.11a, Fig. 3.11b and Fig. 3.11c. The compared regions are indicated with triangular ( $\Delta$ ), circular ( $\circ$ ) and rectangular ( $\square$ ) marks. As it can be seen medium wrap results to better edge detection (see Fig. 3.11b) than very small wrap (see Fig. 3.11a) or very large wrap (see Fig. 3.11c). Additionally, a comparison between edge images resulted by the same  $W_{Ph} = 14$  and different  $S_{Ph}$  is shown in figures Fig. 3.11b, Fig. 3.11d and Fig. 3.11e. As it can be observed increasing larger phase strength results in less noisy edges but also degrades the resolution in edge detection. In Chapter 4 a modified edge detection scheme will be presented to accommodate edge detection in SAR images.

## 3.6 Summary

In this chapter the concept of T-F analysis and its most commonly used tools were discussed. In particular, the STFT and WVD were presented as exemplars of linear and quadratic T-F transforms respectively, referencing the trade-offs that each approach poses. Moreover, an extensive discussion on the AF was held, highlighting its importance on radar applications. Specifically, the canonical definition of the AF was presented in conjunction with its most important properties. In addition, the AF definition based on the KLD was discussed considering its more generalised approach compared to the canonical definition. The concept of the MIMO AF as a tool to evaluate the performance of MIMO radar systems was also introduced, reviewing the most important proposed MIMO AF definitions. In the later part of the chapter, the FrFT and its applications in general and radar signal processing were extensively discussed. Lastly the PST was presented in connection with its application in the field of image edge detection.

# Chapter 4

## Edge Detection in SAR Images using Phase Stretch Transform

### 4.1 Introduction

In this chapter a novel edge detection scheme for SAR images is described. The proposed scheme is based on the phase stretch transform (PST), discussed in Section 3.5. Extending previous work, the proposed scheme accommodates denoising processes and phase artifacts removal to offer accurate edge detection in SAR images. More precisely, 2D median filters are employed to mitigate the speckle noise effect related with SAR images. In addition, a masking method is proposed in order to remove phase artifacts occurring in low intensity parts of the image after the application of PST. The ability of the proposed technique to effectively extract edges is validated using real SAR images from two different datasets. Moreover, the flexibility of the presented scheme to control the degree of the preserved details, depending on the scaling of the original image is presented.

### 4.2 Edge Detection Based on PST

The different steps of the proposed edge detection method are shown in Fig. 4.1. In the first step, the SAR image is smoothed by applying a localisation kernel. A Gaussian localisation filter with variable bandwidth is used in this work. In the next step the smoothed image is denoised to reduce the undesired speckle noise. Here the noise removal process is implemented by applying a 2-D median filter. It is worth noting that while different, more advanced, speckle reduction methods

can be found in the literature (see Section 2.5.2), the median filter is chosen due to its simple implementation.

Afterwards the denoised image is passed through the PST, which returns a phase image. The amount of phase applied to each pixel of the image is frequency dependent meaning that a higher amount of phase is applied to higher frequency features of the image. Since image edges contain higher frequency features, the PST emphasises the edge information in the image by applying more phase to higher frequency features (Asghari and Jalali, 2015).

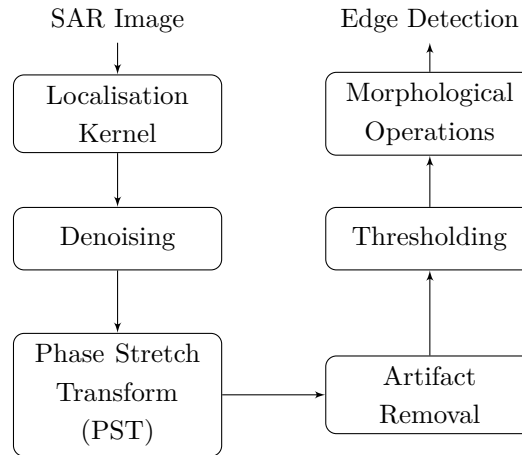


Fig. 4.1 Block diagram of proposed edge detection method.

The resulting phase image is further processed to remove artifacts occurring in the low intensity areas of the denoised image. An example of this phenomenon is illustrated in Fig. 4.2. As it can be seen after applying PST, artifacts appear where extended dark areas are located in the original image (see the top left square in Fig. 4.2b). To remove those unwanted patterns a minimum threshold is firstly applied to the original image to determine the low intensity or “dark” areas that may contain artifacts. In the resulting binary image all the pixels below the threshold will have a value of one while brighter pixels will have a zero value. To ensure that real edges, which may also be located in those “dark” areas, are preserved (see the perimeter of bottom left square in Fig. 4.2b) this binary image is then convolved with the kernel presented in Fig. 4.3. Using this kernel allows us to determine if a pixel is “dark” and how many “dark” neighbours it possesses.

For a better understanding of the artifact removal process, let us consider an example of a “dark” pixel with 8 “dark” neighbours which after the thresholding will result to a  $3 \times 3$  block of ones. After convolving the thresholded binary image with the given kernel, the examined centre pixel will have a value of  $9 + 8 = 17$ . It

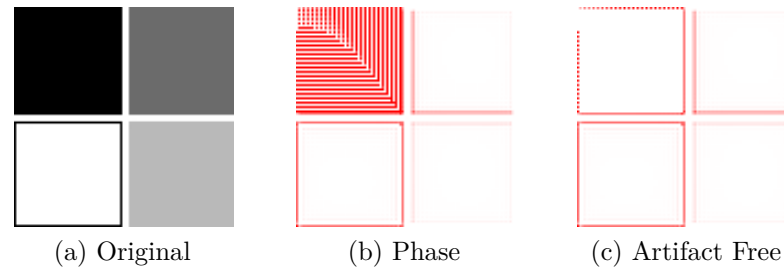


Fig. 4.2 Example of (a) a grayscale image with extended “dark” areas (black color) and the PST output phase image with the intensity of red color representing the intensity of the phase (b) including artifacts and (c) after removing the artifacts.

can be easily derived that for a pixel to be considered “dark” it must have a value equal or greater than 9 (see centre element in kernel presented in Fig 4.3). If a value is greater than 9 then by subtracting 9 from the total value, the number of “dark” neighbours can also be found. Therefore, in the resulted from the convolution image a new threshold can now be applied that will determine if a pixel is “dark” and if it has enough “dark” neighbours to be reasonably to assume that this pixel contains no edge information. This threshold must be at least 9 to ensure that the examined pixel is “dark” while higher values will determine the least number of “dark” neighbours that the pixel should have to not be a part of an edge. Using the resulting binary image as a mask forces the selected pixels in the phase image to have minimum phase ( $-\pi$ ) and as a result to clear the artifacts (compare the inside of the top left square in Fig. 4.2b and Fig. 4.2c).

The resulting image is finally thresholded and morphologically filtered in order to form the edges. In this work four morphological operations are used. First an edge thinning is performed on the binary image (MathWorks, 2017b). Then a perimeter calculation using a 4-connected neighbourhood is applied (MathWorks, 2017c). Isolated pixels removal is also performed, where individual pixels surrounded by zeros are removed (MathWorks, 2017b). Finally object outlining is applied by setting a pixel to zero if all its 4-connected neighbours are one (MathWorks, 2017b).

1	1	1
1	9	1
1	1	1

Fig. 4.3 Kernel used to determine the number of “dark” neighbours surrounding a “dark” pixel.

The parameters of the proposed design are summarised in Table 4.1. Here the parameter  $\Delta f$  defines the width of the applied Gaussian filter. Consequently  $\Delta f$  also determines the frequencies that PST will later apply in the third step of edge detection algorithm (see Fig. 4.1). The parameter  $N$  defines the  $N$ -by- $N$  neighbourhood window of the 2-D median filter applied to denoise the image from speckle noise. Higher values of  $N$  will result to better noise reduction but will blur the image and loose resolution in exchange. The strength ( $S_{\text{Ph}}$ ) and wrap ( $W_{\text{Ph}}$ ) of the phase kernel determine its phase derivative profile. In principle, values of  $W_{\text{Ph}}$  resulting in medium warp have better noise performance, while large values of  $S_{\text{Ph}}$  provide less edge noise, but also reduce the resolution (Asghari and Jalali, 2015). The dark threshold  $T_{\text{d}}$  determines the intensity limit above of which a pixel in the denoised image is considered “dark”. For convenience  $T_{\text{d}}$  will be expressed as a percentage of the maximum intensity in the image. The artifact threshold  $T_{\text{a}}$  controls the minimum number of “dark” neighbours that a “dark” pixel must have not to be considered as an edge and therefore may contain only artifacts. Finally the edge threshold  $T_{\text{e}}$  sets the minimum phase that a pixel must have to be considered as an edge.

Table 4.1 Design Parameters of Edge Detection Algorithm

Parameter	Variable	Description
Localisation Kernel	$\Delta f$	Bandwidth of the Gaussian localisation filter.
Denoising Factor	$N$	Size of the 2-D median filter.
Phase Kernel	$S_{\text{Ph}}$	Strength of the phase kernel.
	$W_{\text{Ph}}$	Warp of the phase kernel.
Dark Threshold	$T_{\text{d}}$	Minimum threshold for pixels to be considered “dark”.
Artifact Threshold	$T_{\text{a}}$	Maximum threshold for pixels containing artifacts.
Edge Threshold	$T_{\text{e}}$	Maximum threshold for pixels containing edges.

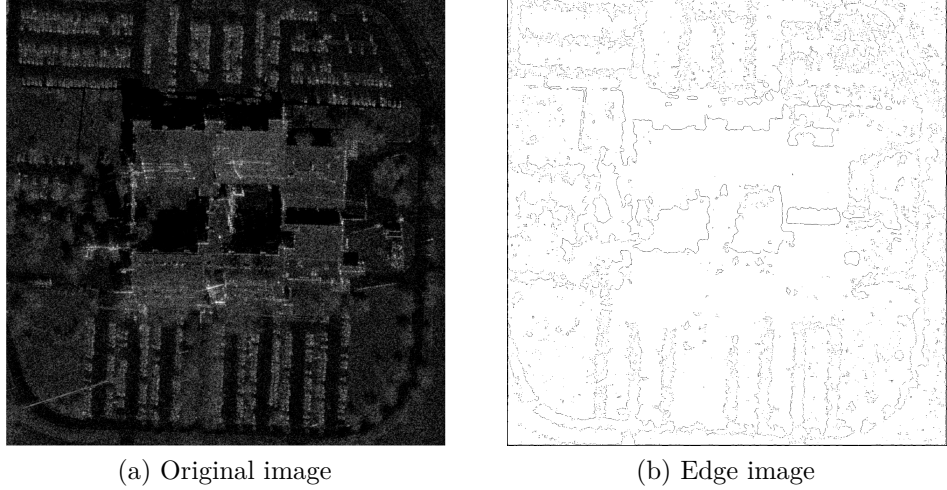


Fig. 4.4 Edge detection performance of the proposed technique on a sample from the Coherent Change Detection Challenge data set, (a) Original sample, (b) Detected edges using the proposed method using the following parameters:  $\Delta f = 1.8$ ,  $N = 12$ ,  $S_{Ph} = 5$ ,  $W_{Ph} = 14$ ,  $T_d = 3.3\%$ ,  $T_a = 16$ ,  $T_e = 0.2$ .

### 4.3 Experimental Results

In this section the performance of the method proposed in Section 4.2 is experimentally evaluated. For the experimental results two datasets were used. First the proposed technique is applied on the X-band data from the Coherent Change Detection Challenge (CCDC) dataset provided by the Air Force Research Laboratory (AFRL)(Scarborough et al., 2010). The data are in the form of focused complex images with range and cross-range resolution of 0.3m, while the original size of the image is  $4501 \times 4501$  pixels. The proposed method was also applied in C-band data from the Vancouver, BC dataset included in RADARSAT-2 sample dataset (Corporation, 2007). In this case the original size of the image is  $5954 \times 7930$  pixels and it has a cross-range resolution of 3 m. Only one acquisition from each dataset is utilised for the tests performed using the intensity of the SAR image to form a gray-scale image. Additionally due to the large size of the original images, smaller image samples are preferably used in the edge detection algorithm for practical reasons. It is worth noting that in all described examples the various algorithm parameters were assigned manually. The values of the parameters were chosen through observations according to the properties discussed in Section 3.5.1 and Section 4.2.

The edge detection capability of the proposed method in the CCDC data set is illustrated in Fig. 4.4. As it can be seen in Fig. 4.4a, the original image does

not suffer from high level of white noise and therefore a large value of  $\Delta f = 1.8$  is used for small smoothing in the image. Moreover a median filter of  $N = 12$  is applied to reduce the high speckle noise. The values of strength and wrap are tuned at  $S_{Ph} = 5$  and  $W_{Ph} = 14$  to provide good resolution along with edge noise reduction. The dark threshold is set at  $T_d = 3.3\%$  of the maximum intensity, while the artifact threshold is  $T_a = 16$  implying that only “dark” pixels with all their neighbours being “dark” will be masked for artifact removal. Finally the edge threshold is set at  $T_e = 0.2$ . The resulting edge image is illustrated in Fig. 4.4b. As it can be observed, the proposed method has the ability to extract the edges in the image while mitigating the noise at the same time.

The performance of the proposed method in the Vancouver, BC dataset is illustrated in Fig. 4.5. The original image used for edge extraction is shown in Fig. 4.5a. In contrast with the CCDC dataset, the image used from Vancouver, BC dataset appears to suffer from higher levels of additive white noise. For this reason a smaller bandwidth  $\Delta f = 0.12$  is used to smooth the image. A median filter of  $N = 14$  is also applied to reduce the speckle noise. In the PST, the strength and wrap parameters of phase kernel are chosen as  $S_{Ph} = 0.7$  and  $W_{Ph} = 10$  respectively to provide better resolution in exchange of higher edge noise. The dark threshold is set at  $T_d = 3.3\%$  of the maximum intensity, while the artifact threshold is  $T_a = 16$ . Finally the edge threshold is set at  $T_e = 0.2$ . The resulting edge image is illustrated at Fig. 4.5b. It is worthy to note that although the presence of the sea makes this image more challenging from the one presented in

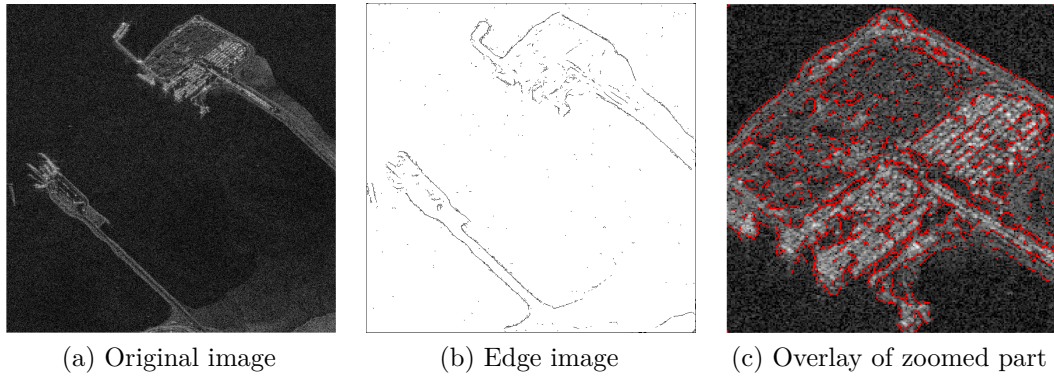


Fig. 4.5 Edge detection performance on a sample from the Vancouver, BC dataset (a) Original sample, (b) Detected edges using the proposed method with parameters:  $\Delta f = 0.12$ ,  $N = 14$ ,  $S_{Ph} = 0.7$ ,  $W_{Ph} = 10$ ,  $T_d = 3.3\%$ ,  $T_a = 16$ ,  $T_e = 0.0042$ , (c) Overlay edges in a part of the sample image using the following parameters:  $\Delta f = 0.2$ ,  $N = 5$ ,  $S_{Ph} = 0.7$ ,  $W_{Ph} = 8$ ,  $T_d = 33\%$ ,  $T_a = 16$ ,  $T_e = 0.008$ .

Fig 4.4, the proposed method can still extract most of the edges while keeping the noise at very low level. Furthermore in Fig. 4.5c an overlay of a smaller part of the sample image with the detected edges is illustrated. In the case of inspecting a smaller area, different settings are used to provide more details for the zoomed part of image. Here the bandwidth is set at  $\Delta f = 0.2$  and the size of the median filter is  $N = 5$ , thus allowing more details to be preserved in the image. In providing finer resolution, the values of  $S_{\text{Ph}} = 0.7$  and  $W_{\text{Ph}} = 10$  are used for the strength and wrap parameters of the PST phase kernel respectively. Moreover, the dark threshold is set at  $T_d = 33\%$ . The reason that  $T_d$  is set much higher than previously is to remove the parts of the image where the sea area is located at and therefore eliminate its noise along with the phase artifacts.

It should be mentioned that here the  $T_d$  is used mainly as a morphological operator since the artifacts appear in pixels with much lower intensities. Finally the artifact threshold and the edge threshold are set at  $T_a = 16$  and  $T_e = 0.008$  respectively. Inspecting Fig. 4.5c, it is observed that more details can be preserved, while removing the noise from the sea areas. Finally, it is worth noting that while in the tuning process the presented parameters appear to achieve the best edge detection performance on the respective images, the algorithm is robust for small deviations of these values.

## 4.4 Summary

In this chapter a novel algorithm for edge detection in SAR images has been presented. This method uses an enhanced scheme based on the PST edge detection method presented in Section 3.5.1. The algorithm reduces the noise effects and removes phase image artefacts, while PST emphasises the edge information applying more phase to higher frequency features. As a consequence the edge detection of the original image can be effectively improved. Experimental results demonstrate that thresholding and further morphological operation leads to the edge extraction despite the noise presence into the provided image. The edge detection capability if the scheme has been tested and verified experimentally using two real datasets.

# Chapter 5

## Novel Fractional Fourier Transform Based Radar Waveforms

### 5.1 Introduction

In this chapter a novel approach of generating radar waveform libraries is presented. The method is based on the application of fractional Fourier transform (FrFT) on code sequences with good ambiguity function (AF) properties such as Barker 13 and P4 25, that were discussed in Section 2.2.3. An efficient low complexity technique to reconstruct the FrFT based waveforms under constant envelope (CE) constraints is also presented. The technique uses a modified Gerchberg-Saxton algorithm (MGSA). Furthermore reuse evaluation of the generated waveforms is conducted showing that multiple near-orthogonal waveforms can be generated when FrFTs of different orders is applied in the same code sequence. The applicability of the proposed design is experimentally validated while its performance is evaluated for a simulated MIMO radar scenario. Finally a novel technique of embedding arbitrary information into radar waveforms based on the FrFT is developed.

### 5.2 FrFT based Waveforms

In this section an approach in designing novel libraries of waveforms is presented. First it will be shown how the previously introduced FrFT (see Section 3.4) can be applied to commonly used radar waveforms, such as phase modulated waveforms with different codes (e.g. Barker or P4 codes) to generate new waveforms. These

waveforms, called *fractional* waveforms, have enhanced properties compared to their original regarding radar performance. Although the principles of the proposed design was firstly introduced in (Clemente et al., 2014b) and is a part of previous work, a detailed description of the waveform generation process is presented to provide better reasoning for the choice and further development of this scheme. In addition, a method is designed to reconstruct the fractional waveform taking into account constant modulus or constant envelope (CE) constraints. Lastly the ability of the proposed design scheme to generate a large number of waveforms with low cross-correlation properties and suitable for MIMO radar applications is explored and validated in terms of hardware implementation and simulation analysis.

### 5.2.1 Fractional Waveforms Design and Libraries

The proposed fractional waveform design is analysed in the next paragraphs. First let us consider a baseband waveform  $s[n]$  where  $n = 1, \dots, N$ . Even though  $s[n]$  can be any arbitrary waveform, the waveforms examined here are those generated by code sequences with good AF properties. A description of such codes is provided in Section 2.2.3. Defining the vector containing the  $K$  symbols of the original code sequence (e.g. Barker code) as  $\mathbf{c} = [c_1, \dots, c_K]^T$ , the waveform  $s[n]$  is generated as:

$$s[n] = \sum_{k=1}^K \text{rect}\left(\frac{n/o - k}{2}\right) c_k \quad (5.1)$$

where  $o$  represents the samples per bit, and  $\text{rect}\{\cdot\}$  is the rectangular function give as:

$$\text{rect}(x) = \begin{cases} 0 & \text{for } |x| \geq 1/2 \\ 1 & \text{for } |x| < 1/2 \end{cases} \quad (5.2)$$

From (5.1) it can be easily derived that each symbol of  $\mathbf{c}$  will be repeated  $o$  times leading to the total length of  $s[n]$  being  $N = o \times K$ . Using the properties of FrFT described in Section 3.4.1, a fractional waveform can be defined as:

$$s_a[u] = \tilde{\mathcal{F}}^a\{s[n]\} = \sqrt{\frac{1 - j \cot \vartheta}{2\pi}} \sum_{n=1}^N \sum_{k=1}^K \text{rect}\left(\frac{n/o - k}{2}\right) c_k e^{j \frac{n^2 + u^2}{2} \cot \vartheta - j u n \csc \vartheta} \quad (5.3)$$

where  $\tilde{\mathcal{F}}^a$  denotes the fast discrete approximation of FrFT (see Section 3.4.2) with a fractional order  $a$  and  $\vartheta = a \frac{\pi}{2}$ . The real and imaginary parts of a Barker 13 code and its corresponding fractional waveform are illustrated in Fig. 5.1. Here, the

fractional waveform of the Barker 13 code is generated using  $o = 50$  and  $a = 0.5$ . As it can be observed, the resulting fractional waveform exhibits a very different structure compared to the original one. On closer inspection of Fig. 5.1, it can be seen that the fractional waveforms are composed of different linear frequency modulated or chirp components. Moreover, it should be noted that a code with only real part could lead to a fractional waveform with non-zero imaginary part in most cases.

Having shown in (5.3) how a fractional waveform can be generated from a canonical waveform  $s[n]$  by applying a FrFT of order  $a$ , we can now define a library  $\mathbf{S}$  composed by  $L_s$  unique waveforms generated by applying different fractional orders:

$$\mathbf{S} = [s_{a_1}[u], s_{a_2}[u], \dots, s_{a_{L_s}}[u]] \quad (5.4)$$

From (5.3) it can be derived that the  $l$ th element of  $\mathbf{S}$  is the sum of  $N$  chirped functions weighted by the original code sequence  $\mathbf{c}$  with a modulation rate that depends on the fractional order  $a$ . The number of chirped components depends on  $N$  which is the product of the code sequence length  $K$  and the sample per bit rate  $o$ . This implies that for a given code  $\mathbf{c}$  different waveforms libraries can be obtained by changing  $o$ . As it will be discussed in the Section 5.2.3 the size  $L_s$  of a library can vary depending on the desired AF properties and correlation that the waveforms should have.

In (Clemente et al., 2014b) an extensive analysis of the suitability of the fractional waveforms for radar applications was presented. More precisely, the effectiveness of the design was quantified in terms of performance ratios between

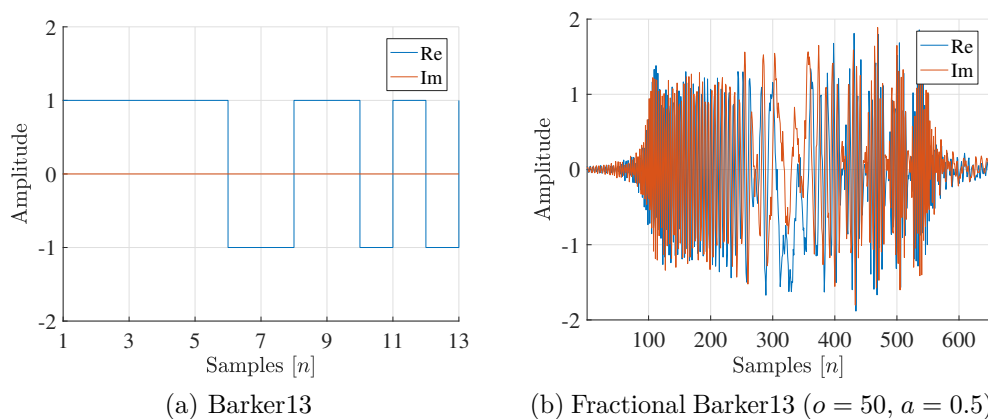


Fig. 5.1 Real (Re) and imaginary (Im) parts of (a) a Barker 13 code and (b) a fractional Barker 13 waveform generated using samples per bit rate  $o = 50$ , and fractional order  $a = 0.5$ .

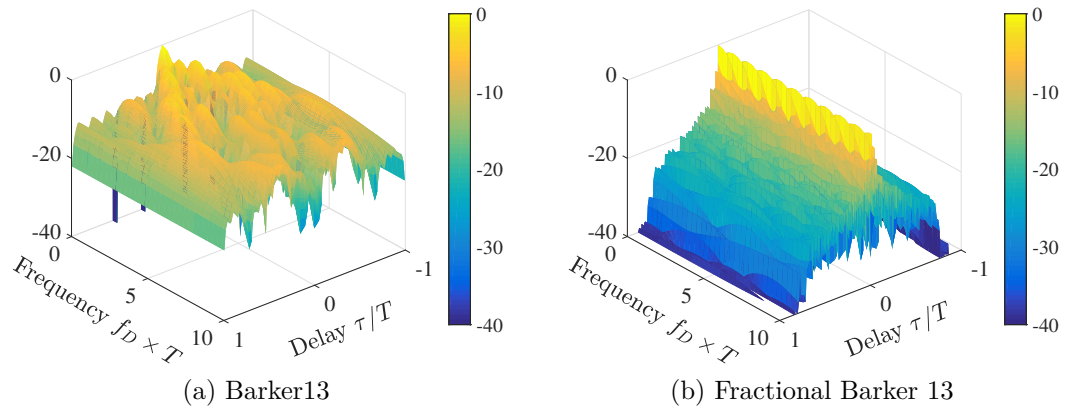


Fig. 5.2 Ambiguity function in logarithmic scale of (a) a Barker 13 code and (b) a fractional Barker 13 waveform generated using  $o = 50$ ,  $a = 0.5$ .

the original and generated waveforms  $s[n]$  and  $s_a[n]$  respectively. It has been shown that the introduced novel libraries have significant advantages in delay resolution, interference and sidelobe level (SLL) reduction (Clemente et al., 2014b).

In Fig. 5.2 the AF of (a) a Barker 13 code sequence and (b) a fractional Barker 13 waveform generated using  $o = 50$ ,  $a = 0.5$  is illustrated. Comparing the two AFs it can be noted that the application of a FrFT leads to a more concentrated AF. This phenomenon is very similar to the effect that LFM has on an unmodulated pulse (see Section 2.2.3). A comparison between the AF of a LFM pulse of time-bandwidth product  $TB = 1300$  and a fractional Barker 13 waveform generated using a bit rate  $o = 200$  and fractional order  $a = 0.25$  is shown in Fig 5.3. As it can be seen, both AF contours of the LFM pulse (Fig. 5.3a) and

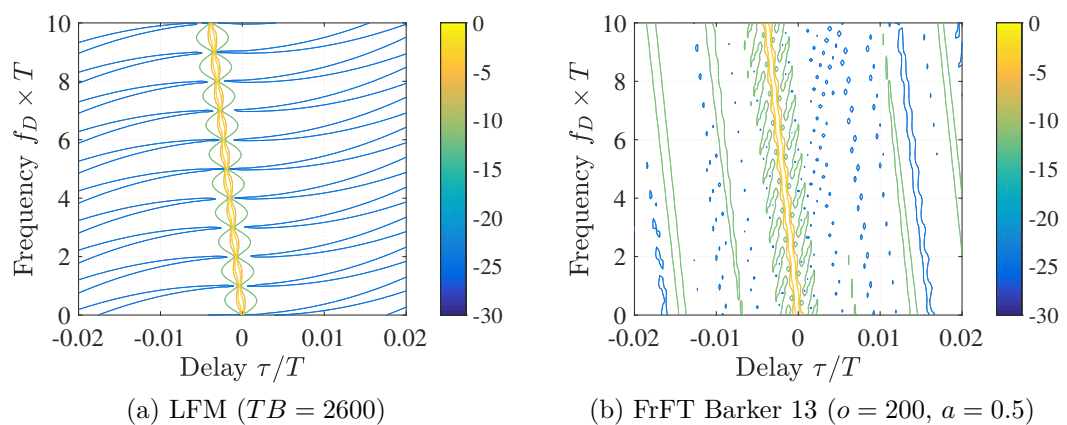


Fig. 5.3 Ambiguity function contour of (a) a LFM pulse with time-bandwidth product  $TB = 2600$  and, (b) a fractional Barker 13 waveform generated using  $o = 200$ ,  $a = 0.5$ .

the fractional barker waveform (Fig. 5.3b) are very similar to each other for values higher than  $-6$  dB (see yellow and orange color-mapped contour lines). In reality, applying a FrFT of order  $a$  in a sequence will rotate its AF in the delay-Doppler plane by an angle  $\vartheta = a\frac{\pi}{2}$ . Namely, it can be derived (see Appendix A) that the AF of an arbitrary signal  $x(t)$  and its FrFT  $x_a(u)$  are related as:

$$\mathcal{A}_{\text{Ca}}(\tau, \omega)\{x(t)\} = \mathcal{A}_{\text{Ca}}(d, \nu)\{x_a(u)\} \quad (5.5)$$

where  $d = \omega \sin \vartheta + \tau \cos \vartheta$  and  $\nu = \omega \cos \vartheta - \tau \sin \vartheta$ . This behaviour is very similar to the relation between the FrFT and WVD discussed in (Almeida, 1994), since the canonical AF can be described as the 2D FT of the WVD (see Section 3.3.1).

### 5.2.2 Constant Envelope Fractional Waveforms

In this subsection the design of novel waveform libraries is addressed under constant envelope (CE) constraints applying a method based on the FrFT and the error reduction algorithm (ERA). Reconstruction of the fractional waveforms described in Section 5.2.1 is achieved by means phase retrieval applying the Gerchberg-Saxton algorithm (GSA) to retain the CE property.

Constant modulus or peak-to-average power ratio (PAPR) is an essential characteristic for real world applications, as radar signal amplifiers usually work in a saturation condition that maximizes their efficiency but preventing amplitude modulation in waveforms at the same time. Unfortunately, despite the fact that fractional waveforms libraries offer good properties, unlike the original code sequences (Barker 13, Frank, P4, etc.), they do not preserve the CE property.

For a better understanding of the CE constraint let  $x[n]$  be an arbitrary waveform. The vector  $x[n]$  can be represented as:

$$x[n] = |x[n]|e^{j\eta[n]} \quad (5.6)$$

where  $|\cdot|$  denotes the amplitude and  $\eta[n]$  is the phase of the waveform. For  $x[n]$  the requirement of CE means that its magnitude must be kept constant for all  $n$ , which is equivalent to:

$$|x[n]| = A, \quad \forall n \quad (5.7)$$

where  $A$  is a suitable positive constant that can be also used to sustain the energy of  $x[n]$  at a desired level (Pillai et al., 2009).

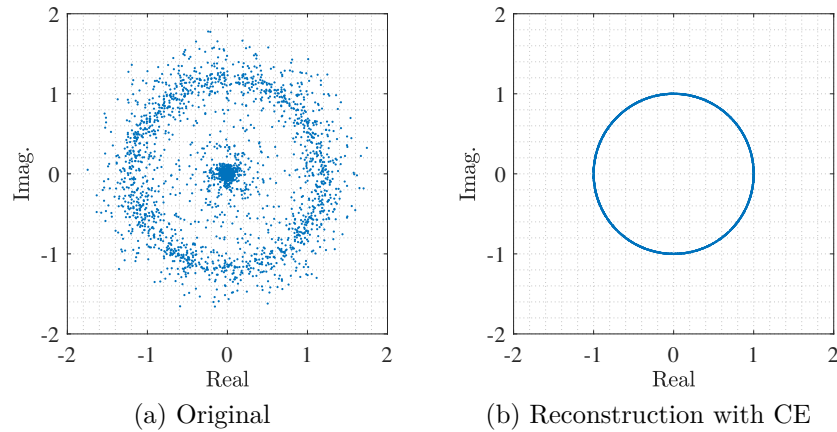


Fig. 5.4 Complex plane representation of a Barker 13 code modulated with FrFT using  $a = 0.5$  and  $o = 200$  before (a) and after reconstruction with CE constraint (b).

Typically in current power amplifiers high linearity implies low power efficiency and vice-versa (Cripps, 2002). This low efficiency operation is due to the fact that the amplifying device must be biased to an average output power level low enough to accommodate peak input signal levels without over-driving the amplifying device. Therefore, linearity requirement can be met by driving the power amplifier well below its saturation point. To achieve better performance the use of non-linear components is required. In Fig. 5.4 samples of a fractional Barker 13 waveform generated using  $a = 0.5$  and  $o = 200$  are illustrated in the complex plane (a) before and (b) after CE constraints have been applied. As it can be seen in Fig.5.4a, for the original fractional waveform, the samples are scattered in the complex plane with varying distance from the origin. On the other hand, after CE constraints have been applied, all the samples are placed in a circle meaning that they have equal distance from the origin and consequently constant modulus (see Fig.5.4b).

A straight-forward approach of enforcing CE on non-CE a waveform  $x[n]$  is to simply divide each sample of the waveform by its absolute value:

$$\tilde{x}[n] = x[n]/|x[n]| \Rightarrow |\tilde{x}[n]| = 1 \quad (5.8)$$

where  $\tilde{x}[n]$  is a CE waveform. While this method is fairly simple and easy to implement, it cannot guaranty that the reconstructed waveform  $\tilde{x}[n]$  will have similar radar performance compared with the original waveform  $x[n]$ . In Fig. 5.5 the spectrum and the auto-correlation (AC) function of a fractional waveform

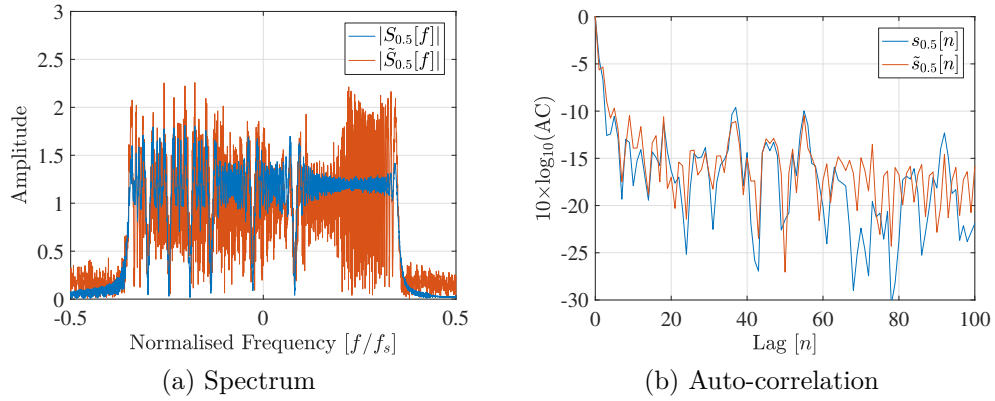


Fig. 5.5 Spectrum and AC function of a fractional waveforms of different fractional Barker 13 waveform generated using  $o = 200$  and  $a = 0.5$  before ( $s_{0.5}$ ) and after ( $\tilde{s}_{0.5}$ ) dividing it by its modulus.

generated using a Barker 13 code with  $o = 200$  and  $a = 0.5$  are illustrated before and after being divided by its modulus. As it can be seen in Fig. 5.5a the signal does not retain its spectrum shape after being divided by its modulus. As described in Section 3.3.1, this, has a direct influence on the AC function of the waveform. In Fig. 5.5b it can be seen that the AC of the waveform has higher sidelobes close to the main peak after dividing by its modulus. In the following paragraph the proposed algorithm of reconstructing fractional waveforms while retaining their good properties is discussed.

### Error-Reduction Algorithm and Waveform Reconstruction

The error-reduction or Gerchberg-Saxton algorithm (GSA) was first introduced in connection with the problem of reconstructing phase from two intensity measurements (Gerchberg and Saxton, 1972). The algorithm can be described by the following simple four steps (Fienup, 1982):

1. Apply FT on an estimate of the reference sequence;
2. Replace the modulus of the resulting computed FT with the modulus of the FT of the reference sequence to form an estimate in the FT domain;
3. Apply IFT on the FT domain estimate;
4. Replace the modulus of the resulted computed sequence with the reference sequence modulus to form a new estimate of the reference sequence.

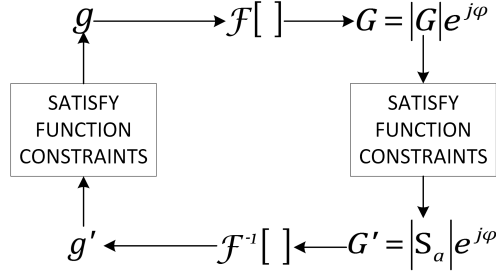


Fig. 5.6 Block diagram of the Gerchberg-Saxton algorithm.

In a more general definition, GSA transforms back and forth between the frequency and time domain, satisfying the constraints in one before returning to the other resulting in a decreased error at each iteration.

For this particular case the reference sequence is a non-CE fractional Fourier modulated waveform  $s_a[n]$  and  $g_k[n]$  is a CE sequence which iterates closer to  $s_a[u]$  in every execution of the GSA loop. Zadoff-Chu sequences, introduced in (Frank et al., 1962), are chosen as starting point of GSA due to its faster and better performance compared to random initial seed sequences according to the results presented in (Santra et al., 2013). To generate Zadoff-Chu sequences a modified formula introduced in (Budisin, 2010) is implemented supporting both odd and even sequence lengths. Additionally, to apply the CE constraint on the new waveforms, the modulus of the referenced sequence has been replaced with a constant,  $A$ , in the fourth step of GSA.

A graphical representation of the algorithm is provided in Fig. 5.6, where the modified GSA (MGSA) loops are repeated. The  $k$ th loop of the MGSA can be described by the following four steps:

$$G_k[f] = |G_k[f]|e^{j\phi_k[f]} = \mathcal{F}[g_k[n]], \quad (5.9)$$

$$G'_k[f] = |S_a[f]|e^{j\phi_k[f]} = |\mathcal{F}[s_a[n]]|e^{j\phi_k[f]} \quad (5.10)$$

$$g'_k[n] = |g'_k[n]|e^{j\psi'_k[n]} = \mathcal{F}^{-1}[G'_k[f]], \quad (5.11)$$

$$g_{k+1}[n] = Ae^{j\psi_{k+1}[n]} = Ae^{j\psi'_k[n]} \quad (5.12)$$

where  $\mathcal{F}[\cdot]$  represents the discrete Fourier transform and,  $\phi_k[n]$  and  $\psi_k[n]$  are the phases in time and frequency domain of  $g_k[n]$ . Through simulation analysis the MGSA appear to converge satisfactory after 50 repetitions. The performance of the proposed reconstruction technique will be discussed in the following paragraphs.

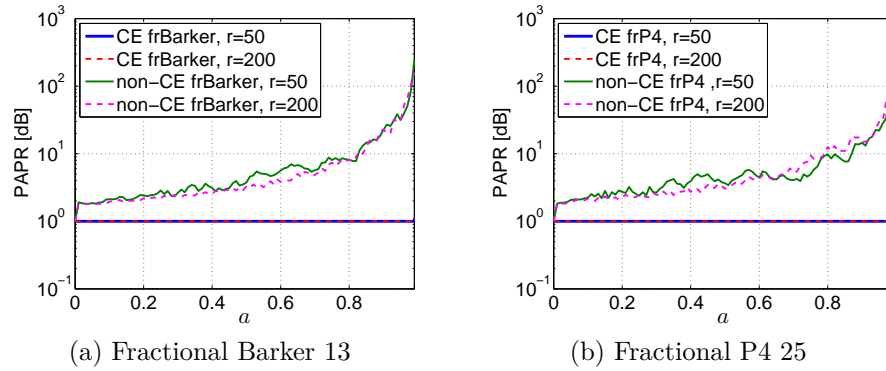


Fig. 5.7 Peak-to-average power ratio (PARP) of CE and non-CE Barker 13 (a) and P4 25 (b) fractional waveforms of different fractional order using  $r = 50$  and  $r = 200$ .

### Performance Evaluation

In verifying the CE constraint, the PAPR of both the constant and non-CE waveforms are evaluated for altering fractional orders and different chip sampling rates. Although the proposed method can be applied in fractional waveforms generated from any code sequence, here the performance parameters are evaluated for the Barker 13 and P4 25 code sequences using samples per bit rate  $o = 50$  and  $o = 200$ . In Fig. 5.7a and Fig 5.7b it is observed that the non-CE waveforms tend to have higher PAPR as the fractional order increases for both canonical sequences. On the other hand, the CE waveforms have unity PAPR for all fractional orders which confirms the CE constraint. In both cases of non-CE waveforms and CE waveforms, the chip rate  $o$  does not have any significant impact.

To quantify the effectiveness of the novel libraries, various AF performance parameters are examined using the following criteria:

- Delay and Doppler resolution, computed as the  $-3$  dB width of the zero-Doppler and zero-delay cut of the AF respectively. Generally, finer resolution is desired to be able to resolve targets that are in very close proximity (see Section 2.2.1);
- Delay and Doppler SLL, computed as the level of the first sidelobe of the zero-Doppler and zero-delay cut of the AF respectively. As discussed in Section 2.2.3, sidelobes are undesired as high SLL can mask reflections from weaker RCS targets;
- Interfering power, computed as the power outside the main lobe. As discussed in Section 3.3, ideally the entire volume of the AF is desired to

be concentrated at its centre. Even if this cannot be practically achieved (see Section 3.3.3), generally power outside the main lobe is considered as interference;

- Interfering power ratio, computed as the ratio between the power in the sidelobes of the AF and main lobe power.

In the presented analysis, constant envelope fractional waveforms are compared with their originals in terms of the performance parameters defined above. According to the key performance definitions previously expressed, better performance results for smaller values of all parameters.

The performance of CE and non-CE FrFT modulated Barker 13 code are compared in Fig. 5.8. Examining the performance ratios when  $o = 50$ , Fig. 5.8a shows that delay resolution is identical for both cases, while Doppler resolution is improved for higher fractional orders after using the CE constraint. Also, Fig. 5.8b demonstrates that delay and Doppler sidelobes have the same behaviour for both CE and non-CE waveforms. Additionally interference and interference power ratio perform similarly for both cases as it is shown in Fig. 5.8c. Examining the the

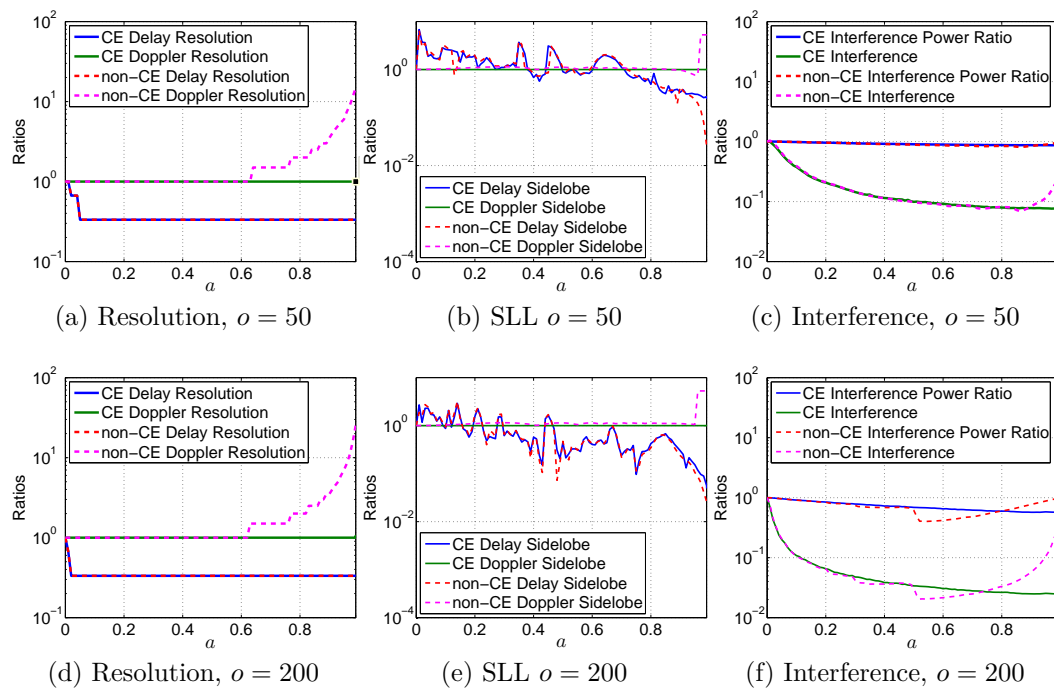


Fig. 5.8 Ratios of the AF quality parameter for fractional Barker 13 waveforms of different  $a$  before and after applying CE constraints in terms of resolution (a), SLL (b) and interference (c) for  $o = 50$  and resolution (d), SLL (e) and interference (f) for  $o = 200$ .

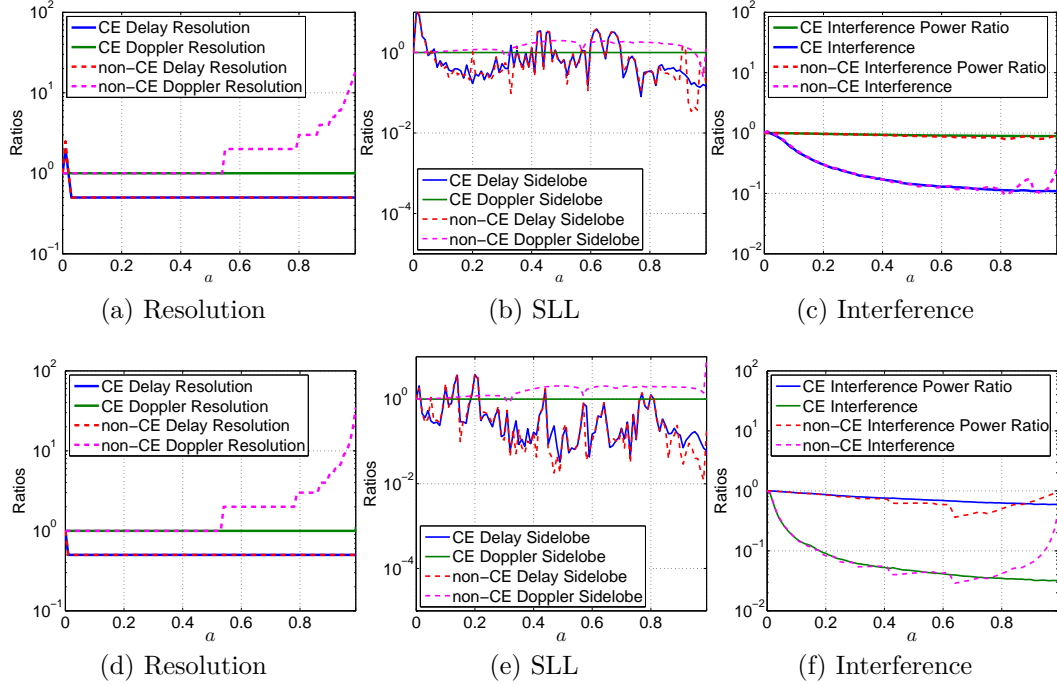


Fig. 5.9 Ratios of the AF quality parameter for fractional P4 25 waveforms of different  $a$  before and after applying CE constraints in terms of resolution (a), SLL (b) and interference (c) for  $o = 50$  and resolution (d), SLL (e) and interference (f) for  $o = 200$ .

performance ratios using  $o = 200$ , it can be observed that after increasing  $o$  the performance of CE and non-CE waveforms has been increased similarly in terms of resolution and sidelobes (see Fig 5.8d and Fig 5.8e). Also interference and interference power ratio have been decreased, for both cases with CE waveform performing better at high fractional orders (see Fig 5.8f).

To compare different canonical sequences, the same simulation analysis is repeated using P4 25 code sequence. In Fig. 5.9 the results of CE and non-CE FrFT for both cases of  $o = 50$  and  $o = 200$  are summarised. Namely, when examining the range and Doppler resolution for  $o = 50$  and  $o = 200$  in Fig.5.9a and Fig.5.9d respectively, it can be seen that the delay resolution remains identical for both CE and non-CE waveforms, while the CE waveforms have better Doppler resolution in higher orders  $a$ . A similar trend can also be observed for the delay SLL in Fig.5.9b and Fig.5.9e, where the CE and non-CE waveforms perform similar to each other for both values of  $o$ , with the non-CE however having lower delay SLL than the CE for certain fractional orders. Moreover, examining the Doppler SLL in the same figures, it can be seen that while the values for the CE waveforms remain constant all the cases of  $o$  and  $a$ , non-CE appear to perform

worse for all fraction orders  $a$  except for a very small region of values close to 1 when  $o = 50$ . Finally, as it can be seen in Fig.5.9c when  $o = 50$  the interference and interference power ratio perform similarly for both CE and non-CE waveforms, while increasing the samples per bit rate to  $o = 200$  offers significantly better performance in CE waveforms for higher values of  $a$ . Those results demonstrate that the performance ratios follow each other very close for both CE and non-CE cases, similarly to the ones presented for the Barker 13 fractional waveforms.

From the presented analysis it follows that the reconstructed waveforms retain the good properties of the fractional waveforms while also satisfying CE constraints. Finally no considerable improvement or declination was observed associated with the bandwidth usage after the modulation in performed simulations.

In conclusion, a constructive technique for numerical estimation of CE waveforms has been described and illustrated on several waveform simulation examples. The performance of the new waveform library has been evaluated as a function of the FrFT order and samples per bit rate. The results illustrate cases where fractional waveforms can be reconstructed under CE constraints while retaining their good AF properties.

### 5.2.3 Diversity In Fractional Waveform Libraries

This subsection focusses on how the diversity between waveforms populating the non-CE and CE fractional libraries discussed in Section 5.2.1 and Section 5.2.2 respectively can be achieved. The performance of these novel waveform libraries are analysed numerically in order to determine the degree of correlation between waveforms generated from the same code sequence  $c[n]$  and sample/bit rate  $o$  but different fractional order  $a$ .

In order to analyse the correlation properties of a waveform library it is assumed that two fractional waveforms  $s_{a_m}[n]$  and  $s_{a_l}[n]$  generated from the same canonical waveform  $s[n]$  and different orders i.e.  $a_m \neq a_l$  and  $a_m, a_l \in [0, 2]$ , are near-orthogonal if their cross-correlation is below the 1<sup>st</sup> SLL of the original sequence  $c[n]$ . The same principle applies also for CE fractional waveform libraries. Namely Barker 13 code has SLL = -22.28 dB while P4 25 has SLL = -22.22. In Fig. 5.10 the SLL-thresholded maxima of the cross-correlations between the waveforms with different  $a$  and the same  $c[n]$  are reported for  $o = 50$ . Examining the results, it is derived that the non-CE waveform libraries (see Fig.5.10a and Fig.5.10b) show significantly less above-the-threshold values compared to their respective CE libraries. This can be justified, as the non-CE waveforms can utilise

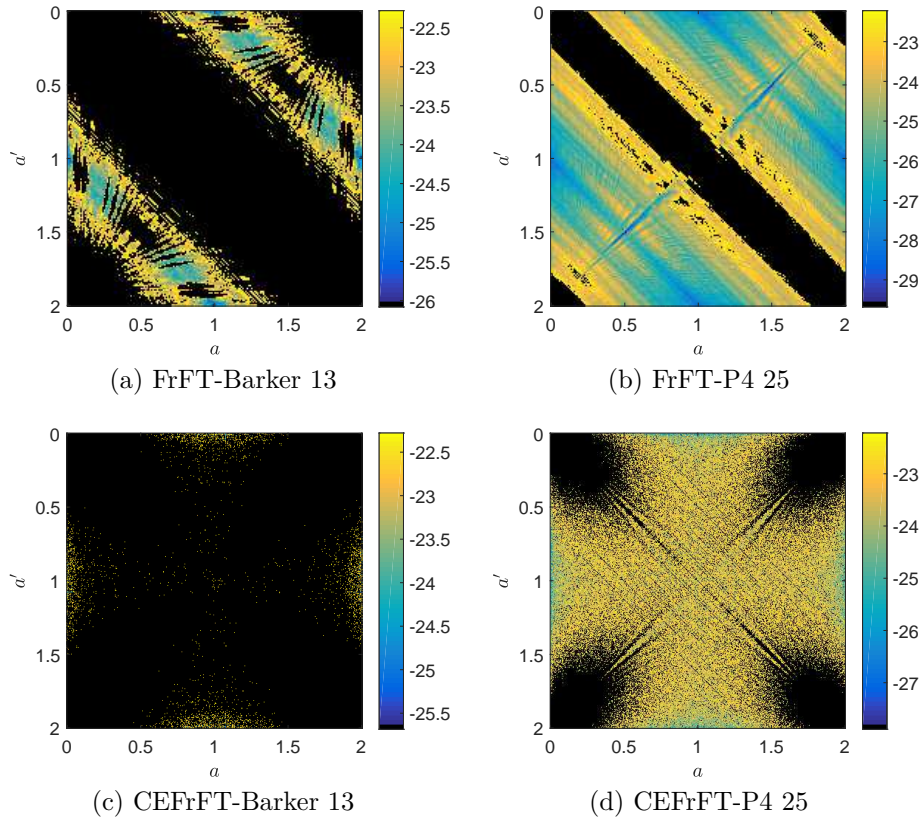


Fig. 5.10 SLL-thresholded maxima of the cross-correlations between the waveforms generated using different  $a$  and the same  $c$  for  $o = 50$ . The cases above the thresholds are shown in black.

their modulus as an extra degree of freedom for diversity compared to the CE waveforms which can vary only in phase.

Moreover in Fig. 5.11 the SLL-thresholded maxima of waveforms generated using  $o = 200$  are illustrated. Comparing the results for the non-CE waveform libraries (see Fig.5.11a and Fig.5.11b) and the CE (see Fig.5.11c and Fig.5.11d), it can be observed that the number of the above-the-threshold values in non-CE and CE libraries is more similar to each other compared to the cases of  $o = 50$ , with the non-CE libraries having lower floor values due to their non constraint modulus.

Comparing the cross-correlation maxima graphs for all waveform cases in Fig.5.10 with their respective subfigures in Fig.5.11, it can be seen that for all the analysed cases the number of waveform pairs with cross-correlation below the threshold is getting greater as  $o$  increases. This effect is apparent due to the higher length of waveforms generated from larger  $o$  and the fact that for higher values of  $o$  the number of chirped components composing the fractional waveforms

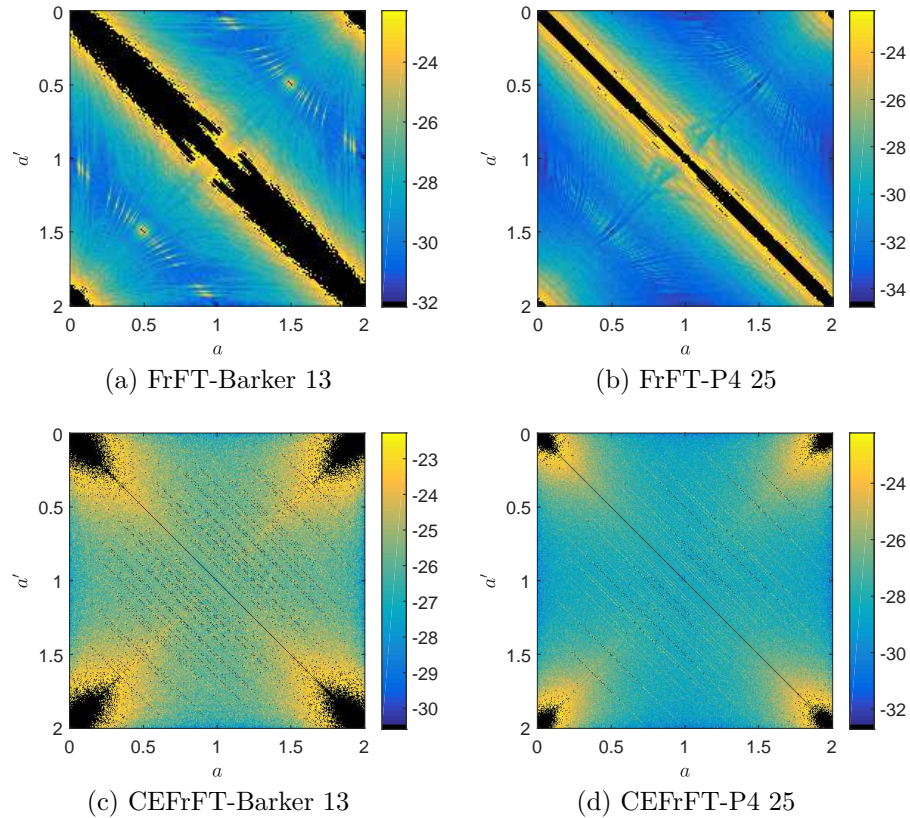


Fig. 5.11 SLL-thresholded maxima of the cross-correlations between the waveforms generated using different  $a$  and the same  $\mathbf{c}$  for  $o = 200$ . The cases above the thresholds are shown in black.

$\mathbf{s}_a$  increases. As a consequence the mismatching between waveforms of the same libraries modulated with different fractional orders becomes stronger leading to a higher number of near-orthogonal waveforms that can populate the library  $\mathbf{S}$ . It is worth noting that different seed sequences (i.e. starting points in GSA) are used for each individual fractional order in simulation examples. This is achieved by changing the root of Zadoff-Chu sequences (Budisin, 2010).

Table 5.1 summarizes maxima (worst cases) of the reuse intervals extracted for both CE and non-CE fractional libraries. The reuse intervals are estimated for each

Table 5.1 Fractional order reuse interval for different values of  $o$

Sequence	Constant Envelope		non-Constant Envelope	
	$o = 50$	$o = 200$	$o = 50$	$o = 200$
Barker 13	1.43	0.21	0.77	0.22
P4 25	0.4	0.12	0.49	0.12

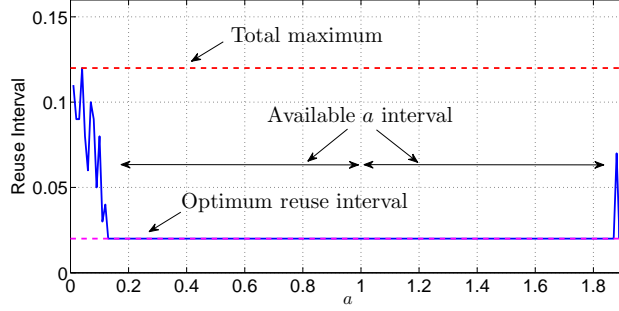


Fig. 5.12 Reuse interval of CE fractional P4 25 waveforms of different  $a$  for  $o = 200$  and its overall and optimum maxima resulting for different interval of  $a$ .

value of  $a$  by measuring the gaps in terms of fractional orders between the used  $s_{a_m}[n]$  and the first  $s_{a_l}[n]$  with a cross-correlation maximum below the threshold. In essence, the reuse interval shows what is the higher step, in fractional order, that a waveform generated using an order  $a$  must have with another waveform in the same library to satisfy the near-orthogonal constraint. Essentially, the reuse interval provides a metric of how many near-orthogonal waveforms can be fitted in the same library. As it can be seen CE libraries present higher reuse intervals for small values of  $o$  compared to the non-CE. However both CE and non-CE libraries have significantly lower reuse interval for higher values of  $o$ . This results in a higher reuse, since the number of near-orthogonal waveforms in the same library is given by the ratio of the available fractional order interval ( $\max(a) = 1$  due to symmetry of FrFT) to their maximum reuse interval. Specifically up to eight orthogonal waveforms can be obtained in the case of P4 25 with  $o = 200$  (i.e.  $1/0.12 \simeq 8$ ). This number can be increased by limiting the values of fractional order to lower reuse interval ranges. In Fig. 5.12 the case in which the fractional order  $a$  has been limited to values between 0.13 and 1 is illustrated. As it can be seen, these limits decreasing maximum to 0.02, which consequently results in a number of available near-orthogonal waveforms greater than 40 (i.e.  $0.87/0.02 \simeq 43$ ).

#### 5.2.4 Validation and Performance Analysis

In the following paragraphs the performance analysis of the novel CE fractional waveforms discussed in Section 5.2.2 will be examined. First the applicability of the proposed waveforms is experimentally validated. Later the performance of the waveform will be examined in terms of simulation analysis in a distributed multiple input-multiple output radar system (DMRS) scenario. Simulation and

experimental results demonstrate the effectiveness of the novel technique and its capability to provide a reliable and robust waveform generation tool.

### Experimental Validation

For our experimental validation three CE fractional waveforms  $s_1$ ,  $s_2$  and  $s_3$  are generated from a Barker 13 code using fractional orders of 0.52, 0.57 and 0.62 respectively and  $r = 200$  samples per chip to establish good AF properties and orthogonality (Ilioudis et al., 2014). Using these waveforms three pulses are constructed as follow:

$$w_1(t) = s_1(t - t_1) \quad (5.13)$$

$$w_2(t) = s_1(t - t_2) + s_2(t - t_2) \quad (5.14)$$

$$w_3(t) = s_1(t - t_3) + s_2(t - t_3) + s_3(t - t_3) \quad (5.15)$$

where  $t_1 < t_2 < t_3$  are the delays applied to separate the pulses. The overall transmitted sequence  $w_{tr}(t)$  is the sum of the pulses described in (5.13), (5.14) and (5.15), i.e. :

$$w_{tr}(t) = w_1(t) + w_2(t) + w_3(t) \quad (5.16)$$

This scenario helps in examining the orthogonality of the waveforms when none, two or three of them are overlapping at  $t_1$ ,  $t_2$  and  $t_3$  respectively.

To transmit the sequence  $w_{tr}(t)$  a vector signal generator (The Keithley Instruments, 2008) is used at a sampling rate of  $f_s = 1.25$  MHz and carrier frequency of  $f_c = 1.4$  GHz. Low-cost software defined radio (SDR) dongles (NooElec, 2013) are then used for reception via MATLAB/Simulink model interface (MathWorks, 2013). To evaluate the orthogonality of the used waveforms, the respective matched filter for each of them is applied to the received signal. The three filtered outputs are illustrated in Fig. 5.13. In particular in Fig. 5.13a three spikes with values close to 0dB indicate the presence of waveform  $s_1$  in each of the three pulses. Similarly in Fig. 5.13b the two spikes on the second and third pulse indicate the presence of  $s_2$  in each respectively, while values close to  $-20$ dB indicate the absence in the first pulse. Finally, as it can be seen in Fig. 5.13c, only the waveform  $s_3$  present in the third pulse. It is therefore concluded that all waveform  $s_1$ ,  $s_2$  and  $s_3$  can be retrieved correctly from the three pulses using a threshold equal or higher to the maximum inference level of  $-17.8$  dB (second pulse in Fig. 5.13c).

In Fig. 5.14 the zero Doppler cuts of waveform's  $s_1$  auto-AF (solid line) and its cross-AF with waveform  $s_2$  (dashed line with dot marks) are illustrated for

both theoretical and experimental results. After comparing the auto-AF for the theoretical and experimental results in Fig. 5.14a and Fig. 5.14b respectively, it can be seen that in the experimental results the main lobe is narrower with two residual sidelobes, whose maximum level is right below  $-13.5$  dB. Analysing the captured data in an extended range indicates that this phenomenon occurs due

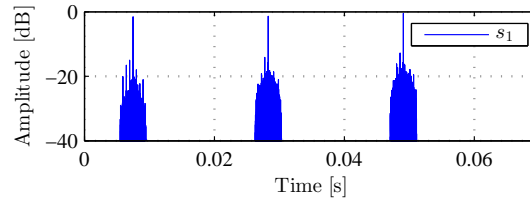
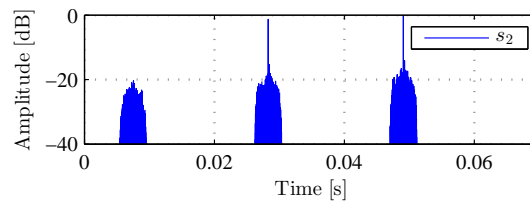
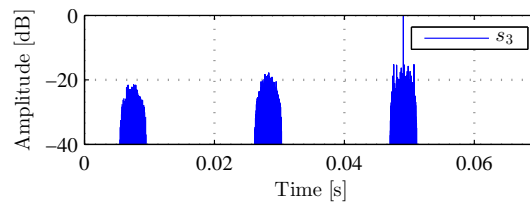
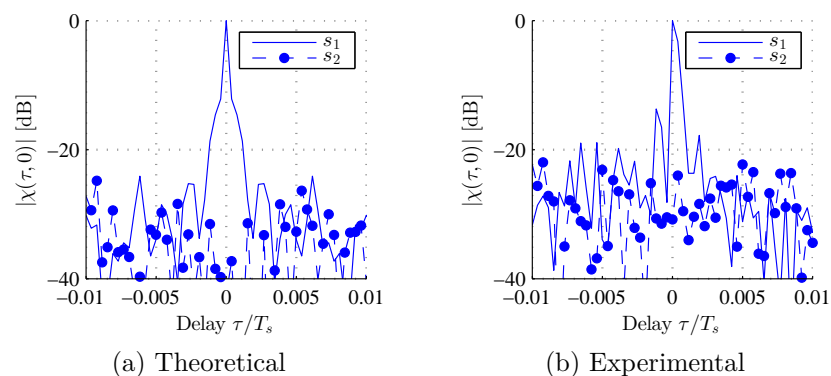
(a)  $s_1$  matched filtering(b)  $s_2$  matched filtering(c)  $s_3$  matched filtering

Fig. 5.13 Matched filter outputs of the transmitted sequence  $w_{tr}$  after applying the matched filter with (a)  $s_1$ , (b)  $s_2$  and (c)  $s_3$  respectively.



(a) Theoretical

(b) Experimental

Fig. 5.14 Theoretical (a) and experimental (b) Zero Doppler cut of waveform's  $s_1$  auto-AF and its cross-AF with waveform  $s_2$

to noise and performance limitations (e.g. sample drop, latency) on the receiver. Furthermore the maximum level of the cross-AF in theoretical and experimental results remains below  $-22.3$  dB and  $-20.4$  dB respectively. This shows a good level of orthogonality between the three used waveforms.

### MIMO Radar Signal Model and Localization

Let us consider a MIMO radar system comprising  $N_{\mathcal{T}}$  transmitters,  $N_{\mathcal{R}}$  receivers and  $N_{\mathcal{K}}$  targets. The position of the  $i$ th transmitter,  $j$ th receiver and  $\kappa$ th target are denoted by  $\mathbf{x}_{i,\mathcal{T}}$ ,  $\mathbf{x}_{j,\mathcal{R}}$  and  $\mathbf{x}_{k,\mathcal{K}}$  respectively, where  $\mathbf{x} = [x, y]$  denotes the Cartesian co-ordinates in  $x$ -axis and  $y$ -axis. It is assumed that the MIMO radar configuration consists of stationary sensors and point targets with spatial homogeneous reflectivities modelled by the complex value  $\zeta^k$ . The emitted signal from  $i$ th transmitter  $s_i(t)$  is a complex signal with  $1/T \int_T |s_i(t)|^2 dt = 1$ , where  $T$  denotes the transmitting duration. It is also assumed that the transmitters are using orthogonal signals satisfying the condition:

$$\int_{-\infty}^{\infty} s_{i_1}(t)^* s_{i_2}(t - \tau) dt = 0, \quad \text{for all } i_1 \neq i_2 \quad (5.17)$$

where  $\{\cdot\}^*$  denotes the complex conjugate operator.

The received signal in the  $j^{\text{th}}$  receiver can be expressed as the superposition of the reflected signals from every target:

$$r_j(t) = \sum_{k=1}^{\mathcal{K}} \sum_{i=1}^{\mathcal{T}} h_{ij}^k s_i(t - \tau_{ij}^k) + n_j(t) \quad (5.18)$$

where  $\tau_{ij}^k$  defines the propagation delay of a signal emitted from  $i$ th transmitter, reflected from  $k$ th target and received by  $j$ th receiver and  $n_j(t)$  corresponds to a complex white Gaussian additive noise with zero mean and variance  $\sigma_n^2$ . Additionally  $h_{ij} = \zeta^k \exp(j\omega_{D_{ij}}^k t)$  captures the attenuation  $\zeta^k$  and Doppler shift  $\omega_{D_{ij}}^k$  in the  $ij$ th pair due to the reflection from the  $k$ th target. The time delay is calculated as:

$$\tau_{ij}^k = \frac{1}{c} \left( \sqrt{(x_{k,\mathcal{K}} - x_{i,\mathcal{T}})^2 - (y_{k,\mathcal{K}} - y_{i,\mathcal{T}})^2} + \sqrt{(x_{k,\mathcal{K}} - x_{j,\mathcal{R}})^2 - (y_{k,\mathcal{K}} - y_{j,\mathcal{R}})^2} \right) \quad (5.19)$$

Using the delay  $\tau_{ij}^k$  observed in a transmitter-receiver pair the distance of the target from each sensor can be described in circular or ellipsoid range bins for monostatic or bistatic radar configurations respectively.

### Simulation Analysis

Here a DMRS scenario is used to evaluate the performance of novel fractional waveform libraries compared to different approaches. The tested DMRS scenario consists of three transmitters and three receivers co-located in pairs, i.e.  $N_{\mathcal{T}} = 3$ ,  $N_{\mathcal{R}} = 3$  and  $\mathbf{x}_{i,\mathcal{T}} = \mathbf{x}_{j,\mathcal{R}}$  for  $i = j$ . The geometry of the overall system is illustrated in Fig. 5.15. The sensors are positioned symmetrically in the surveillance area with location calculated from  $\mathbf{x}_{i,\mathcal{T}} = \mathbf{x}_{i,\mathcal{R}} = [R \cos(\phi_i), R \sin(\phi_i)]$  with  $R = 500$  m and  $\theta_{\text{be}} = [0, 2\pi/3, 4\pi/3]$  being the range and bearing of the  $i$ th monostatic transmitter-receiver pair respectively. This orientation is chosen to achieve optimum localization near the center of the scene (Godrich et al., 2010). Additionally two targets are placed in the surveillance region, i.e.  $N_{\mathcal{K}} = 2$ .

In the simulation analysis three different sets of near-orthogonal waveforms were used to evaluate their impact in localization performance. Firstly, the three CE fractional waveforms are used. Secondly three linear frequency modulated (LFM) waveforms are used using up-chirp, down-chirp and half up-chirp half down-chirp modulation as defined in (5.20), (5.21) and (5.22) respectively as

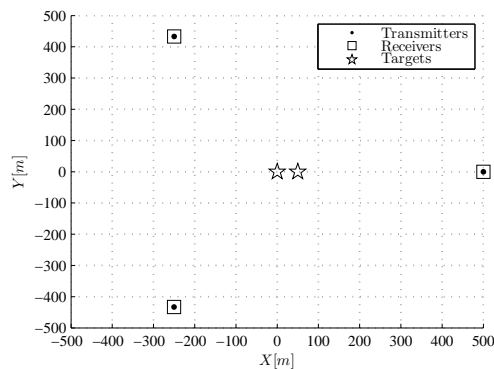


Fig. 5.15 Sensors and targets geometry in a surveillance area

Table 5.2 Time-Bandwidth Product

Library	$T \times B$		
CE-FrFT	1872	2012	2132
LMF	2069	2064	2194
DSSS	2340	2028	1456

follows:

$$s_{\text{LFM},1}(t) = e^{j\pi \frac{BW}{T} t^2} \quad (5.20)$$

$$s_{\text{LFM},2}(t) = e^{j\pi \frac{BW}{T} (T-t)t} \quad (5.21)$$

$$s_{\text{LFM},3}(t) = \begin{cases} e^{j\pi \frac{2BW}{T} t^2} & t < T/2 \\ e^{j\pi \frac{2BW}{T} (T-t)t} & t \geq T/2 \end{cases} \quad (5.22)$$

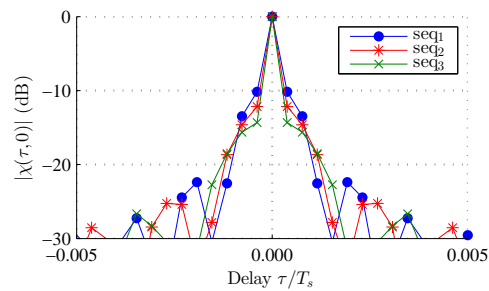
where  $BW$  is the occupied bandwidth and  $T$  is the signal duration. Finally LFM waveforms using direct sequence spread spectrum (DSSS) to achieve orthogonality (Majumder et al., 2013) are also tested.

In DSSS technique each waveform is coded with different orthogonal sequences and uses different chirp rates to achieve better orthogonality. In our simulations a 2048 Walsh-Hadamard code is used and three chirp rates  $B/T$ ,  $(B/2)/T$ ,  $(B/3)/T$  for each of the three waveforms respectively, where  $B$  is the appropriate bandwidth to be used with the chosen code as calculated in (Majumder et al., 2013). All the waveform sets are allocated on an available bandwidth of  $BW = 500\text{MHz}$  and have a duration of  $T = 5.2\mu\text{s}$ . The AF zero-Doppler cut of the three sequences from each set is shown in Fig. 5.16. In Fig. 5.16a and Fig. 5.16b it is observed that both CE-FrFT and LFM sets have SLL constantly below  $-20\text{dB}$ . In constraint waveforms obtained using DSSS modulation achieve different SLL with the first one having a maximum of  $-10\text{dB}$  and the second and third waveforms reaching levels up to  $-6\text{dB}$ . The frequency characteristics of the three sets are illustrated in Fig. 5.17. As it can be seen all sets are occupying approximately the same bandwidth while the sample rate at the transmitter ensures that none of the waveforms' bandwidth exceed the  $500\text{MHz}$ . Finally the time-bandwidth products of the waveforms in each library are presented in Table 5.2.

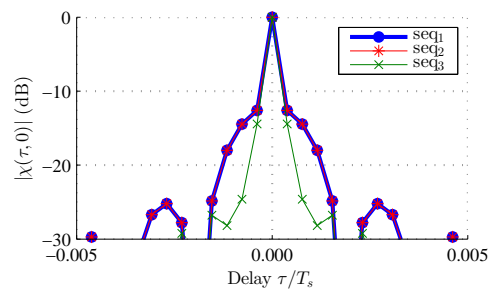
Through the literature numerous coherent and non-coherent techniques have been proposed for target localization in MIMO radar systems (Godrich et al., 2010), (Gorji et al., 2013). In this work a best linear unbiased estimator (BLUE) based

on the time of arrival (TOA) is chosen for its closed-form expression (Godrich et al., 2010). This estimator uses the TOA or  $\tau_{ij}^k$  as defined in (5.19) and the bearing of the  $i$ th transmitter and  $j$ th receiver to estimate the position of the  $k$ th target. In the examined scenario nine possible  $[i, j]$  transmitter-receiver pairs can be defined, three in monostatic configurations  $[1, 1]$ ,  $[2, 2]$  and  $[3, 3]$ , and six in bistatic  $[1, 2]$ ,  $[1, 3]$ ,  $[2, 1]$ ,  $[2, 3]$ ,  $[3, 1]$  and  $[3, 2]$ . It should be noted that each observed delay for every transmitter-receiver pair is correctly correlated with its respective target before applying BLUE.

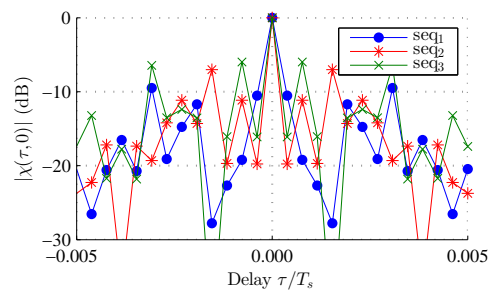
One target is positioned at the center of the scene  $\mathbf{x}_{1,\mathcal{K}} = [0, 0]$  while the second target is placed left of the center at different location on the horizontal



(a) CE Fractional

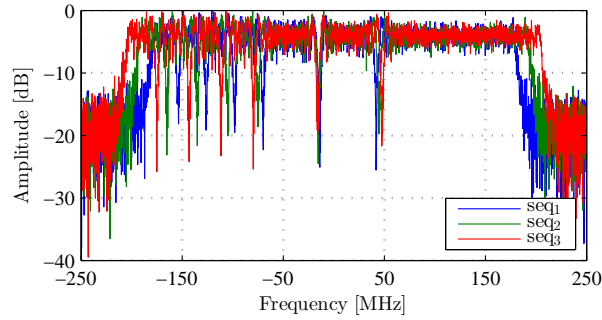


(b) LFM

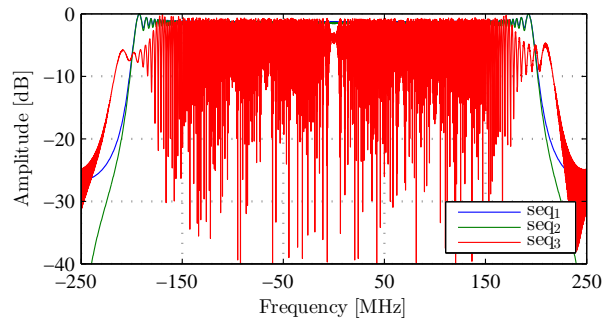


(c) DSSS

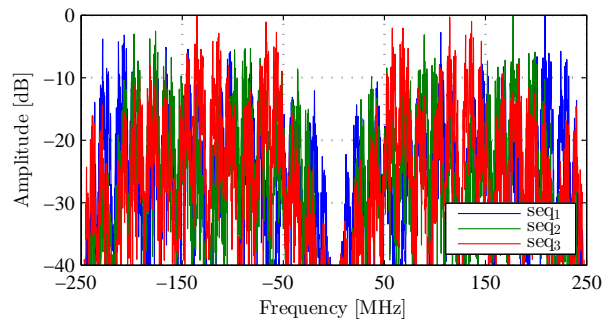
Fig. 5.16 Ambiguity Function Zero-Doppler cut for all three waveforms in (a) CE fractional, (b) LFM and (c) DSSS sets.



(a) CE Fractional



(b) LFM



(c) DSSS

Fig. 5.17 Occupied bandwidth for each waveform of (a) CE fractional, (b) LFM and (c) DSSS sets.

axis  $\mathbf{x}_{2,\mathcal{K}} = [0, \hat{d}]$  with  $\hat{d} \in [0, 3]$  m. Estimates of targets' locations are made as the distance between the two targets increases. The mean error after 20 Monte Carlo runs between the true and estimated location of the first target using the three families of waveforms was calculated for a signal to noise ratio SNR= 20dB. In Fig. 5.18 the simulated results are illustrated. As it can be seen, the CE fractional and LFM waveforms have very similar performance with the estimation error remaining relatively small for all different distances. On the other hand DSSS waveforms return a fluctuating error which reaches the value of 1.7m. In Fig. 5.19 the mean localization error of the left target is also presented for the same scenario.

Similarly to the first case CE fractional and LFM waveform sets have similar performance with the mean error remaining below 0.3m for distances higher than 2.1m. For smaller distances the mean error becomes very high and the localization of the target is not reliable. Furthermore the DSSS set also performs in a similar way to the previous case with the error fluctuating and reaching values of 1.7m for distances higher than 2.6m while for smaller distances the localization error is very high. The range profile of the two targets when their distance is 2.5m for the [2,2] pair is illustrated in Fig. 5.20. From the results it can be seen how the DSSS fails to correctly detect the position of the second target due to the high SLL. On the other hand when LFM and CE fractional waveforms are applied, the system is able to distinguish correctly their different locations.

The simulation results indicate that the CE fractional waveforms have similar performance to the traditional LFM waveforms in a MIMO radar scenario

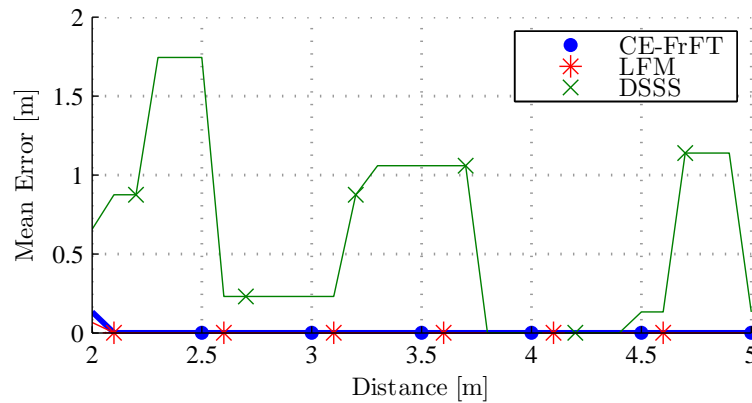


Fig. 5.18 Mean error of center target's real and estimated location for different horizontal distances from the left target using three different waveform libraries.

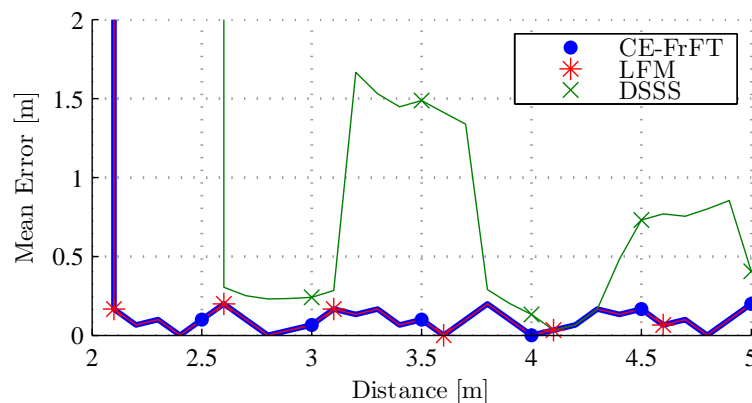


Fig. 5.19 Mean error of left target's real and estimated location for different horizontal distances from the center target using three different waveform libraries.

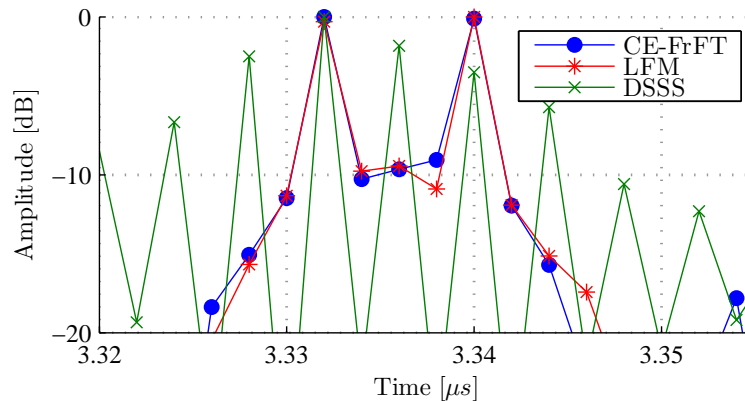


Fig. 5.20 Range profile of the two targets with distance 2.5m to each other in the first transmitter-receiver pair (2,2) (north-west) using CE fractional, LFM and DSSS waveform sets.

while outperforming the DSSS modulation technique. Additionally as shown in Section 5.2.3 the proposed technique can generate numerous near-orthogonal waveforms with good AF performance using, different modulated sequences (e.g. Barker13 and P4 25), and changing their samples per bit rate and the order of the FrFT. Therefore the proposed technique offers an efficient method of generating waveforms suitable for MIMO radar applications.

## 5.3 Information embedded Fractional Waveforms

As described in Section 2.4.2 in many application simultaneous radar and communication operations are required. Moreover in Section 5.2.1 a scheme of generating fractional waveforms by applying FrFT of different fractional order on code sequences with good AF parameters was discussed. In this section a novel modulation scheme based on fractional waveform design is presented for joint radar communication systems.

First let us consider an arbitrary binary code sequence  $\mathbf{c}$  containing the digital message to be transmitted. By applying inverse demultiplexing,  $\mathbf{c}$  can be divided into a number of parallel binary codes  $\mathbf{c}_i$  with  $i = 1, \dots, N_c$ . Each of these code sequences  $\mathbf{c}_i$  is first oversampled by a factor  $o$  and then mapped into symbol sequences  $m_i[n]$  with  $n = 1, \dots, N_m$  using some modulation constellation (BPSQ, QPSK, etc.). The length of the symbol sequences  $N_m$  can vary depending on the length of the message  $\mathbf{c}$ , the number of parallel code sequences  $I$ , the sample/bit

rate  $o$ , and the modulation constellation used. Moreover, the bandwidth of  $m_i[n]$ ,  $B_m$ , will depend on  $\mathbf{c}$  and  $o$ . In real applications  $N_m$  and  $B_m$  can also vary due to other factors such as additive guard and signal filtering. Since those factors will not influence the principles of the proposed multiplexing scheme, they are not in the scope of this work and will not be taken into account.

In a conventional orthogonal frequency division multiplexing (OFDM) scheme, the symbol sequences  $m_i[n]$  would be multiplexed by applying an inverse fast Fourier transform (IFFT) on each set of  $N_c$  symbols giving a time-domain signal (Molisch, 2007). In a similar approach, the proposed technique applies a FrFT of different order  $a_i$  on each symbol sequence  $m_i[n]$  to generate a number of  $N_c$  near-orthogonal fractional waveforms  $s_i[n]$ :

$$s_i[n] = \tilde{\mathcal{F}}^{a_i}\{m_i[n]\} \quad (5.23)$$

where  $a_i \in [0, 2)$  and  $a_i \neq a_{i'}$ , if  $i \neq i'$ . Here it should be also noted that while the length of the fractional waveforms remains  $N_m$ , the bandwidth of  $s_i$ ,  $B_{s_i}$  will be higher than  $B_m$  and will depend on the applied fractional order  $a_i$ . From (5.23) the communication-radar (Co-Radar) waveform can be generated by summing all the fractional waveforms:

$$s_{\text{Co}}[n] = \sum_i^{N_c} s_i[n] \quad (5.24)$$

Since all the added fractional waveforms will have the same length, the final Co-Radar waveform  $s_{\text{Co}}$  will also have a length of  $N_m$ . On the other hand the bandwidth of  $s_{\text{Co}}$  can be approximated by the maximum bandwidth of the fractional waveforms composing  $s_{\text{Co}}$ , i.e.  $B_{\text{Co}} \approx \max B_{s_i}$ . A block diagram of the proposed multiplexing scheme is illustrated in Fig. 5.21. In essence, the proposed technique maps the  $N_c$  different channels into different near-orthogonal chirp sub-carriers. The spectrogram of two Co-Radar waveforms is illustrated in Fig. 5.22 for (a)  $N_c = 6$  and (b)  $N_c = 20$  chirp sub-carriers. To achieve occupancy of the entire available time and bandwidth the fractional order of each sub-carrier is given as:  $a_i = 2(i - 1)/N_c$ . This configuration also places the chirp sub-carriers as far as possible with each other in the time-frequency space leading in less overlapping.

To demultiplex the signal and extract the binary information the inverse process must be followed adding however an extra step. First  $N_c$  number FrFTs are applied on Co-Radar waveform  $s_{\text{Co}}$ . Each FrFT will have a fractional order

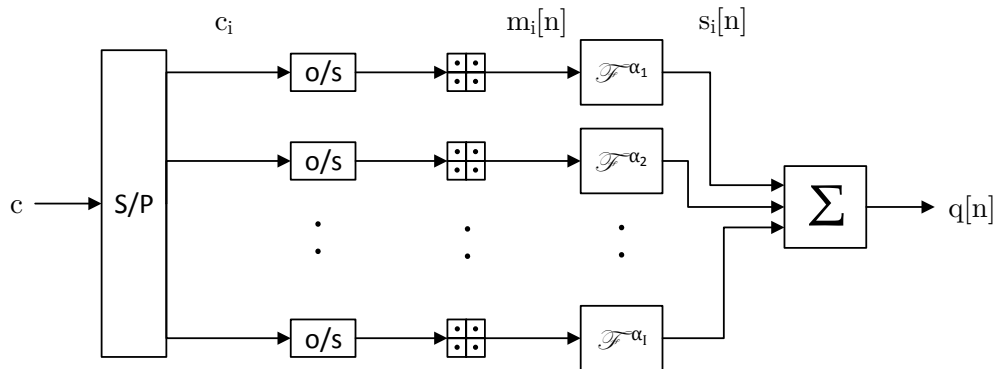
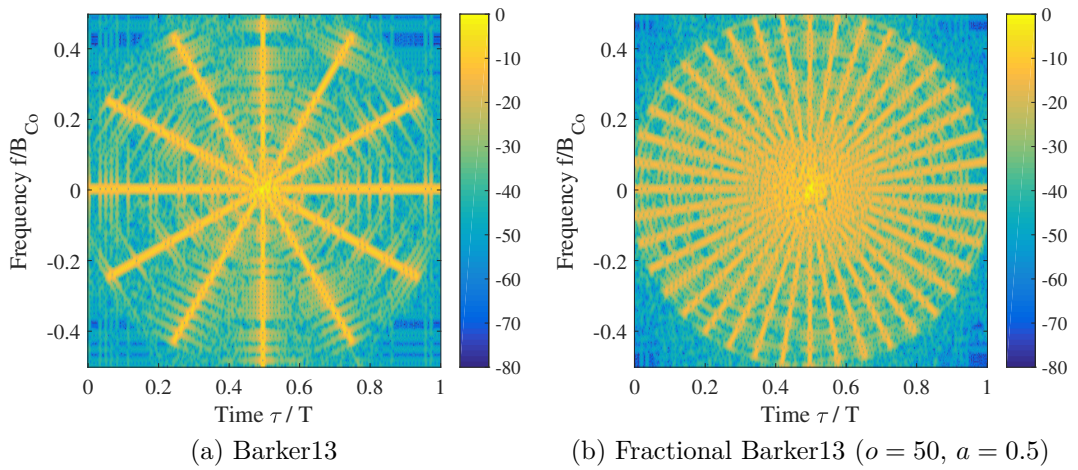


Fig. 5.21 Block diagram of the proposed multiplexing scheme.

Fig. 5.22 Time-frequency representation through spectrogram a Co-radar waveform with (a)  $N_c = 6$  and (b)  $N_c = 20$  chirp sub-carriers.

opposite to the one applied on the multiplexer, i.e.:

$$\hat{s}_i[n] = \tilde{\mathcal{F}}^{-a_i} \{s_{C_o}[n]\} \quad (5.25)$$

The resulting waveform  $\hat{s}_i[n]$  still has a bandwidth of  $B_{C_o}$  and contains all the  $I$  channels. However after applying a FrFT of opposite order, i.e.  $-a_i$ , the  $i$ -th sub-carrier has been moved to baseband. By applying a low-pass filter with cut-off frequency  $f_{cut} \approx B_m/2$  waveform  $\hat{m}[n]$  is generated. Since the chirp sub-carriers are not orthogonal  $\hat{m}[n] \neq m[n]$ . However after applying the correct de-mapper and convolving the signal with a square pulse of length equal to  $o$ , the majority of, or even all, the information can be reconstructed.

In (Gaglione et al., 2016a) a complete Co-Radar system based on the proposed scheme was presented. Among others, techniques to achieve synchronisation for correct reconstruction and techniques to mitigate information retrieving errors are discussed. Namely, coarse/acquisition (C/A) codes are proposed to accomplish synchronisation on the receiver ensuring that the FrFTs are correctly on the receiver. Moreover, techniques such as adding a guard and/or applying an interleaver on the symbol waveforms  $m[n]$  were shown to be able to allow full information retrieval on the receiver (Gaglione et al., 2016a). The proposed system was also experimentally validated through implementation in software defined radios (SDR) in (Gaglione et al., 2016b).

### Co-Radar Waveforms AF

In order to assess the performance of the proposed multiplexing scheme in radar applications the properties of its AF are examined. At this point it should be noted that for radar operations the waveform can be used as is and no demultiplexing of the signal is required and the waveform is used as is. Moreover, since the structure of the waveform depends among other on the information sequence  $\mathbf{c}$ , which in a standard communication-radar transmission cannot be controlled, the AF function of the waveforms will not be constant. On the other hand, other controlled parameters such as sample per bit rate, modulation constellation map and most importantly number and choice of the chirp sub-carriers play very significant role on the structure of the AF. From the Co-Radar signal definition in (5.24) the AF can be expressed as:

$$\begin{aligned}
\mathcal{A}_{\text{Co}}(\tau, f_d) &= \sum_{n=1}^{N_m} s_{\text{Co}}[n] s_{\text{Co}}^*[n + \lfloor \tau f_s \rfloor] e^{j2\pi f_d n / f_s} \\
&= \sum_{n=1}^{N_m} \left( \sum_{i=1}^{N_c} s_i[n] \sum_{i'=1}^{N_c} s_{i'}^*[n + \lfloor \tau f_s \rfloor] e^{j2\pi f_d n / f_s} \right) \\
&= \sum_{n=1}^{N_m} \left( \sum_{i=1}^{N_c} (s_i[n] s_i^*[n + \lfloor \tau f_s \rfloor]) e^{j2\pi f_d n / f_s} \right. \\
&\quad \left. + \sum_{i=1}^{N_c} \sum_{i'=1}^{N_c} ((1 - \delta(i - i')) s_i[n] s_{i'}^*[n + \lfloor \tau f_s \rfloor]) e^{j2\pi f_d n / f_s} \right) \\
&= \mathcal{A}_{\text{Co,Orth}}(\tau, f_d) + \mathcal{A}_{\text{Co,Cross}}(\tau, f_d)
\end{aligned} \tag{5.26}$$

where  $\tau$  and  $f_d$  denote the time and Doppler shifts respectively,  $f_s$  is the sampling frequency and  $\lfloor \cdot \rfloor$  is the mathematical floor function. As it can be seen, the AF

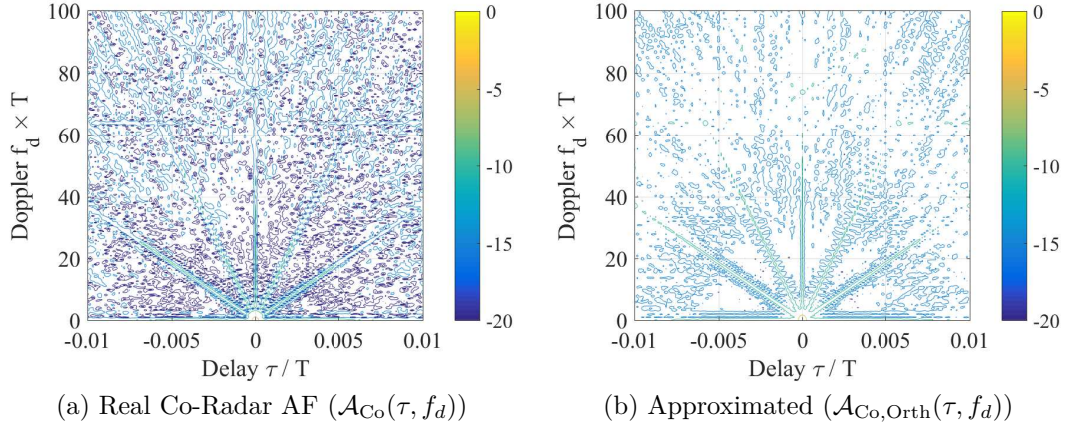


Fig. 5.23 Real ((a)) and approximated ((b)) AF of a Co-Radar waveform generated for  $N_c = 6$ .

in equation (5.26) can be factorized into two terms:

$$\mathcal{A}_{Co,Orth}(\tau, f_d) = \sum_{i=1}^{N_c} \sum_{n=1}^{N_m} (s_i[n] s_i^*[n + \lfloor \tau f_s \rfloor]) e^{j2\pi f_d n / f_s} \quad (5.27)$$

which is the AF assuming that all the sub-carriers are orthogonal and:

$$\mathcal{A}_{Co,Cross}(\tau, f_d) = \sum_{i=1}^{N_c} \sum_{i'=1}^{N_c} \sum_{n=1}^{N_m} ((1 - \delta(i - i')) s_i[n] s_{i'}^*[n + \lfloor \tau f_s \rfloor]) e^{j2\pi f_d n / f_s} \quad (5.28)$$

which is the cross-AF between different sub-carriers. Examining (5.27) it can be seen that it actually expresses the sum of all the the sub-carriers AF. Assuming that  $\mathcal{A}_{Co,Orth}(\tau, f_d) \gg \mathcal{A}_{Co,Cross}(\tau, f_d)$  the total AF of the Co-Radar signal can be approximated as  $\mathcal{A}_{Co}(\tau, f_d) \approx \mathcal{A}_{Co,Orth}(\tau, f_d)$ . While this approximation might not hold, especially for a large number of sub-carriers  $N_c$  where the overlapping can be more intense, it can still provide a good indication of the AF shape during the design process. In Fig. 5.23 the contour of (a) the real AF  $\mathcal{A}_{Co}$  and (b) its approximation  $\mathcal{A}_{Co,Orth}(\tau, f_d)$  are illustrated respectively for  $N_c = 6$ . As it can be seen the two AFs are quite similar with both of them being composed by 6 ridges crossing the centre of axis (note that the ridge extending in the time axes is whole while the rest 5 are extended in the negative Doppler). Those ridges actually correspond to the AF of each sub-carrier which in essence is a fractional waveform generated by a random information binary code. In Fig. 5.24 similar illustrations are held for the (a) the real and (b) approximated AF for  $N_c = 20$ . In this case it can be seen that for areas close to the centre of the axis the ridges are much

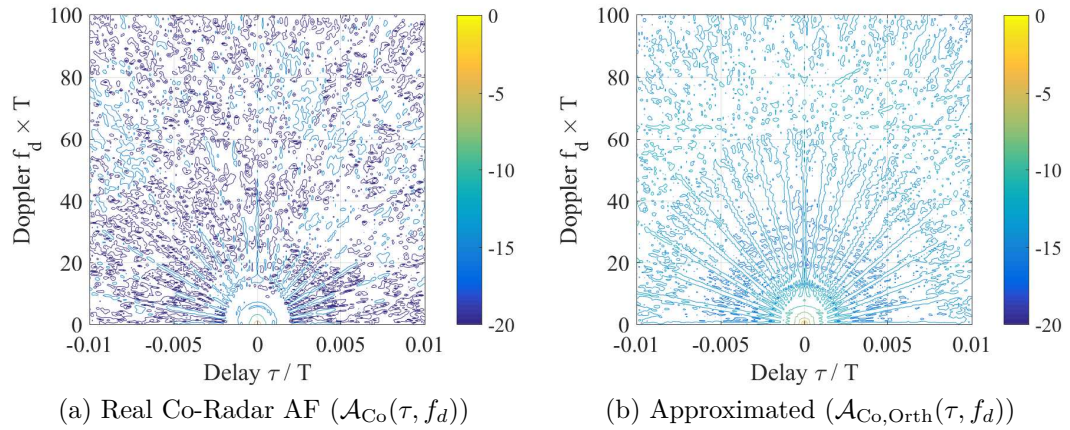


Fig. 5.24 Real ((a)) and approximated ((b)) AF of a Co-Radar waveform generated for  $N_c = 20$ .

less distinguishable in the real AF (Fig. 5.24a) compare to its approximation (Fig. 5.24b). This is caused due to the higher degree and area of overlap that a larger number of sub-carriers introduce.

## 5.4 Summary

In this section a novel waveform library generation scheme based on the fractional Fourier transform (FrFT) was introduced. Moreover an efficient algorithm based on a modified Gerchberg-Saxton algorithm (MGSA) was employed in order to reconstruct the proposed fractional waveform libraries under constant envelope (CE) constraints. Simulation analysis showed the good properties of the waveforms and that high diversity between waveforms in fractional and CE fractional libraries can be achieved. The applicability of the proposed waveforms was also experimentally validated while their performance was evaluated and compared with more conventional techniques in a distributed MIMO radar scenario.

The results highlight the suitability of the proposed design scheme for various radar applications such as co-located and distributed MIMO radar, pulse agile radar and in electronic countermeasures such as low probability of intercept (PLI) radar. Lastly a novel multiplexing scheme based on the FrFT was introduced, allowing information to be embedded into waveforms suitable for radar operations. The performance of the proposed waveform design was evaluated in terms of AF properties.

# Chapter 6

## Generalised MIMO Ambiguity Function

### 6.1 Introduction

In this chapter a novel generalised signal model is presented to accommodate both narrowband and wideband signals in a MIMO sensor system scenario. The derived model is then used to define a MIMO AF based on the KLD. Moreover, the proposed formulation is parametrised by the auto-correlation and cross-correlation matrices of the expected and received with expected signal matrices, and the channel correlation matrices allowing a flexible modelling approach. A comparison between the proposed definition and the more conventional approach of summing the squared matched filter outputs is held for different sensors and waveforms configurations.

### 6.2 Signal Model

Let us consider a MIMO radar system configuration consisting of  $N_{\mathcal{T}}$  transmitters and  $N_{\mathcal{R}}$  receivers, with all their antennas having an isotropic radiation pattern. The location and velocity of the  $i$ -th transmitter and the  $j$ -th receiver are denoted in the Cartesian plane by the column vectors  $\mathbf{x}_{i,\mathcal{T}}$  and  $\mathbf{u}_{i,\mathcal{T}}$  for  $i = 1, \dots, N_{\mathcal{T}}$ , and  $\mathbf{x}_{j,\mathcal{R}}$  and  $\mathbf{u}_{j,\mathcal{R}}$  for  $j = 1, \dots, N_{\mathcal{R}}$  respectively. Moreover, assume an extended target within the surveillance area consisted by a finite number  $N_{\mathcal{Q}}$  of independent isotropic scatterers with location and velocity defined respectively by  $\mathbf{x}_{q,\mathcal{Q}}$  and  $\mathbf{u}_{q,\mathcal{Q}}$  for  $q = 1, \dots, N_{\mathcal{Q}}$ . The reflectivity of the scatterer is modelled by an independent and identically distributed (i.i.d) complex random variable  $\zeta_q$  with zero mean and

variance  $\mathcal{E}\{|\zeta_q|^2\} = \sigma_0^2/N_{\mathcal{Q}}$ , where  $\sigma_0^2$  is the average radar cross section (RCS) of the target. Additionally the target is assumed to follow the classic Swerling I model, while its RCS centre of gravity is located at  $\mathbf{x}_{0,\mathcal{Q}}$  and its velocity is  $\mathbf{v}_{0,\mathcal{Q}}$ .

The propagation of a signal from a transmitter to a receiver consists of three sequential steps: 1) the propagation from a transmitter to the scatterers of the target, 2) the reflection from the scatterers and 3) the propagation from the target to a receiver. Considering a stationary system, the delay of a signal emitted by  $i$ -th transmitter, reflected by the  $q$ -th scatterers and received by  $j$ -th receiver can be written as:

$$\tau_{j,i}^{(q)} = \frac{|\mathbf{D}_{i,\mathcal{T}}^{(q)}| + |\mathbf{D}_{j,\mathcal{R}}^{(q)}|}{c} \quad (6.1)$$

where  $\mathbf{D}_{i,\mathcal{T}}^{(q)} = \mathbf{x}_{q,\mathcal{Q}} - \mathbf{x}_{i,\mathcal{T}}$  and  $\mathbf{D}_{j,\mathcal{R}}^{(q)} = \mathbf{x}_{q,\mathcal{Q}} - \mathbf{x}_{j,\mathcal{R}}$  are the distance vectors from the  $q$ -th scatter of the target to the  $i$ -th transmitter and  $j$ -th receiver respectively, and  $c$  is the speed of light. If the relative motion within the transmitter-target-receiver system is also taken into account, the delay of the signal will vary in time and can be described in a Taylor series  $\tilde{\tau}_{j,i}^{(q)}(t)$  around a certain time reference  $\tau_{j,i}^{(q)}$ :

$$\tilde{\tau}_{j,i}^{(q)}(t) = \tau_{j,i}^{(q)} + (t - \tau_{j,i}^{(q)}) \frac{d}{dt} \tilde{\tau}_{j,i}^{(q)}(\tau_{j,i}^{(q)}) + \frac{(t - \tau_{j,i}^{(q)})^2}{2!} \frac{d^2}{dt^2} \tilde{\tau}_{j,i}^{(q)}(\tau_{j,i}^{(q)}) + \dots \quad (6.2)$$

where  $d^n/dt^n$  denotes the  $n$ -th order derivative with respect to time. Under the assumption that the total range varies slowly with time over the coherent processing interval, the higher order components can be neglected (Tsao et al., 1997) and the delay in (6.2) can be approximated by:

$$\tilde{\tau}_{j,i}^{(q)}(t) \approx \tau_{j,i}^{(q)} + (t - \tau_{j,i}^{(q)}) \frac{d}{dt} \tilde{\tau}_{j,i}^{(q)}(\tau_{j,i}^{(q)}) \quad (6.3)$$

Furthermore, the first-order derivative can be calculated as:

$$\frac{d}{dt} \tilde{\tau}_{j,i}^{(q)}(\tau_{j,i}^{(q)}) = \left( (\mathbf{U}_{i,\mathcal{T}}^{(q)})^T \frac{\mathbf{D}_{i,\mathcal{T}}^{(q)}}{|\mathbf{D}_{i,\mathcal{T}}^{(q)}|} + (\mathbf{U}_{j,\mathcal{R}}^{(q)})^T \frac{\mathbf{D}_{j,\mathcal{R}}^{(q)}}{|\mathbf{D}_{j,\mathcal{R}}^{(q)}|} \right) / c \quad (6.4)$$

where  $\mathbf{U}_{i,\mathcal{T}}^{(q)} = \mathbf{v}_{q,\mathcal{Q}} - \mathbf{v}_{i,\mathcal{T}}$  and  $\mathbf{U}_{j,\mathcal{R}}^{(q)} = \mathbf{v}_{q,\mathcal{Q}} - \mathbf{v}_{j,\mathcal{R}}$  are the relative velocity vectors between the  $q$ -th scatter and the  $i$ -th transmitter and  $j$ -th receiver respectively at the time reference  $\tau_{j,i}^{(q)}$ . For sake of simplification, it is assumed that all the scatters have the same velocity as the gravity centre of the target ,i.e.  $\mathbf{v}_{q,\mathcal{Q}} = \mathbf{v}_{0,\mathcal{Q}}$ , and since  $|\mathbf{x}_{q,\mathcal{Q}} - \mathbf{x}_{0,\mathcal{Q}}| \ll |\mathbf{x}_{0,\mathcal{Q}} - \mathbf{x}_{i,\mathcal{T}}|$  and  $|\mathbf{x}_{q,\mathcal{Q}} - \mathbf{x}_{0,\mathcal{Q}}| \ll |\mathbf{x}_{0,\mathcal{Q}} - \mathbf{x}_{j,\mathcal{R}}|$  the expression

in (6.4) can be simplified as:

$$\frac{d}{dt} \tilde{\tau}_{j,i}^{(q)}(\tau_{j,i}^{(q)}) \approx \frac{d}{dt} \tilde{\tau}_{j,i}(\tau_{j,i}) = \left( (\mathbf{U}_{i,\mathcal{T}})^T \frac{\mathbf{D}_{i,\mathcal{T}}}{|\mathbf{D}_{i,\mathcal{T}}|} + (\mathbf{U}_{j,\mathcal{R}})^T \frac{\mathbf{D}_{j,\mathcal{R}}}{|\mathbf{D}_{j,\mathcal{R}}|} \right) / c \quad (6.5)$$

where  $\mathbf{U}_{i,\mathcal{T}} = \mathbf{v}_{0,\mathcal{Q}} - \mathbf{v}_{i,\mathcal{T}}$  and  $\mathbf{U}_{j,\mathcal{R}} = \mathbf{v}_{0,\mathcal{Q}} - \mathbf{v}_{j,\mathcal{R}}$  are the relative velocity vectors and,  $\mathbf{D}_{i,\mathcal{T}} = \mathbf{x}_{0,\mathcal{Q}} - \mathbf{x}_{i,\mathcal{T}}$  and  $\mathbf{D}_{j,\mathcal{R}} = \mathbf{x}_{0,\mathcal{Q}} - \mathbf{x}_{j,\mathcal{R}}$  are the distance vectors between the centre of gravity of the target and the  $i$ -th transmitter and  $j$ -th receiver respectively at the time reference  $\tau_{j,i} = (|\mathbf{D}_{i,\mathcal{T}}| + |\mathbf{D}_{j,\mathcal{R}}|)/c$ .

Accounting for the two-way radar equation and for unit RCS, the energy propagated from  $i$ -th transmitter,  $q$ -th scatter and  $j$ -th receiver path is calculated as:

$$E_{j,i}^{(q)} = \frac{\hat{E}_{i,\mathcal{T}} G_{i,\mathcal{T}} G_{j,\mathcal{R}} \lambda^2}{(4\pi)^3 |\mathbf{D}_{i,\mathcal{T}}^{(q)}|^2 |\mathbf{D}_{j,\mathcal{R}}^{(q)}|^2 L_{j,i}} \quad (6.6)$$

where  $\hat{E}_{i,\mathcal{T}}$  and  $G_{i,\mathcal{T}}$  are the energy and gain at the  $i$ -th transmitter respectively,  $G_{j,\mathcal{R}}$  is the gain at the  $j$ -th receiver,  $\lambda$  is the wavelength of the carrier, and  $L_{j,i}$  denotes other non free-space losses in the  $i$ -th transmitter  $j$ -th receiver path. Taking the reasonable assumption that the distance between the different scatters and the RCS centre of gravity of the target is significantly smaller than its distance from each transmitter and receiver, the approximation  $|\mathbf{D}_{i,\mathcal{T}}^{(q)}|^2 |\mathbf{D}_{j,\mathcal{R}}^{(q)}|^2 \approx |\mathbf{D}_{i,\mathcal{T}}|^2 |\mathbf{D}_{j,\mathcal{R}}|^2$  can be substituting in (6.6) leading to the following relation:

$$E_{j,i}^{(q)} \approx E_{j,i} = \frac{\hat{E}_{i,\mathcal{T}} G_{i,\mathcal{T}} G_{j,\mathcal{R}} \lambda^2}{(4\pi)^3 |\mathbf{D}_{i,\mathcal{T}}|^2 |\mathbf{D}_{j,\mathcal{R}}|^2 L_{j,i}} \quad (6.7)$$

The received signal at the  $j$ -th receiver due to the  $i$ -th transmitter can be therefore expressed as:

$$\hat{r}_{j,i}(t) = \sqrt{E_{j,i}} \sum_{q=1}^{N_{\mathcal{Q}}} \zeta_q g_i \left( t - \tilde{\tau}_{j,i}^{(q)}(t) \right) + n_j(t) \quad (6.8)$$

where  $g_i(t)$  is the normalised signal,  $\int_{\mathcal{T}} |g_i(t)|^2 dt = 1$ , emitted from the  $i$ -th transmitter, and  $n_j(t)$  is a complex additive Gaussian noise with distribution  $\mathcal{CN}(0, \sigma_n^2)$ , where  $\sigma_n^2$  is the variance of the noise. Additionally, by substituting (6.3) in (6.8) the received signal can be expressed as:

$$\hat{r}_{j,i}(t) = \sqrt{E_{j,i}} \sum_{q=1}^{N_{\mathcal{Q}}} \zeta_q g_i \left( \alpha_{j,i}(t - \tau_{j,i}^{(q)}) \right) + n_j(t) \quad (6.9)$$

where  $\alpha_{j,i}$  is the time scaling factor defined as:

$$\alpha_{j,i} = 1 - \frac{d}{dt} \tilde{\tau}_{j,i}(\tau_{j,i}) \quad (6.10)$$

Moreover, considering the assumption that the percentage bandwidth of  $g_i(t)$  is “reasonably small” (e.g. less than 50% of  $f_c$  (Rihaczek, 1996)), the narrow-band signal expression can be adopted:

$$g_i(t) = s_i(t) e^{j2\pi f_c t} \quad (6.11)$$

where  $s_i(t)$  is the complex envelope of the signal on the  $i$ -th transmitter and  $f_c$  is the carrier frequency. By substituting (6.11) in (6.9) and after removing the carrier the received signal be expressed as:

$$r_{j,i}(t) = \sqrt{E_{j,i}} \sum_{q=1}^{N_Q} \zeta_q e^{\phi_{j,i}^{(q)}} s_i(\alpha_{j,i}(t - \tau_{j,i}^{(q)})) e^{j\omega_{j,i} t} + n_j(t) \quad (6.12)$$

where  $\omega_{j,i} = 2\pi f_c(a_{j,i} - 1)$  and  $\phi_{j,i}^{(q)} = -j2\pi f_c a_{j,i} \tau_{j,i}^{(q)}$  account respectively for the angular frequency and phase shifts applied to the signal due to the relative motion and delay in the  $i$ -th transmitter,  $q$ -th scatter,  $j$ -th receiver system. Assuming that the resolution of the baseband signals  $s_i(t)$  is not high enough to distinguish the individual scatters, i.e.  $s_i(t - \tau_{j,i}^{(q)}) \approx s_i(t - \tau_{j,i})$ , the received signal in (6.12) can be further simplified as:

$$r_{j,i}(t) = \sqrt{E_{j,i}} \sum_{q=1}^{N_Q} \zeta_q e^{\phi_{j,i}^{(q)}} s_i(\alpha_{j,i}(t - \tau_{j,i})) e^{j\omega_{j,i} t} + n_j(t) \quad (6.13)$$

For simplicity, two intermediate variables are introduced:

$$h_{j,i}^{(q)}(\theta) = \sqrt{E_{j,i}} \zeta_q e^{\phi_{j,i}^{(q)}} \quad (6.14)$$

$$y_{j,i}(t, \theta) = s_i(\alpha_{j,i}(t - \tau_{j,i})) e^{j\omega_{j,i} t} \quad (6.15)$$

where  $\theta = [\mathbf{x}_0, \mathbf{v}_0]^T$  and therefore (6.13) can be expressed as:

$$r_{j,i}(t, \theta) = \sum_{q=1}^{N_Q} h_{j,i}^{(q)}(\theta) y_{j,i}(t, \theta) + n_j(t) \quad (6.16)$$

Since the received signal is sampled at the receiver before being processed, it is more practical to define it by using a  $M \times 1$  column vector, where  $M$  is the number

of captured samples. First  $\mathbf{s}_i$  is defined as a  $M \times 1$  column vector composed of the discrete samples of  $s_i(t)$ . Additionally a  $M \times M$  matrix  $\mathbf{a}_{j,i}(\theta)$  is introduced accounting for the time delay, time scaling, and frequency shift experienced by  $s_i$  in the respective transmitter-receiver pair. A complete formulation of  $\mathbf{a}_{j,i}(\theta)$  is given in Appendix B.1. Using the aforementioned notations, the  $M \times 1$  column vector populated by the discrete samples of  $y_{j,i}(t, \theta)$  can be derived as:

$$\mathbf{y}_{j,i}(\theta) = \mathbf{a}_{j,i}(\theta)\mathbf{s}_i \quad (6.17)$$

Additionally, the  $M \times 1$  column vector describing the sampled  $r_{j,i}(t)$  can be expressed as:

$$\mathbf{r}_{j,i}(\theta) = \mathbf{y}_{j,i}(\theta)h_{j,i}(\theta) + \mathbf{n}_j \quad (6.18)$$

where  $\mathbf{n}_j$  is the  $M \times 1$  column vector associated with the  $n_j(t)$ , and  $h_{j,i}(\theta)$  is defined as:

$$h_{j,i}(\theta) = \sum_{q=1}^{N_{\mathcal{Q}}} h_{j,i}^{(q)}(\theta) \quad (6.19)$$

The variable  $h_{j,i}(\theta)$  can also be expressed as:

$$h_{j,i}(\theta) = \sqrt{E_{j,i}} \mathbf{k}_{j,i}(\theta) \mathbf{z} \quad (6.20)$$

where  $\mathbf{k}_{j,i}(\theta)$  is the  $1 \times N_{\mathcal{Q}}$  row vector matrix defined as:

$$\mathbf{k}_{j,i}(\theta) = \left[ e^{\phi_{j,i}^{(1)}}, e^{\phi_{j,i}^{(2)}}, \dots, e^{\phi_{j,i}^{(N_{\mathcal{Q}})}} \right] \quad (6.21)$$

and  $\mathbf{z}$  is the  $N_{\mathcal{Q}} \times 1$  column vector matrix given by:

$$\mathbf{z} = \left[ \zeta_1, \zeta_2, \dots, \zeta_{N_{\mathcal{Q}}} \right]^T \quad (6.22)$$

In examining the total signal at each receiver, we define  $\mathbf{y}_j(\theta)$  as the  $M \times N_{\mathcal{T}}$  matrix given by:

$$\mathbf{y}_j(\theta) = \mathbf{a}_j(\theta)\mathbf{s} \quad (6.23)$$

where  $\mathbf{a}_j(\theta)$  is the  $M \times MN_{\mathcal{T}}$  block matrix defined as:

$$\mathbf{a}_j(\theta) = [\mathbf{a}_{j,1}(\theta), \mathbf{a}_{j,2}(\theta), \dots, \mathbf{a}_{j,N_{\mathcal{T}}}(\theta)] \quad (6.24)$$

and  $\mathbf{s}$  is the  $N_{\mathcal{T}}M \times N_{\mathcal{T}}$  block diagonal matrix given by:

$$\mathbf{s} = \begin{bmatrix} \mathbf{s}_1 & 0 & \cdots & 0 \\ 0 & \mathbf{s}_2 & \cdots & 0 \\ \vdots & \vdots & \ddots & \vdots \\ 0 & 0 & \cdots & \mathbf{s}_{N_{\mathcal{T}}} \end{bmatrix} \quad (6.25)$$

Additionally,  $\mathbf{h}_j(\theta)$  is defined as the  $N_{\mathcal{T}} \times 1$  column vector given by:

$$\mathbf{h}_j(\theta) = \sqrt{\mathbf{E}_j(\theta)} \mathbf{k}_j(\theta) \mathbf{z} \quad (6.26)$$

where  $\mathbf{E}_j(\theta)$  is the  $N_{\mathcal{T}} \times N_{\mathcal{T}}$  diagonal matrix given by:

$$\mathbf{E}_j(\theta) = \begin{bmatrix} E_{1,j} & 0 & \cdots & 0 \\ 0 & E_{2,j} & \cdots & 0 \\ \vdots & \vdots & \ddots & \vdots \\ 0 & 0 & \cdots & E_{N_{\mathcal{T}},j} \end{bmatrix} \quad (6.27)$$

and  $\mathbf{k}_j(\theta)$  is a  $N_{\mathcal{T}} \times N_{\mathcal{Q}}$  matrix given by:

$$\mathbf{k}_j(\theta) = [\mathbf{k}_{j,1}(\theta), \mathbf{k}_{j,2}(\theta), \dots, \mathbf{k}_{j,N_{\mathcal{T}}}(\theta)]^T \quad (6.28)$$

Using (6.23) and (6.26), the  $M \times 1$  column vector of the overall received signal on the  $j$ -th receiver can be expressed as:

$$\mathbf{r}_j(\theta) = \mathbf{y}_j(\theta) \mathbf{h}_j(\theta) + \mathbf{n}_j \quad (6.29)$$

For a total examination of the complete MIMO system,  $\mathbf{Y}(\theta)$  is defined as the  $N_{\mathcal{R}}M \times N_{\mathcal{T}}N_{\mathcal{R}}$  block diagonal matrix given by:

$$\mathbf{Y}(\theta) = \mathbf{A}(\theta) \mathbf{S} \quad (6.30)$$

where  $\mathbf{A}(\theta)$  is the  $N_{\mathcal{R}}M \times MN_{\mathcal{T}}N_{\mathcal{R}}$  block diagonal matrix defined as:

$$\mathbf{A}(\theta) = \begin{bmatrix} \mathbf{a}(\theta, 1) & 0 & \cdots & 0 \\ 0 & \mathbf{a}(\theta, 2) & \cdots & 0 \\ \vdots & \vdots & \ddots & \vdots \\ 0 & 0 & \cdots & \mathbf{a}(\theta, N_{\mathcal{R}}) \end{bmatrix} \quad (6.31)$$

and  $\mathbf{S}$  is the  $N_{\mathcal{R}}N_{\mathcal{T}}M \times N_{\mathcal{T}}N_{\mathcal{R}}$  block diagonal matrix given by:

$$\mathbf{S} = \mathbf{I}_{N_{\mathcal{R}}} \otimes \mathbf{s} = \begin{bmatrix} \mathbf{s} & 0 & \cdots & 0 \\ 0 & \mathbf{s} & \cdots & 0 \\ \vdots & \vdots & \ddots & \vdots \\ 0 & 0 & \cdots & \mathbf{s} \end{bmatrix} \quad (6.32)$$

Moreover the  $N_{\mathcal{R}}N_{\mathcal{T}} \times 1$  block matrix  $\mathbf{H}(\theta)$  is defined as:

$$\mathbf{H}(\theta) = \sqrt{\mathbf{E}(\theta)}\mathbf{K}(\theta)\mathbf{Z} \quad (6.33)$$

where  $\mathbf{K}(\theta)$  is the  $N_{\mathcal{R}}N_{\mathcal{T}} \times N_{\mathcal{Q}}N_{\mathcal{R}}$  block matrix defined as:

$$\mathbf{K}(\theta) = \begin{bmatrix} \mathbf{k}_1(\theta) & 0 & \cdots & 0 \\ 0 & \mathbf{k}_2(\theta) & \cdots & 0 \\ \vdots & \vdots & \ddots & \vdots \\ 0 & 0 & \cdots & \mathbf{k}_{N_{\mathcal{R}}}(\theta) \end{bmatrix} \quad (6.34)$$

and  $\mathbf{Z}$  is the  $N_{\mathcal{R}}N_{\mathcal{Q}} \times 1$  block matrix given by:

$$\mathbf{Z} = \mathbf{1}_{N_{\mathcal{R}}} \otimes \mathbf{z} \quad (6.35)$$

where  $\mathbf{1}_m$  is the  $m \times 1$  column vector of ones. Moreover,  $\mathbf{E}(\theta)$  is the  $N_{\mathcal{R}}N_{\mathcal{T}} \times N_{\mathcal{T}}N_{\mathcal{R}}$  diagonal matrix given by:

$$\mathbf{E}(\theta) = \begin{bmatrix} \mathbf{E}_1(\theta) & 0 & \cdots & 0 \\ 0 & \mathbf{E}_2(\theta) & \cdots & 0 \\ \vdots & \vdots & \ddots & \vdots \\ 0 & 0 & \cdots & \mathbf{E}_{N_{\mathcal{R}}}(\theta) \end{bmatrix} \quad (6.36)$$

The total MIMO system's output can now be defined as the  $N_{\mathcal{R}}M \times 1$  block matrix  $\mathbf{r}(\theta)$  populated by the samples of the discrete signal captured in all receivers given by:

$$\mathbf{r}(\theta) = [\mathbf{r}_1(\theta), \mathbf{r}_2(\theta), \dots, \mathbf{r}_{N_{\mathcal{R}}}(\theta)]^T \quad (6.37)$$

or

$$\mathbf{r}(\theta) = \mathbf{Y}(\theta)\mathbf{H}(\theta) + \mathbf{n} \quad (6.38)$$

where  $\mathbf{n}$  is a  $N_{\mathcal{R}}M \times 1$  block diagonal matrix defined as:

$$\mathbf{n} = [\mathbf{n}_1, \mathbf{n}_2, \dots, \mathbf{n}_{N_{\mathcal{R}}}]^T \quad (6.39)$$

It should be mentioned at this point that no specific assumptions have been made regarding the geometry of the system. In the next section the behaviour of the phase channel matrix  $\mathbf{H}(\theta)$  in different spatial configurations will be discussed.

## 6.3 Channel Correlation

As was shown in the previous section the received signal is composed of its envelope time shift, scaling matrix  $\mathbf{Y}(\theta)$  and the channel matrix  $\mathbf{H}(\theta)$  accounting for phase and amplitude shifts. In this section the covariance matrix of  $\mathbf{H}(\theta)$  will be modelled for arbitrary spatial system configurations. Additionally, the two extremes of co-located and widely distributed cases will be examined separately. The proposed formulation was introduced in (Fishler et al., 2006). In this work, this conceptual framework is extended taking into account the relative velocity between target and sensors.

Following the signal model in Section 6.2, the covariance matrix  $\mathbf{C}(\theta)$  of the channel matrix  $\mathbf{H}(\theta)$  can be calculated as:

$$\begin{aligned} \mathbf{C}(\theta) &= \mathcal{E}\{\mathbf{H}(\theta)\mathbf{H}(\theta)^\dagger\} \\ &= \mathcal{E}\left\{\sqrt{\mathbf{E}(\theta)}\mathbf{K}(\theta)\mathbf{Z}\mathbf{Z}^\dagger\mathbf{K}(\theta)^\dagger\sqrt{\mathbf{E}(\theta)}\right\} \\ &= \sqrt{\mathbf{E}(\theta)}\mathbf{K}(\theta)\mathcal{E}\{\tilde{\mathbf{Z}}\}\mathbf{K}(\theta)^\dagger\sqrt{\mathbf{E}(\theta)} \end{aligned} \quad (6.40)$$

where, under the assumption that the complex reflectivity of the scatters is uncorrelated i.e.  $\mathcal{E}\{\zeta_q^\dagger\zeta_{q'}\} = \delta(q - q')|\zeta_q|^2$ , the  $N_{\mathcal{R}}N_{\mathcal{Q}} \times N_{\mathcal{Q}}N_{\mathcal{R}}$  matrix  $\tilde{\mathbf{Z}} = \mathbf{Z}\mathbf{Z}^\dagger$  is given as:

$$\tilde{\mathbf{Z}} = \mathbf{1}_{N_{\mathcal{R}}} \otimes \begin{bmatrix} |\zeta_1|^2 & 0 & \dots & 0 \\ 0 & |\zeta_2|^2 & \dots & 0 \\ \vdots & \vdots & \ddots & \vdots \\ 0 & 0 & \dots & |\zeta_{N_{\mathcal{Q}}}|^2 \end{bmatrix} \quad (6.41)$$

From (6.40) and (6.41) it can be easily shown that each element of  $\mathbf{C}(\theta)$  could be written as follows:

$$\mathbf{C}(\theta)_{(i,j)(i',j')} = \sqrt{E_{i,j}E_{i',j'}} \sum_{q=1}^{N_Q} |\zeta_q|^2 e^{\phi_{j,i}^{(q)} - \phi_{j',i'}^{(q)}} \quad (6.42)$$

where the subscript index  $(i,j)(i',j')$  imply the element in  $\mathbf{C}(\theta)$  referring to the correlation between the  $i$ -th,  $j$ -th and  $i'$ -th,  $j'$ -th transmitter-receiver channels, or more precisely, the element of which the row and column are given as  $i + N_{\mathcal{T}}(j - 1)$  and  $i' + N_{\mathcal{T}}(j' - 1)$  respectively.

To get a better understanding of how the summation in (6.42) behaves, first let us express the delay  $\tau_{j,i}^{(q)}$  as a function of sensors and scatters coordinates (Fishler et al., 2006):

$$\begin{aligned} \tau_{i,\mathcal{T}}^{(q)} &= \frac{\sqrt{(x_{q,\mathcal{Q}} - x_{i,\mathcal{T}})^2 + (y_{q,\mathcal{Q}} - y_{i,\mathcal{T}})^2}}{c} \\ &= \frac{\sqrt{((x_{0,\mathcal{Q}} + \tilde{x}_{q,\mathcal{Q}}) - x_{i,\mathcal{T}})^2 + ((y_{0,\mathcal{Q}} + \tilde{y}_{q,\mathcal{Q}}) - y_{i,\mathcal{T}})^2}}{c} \\ &\approx \frac{\sqrt{(x_{0,\mathcal{Q}} - x_{i,\mathcal{T}})^2 + 2\tilde{x}_{q,\mathcal{Q}}(x_{0,\mathcal{Q}} - x_{i,\mathcal{T}}) + (y_{0,\mathcal{Q}} - y_{i,\mathcal{T}})^2 + 2\tilde{y}_{q,\mathcal{Q}}(y_{0,\mathcal{Q}} - y_{i,\mathcal{T}})}}{c} \\ &\approx \frac{\sqrt{(x_{0,\mathcal{Q}} - x_{i,\mathcal{T}})^2 + (y_{0,\mathcal{Q}} - y_{i,\mathcal{T}})^2}}{c} + \frac{\tilde{x}_{q,\mathcal{Q}}(x_{0,\mathcal{Q}} - x_{i,\mathcal{T}}) + \tilde{y}_{q,\mathcal{Q}}(y_{0,\mathcal{Q}} - y_{i,\mathcal{T}})}{c\sqrt{(x_{0,\mathcal{Q}} - x_{i,\mathcal{T}})^2 + (y_{0,\mathcal{Q}} - y_{i,\mathcal{T}})^2}} \\ &= \tau_{i,\mathcal{T}} + \frac{\tilde{\mathbf{x}}_{q,\mathcal{Q}}^T \mathbf{D}_{i,\mathcal{T}}}{c|\mathbf{D}_{i,\mathcal{T}}|} \end{aligned} \quad (6.43)$$

where  $\tilde{\mathbf{x}}_{q,\mathcal{Q}} = [\tilde{x}_{q,\mathcal{Q}}, \tilde{y}_{q,\mathcal{Q}}]^T$ , with  $\tilde{x}_{q,\mathcal{Q}} = x_{q,\mathcal{Q}} - x_{0,\mathcal{Q}}$  and  $\tilde{y}_{q,\mathcal{Q}} = y_{q,\mathcal{Q}} - y_{0,\mathcal{Q}}$  being the coordinates of the  $q$ -th scatter when the target's centre of gravity is considered the centre of axes. Following the same process for the delay from the  $q$ -th scatter to the  $j$ -th receiver the total phase can be approximated as:

$$\phi_{j,i}^{(q)} = \phi_{j,i} + \tilde{\phi}_{j,i}^{(q)} \quad (6.44)$$

where  $\phi_{j,i} = -j2\pi f_c \alpha_{j,i} \tau_{j,i}$  and  $\tilde{\phi}_{j,i}^{(q)}$  is given as:

$$\tilde{\phi}_{j,i}^{(q)} = -j2\pi \alpha_{j,i} \left( \tilde{\mathbf{x}}_{q,\mathcal{Q}}^T \left( \frac{\mathbf{D}_{i,\mathcal{T}}}{|\mathbf{D}_{i,\mathcal{T}}|} + \frac{\mathbf{D}_{j,\mathcal{R}}}{|\mathbf{D}_{j,\mathcal{R}}|} \right) \right) / \lambda \quad (6.45)$$

Using (6.44), the summation term in (6.42) can now be approximated as:

$$\sum_{q=1}^{N_Q} |\zeta_q|^2 e^{\phi_{j,i}^{(q)} - \phi_{j',i'}} = e^{\phi_{j,i} - \phi_{j',i'}} \sum_{q=1}^{N_Q} |\zeta_q|^2 e^{\tilde{\phi}_{j,i}^{(q)} - \tilde{\phi}_{j',i'}} \quad (6.46)$$

As discussed in Section 6.2, the target is assumed to be composed of a large number of  $N_Q$  scatters. While the location of each scatter does not have to be directly specified, two conditions must be met. First, two scatters cannot share the same location, i.e.  $\mathbf{x}_{q,Q} \neq \mathbf{x}_{q',Q}$  for  $q \neq q'$ . In addition, assuming a uniform target with symmetry in  $x$  and  $y$  axes, for any scatter  $q$  its distance from the target's centre of gravity along the x-axis and y-axis cannot be larger than the half of the target's dimensions  $\Delta_x$  and  $\Delta_y$  in the respective axis, i.e.  $|\tilde{x}_{q,Q}| \leq \Delta_x/2$  and  $|\tilde{y}_{q,Q}| \leq \Delta_y/2$ . Accounting for these two conditions, it is reasonable describe the reflectivity  $\zeta_q$  by a continuous, spatial function rather than the index  $q$ :

$$\zeta_q = \mathcal{Z}(\tilde{x}_{q,Q}, \tilde{y}_{q,Q}) \quad (6.47)$$

where  $\mathcal{Z}(x, y)$  denotes the reflectivity of the target at the  $x$  and  $y$  point relative to its centre of gravity  $\mathbf{x}_{0,Q}$ . Assuming that the scatters' location in the area occupied by the target is sampled from a uniform distribution, for very large numbers of  $N_Q$  it can be approximated:

$$\mathcal{E} \left\{ |\mathcal{Z}(x, y)|^2 \right\} = \mathcal{E} \left\{ |\zeta_q|^2 \right\}, \quad \forall x \in [-\Delta_x/2, \Delta_x/2], y \in [-\Delta_y/2, \Delta_y/2] \quad (6.48)$$

Moreover since the average RCS  $\sigma_0^2$  of the target is expressed as the summation of the reflectivity from all scatters it can be easily derived that:

$$\int_{-\Delta_x/2}^{\Delta_x/2} \int_{-\Delta_y/2}^{\Delta_y/2} \mathcal{E} \left\{ |\mathcal{Z}(x, y)|^2 \right\} dy dx = \mathcal{E} \left\{ \int_{-\Delta_x/2}^{\Delta_x/2} \int_{-\Delta_y/2}^{\Delta_y/2} |\mathcal{Z}(x, y)|^2 dy dx \right\} = \sigma_0^2 \quad (6.49)$$

From (6.49), the expected reflectivity at any location is given as:

$$\mathcal{E} \left\{ |\mathcal{Z}(x, y)|^2 \right\} = \frac{\sigma_0}{\Delta_x \Delta_y}, \quad \forall x \in [-\Delta_x/2, \Delta_x/2], y \in [-\Delta_y/2, \Delta_y/2] \quad (6.50)$$

Using (6.48) and (6.50), the weighted phases summation in (6.46) can be therefore reformed as:

$$\begin{aligned}
\mathcal{E} \left\{ \sum_{q=1}^{N_Q} |\zeta_q|^2 e^{\tilde{\phi}_{j,i}^{(q)} - \tilde{\phi}_{j',i'}^{(q)}} \right\} &= \int_{-\Delta_x/2}^{\Delta_x/2} \int_{-\Delta_y/2}^{\Delta_y/2} \mathcal{E} \left\{ |\mathcal{Z}(x, y)|^2 \right\} \\
&\quad \times e^{-j2\pi[x, y] \left( \alpha_{j,i} \left( \frac{\mathbf{D}_{i,\mathcal{T}}}{|\mathbf{D}_{i,\mathcal{T}}|} + \frac{\mathbf{D}_{j,\mathcal{R}}}{|\mathbf{D}_{j,\mathcal{R}}|} \right) - \alpha_{j',i'} \left( \frac{\mathbf{D}_{i',\mathcal{T}}}{|\mathbf{D}_{i',\mathcal{T}}|} + \frac{\mathbf{D}_{j',\mathcal{R}}}{|\mathbf{D}_{j',\mathcal{R}}|} \right) \right) / \lambda} dy dx \\
&= \frac{\sigma_0^2}{\Delta_x \Delta_y} \int_{-\Delta_x/2}^{\Delta_x/2} e^{-j2\pi x \left( \alpha_{j,i} \left( \frac{x_i - x_0}{|\mathbf{D}_{i,\mathcal{T}}|} + \frac{x_j - x_0}{|\mathbf{D}_{j,\mathcal{R}}|} \right) - \alpha_{j',i'} \left( \frac{x_{i'} - x_0}{|\mathbf{D}_{i',\mathcal{T}}|} + \frac{x_{j'} - x_0}{|\mathbf{D}_{j',\mathcal{R}}|} \right) \right) / \lambda} dx \\
&\quad \times \int_{-\Delta_y/2}^{\Delta_y/2} e^{-j2\pi y \left( \alpha_{j,i} \left( \frac{y_i - y_0}{|\mathbf{D}_{i,\mathcal{T}}|} + \frac{y_j - y_0}{|\mathbf{D}_{j,\mathcal{R}}|} \right) - \alpha_{j',i'} \left( \frac{y_{i'} - y_0}{|\mathbf{D}_{i',\mathcal{T}}|} + \frac{y_{j'} - y_0}{|\mathbf{D}_{j',\mathcal{R}}|} \right) \right) / \lambda} dy \\
&= \sigma_0^2 \text{sinc} \left( \pi \Delta_x \left( \alpha_{j,i} \left( \frac{x_i - x_0}{|\mathbf{D}_{i,\mathcal{T}}|} + \frac{x_j - x_0}{|\mathbf{D}_{j,\mathcal{R}}|} \right) - \alpha_{j',i'} \left( \frac{x_{i'} - x_0}{|\mathbf{D}_{i',\mathcal{T}}|} + \frac{x_{j'} - x_0}{|\mathbf{D}_{j',\mathcal{R}}|} \right) \right) / \lambda \right) \\
&\quad \times \text{sinc} \left( \pi \Delta_y \left( \alpha_{j,i} \left( \frac{y_i - y_0}{|\mathbf{D}_{i,\mathcal{T}}|} + \frac{y_j - y_0}{|\mathbf{D}_{j,\mathcal{R}}|} \right) - \alpha_{j',i'} \left( \frac{y_{i'} - y_0}{|\mathbf{D}_{i',\mathcal{T}}|} + \frac{y_{j'} - y_0}{|\mathbf{D}_{j',\mathcal{R}}|} \right) \right) / \lambda \right)
\end{aligned} \tag{6.51}$$

The relationship between the integral of complex exponentials and the sinc function is given in Appendix B.2. A more simplified expression of  $\mathbf{C}(\theta)$  can now be given as:

$$\mathbf{C}(\theta) = \sqrt{\mathbf{E}(\theta)} \mathbf{K}_0(\theta) \mathcal{E} \{ \mathbf{\Omega}(\theta) \} \mathbf{K}_0(\theta)^\dagger \sqrt{\mathbf{E}(\theta)} \tag{6.52}$$

Here,  $\mathbf{K}_0(\theta)$  is the  $N_{\mathcal{R}} N_{\mathcal{T}} \times N_{\mathcal{T}} N_{\mathcal{R}}$  diagonal matrix populated by the steering vectors of each transmitter receiver pair:

$$\mathbf{K}_0(\theta) = \begin{bmatrix} e^{\phi_{1,1}} & 0 & \dots & 0 \\ 0 & e^{\phi_{1,2}} & \dots & 0 \\ \vdots & \vdots & \ddots & \vdots \\ 0 & 0 & \dots & e^{\phi_{N_{\mathcal{R}}, N_{\mathcal{T}}}} \end{bmatrix} \tag{6.53}$$

and  $\mathbf{\Omega}(\theta)$  is the  $N_{\mathcal{R}} N_{\mathcal{T}} \times N_{\mathcal{T}} N_{\mathcal{R}}$  channel correlation matrix with each of its element given by (6.51), i.e. :

$$\begin{aligned}
\mathbf{\Omega}(\theta)_{(i,j)(i',j')} &= \\
&\sigma_0^2 \text{sinc} \left( \pi \Delta_x \left( \alpha_{j,i} \left( \frac{x_i - x_0}{|\mathbf{D}_{i,\mathcal{T}}|} + \frac{x_j - x_0}{|\mathbf{D}_{j,\mathcal{R}}|} \right) - \alpha_{j',i'} \left( \frac{x_{i'} - x_0}{|\mathbf{D}_{i',\mathcal{T}}|} + \frac{x_{j'} - x_0}{|\mathbf{D}_{j',\mathcal{R}}|} \right) \right) / \lambda \right) \\
&\quad \times \text{sinc} \left( \pi \Delta_y \left( \alpha_{j,i} \left( \frac{y_i - y_0}{|\mathbf{D}_{i,\mathcal{T}}|} + \frac{y_j - y_0}{|\mathbf{D}_{j,\mathcal{R}}|} \right) - \alpha_{j',i'} \left( \frac{y_{i'} - y_0}{|\mathbf{D}_{i',\mathcal{T}}|} + \frac{y_{j'} - y_0}{|\mathbf{D}_{j',\mathcal{R}}|} \right) \right) / \lambda \right)
\end{aligned} \tag{6.54}$$

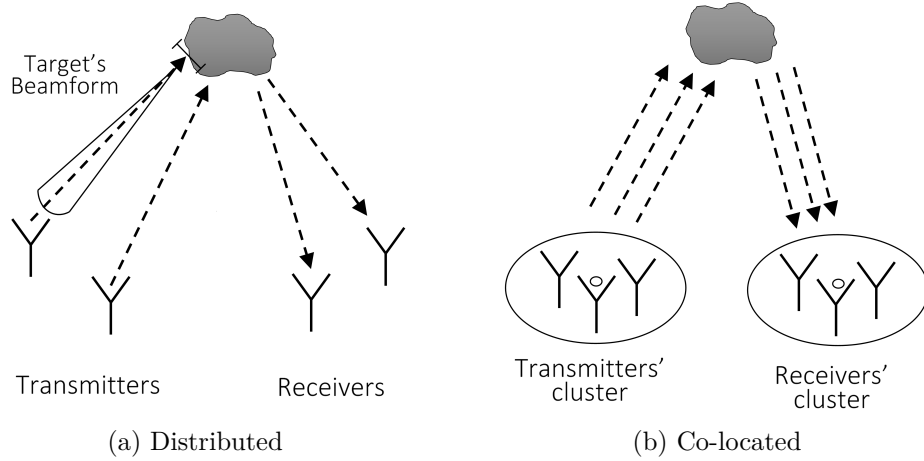


Fig. 6.1 System geometry assuming (a) distributed and (b) co-located sensor allocation.

In the following, two different cases of system geometries, the distributed and co-located, will be examined. A high level illustration of the two systems geometries is illustrated in Figure 6.1.

### 6.3.1 Distributed System

The first spatial configuration considered is the widely distributed case. In this scenario the system's sensors are assumed to be located with a large enough distance between them, so that the beam-width of an antenna the same size as the target to not be able to illuminate two sensors simultaneously (Fishler et al., 2006), see Figure 6.1a. The correlation matrix  $\mathbf{\Omega}(\theta)$  can therefore be approximated by a diagonal matrix indicating that the  $i$ -th,  $j$ -th and  $i'$ -th,  $j'$ -th transmitter-receiver channels are uncorrelated. From (6.51) it can be seen that for the non-diagonal elements of  $\mathbf{\Omega}(\theta)$  to be approximated by 0 at least one of the following conditions must hold:

$$\left| \alpha_{j,i} \left( \frac{x_i - x_0}{|\mathbf{D}_{i,\mathcal{T}}|} + \frac{x_j - x_0}{|\mathbf{D}_{j,\mathcal{R}}|} \right) - \alpha_{j',i'} \left( \frac{x_{i'} - x_0}{|\mathbf{D}_{i',\mathcal{T}}|} + \frac{x_{j'} - x_0}{|\mathbf{D}_{j',\mathcal{R}}|} \right) \right| \geq \frac{\lambda}{\Delta_x} \quad (6.55)$$

$$\left| \alpha_{j,i} \left( \frac{y_i - y_0}{|\mathbf{D}_{i,\mathcal{T}}|} + \frac{y_j - y_0}{|\mathbf{D}_{j,\mathcal{R}}|} \right) - \alpha_{j',i'} \left( \frac{y_{i'} - y_0}{|\mathbf{D}_{i',\mathcal{T}}|} + \frac{y_{j'} - y_0}{|\mathbf{D}_{j',\mathcal{R}}|} \right) \right| \geq \frac{\lambda}{\Delta_y} \quad (6.56)$$

The resulting conditions are similar to those presented in (Haimovich et al., 2008), scaled however by the time scaling factor and more importantly having dependency on targets position. Using (6.55) and (6.56), and assuming a coordinate system with centre of axes the target's centre of gravity and  $\alpha_{j,i} \approx 1$  for all transmitter-

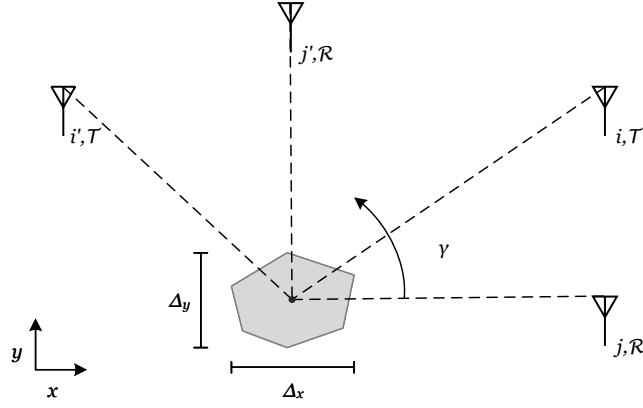


Fig. 6.2 Example of two transmitter-receiver pairs  $(i, j)$  and  $(i', j')$  and a target with dimensions  $\Delta_x$  and  $\Delta_y$ , with each sensor's line of sight (dashed line) having a different angle  $\gamma$  with the positive x-axis

receiver pairs, these conditions can also be expressed as:

$$\left| \cos(\gamma_i) - \cos(\gamma_{i'}) + \cos(\gamma_j) - \cos(\gamma_{j'}) \right| \geq \frac{\lambda}{\Delta_x} \quad (6.57)$$

$$\left| \sin(\gamma_i) - \sin(\gamma_{i'}) + \sin(\gamma_j) - \sin(\gamma_{j'}) \right| \geq \frac{\lambda}{\Delta_y} \quad (6.58)$$

where  $\gamma$  denotes the aspect angle, starting from the positive x-axis, of which the respective node is facing the target. For a better understanding, in Figure 6.2 an illustration of the described geometry is given. As it can be seen from the aforementioned conditions, to assume that a system is widely distributed a prior knowledge of the target's expected position is required.

If one of the conditions in (6.55) and (6.56) or (6.57) and (6.58) are satisfied, the elements of the matrix  $\mathbf{H}(\theta)$  can be assumed uncorrelated and thus its covariance matrix  $\mathbf{C}(\theta)$  can be expressed as:

$$\mathbf{C}(\theta) = \sqrt{\mathbf{E}(\theta)} \mathbf{K}_0(\theta) \mathbf{I}_{N_{\mathcal{R}} N_{\mathcal{T}}} \mathbf{K}_0(\theta)^\dagger \sqrt{\mathbf{E}(\theta)} = \sigma_0^2 \mathbf{E}(\theta) \quad (6.59)$$

Unlike the widely distributed system, the channels of co-located system are fully correlated. This second special case of antenna configuration is discussed in the following paragraphs.

### 6.3.2 Co-Located System

In a co-located configuration, it is assumed that the sensors can be divided into two groups, one composed of transmitter and one of receiver nodes. Furthermore,

sensors in the same group are located in a very close proximity to each other compared to their distance from the target, see Figure 6.1b. The system's sensors can therefore be modelled into two clusters, one composed of the transmitters and one by the receivers with centres of gravity at  $x_{0,\mathcal{T}}$  and  $x_{0,\mathcal{R}}$  respectively. It is therefore reasonable to assume that all the sensors in each cluster experience the same delay to and from the individual scatters of the target. Moreover, it is assumed that all the sensors in each cluster experience similar velocity,  $u_{0,\mathcal{T}}$  for transmitters and  $u_{0,\mathcal{R}}$  for receivers respectively.

Under these assumptions it is valid to approximate the same time scaling factor for all the transmitter-receiver pairs:

$$\alpha_{j,i} \approx \alpha = 1 - \left( (\mathbf{U}_{0,\mathcal{T}})^T \frac{\mathbf{D}_{0,\mathcal{T}}}{|\mathbf{D}_{0,\mathcal{T}}|} + (\mathbf{U}_{0,\mathcal{R}})^T \frac{\mathbf{D}_{0,\mathcal{R}}}{|\mathbf{D}_{0,\mathcal{R}}|} \right) / c \quad (6.60)$$

where  $\mathbf{D}_{0,\mathcal{T}} = \mathbf{x}_{0,\mathcal{Q}} - \mathbf{x}_{0,\mathcal{T}}$  and  $\mathbf{D}_{0,\mathcal{R}} = \mathbf{x}_{0,\mathcal{Q}} - \mathbf{x}_{0,\mathcal{R}}$  are the distance vectors, and  $\mathbf{U}_{0,\mathcal{T}} = \mathbf{u}_{0,\mathcal{Q}} - \mathbf{u}_{0,\mathcal{T}}$  and  $\mathbf{U}_{0,\mathcal{R}} = \mathbf{u}_{0,\mathcal{Q}} - \mathbf{u}_{0,\mathcal{R}}$  are the relative velocity vectors between the target's centre of gravity and the transmitters' and receivers' centre of gravity respectively. Additionally, the total time delay in the  $i$ -th transmitter, target,  $j$ -th receiver path can be expressed as:

$$\tau_{i,j} = \tau_{i,\mathcal{T}} + \tau_{j,\mathcal{R}} \quad (6.61)$$

where  $\tau_{i,\mathcal{T}} = |\mathbf{D}_{0,\mathcal{T}}|/c$  and  $\tau_{j,\mathcal{R}} = |\mathbf{D}_{0,\mathcal{R}}|/c$  are the delays from the transmitter and the receiver to the gravity centre of target respectively. From (6.60) and (6.61) it is derived that the observed phase  $\phi_{j,i}$  can be decomposed as:

$$\phi_{i,j} \approx \phi_{i,\mathcal{T}} + \phi_{j,\mathcal{R}} \quad (6.62)$$

where  $\phi_{i,\mathcal{T}} = 2\pi f_c \alpha \tau_{i,\mathcal{T}}$  and  $\phi_{j,\mathcal{R}} = 2\pi f_c \alpha \tau_{j,\mathcal{R}}$ . Under this approximation it can be seen that  $\mathbf{K}_0(\theta)$  in (6.53) can be also be decomposed as:

$$\mathbf{K}_0(\theta) = \mathbf{K}_{\mathcal{T}}(\theta) \mathbf{K}_{\mathcal{R}}(\theta) \quad (6.63)$$

where  $\mathbf{K}_{\mathcal{T}}(\theta)$  is the  $N_{\mathcal{R}}N_{\mathcal{T}} \times N_{\mathcal{T}}N_{\mathcal{R}}$  diagonal matrix defined as:

$$\mathbf{K}_{\mathcal{T}}(\theta) = \mathbf{I}_{N_{\mathcal{R}}} \otimes \begin{bmatrix} e^{\phi_{1,\mathcal{T}}} & 0 & \dots & 0 \\ 0 & e^{\phi_{1,\mathcal{T}}} & \dots & 0 \\ \vdots & \vdots & \ddots & \vdots \\ 0 & 0 & \dots & e^{\phi_{N_{\mathcal{T}},\mathcal{T}}} \end{bmatrix} \quad (6.64)$$

and  $\mathbf{K}_{\mathcal{R}}(\theta)$  is the  $N_{\mathcal{R}}N_{\mathcal{T}} \times N_{\mathcal{T}}N_{\mathcal{R}}$  diagonal matrix given by:

$$\mathbf{K}_{\mathcal{R}}(\theta) = \begin{bmatrix} e^{\phi_{1,\mathcal{R}}} & 0 & \dots & 0 \\ 0 & e^{\phi_{1,\mathcal{R}}} & \dots & 0 \\ \vdots & \vdots & \ddots & \vdots \\ 0 & 0 & \dots & e^{\phi_{N_{\mathcal{R}},\mathcal{T}}} \end{bmatrix} \otimes \mathbf{I}_{N_{\mathcal{T}}} \quad (6.65)$$

The channel matrix  $\mathbf{H}(\theta)$  in (6.33) can therefore be expressed as:

$$\mathbf{H}(\theta) = \sqrt{\mathbf{E}(\theta)}\mathbf{K}_{\mathcal{T}}(\theta)\mathbf{K}_{\mathcal{R}}(\theta)\mathbf{Z} \quad (6.66)$$

From (6.54) it can be easily derived that if  $\alpha_{j,i} \approx \alpha$  and  $\mathbf{x}_{i,\mathcal{T}} \approx \mathbf{x}_{0,\mathcal{T}}$ , the matrix  $\mathbf{\Omega}(\theta)$  will be populated by ones. As a result the elements of the channel matrix  $\mathbf{H}(\theta)$  are completely correlated.

From (6.42) and (6.51) it follows that to approximate the co-located configuration, all the following conditions should be satisfied:

$$\left| \alpha_{j,i} \left( \frac{x_i - x_0}{|\mathbf{D}_{i,\mathcal{T}}|} + \frac{x_j - x_0}{|\mathbf{D}_{j,\mathcal{R}}|} \right) - \alpha_{j',i'} \left( \frac{x_{i'} - x_0}{|\mathbf{D}_{i',\mathcal{T}}|} + \frac{x_{j'} - x_0}{|\mathbf{D}_{j',\mathcal{R}}|} \right) \right| \ll \frac{\lambda}{\Delta_x} \quad (6.67)$$

$$\left| \alpha_{j,i} \left( \frac{y_i - y_0}{|\mathbf{D}_{i,\mathcal{T}}|} + \frac{y_j - y_0}{|\mathbf{D}_{j,\mathcal{R}}|} \right) - \alpha_{j',i'} \left( \frac{y_{i'} - y_0}{|\mathbf{D}_{i',\mathcal{T}}|} + \frac{y_{j'} - y_0}{|\mathbf{D}_{j',\mathcal{R}}|} \right) \right| \ll \frac{\lambda}{\Delta_y} \quad (6.68)$$

It is obvious that if  $\alpha_{j,i} \approx \alpha$  and  $\mathbf{x}_{i,\mathcal{T}} \approx \mathbf{x}_{0,\mathcal{T}}$ , the left part of the inequalities will always be approximately zero and therefore the co-located system can be considered independent of the position of the target.

## 6.4 MIMO Ambiguity Function Formulation

In this section a definition of the AF based on the Kullback-Leibler divergence (KLD) and the signal model described in Section 6.2 is provided. At this point it should be noted that the notion of using the KLD to describe ambiguity in radar and sonar measurement was originally introduced in (Rendas and Moura, 1998) see (Section 3.3.4) for the mono-static system case. This work is mainly focused on examining how this definition can be applied for a generalised MIMO radar framework.

### Kullback Leibler divergence (KLD)

In Section 6.2, the total received signal  $\mathbf{r}(\theta)$  in (6.38) is described as the summation of products between i.i.d random variables in  $\mathbf{H}(\theta)$  multiplied by the deterministic signals in  $\mathbf{Y}(\theta)$ . For a large number of scatters  $\mathbf{N}_{\mathcal{Q}}$  and according to the central limit theorem, the received signal follows a Gaussian distribution  $\mathbf{r} \sim \mathcal{CN}(0, \mathbf{R}_{\theta})$ . Moreover, the covariance matrix  $\mathbf{R}_{\theta}$  of the received signal can be calculated as:

$$\begin{aligned}
 \mathbf{R}_{\theta} &= \mathcal{E}\{\mathbf{r}(\theta)\mathbf{r}(\theta)^{\dagger}\} \\
 &= \mathcal{E}\{(\mathbf{Y}(\theta)\mathbf{H}(\theta) + \mathbf{n})(\mathbf{Y}(\theta)\mathbf{H}(\theta) + \mathbf{n})^{\dagger}\} \\
 &= \mathbf{Y}(\theta)\mathcal{E}\{\mathbf{H}(\theta)\mathbf{H}(\theta)^{\dagger}\}\mathbf{Y}(\theta)^{\dagger} + \sigma_n^2\mathbf{I}_{MN_{\mathcal{R}}} \\
 &= \mathbf{Y}(\theta)\mathbf{C}(\theta)\mathbf{Y}(\theta)^{\dagger} + \sigma_n^2\mathbf{I}_{MN_{\mathcal{R}}}
 \end{aligned} \tag{6.69}$$

The KLD between two  $MN_{\mathcal{R}}$  sized normal probability measures with zero mean and covariance matrices  $R_{\theta_0}$  and  $R_{\theta}$  is (Rendas and Moura, 1998):

$$\mathcal{I}(\theta_0 : \theta) = \frac{1}{2} \left( \text{tr} \left\{ \mathbf{R}_{\theta}^{-1} \mathbf{R}_{\theta_0} \right\} - MN_{\mathcal{R}} - \ln \left( \det \left\{ \mathbf{R}_{\theta}^{-1} \mathbf{R}_{\theta_0} \right\} \right) \right) \tag{6.70}$$

where  $\mathcal{I}(\theta_0 : \theta) \triangleq \mathcal{I}(p(\mathbf{r}|\theta_0), p(\mathbf{r}|\theta))$ . In this case the two normal probability measures are those described by the return from the target being at the spatial/velocity location  $\theta_0$  and the expected location  $\theta$  respectively. Using (6.69) and applying linear algebra (see Appendix B.3) it can be shown that:

$$\mathbf{R}_{\theta}^{-1} = \frac{1}{\sigma_n^2} \left( \mathbf{I}_{MN_{\mathcal{R}}} - \mathbf{Y}(\theta)\mathbf{C}(\theta)[\mathbf{Y}(\theta)^{\dagger}\mathbf{Y}(\theta)\mathbf{C}(\theta) + \sigma_n^2\mathbf{I}_{N_{\mathcal{T}}N_{\mathcal{R}}}]^{-1}\mathbf{Y}(\theta)^{\dagger} \right) \tag{6.71}$$

$$\det \{\mathbf{R}_{\theta}\} = \det \left\{ \mathbf{Y}(\theta)^{\dagger}\mathbf{Y}(\theta)\mathbf{C}(\theta) + \sigma_n^2\mathbf{I}_{N_{\mathcal{T}}N_{\mathcal{R}}} \right\} \tag{6.72}$$

Using (6.71) and (6.72) the trace and logarithmic determinant terms of the KLD in (6.70) are written as:

$$\begin{aligned}
\text{tr} \{ \mathbf{R}_\theta^{-1} \mathbf{R}_{\theta_0} \} &= \text{tr} \left\{ \frac{1}{\sigma_n^2} \left( \mathbf{I}_{MN_{\mathcal{R}}} - \mathbf{Y}(\theta) \mathbf{C}(\theta) \left[ \mathbf{Y}(\theta)^\dagger \mathbf{Y}(\theta) \mathbf{C}(\theta) + \sigma_n^2 \mathbf{I}_{N_{\mathcal{T}N_{\mathcal{R}}}} \right]^{-1} \mathbf{Y}(\theta)^\dagger \right) \right. \\
&\quad \left. \times \left( \mathbf{Y}(\theta_0) \mathbf{C}(\theta_0) \mathbf{Y}(\theta_0)^\dagger + \sigma_n^2 \mathbf{I}_{MN_{\mathcal{R}}} \right) \right\} \\
&= -\text{tr} \left\{ \mathbf{\Psi}(\theta_0, \theta)^\dagger \frac{\mathbf{C}(\theta_0)}{\sigma_n^2} \mathbf{\Psi}(\theta_0, \theta) \frac{\mathbf{C}(\theta)}{\sigma_n^2} \left[ \mathbf{\Phi}(\theta) \frac{\mathbf{C}(\theta)}{\sigma_n^2} + \mathbf{I}_{N_{\mathcal{T}N_{\mathcal{R}}}} \right]^{-1} \right\} \\
&\quad + \text{tr} \left\{ \mathbf{\Phi}(\theta_0) \frac{\mathbf{C}(\theta_0)}{\sigma_n^2} \right\} + MN_{\mathcal{R}} \\
&\quad - \text{tr} \left\{ \mathbf{\Phi}(\theta) \frac{\mathbf{C}(\theta)}{\sigma_n^2} \left[ \mathbf{\Phi}(\theta) \frac{\mathbf{C}(\theta)}{\sigma_n^2} + \mathbf{I}_{N_{\mathcal{T}N_{\mathcal{R}}}} \right]^{-1} \right\} \tag{6.73}
\end{aligned}$$

$$\begin{aligned}
\ln(\det[\mathbf{R}_\theta^{-1} \mathbf{R}_{\theta_0}]) &= \ln \left( \sigma_n^{-2MN_{\mathcal{R}}} \det \left\{ \mathbf{Y}(\theta)^\dagger \mathbf{Y}(\theta) \frac{\mathbf{C}(\theta)}{\sigma_n^2} + \mathbf{I}_{N_{\mathcal{T}N_{\mathcal{R}}}} \right\}^{-1} \right. \\
&\quad \left. \times \sigma_n^{2MN_{\mathcal{R}}} \det \left\{ \mathbf{Y}(\theta_0)^\dagger \mathbf{Y}(\theta_0) \frac{\mathbf{C}(\theta_0)}{\sigma_n^2} + \mathbf{I}_{N_{\mathcal{T}N_{\mathcal{R}}}} \right\} \right) \\
&= -\ln \left( \det \left\{ \mathbf{\Phi}(\theta) \frac{\mathbf{C}(\theta)}{\sigma_n^2} + \mathbf{I}_{N_{\mathcal{T}N_{\mathcal{R}}}} \right\} \right) \\
&\quad + \ln \left( \det \left\{ \mathbf{\Phi}(\theta_0) \frac{\mathbf{C}(\theta_0)}{\sigma_n^2} + \mathbf{I}_{N_{\mathcal{T}N_{\mathcal{R}}}} \right\} \right) \tag{6.74}
\end{aligned}$$

Here, for simplicity and better understanding the waveform correlation matrices are defined as:

$$\mathbf{\Phi}(\theta) = \mathbf{Y}(\theta)^\dagger \mathbf{Y}(\theta) \tag{6.75}$$

$$\mathbf{\Psi}(\theta_1, \theta_2) = \mathbf{Y}(\theta_1)^\dagger \mathbf{Y}(\theta_2) \tag{6.76}$$

Finally, the KLD between the two probability measures can be rewritten as:

$$\begin{aligned}
\mathcal{I}(\theta_0 : \theta) = & \frac{1}{2} \left( - \operatorname{tr} \left\{ \mathbf{\Psi}(\theta_0, \theta)^\dagger \frac{\mathbf{C}(\theta_0)}{\sigma_n^2} \mathbf{\Psi}(\theta_0, \theta) \frac{\mathbf{C}(\theta)}{\sigma_n^2} [\mathbf{\Phi}(\theta) \frac{\mathbf{C}(\theta)}{\sigma_n^2} + \mathbf{I}_{N_{\mathcal{T}}N_{\mathcal{R}}}]^{-1} \right\} \right. \\
& + \operatorname{tr} \left\{ \mathbf{\Phi}(\theta_0) \frac{\mathbf{C}(\theta_0)}{\sigma_n^2} \right\} - \operatorname{tr} \left\{ \mathbf{\Phi}(\theta) \frac{\mathbf{C}(\theta)}{\sigma_n^2} [\mathbf{\Phi}(\theta) \frac{\mathbf{C}(\theta)}{\sigma_n^2} + \mathbf{I}_{N_{\mathcal{T}}N_{\mathcal{R}}}]^{-1} \right\} \\
& + \ln \left( \det \left\{ \mathbf{\Phi}(\theta) \frac{\mathbf{C}(\theta)}{\sigma_n^2} + \mathbf{I}_{N_{\mathcal{T}}N_{\mathcal{R}}} \right\} \right) \\
& \left. - \ln \left( \det \left\{ \mathbf{\Phi}(\theta_0) \frac{\mathbf{C}(\theta_0)}{\sigma_n^2} + \mathbf{I}_{N_{\mathcal{T}}N_{\mathcal{R}}} \right\} \right) \right) \quad (6.77)
\end{aligned}$$

which is derived by substituting (6.73) and (6.74) in (6.70). Note the KLD is expressed in terms of auto-correlation, cross-correlation and channel covariance matrices.

### MIMO Ambiguity Function

Applying a similar analysis to the one presented in (Rendas and Moura, 1998) for a single-input single-output system (SISO), and taking into consideration that it is desired for the AF to take values between 0 and 1, the MIMO AF is defined as:

$$\mathcal{A}_{\text{MIMO}}(\theta_0, \theta) \triangleq 1 - \frac{\mathcal{I}(\theta_0 : \theta)}{\mathcal{I}_{\text{ub}}(\theta_0)} \quad (6.78)$$

where  $\mathcal{I}_{\text{ub}}(\theta_0)$  is the upper-bound of  $\mathcal{I}(\theta_0 : \theta)$ . Examining the different terms in (6.77) it can be easily shown that all the traces and logarithms will return positive values. Moreover, to maximise  $\mathcal{I}(\theta_0 : \theta)$ , the upper bound of each term can be examined separately and then combined altogether. It is worth noting that since the terms in (6.77) are not independent, treating them separately will not provide a tight upper bound, i.e.  $\mathcal{I}_{\text{ub}}(\theta_0) \geq \max_{\theta} \mathcal{I}(\theta_0 : \theta)$ , but a more relaxed limit.

Considering the first term in (6.77) and assuming that there is at least one  $\theta$  for which  $\mathbf{Y}(\theta)^\dagger \mathbf{Y}(\theta_0) = 0$ , it can be shown that the maximum value of this term is also zero. This can occur, for example, if the difference between the tested and actual Doppler shift is large enough so that the  $Y(\theta)$  and  $Y(\theta_0)$  do not overlap in the frequency domain. Furthermore, by using the eigenvalue decomposition of the matrix product  $\mathbf{\Phi}(\theta)\mathbf{C}(\theta)$  (see Appendix B.4) the maximum value of the third

term in (6.77) is calculated from the following relation:

$$-\operatorname{tr} \left\{ \frac{\mathbf{\Phi}(\theta)\mathbf{C}(\theta)/\sigma_n^2}{\mathbf{\Phi}(\theta)\mathbf{C}(\theta)/\sigma_n^2 + \mathbf{I}_{N_{\mathcal{T}}N_{\mathcal{R}}}} \right\} \leq -\frac{\operatorname{SNR}_{\theta}}{\operatorname{SNR}_{\theta} + 1} \quad (6.79)$$

where  $\operatorname{SNR}_{\theta} = \operatorname{tr} \{ \mathbf{\Phi}(\theta)\mathbf{C}(\theta) \} / \sigma_n^2$  denotes the total *expected* signal-to-noise ratio in the resolution bin  $\theta$ . Here the term *expected* is used as the  $\operatorname{SNR}_{\theta}$  is calculated using the auto-correlation matrix of  $\mathbf{Y}(\theta)$  and not its cross correlation with  $\mathbf{Y}(\theta_0)$ . Using the same procedure (see Appendix B.4), the maximum value of the fourth and fifth terms in (6.77) can be written as:

$$\ln \left( \det \left\{ \mathbf{\Phi}(\theta)\mathbf{C}(\theta)/\sigma_n^2 + \mathbf{I}_{N_{\mathcal{T}}N_{\mathcal{R}}} \right\} \right) \leq \operatorname{SNR}_{\theta} \quad (6.80)$$

$$-\ln \left( \det \left\{ \mathbf{\Phi}(\theta_0)\mathbf{C}(\theta_0)/\sigma_n^2 + \mathbf{I}_{N_{\mathcal{T}}N_{\mathcal{R}}} \right\} \right) \leq 0 \quad (6.81)$$

Using (6.79), (6.80) and (6.81) the upper bound of the KLD in (6.77) can be calculated as:

$$\mathcal{I}_{\text{ub}}(\theta_0) = \frac{1}{2} \left( \operatorname{SNR}_{\theta_0} + \max_{\theta} \left( \operatorname{SNR}_{\theta}^2 / (\operatorname{SNR}_{\theta} + 1) \right) \right) \quad (6.82)$$

Inspecting (6.82) it is observed that the KLD can get its maximum value at the resolution bin  $\theta$ , in which the  $\operatorname{SNR}_{\theta}$  is also maximum. This is expected as the ability to discriminate between the true and the approximated PDFs  $p(\mathbf{r}|\theta_0)$  and  $p(\mathbf{r}|\theta)$  will be better for  $\theta$  in which the SNR is higher. A closer examination reveals that the term  $\operatorname{SNR}_{\theta}$  can be expressed as:

$$\operatorname{SNR}_{\theta} = \sum_{j,j'}^{N_{\mathcal{R}}} \sum_{i,i'}^{N_{\mathcal{T}}} \operatorname{Re} \left\{ \mathbf{\Phi}(\theta)_{(i,j)(i',j')} \mathbf{C}(\theta)_{(i,j)(i',j')} \right\} \quad (6.83)$$

were the double index in the summations indicates the unique pairs i.e.  $\sum_{m,m'}[\cdot] = \sum_m \sum_{m'=1}^m[\cdot]$ . It can be therefore deduced that the defined  $\operatorname{SNR}_{\theta}$  value is highly dependent on the geometry of the system through the channel correlation matrix  $\mathbf{C}(\theta)$ , and the design of the operating waveforms through the waveform correlation matrix  $\mathbf{\Phi}(\theta)$ . For example waveforms for which the cross-correlation has a negative real part assuming that the target is located  $\theta$ , will have lower  $\operatorname{SNR}_{\theta}$  in cases of positive channel correlation than if the channels were uncorrelated.

Having defined an upper bound it can be ensured that  $\mathcal{A}_{\text{MIMO}}(\theta_0, \theta) \geq 0, \forall \theta$ . From (3.21) it can be shown that:

$$\mathcal{I}(\theta_0 : \theta) \geq 0 \quad \forall \theta_0, \theta \quad (6.84)$$

The equality in (6.84) holds for  $\theta = \theta_0 \rightarrow \mathcal{I}(\theta_0 : \theta) = 0$  and therefore from (6.78)  $\mathcal{A}_{\text{MIMO}} \leq 1$ .

## 6.5 Reduction to Woodward AF

In this section it is demonstrated that the proposed MIMO AF could be reduced to the canonical AF if a more simplified and closer to the canonical signal model is considered. First let us assume a co-located monostatic system with a point-modelled target located at the resolution bin  $\theta_0$ . Additionally let us assume a narrowband signal model, where the SNR remains constant across resolution bins. The KLD in (6.77) can be expressed as:

$$\mathcal{I}(\theta_0 : \theta) = \frac{\text{SNR}^2}{2(\text{SNR} + 1)} \left( 1 - \frac{1}{\Phi} |y(\theta_0)^\dagger y(\theta)|^2 \right) \quad (6.85)$$

where  $\Phi = |y(\theta)^\dagger y(\theta)| = |s|^2$  and  $\text{SNR} = \Phi \varepsilon / \sigma_n^2$ , with  $\varepsilon$  being the power parameter. Since the negative signed parameter in (6.85) can only take positive values, the upper bound can be extracted as:

$$\mathcal{I}_{\text{ub}}(\theta_0) = \frac{\text{SNR}^2}{2(\text{SNR} + 1)} \quad (6.86)$$

Under the assumption that the signal is also normalised i.e.  $|s|^2 = 1$ , the AF can be derived as:

$$\mathcal{A}(\theta_0, \theta) = |y(\theta_0)^\dagger y(\theta)|^2 \quad (6.87)$$

Equation (6.87) shows that the proposed MIMO AF reduced to the Woodward's AF for the same signal model.

## 6.6 Example and Illustrations

In this section a number of MIMO radar system configurations will be examined to illustrate the behaviour of the proposed MIMO AF. To offer a broader understanding and keep the results generalised all the spatial values, values of speed,

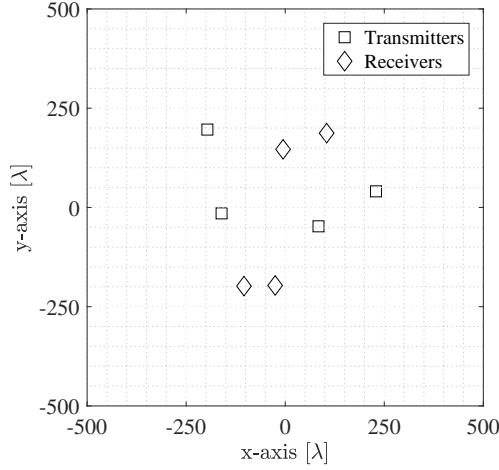


Fig. 6.3 Sensors geometry in the surveillance area

and bandwidths will be expressed as factors of the carrier wavelengths  $\lambda$ , carrier speed  $c$ , and as factor of the carrier frequency  $f_c$  respectively.

In Figure 6.3 the geometry of the sensors that will be used in this section is presented. We define a  $(10^3 \times 10^3)\lambda^2$  surveillance area with the position of the sensors being chosen randomly in a  $(500 \times 500)\lambda^2$  area centred at the centre of the scene. Moreover, the velocities of the sensors are considered 0 in both axes i.e.  $\mathbf{u}_{i,\mathcal{T}} = [0, 0]^T, i = 1, \dots, N_{\mathcal{T}}$  and  $\mathbf{u}_{j,\mathcal{R}} = [0, 0]^T, i = 1, \dots, N_{\mathcal{R}}$ . In the following, this system will be examined for different configurations.

### 6.6.1 Normalised Channel Correlation Matrix

In Section 6.3 a formulation of the covariance matrix was presented. To better illustrate how the channel correlation matrix varies through the different resolution bins, in Fig. 6.4a the normalised summation of the absolute value of non-diagonal elements in  $\mathbf{\Omega}(\theta)$  is illustrated for a target with dimensions  $\Delta_x = \Delta_y = \lambda$ . This quantity denotes the degree of correlation that the channels will have if the target is positioned at the resolution bin  $\theta$ . Namely, the value for each resolution bin  $\theta$  is calculated as:

$$\hat{\Omega}(\theta) = \frac{\sum_j^{N_{\mathcal{R}}} \sum_i^{N_{\mathcal{T}}} \sum_{j'}^{N_{\mathcal{R}}} \sum_{i'}^{N_{\mathcal{T}}} (1 - \delta(i - i')\delta(j - j')) |\mathbf{\Omega}(\theta)_{(j,i)(j',i')}|}{N_{\mathcal{R}}N_{\mathcal{T}}(N_{\mathcal{R}}N_{\mathcal{T}} - 1)} \quad (6.88)$$

From (6.88) it can be seen that for values of  $\hat{\Omega}(\theta)$  close to 1 the system can be considered fully co-located while for values close to 0 the system can be considered widely distributed. As it can be seen areas closer to the centre of the scene where the target is surrounded by sensors from many directions are characterised by

higher decorrelation between the channels. On the other hand, in more distant areas the system can be categorised as co-located as the sensors are facing the target from similar aspect angles. The same illustration for a target of dimensions  $\Delta_x = 1/2\lambda$  and  $\Delta_y = 2\lambda$  is presented in Fig. 6.4b. As it can be seen, the area in which the channels are considered uncorrelated has been stretched parallel to the  $x$ -axis and squashed parallel to the  $y$ -axis due to the different shape of the target.

### 6.6.2 Disrtributed and Co-located System Performance

In this section the performance of the system will be assessed for different target placement and different operating waveforms. In all examples we consider a constant energy parameter for all resolution bins i.e  $\sqrt{\mathbf{E}(\theta)} = \mathbf{I}_{N_R N_T}$ .

#### Orthogonal waveforms

First let us consider a library of four orthogonal waveforms operating at each transmitter. The sequences used in the system are orthogonal frequency division multiplexed linear frequency modulated (OFDM-LFM) waveforms described as:

$$s_i(t) = e^{j\pi B(\frac{1}{T}t+i-1)t} \quad (6.89)$$

where  $T$  and  $B$  are the corresponding period and the bandwidth of the signal. All the variables of the system are summarised on Table 6.1. In Fig. 6.5 the proposed MIMO AF is illustrated in logarithmic scale for a target with velocity

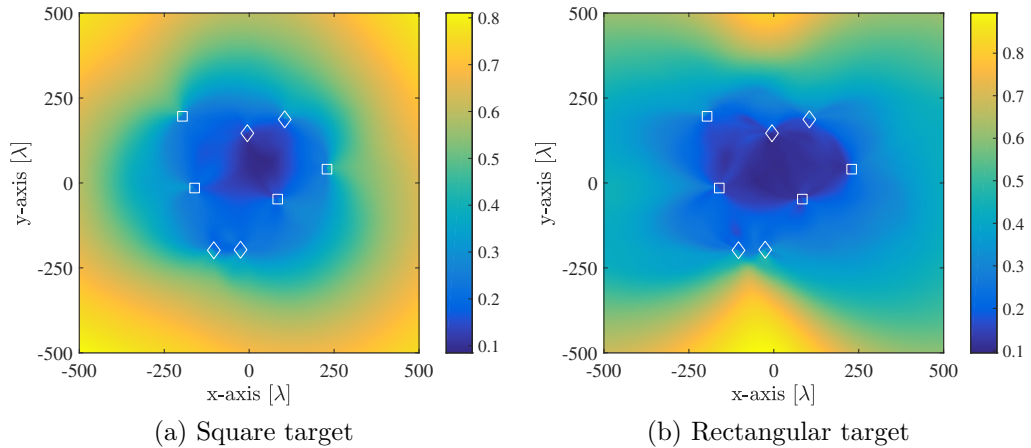


Fig. 6.4 Normalized sum of non diagonal elements of the channel correlation matrix  $\mathbf{\Omega}$  for target dimensions (a)  $\Delta_x = \Delta_y = \lambda$  and (b)  $\Delta_x = 1/2\lambda$  and  $\Delta_y = 2\lambda$ ; transmitters and receivers are denoted by squares ( $\square$ ) and rhombi ( $\diamond$ ) respectively.

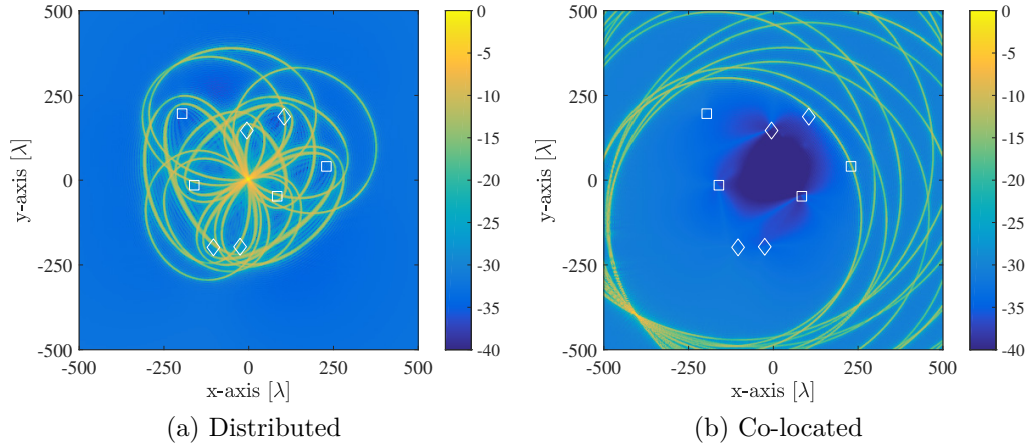


Fig. 6.5 MIMO AF when the target's centre of gravity is positioned in (a)  $\mathbf{x}_{0,\mathcal{Q}} = [0, 0]^T$  and (b)  $\mathbf{x}_{0,\mathcal{Q}} = [-400, -400]^T$ , and orthogonal waveforms and constant energy parameter is considered; transmitters and receivers are denoted by squares ( $\square$ ) and rhombi ( $\diamond$ ) respectively.

$\mathbf{u}_{0,\mathcal{Q}} = [0, 0]^T$  and centre of gravity is positioned at (a)  $\mathbf{x}_{0,\mathcal{Q}} = [0, 0]^T$  and (b)  $\mathbf{x}_{0,\mathcal{Q}} = [-400\lambda, -400\lambda]^T$ .

Consulting Fig. 6.4 it can be seen that in the first target placement the system is closer to the widely distributed geometry while in the second case is modeled better by the co-located. In Fig. 6.6 a zoomed version of the MIMO AF for these

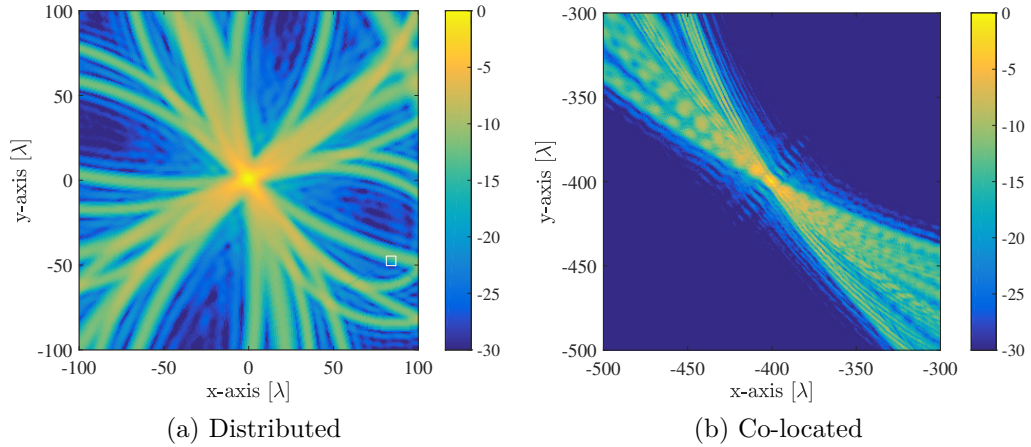


Fig. 6.6 Zoomed part of the MIMO AF when the target's centre of gravity is positioned in (a)  $\mathbf{x}_{0,\mathcal{Q}} = [0, 0]^T$  and (b)  $\mathbf{x}_{0,\mathcal{Q}} = [-400, -400]^T$ , and orthogonal waveforms and constant energy parameter is considered.

two case is illustrated for regions close to the target's position. In both cases, the MIMO AF is populated by 16 ellipsoid shaped ridges corresponding to each bistatic transmitter-target-receiver system, all of which intersect at the target's

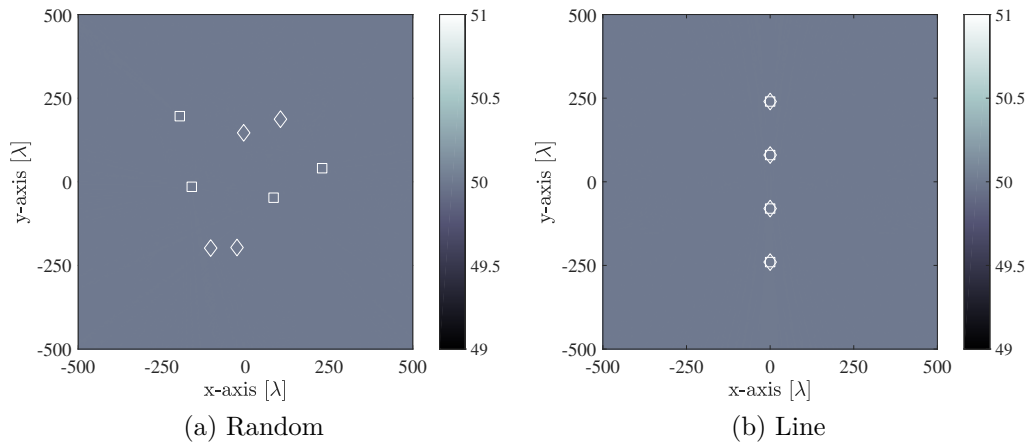


Fig. 6.7 Values of  $\text{SNR}_\theta$  in (a) random and (b) line sensor configuration, when orthogonal waveforms and constant energy parameter are considered; transmitters and receivers are denoted by squares ( $\square$ ) and rhombi ( $\diamond$ ) respectively.

location. On closer inspection it can be seen that in the distributed case these ridges are added incoherently to form a “smooth” representation with peak at the position of the target. In contrast, in the co-located case fluctuations are present due to the way the ridges from different correlated channels are added with each other. The ridges can be added constructively or destructively depending on the ridges being in-phase or off-phase and the correlation of the different channels being negative or positive. The values of  $\text{SNR}_\theta$  for this scenario are illustrated in Fig. 6.7a. As it can be seen, the  $\text{SNR}_\theta$  remains constant in the entire area. This is expected as from (6.83) it can be seen that for orthogonal waveforms the sum will always be the total energy of the signals multiplied by the ratio  $N_R N_T \sigma_0^2 / \sigma_n^2$ . To confirm that changing the system’s geometry will not impact the values of  $\text{SNR}_\theta$ , a different configuration is illustrated in 6.7b. Here, the sensors are placed in a horizontal line with the a transmitter and receiver being placed together at each point. As it can be seen, the  $\text{SNR}_\theta$  remains constant in all the examined area for both configurations.

### Correlated Waveforms

In the second example the same system variables summarised in Table 6.1 will be assumed. In contrast to the previous section, here we assume that the transmitters are using fully correlated waveforms given by:

$$s_i(t) = e^{j\pi \frac{B}{T} t^2}, i = 1, \dots, 4 \quad (6.90)$$

Table 6.1 Theoretical MIMO System Variables

Description	Variable	Value
Signal Bandwidth	$B$	$0.1f_c$
Signal Period	$T$	$10^3/B$
Target x-axis dimension	$\Delta_x$	$\lambda$
Target y-axis dimension	$\Delta_y$	$\lambda$
Target RCS variance	$\sigma_0^2$	1
Noise variance	$\sigma_n^2$	$16 \times 10^{-5}$

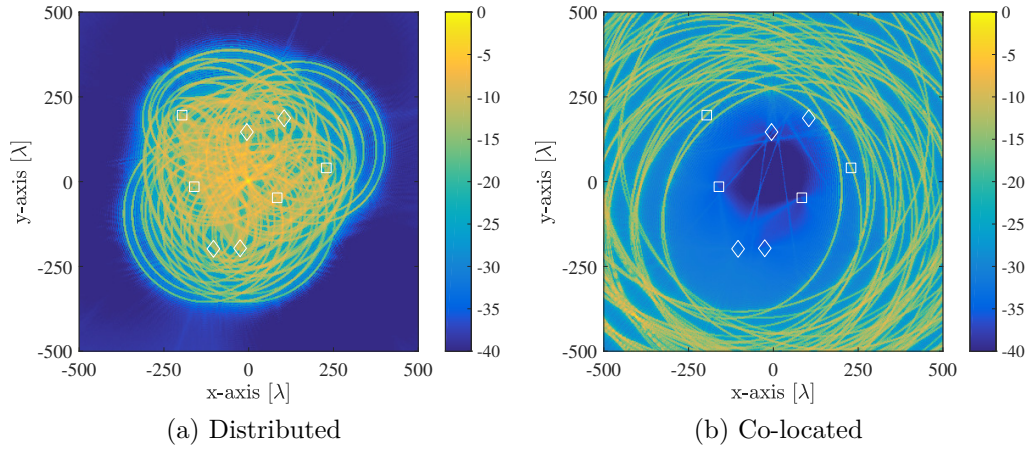


Fig. 6.8 MIMO AF when the target's centre of gravity is positioned in (a)  $\mathbf{x}_{0,\mathcal{Q}} = [0, 0]^T$  and (b)  $\mathbf{x}_{0,\mathcal{Q}} = [-400, -400]^T$ , and fully correlated waveforms and constant energy parameter is considered; transmitters and receivers are denoted by squares ( $\square$ ) and rhombi ( $\diamond$ ) respectively.

In Fig. 6.8 the MIMO AF of the system is illustrated for the two different positions of the target. Additionally, Fig. 6.9 provides a zoomed version of the MIMO AF for areas close to the target. Examining both figures it can be seen that in for highly correlated waveforms the number of ellipsoid ridges populating the MIMO AF is higher than when low cross-correlation waveforms are used. In fact 64 ridges are formed as the different transmitters cannot be decorrelated at the receivers. A direct consequence of that is that the extra ridges will not fall on the target's resolution bin if the resolution of the baseband signal  $s_i$ , as determined by its bandwidth, is high enough. The impact of this phenomenon is more apparent in the distributed case and becomes less apparent as the system approaches the fully co-located case, where all the ridges will eventually overlap.

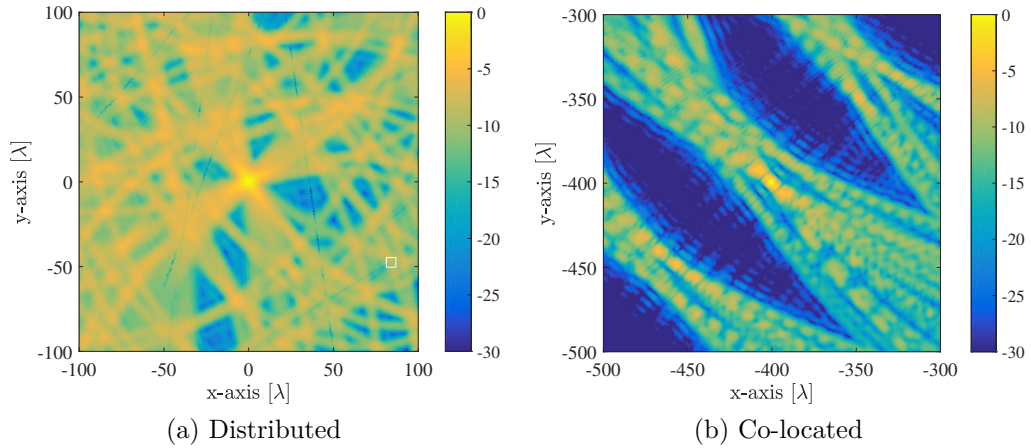


Fig. 6.9 Zoomed part of the MIMO AF when the target's centre of gravity is positioned in (a)  $\mathbf{x}_{0,\mathcal{Q}} = [0, 0]^T$  and (b)  $\mathbf{x}_{0,\mathcal{Q}} = [-400, -400]^T$ , and fully correlated waveforms and constant energy parameter is considered.

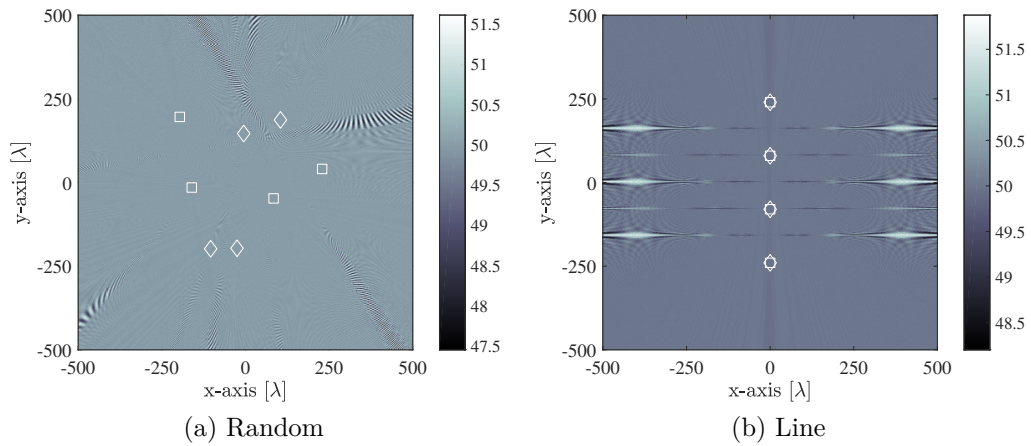


Fig. 6.10 Values of  $\text{SNR}_\theta$  in (a) random and (b) line sensor configuration, when fully correlated waveforms and constant energy parameter are considered; transmitters and receivers are denoted by squares ( $\square$ ) and rhombi ( $\diamond$ ) respectively.

Moreover in Figure 6.10 the values of  $\text{SNR}_\theta$  are illustrated across the surveillance area. By comparing the results with the ones in Figure 6.7 it can be seen that when the waveforms are non orthogonal fluctuations in the  $\text{SNR}_\theta$  occur. From (6.83) it can be seen that those fluctuations depend on the correlation between the channels and the degree of correlation that the waveforms will have at each resolution bin  $\theta$ . Comparing the random and line sensor configuration in 6.10a and 6.10b respectively it can be easily seen that by manipulating the system geometry it is possible to increase the  $\text{SNR}_\theta$  in areas of interest.

## 6.7 Simulations and Comparison

In this section the performance of the proposed AF will be examined in a simulated MIMO radar scenario. It should be noted that the main difference compared to the analysis presented in Section 6.6, is that here the received signal is extracted by simulating the returns of an extended target and not by using the mathematical model of the covariance matrix  $\mathbf{R}_{\theta_0}$  presented in (6.69). The impact of estimating the covariance matrices and required modifications are needed to be made on proposed MIMO AF will be discussed in the following paragraphs.

### 6.7.1 Modified AF

One of the main matters in applying the proposed AF definition using the KLD in (6.77) for simulated or real data, is that the received signal  $\mathbf{r}_0$  cannot be decomposed into its individual terms. As a result, the formulation in (6.77) has to be modified to accommodate the processing on the entire received signal  $\mathbf{r}_0$  and not each individual factor i.e.  $\mathbf{Y}(\theta_0)$ ,  $\mathbf{C}(\theta_0)$ , and  $\sigma_n$ . The trace and logarithmic terms of the KDL in (6.70) for a received signal  $\mathbf{r}_0$  with covariance matrix  $\mathbf{R}_0 = \mathbf{r}_0 \mathbf{r}_0^\dagger$  are derived as follows:

$$\text{tr} \left\{ \mathbf{R}_\theta^{-1} \mathbf{R}_0 \right\} = \frac{1}{\sigma_n^2} \mathbf{r}_0^\dagger \mathbf{r}_0 - \hat{\Psi}(\theta) \frac{\mathbf{C}(\theta)}{\sigma_n^2} \left[ \Phi(\theta) \frac{\mathbf{C}(\theta)}{\sigma_n^2} + \mathbf{I}_{N_{\mathcal{T}} N_{\mathcal{R}}} \right]^{-1} \hat{\Psi}(\theta)^\dagger \quad (6.91)$$

$$\begin{aligned} \ln |\mathbf{R}_\theta^{-1} \mathbf{R}_0| &= -2MN_{\mathcal{R}} \ln(\sigma_n^2) - \ln \left( \det \left\{ \Phi(\theta) \frac{\mathbf{C}(\theta)}{\sigma_n^2} + \mathbf{I}_{N_{\mathcal{T}} N_{\mathcal{R}}} \right\} \right) \\ &\quad + \ln \left( \det \left\{ \mathbf{r}_0 \mathbf{r}_0^\dagger \right\} \right) \end{aligned} \quad (6.92)$$

where  $\hat{\Psi}(\theta)$  is the  $1 \times N_{\mathcal{R}} N_{\mathcal{T}}$  row vector populated by the output of the received signal matched filtered for each transmitter-receiver pair i.e.:

$$\hat{\Psi}(\theta) = \mathbf{r}_0^\dagger \mathbf{Y}(\theta) \quad (6.93)$$

Due to the high computational cost, the logarithmic terms in (6.92) will not be taken into account in the MIMO AF computation. Therefore the approximated KLD  $\hat{\mathcal{I}}(\theta_0, \theta)$  assuming that  $\det \left\{ \mathbf{R}_\theta^{-1} \mathbf{R}_0 \right\} = 1$  for every test resolution bin  $\theta$  is described as:

$$\hat{\mathcal{I}}(\theta_0, \theta) = \frac{1}{2} \left( \text{tr}[\mathbf{R}_\theta^{-1} \mathbf{R}_0] - MN_{\mathcal{R}} \right) \quad (6.94)$$

Moreover the results are normalised so that the minimum and maximum values are always 0 and 1 respectively. The definition of the MIMO AF used in this scenario is given as:

$$\hat{\mathcal{A}}_{\text{MIMO}}(\theta_0, \theta) = 1 - \frac{\hat{\mathcal{I}}(\theta_0, \theta) - \min_{\theta} \hat{\mathcal{I}}(\theta_0, \theta)}{\max_{\theta} \hat{\mathcal{I}}(\theta_0, \theta) - \min_{\theta} \hat{\mathcal{I}}(\theta_0, \theta)} \quad (6.95)$$

The main reason of normalising the results is to provide an easier comparison between the theoretical and other proposed AFs.

### 6.7.2 Correlation matrix approximation

A secondary matter in using the proposed definition on simulated or real data is that the definition of the channel correlation matrix in (6.54) and consequently the matrix  $\mathbf{C}(\theta_0)$  is based in assumption that the target is composed of scatters with a reflectivity modelled by i.i.d complex random variables (see Section 6.3). The main result of this assumption is that  $\mathcal{E} \{ \zeta_q^\dagger \zeta_{q'} \} = \delta(q - q') |\zeta_q|^2$ , which is not true if only an individual measurement of  $\zeta_q$  is taken. To address this issue a coherent processing of  $N_{\mathcal{P}}$  pulses is assumed. As a consequence, the received signal  $\mathbf{r}_0$  has to be expressed by a  $M \times N_{\mathcal{P}}$  matrix, each column of which contains the  $M$  samples of one coherent acquisition. Consequently the matrix  $\hat{\Psi}(\theta)$  will also change its size to  $N_{\mathcal{P}} \times N_{\mathcal{R}} N_{\mathcal{T}}$ . Moreover the trace in (6.91) is reformed as follows:

$$\text{tr} \{ \mathbf{R}_{\theta}^{-1} \mathbf{R}_0 \} = \frac{1}{\sigma_n^2} \text{tr} \left\{ \mathbf{r}_0^\dagger \mathbf{r}_0 - \hat{\Psi}(\theta) \frac{\mathbf{C}(\theta)}{\sigma_n^2} \left[ \Phi(\theta) \frac{\mathbf{C}(\theta)}{\sigma_n^2} + \mathbf{I}_{N_{\mathcal{T}} N_{\mathcal{R}}} \right]^{-1} \hat{\Psi}(\theta)^\dagger \right\} \quad (6.96)$$

To evaluate the degree of similarity between the theoretical value of  $\mathbf{C}(\theta_0)$  and the one expected from the simulation  $\hat{\mathbf{C}}(\theta_0)$ , the Frobenius norm of their difference is calculated, i.e.  $\| \{ \hat{\mathbf{C}}(\theta_0) - \mathbf{C}(\theta_0) \} \|$ . The system configuration is the one described in Fig. 6.3 with the target located at  $\mathbf{x}_0 = [0, 0]^T$  and (a)  $\mathbf{x}_0 = [-400, -400]^T$ , while the x-axis and y-axis dimensions of the target are  $\Delta_x = \Delta_y = \lambda$ . Consulting Fig. 6.4a it can be observed that for the target location  $\mathbf{x}_0 = [0, 0]^T$ , the system can be approximated as distributed and therefore  $\mathbf{C}(\theta_0)$  can be approximated by a diagonal matrix. On the other hand when the target is located at  $\mathbf{x}_0 = [-400, -400]^T$ , the system can be approximated as co-located and  $\mathbf{C}(\theta_0)$  will be a fully populated matrix. In Fig. 6.11 the resulting norm after a Monte Carlo of 1000 iterations is illustrated for different number on coherent

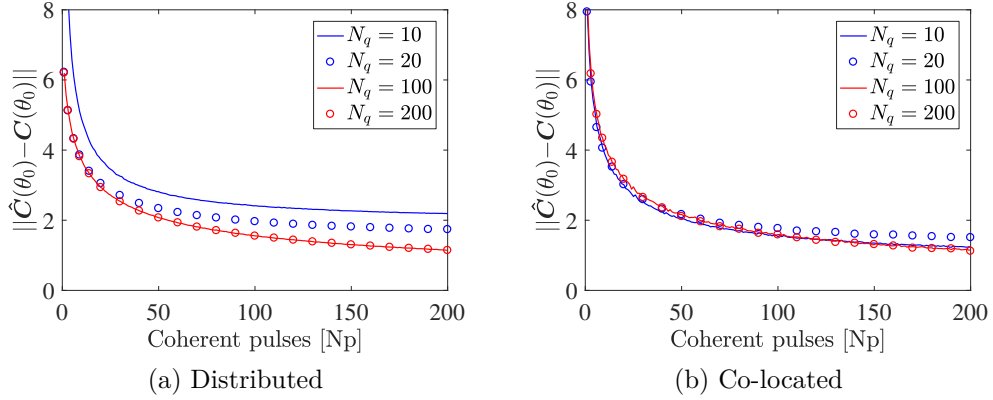


Fig. 6.11 Euclidean distance between the theoretical and simulated channel correlation matrix for an approximated (a) distributed and (b) co-located system.

pulses  $N_{\mathcal{P}}$  and different number of scatters  $N_{\mathcal{Q}}$ . It is worth noting that while the Frobenius norm provides a good measure of similarity, in the examined case it also highly depends on the size of the matrices  $N_{\mathcal{R}}N_{\mathcal{T}} \times N_{\mathcal{T}}N_{\mathcal{R}}$ .

Examining the impact of  $N_{\mathcal{Q}}$ , in Figure 6.11 it can be seen that generally larger number of scatters result to smaller norm and therefore better similarity between the theoretical and simulated channel correlation matrices. This is expected as returns from more scatters will result to better approximation of the sinc functions in (6.51) as discussed in Section 6.3. Moreover, comparing the results for different values of  $N_{\mathcal{Q}}$  in the distributed case, it can be seen in Figure 6.11a that the improvement saturated for  $N_{\mathcal{Q}} > 100$ . On the other hand, for the co-located case it appears that the approximation behaves similar for all the examined values of  $N_{\mathcal{Q}}$ .

Comparing the results for different values of it can be seen the norm of the difference, expressed as Euclidean distance, between the theoretical and simulated  $\mathbf{C}(\theta_0)$  is decreasing as the number of coherent pulses  $N_{\mathcal{P}}$  increases. This is expected, as in each pulse a new observation for each  $\zeta_q$  is also acquired, i.e.  $\boldsymbol{\zeta}_q = [\zeta_q(1), \dots, \zeta_q(N_{\mathcal{P}})]^T$ . It can be therefore derived that as  $N_{\mathcal{P}}$  increases the sample cross-correlation  $\boldsymbol{\zeta}_q^\dagger \boldsymbol{\zeta}_{q'}$  will be approximately zero. However, as previously mentioned, the norm will also depend on the  $N_{\mathcal{Q}}$ . In fact, for  $N_{\mathcal{P}} = 10^4$  (not included in Figure 6.11) the norm for  $N_{\mathcal{Q}} = 10$  is close to 1.9 and 1.1 for the distributed and co-located cases respectively, while for  $N_{\mathcal{Q}} = 200$  these norms drop to 0.2 and 0.15 respectively.

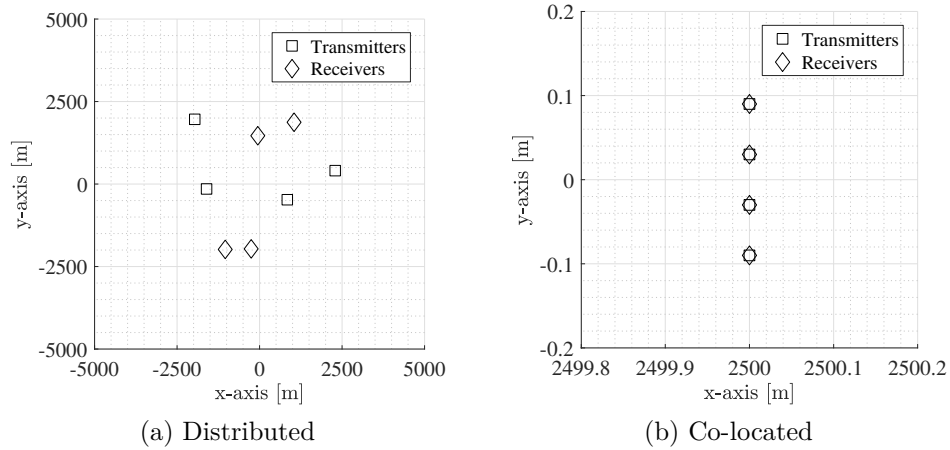


Fig. 6.12 Sensor geometry for the simulated system in (a) distributed and (b) co-located configuration.

### 6.7.3 Simulated results

To evaluate the performance of the proposed AF, a  $4 \times 4$  MIMO radar system with an extended target is simulated. The variables of the system are summarised in Table 6.2, while a coherent processing of  $N_{\mathcal{P}} = 50$  pulses is used to generate the MIMO AF. For comparison, the more canonical approach of summing the square matched filter outputs is also employed, calculated as:

$$\hat{\mathcal{A}}_{\text{can,MIMO}} = \text{tr} \left\{ \hat{\Psi}(\theta)^\dagger \hat{\Psi}(\theta) \right\} \quad (6.97)$$

The performance of the proposed and canonical MIMO AF is compared for a distributed and co-located system geometric configurations as illustrated in Fig.6.12a and Fig.6.12b respectively. It should be noted that in all simulation, a  $5 \times 5\text{Km}^2$  area is examined with the target located at  $\mathbf{x}_{0,\mathcal{Q}} = [0, 0]$ .

#### Distributed System

In the following paragraphs, the distributed system in Fig. 6.12a is simulated to examine the behaviour of the proposed and canonical MIMO AF definition. First the system is explored using the orthogonal waveforms described in (6.89). In Fig. 6.13 the proposed and canonical MIMO AFs are illustrated. Comparing Fig. 6.13a and Fig. 6.13b, it is observed that both MIMO AFs have identical behaviour being composed of 16 ridges corresponding to the  $N_{\mathcal{T}}N_{\mathcal{R}} = 16$  individual transmitter-receiver pairs. The similarity in the results is expected and can be

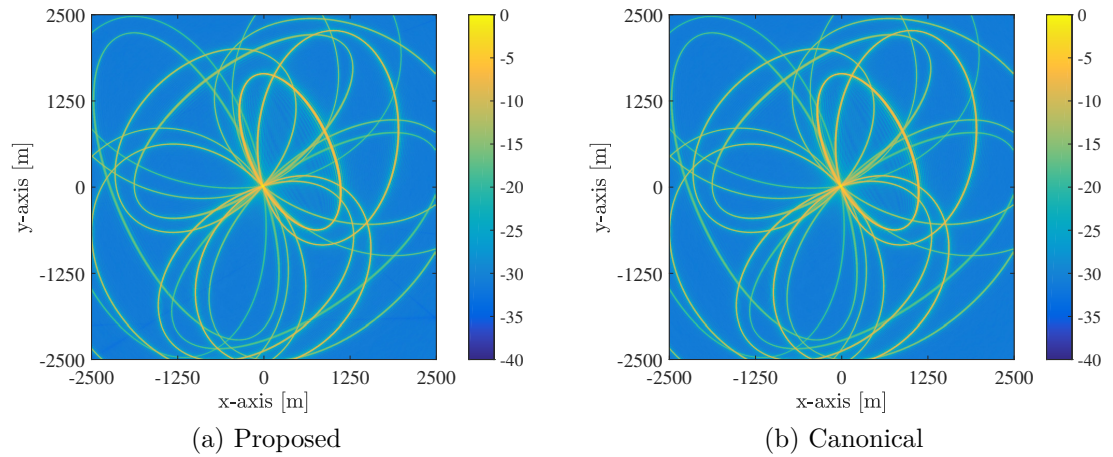


Fig. 6.13 Illustration of (a) proposed and (b) traditional MIMO AF in a distributed system configuration using orthogonal waveforms.

easily validated theoretically by replacing the correlation matrices  $\Phi(\theta)$  and  $\mathbf{C}(\theta)$  with diagonals in (6.96).

Using the same geometry, the system was simulated using the fully correlated waveforms described in (6.90). In Fig. 6.14 the two MIMO AFs are illustrated. As it can be observed in Fig. 6.14a and Fig. 6.14b both MIMO AFs are composed of a larger number of ridges compared to when orthogonal waveforms are used.

Table 6.2 Simulated MIMO System Variables

Description	Variable	Value
Carrier frequency	$f_0$	10MHz
Signal bandwidth	$B$	10GHz
Signal period	$T$	$50\mu s$
Target x-axis dimension	$\Delta_x$	1m
Target y-axis dimension	$\Delta_y$	1m
Target RCS variance	$\sigma_0^2$	1 m
Noise variance	$\sigma_n^2$	$1^{-13}$
Gain on transmitters	$G_{\mathcal{T}}$	40dB
Gain on receivers	$G_{\mathcal{R}}$	40dB
Energy on transmitters	$\hat{E}_{\mathcal{T}}$	20dB

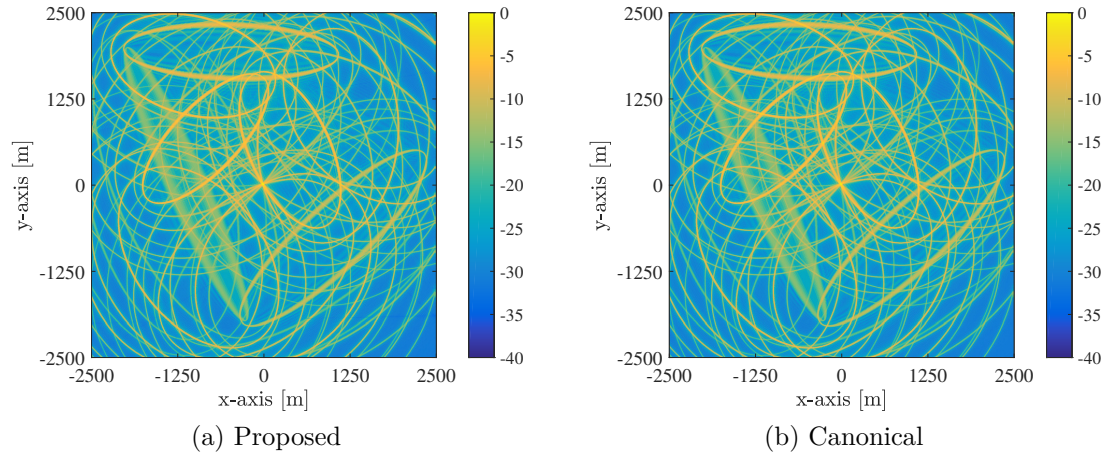


Fig. 6.14 Illustration of (a) proposed and (b) traditional MIMO AF in a distributed system configuration using correlated waveforms.

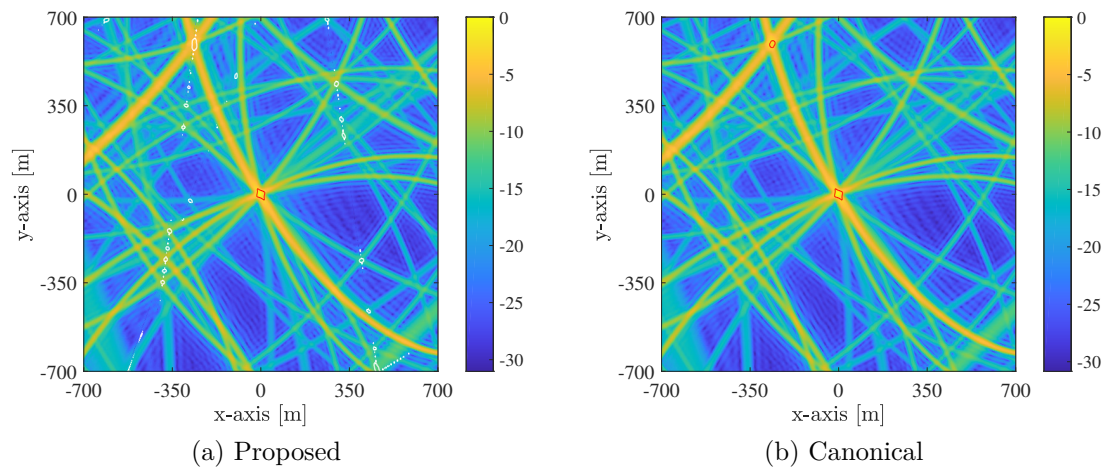


Fig. 6.15 Illustration of (a) proposed and (b) traditional MIMO AF in a distributed system configuration using correlated waveforms. The red line marks the  $-3\text{dB}$  contours of the MIMO AFs, while the white line marks the contour where the proposed MIMO AF is 50% lower than the canonical.

The actual number of ridges is  $N_T^2 N_R = 64$ , as discussed in Section 6.6.2. For a better examination, Fig. 6.15 offer a zoomed illustration of the MIMO AFs for an area close to the target. Moreover a red line marks the  $-3\text{dB}$  contour of the two MIMO AFs, while in Fig. 6.15a the contour for which the proposed MIMO AF is 50% lower than the canonical is shown in white. Examining Fig. 6.15a, it can be seen that the proposed MIMO AF has values over  $-3\text{dB}$  only in the main lobe to where the target is placed. In contrast, in Fig. 6.15b it is shown that the canonical MIMO AF exhibits a sidelobe of values higher than  $-3\text{dB}$  in a distant point from the target's position. This is caused due to the way the canonical MIMO AF

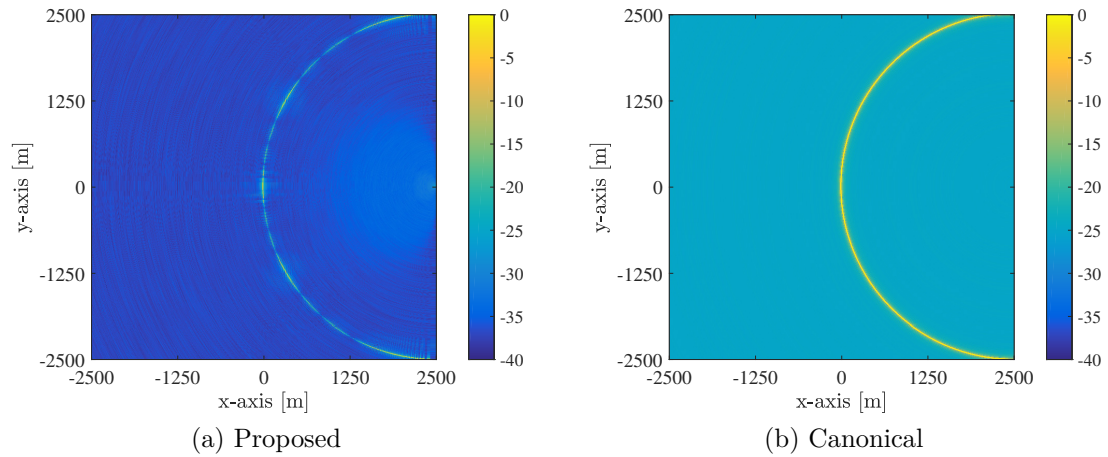


Fig. 6.16 Illustration of (a) proposed and (b) traditional MIMO AF in a co-located system configuration using orthogonal waveforms.

is constructed by adding all the resulting ridges constructively. Inspection of Fig. 6.15a shows that in those areas in which the different ridges are crossing, the value of the proposed MIMO AF is at least half of those in the canonical.

### Co-located System

In this example scenario the co-located system configuration in Fig. 6.12b is used. In Fig. 6.16 the resulting MIMO AFs are illustrated when the operating waveforms are orthogonal as given in (6.89). As it can be seen in both cases the MIMO AF is described by a circular ridge crossing the position of the target. In reality, as described in Section 6.6.2, this ridge is composed of 16 secondary ridges corresponding to the individual transmitter-receiver pairs. To provide closer inspection, Fig. 6.17 illustrate the two different MIMO AFs only for the area close to the target, while a red line marks the  $-3\text{dB}$  contour. As it can be seen in Fig. 6.17a the proposed MIMO AF has a distinctive peak at the area surrounding the target while it reduces and fluctuates moving further away. This phenomenon is caused by the constructive and destructive correlation of the different transmitter-target-receiver channels, as discussed in Section 6.6.2. On the other hand, after examining the canonical MIMO AF in Fig. 6.17b it is observed that it remains constant moving on the main ridge.

Using the same configuration the system was simulated for fully correlated waveforms as given in (6.90). In Fig. 6.18 the MIMO AFs for the proposed and canonical definition are presented. As it can be seen, the main structure of the two MIMO AFs is similar the case of orthogonal waveforms, with a single circular

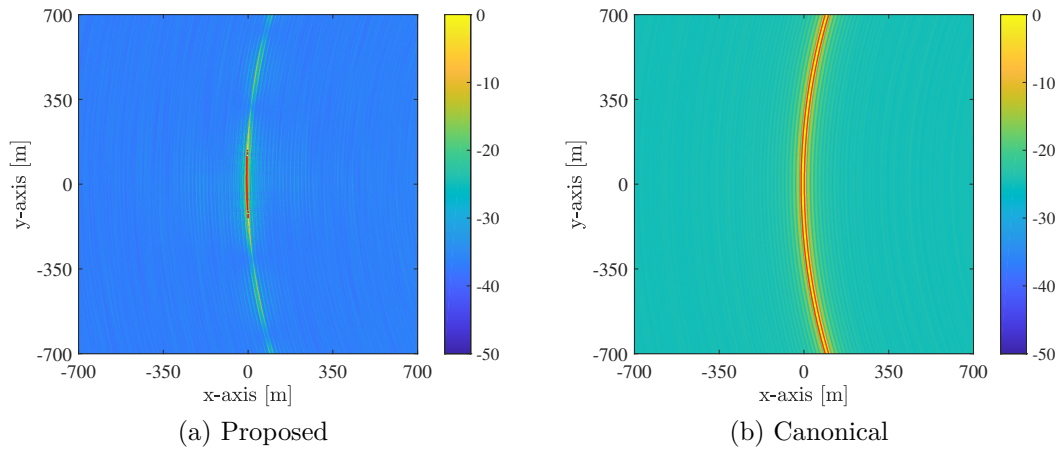


Fig. 6.17 Illustration of (a) proposed and (b) traditional MIMO AF for area close to the target, in a co-located system configuration using orthogonal waveforms. The red line marks the  $-3\text{dB}$  contours of the MIMO AFs.

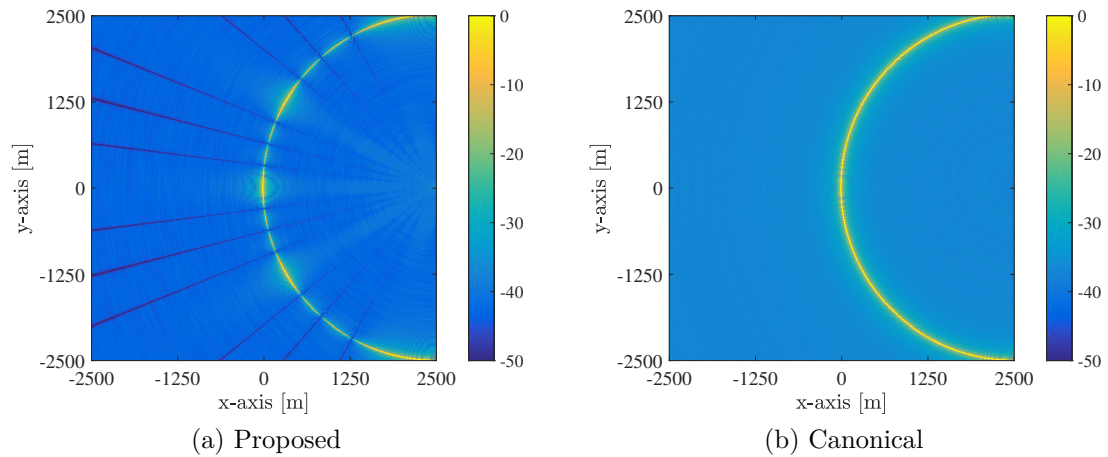


Fig. 6.18 Illustration of (a) proposed and (b) traditional MIMO AF in a co-located system configuration using fully correlated waveforms.

ridge crossing the target. In this case however, the main ridge is composed of  $N_{\mathcal{T}}^2 N_{\mathcal{R}} = 64$  secondary ridges. This increase on the number of secondary ridges leads to a lower floor level as it can be observed in both figures. Moreover, in Fig.6.18a regions of very low values can be seen as lines radiating out from the position of the sensors are present. Those line are connected with the fluctuation of the  $\text{SNR}_{\theta}$ , as discussed in Section 6.6.2. In Fig. 6.19 the MIMO AFs for the area close to the target are illustrated. As it can be seen, the canonical MIMO AF in Fig. 6.19b has a very similar behaviour as in Fig. 6.17b with a lower floor level. Looking at the proposed MIMO AF in Fig. 6.19a it is observed that the  $-3\text{dB}$  contour (see red line) is larger than when orthogonal waveforms are used as

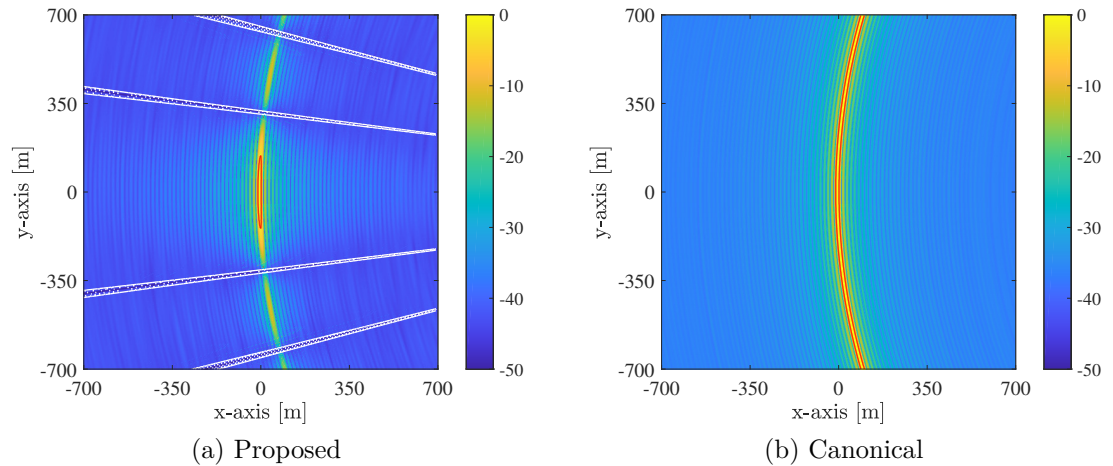


Fig. 6.19 Illustration of (a) proposed and (b) traditional MIMO AF for area close to the target, in a co-located system configuration using fully correlated waveforms. The red line marks the  $-3\text{dB}$  contours of the MIMO AFs, while the white line marks the  $10\text{dB}$  contour of  $\text{SNR}_\theta$ .

it can be seen in Fig. 6.17a, with the floor level however being significantly lower in the correlated waveform case. For a better understanding on how the  $\text{SNR}_\theta$  have an effect on the proposed MIMO AF, the contour of the  $10\text{dB}$   $\text{SNR}_\theta$  is also drawn in Fig. 6.19a. As it is seen, the values of  $\text{SNR}_\theta$  can dictate the fluctuations of the proposed MIMO AF placing increasing and decreasing its values.

## 6.8 Summary

In this chapter a new, generalised MIMO AF is presented. The proposed definition is based on the Kullback Leibler divergence and applied in a MIMO radar signal model. Theoretical analysis showed that the proposed MIMO AF can be factorised in auto-correlation and cross-correlation signal matrices, and channel correlation matrices. In addition, it is proven that the proposed MIMO AF takes values between 0 and 1 while also being flexible for various system spatial configuration assumptions. The relationship of the proposed MIMO AF with the commonly used definition is also examined, showing that it reduces to the canonical Woodward definition when the same signal model is assumed. Moreover, the behaviour of the proposed MIMO AF was investigated for different target placements and operating waveform highlighting the advantages of each configuration. Finally, the performance of the proposed AF was demonstrated in a simulated MIMO radar system. Comparing the results for the described simulated scenarios it can

---

be derived that the proposed definition offers better target localisation offering higher spatial resolution and lower floor levels.

# Chapter 7

## Conclusions and Future Works

### 7.1 Conclusion

In this thesis, a variety of important signal processing algorithms have been analysed for multi-input multi-output (MIMO) radar system, concerning the edge detection based on phase stretch transform (PST) for synthetic aperture radar (SAR) imaging systems, the design of radar waveforms libraries utilising the advantageous properties of fractional Fourier transform (FrFT), and the synthesis of a generalised MIMO ambiguity function based on the Kullback Leibler divergence (KLD).

In Chapter 2 an extensive research review was presented, dedicated to a number of very important aspects of modern radar systems. Key areas, such as basic radar concepts and advanced radar techniques were discussed mainly focused on radar waveform design and pulse compression through signal processing techniques. In addition, the concept of multisensor radar systems was introduced exploring their categorisation relating to their geometry and operating waveforms. Furthermore, the topical subject of spectrum sharing (SS) was presented referring the recent advances with regard to waveform diversity (WD) in MIMO radar. Proposed WD schemes such as orthogonal frequency division multiplexing (OFDM) and discrete frequency-coding waveforms (DFCW) were discussed exploring the design of multiple waveforms with good auto-correlation properties and low cross-correlation peak levels. The aim of these designs was to generate waveforms suitable for MIMO radar applications. Moreover, recently proposed techniques that allow joint communication and radar operations were investigated, including schemes exploiting WD, sidelobe amplitude modulation (AM), multiwaveform amplitude shift keying (ASK), and phase modulation (PM). Lastly, the concept

of SAR was introduced, while current challenges in SAR images processing were presented.

In Chapter 3 the basic concepts of time-frequency (T/F) analysis were discussed in connection with the commonly used tools associated with it. Moreover, the importance of the ambiguity function (AF) was discussed by highlighting its significant properties and referring to various proposed definitions, such as traditional or Woodward AF and the Kullback Leibler divergence (KLD) based definition. In addition, the fractional Fourier transform (FrFT) and the phase stretch transform (PST) were extensively presented. First, the notion of fractional domain and the FrFT were discussed included the FrFT properties, implementations (i.e. discrete and fast approximation) and applications in signal processing. Later on, the PST was introduced included, referencing also its application in SAR image compression and biomedical diagnoses. Moreover, a specific mention was made to aspects of PST in image edge detection. A provided example illustrated how the PST based edge detection algorithm can effectively extract edges while trading between noise reduction and resolution.

An algorithm for edge detection in SAR images was presented in Chapter 4. This method is an enchanted scheme based on the previously proposed PST based edge detection method. Examining its different steps, it has been shown that the presented algorithm reduces the noise effects and removes phase image artefacts, while the PST emphasises the edge information applying more phase to higher frequency features. The good performance of the presented edge detection algorithm has been tested and verified experimentally using two real datasets. Experimental results demonstrated that thresholding and further morphological operation leads to the edge extraction despite the noise presence into the original image. Moreover, it was observed that more details could be preserved, while removing completely the noise from the sea areas.

In Chapter 5, a novel scheme was introduced that is capable to create waveform libraries utilising the FrFT. The potentials of the FrFT based or also called fractional waveforms were demonstrated through mathematical analysis and an illustrative example for Barker 13 code, examining the resulted waveforms and their AFs. Subsequently, an efficient algorithm based on a modified Gerchberg-Saxton algorithm (MGSA) was proposed, to reconstruct the proposed fractional waveform libraries under constant envelope (CE) constrains. Simulation analysis showed the good properties of the waveforms and that high diversity between waveforms could be achieved in fractional and CE fractional libraries. The development and reconstruction of the novel waveform libraries for MIMO radar

was one of the most significant contributions in this thesis. It is worthy to note that the applicability of the proposed waveforms was also experimentally validated, while their performance was evaluated and compared with conventional techniques in a distributed MIMO radar scenario. The results confirmed that the proposed design scheme is very competent for various radar applications such as those related to co-located and distributed MIMO radar, pulse agile radar and electronic countermeasures. Moreover, a novel multiplexing scheme based on the FrFT was introduced allowing the radar systems to operate in message exchange mode via embedding the information into waveforms. The efficiency of the proposed waveform design was evaluated in connection with the AF properties of communicative radar (Co-radar) waveform.

In Chapter 6, a MIMO AF is presented based on the Kullback Leibler divergence and applied in a MIMO radar system framework. Theoretical analysis showed that the proposed MIMO AF can be factorised in auto-correlation and crosscorrelation signal matrices, and channel correlation matrices. In addition, the MIMO AF maximally stretched between 0 and 1 while also being flexible for various system spatial configuration assumptions. The relationship of the proposed MIMO AF with other proposed definition is also examined. Moreover, the behaviour of the proposed MIMO AF was investigated for different target placements and operating waveform. Finally, the performance of the AF was demonstrated in a simulated MIMO radar system.

## 7.2 Future Work

In the presented work there are various topics worthy of future research. In Chapter 5, novel waveform libraries design has proposed suitable for MIMO radar systems based on FrFT. These radar waveforms are very effective in target localisation problem, but may suffer from the introduced noise. Although the proposed constant envelope fractional waveform has shown good performance, the further fractional domain optimisation still remains an interesting challenge. A future developed approach may increase the estimation of target parameters against the mismatches through improved filtering approach. One of the most important current challenges in MIMO radar is the search for fully orthogonal waveforms aimed to remove interference problems between the antennae during both the transmission and pulse compression phases. Future requirements may include novel design of fully orthogonal waveforms to increase transmitted information in

the same bandwidth. Utilisation of multi-order FrFT (MoFrFT) can also provide additional degrees of freedom potentially leading to better optimised waveform libraries.

Moreover the novel technique of embedding arbitrary information into radar waveforms could be further investigated employing the potentials of the FrFT. Radar waveform design based on FrFT is proved to be a much promising methodology in extending message exchange between radar systems. In addition, the applicability and adaptation of the proposed designs will be evaluated in modern radar/communication application areas including vehicular communications. In addition, diversity between different Co-Radar waveforms can allow simultaneous radar and communication operations between different platforms.

Considering the research presented in Chapter 6, future work may include further investigating of the generalised MIMO AF. The proposed formulation could be further parametrised to increase flexibility of the signal model approach. Also, an extension would be the formulation simplification, approximating some of its terms to decrease the complexity and therefore the total time consumed for AF calculation. In addition the presented work on the generalised AF may extend to search from matched filter processing to mismatched filtering aimed to improve the the systems performance.

The presented edge detection technique in Chapter 4 is much promising and has the potential advantages to further improve noise removal and edge appearance. Future work could explore the PST parameter optimisation in recovering image edges. This may involve the design of a dynamic parameter regulation that could optimise the removal of the embedded noise while eliminating the phase image artifacts.

# Appendix A

## A.1 Further FrFT Properties

In this section a number of properties of further FrFT properties not listed in Section 3.4.1 are provided. In all properties  $x(t)$  denotes an arbitrary signal.

### Inverse FrFT

$$x(t) = \mathcal{F}^{-a}\{x_a(u)\} = \int_{-\infty}^{\infty} x_a(u)K_{-a}(u, t)du \quad (\text{A.1})$$

### Time Shift

$$\mathcal{F}^a x(t - \tau) = x_a(u - \tau \cos \vartheta) e^{j\tau^2/2 \sin \vartheta \cos \vartheta - ju\tau \sin \vartheta} \quad (\text{A.2})$$

### Phase modulation

$$\mathcal{F}^a x(t) e^{j\omega t} = x_a(u + \omega \sin \vartheta) e^{-j\omega^2/2 \sin \vartheta \cos \vartheta - ju\omega \cos \vartheta} \quad (\text{A.3})$$

Moreover some other useful relations regarding the FrFT kernel are listed below:

$$K_a^*(t, u) = K_{-a}(t, u) \quad (\text{A.4})$$

$$K_a(t, u) = K_a(u, t) \quad (\text{A.5})$$

where  $K_a(t, u)$  is the FrFT kernel of an order  $a$ . These properties and relations will be useful in later sections.

## A.2 FrFT and AF relationship Proof

In this section the relationship between the traditional AF and the FrFT will be derived. In the following lines we denote the AF of an arbitrary signal  $x(t)$  as  $\mathcal{A}(\tau, \omega)\{x(t)\}$  following the definition provided in (Hlawatsch and Boudreaux-Bartels, 1992):

$$\mathcal{A}(\tau, \omega)\{x(t)\} = \int_{-\infty}^{\infty} x(t + \frac{\tau}{2})x^*(t - \frac{\tau}{2})e^{-j\omega t} dt \quad (\text{A.6})$$

This definition is slightly different but equivalent to the AF described in Section 3.3.1. Namely computing the modulo of (A.6) results to the same definition as in (3.5).

The following approach is very similar to the one held in (Almeida, 1994) for the Winger distribution. For ease of notation the Doppler has been replaced with the phase  $\omega = 2\pi f_D$ . Based on the definition in (A.6), the AF of an arbitrary signal  $x(t)$  is given as:

$$\begin{aligned} \mathcal{A}(\tau, \omega)\{x(t)\} &= \int_{-\infty}^{\infty} x(t + \frac{\tau}{2})x^*(t - \frac{\tau}{2})e^{-j\omega t} dt & (\text{A.7}) \\ &\stackrel{(\text{A.9})}{=} e^{j\omega\tau/2} \int_{-\infty}^{\infty} x(t)x^*(t - \tau)e^{-j\omega t} dt \\ &\stackrel{(\text{A.1})}{=} e^{j\omega\tau/2} \int_{-\infty}^{\infty} x(t)e^{-j\omega t} \int_{-\infty}^{\infty} \mathcal{F}^a\{x(t - \tau)\}K_{-a}^*(u, t)du dt \\ &\stackrel{(\text{A.2})}{=} e^{j\omega\tau/2} \int_{-\infty}^{\infty} x(t)e^{-j\omega t} \int_{-\infty}^{\infty} x_a^*(t - \tau \cos \vartheta)e^{-j\tau^2/2 \sin \vartheta \cos \vartheta + ju\tau \sin \vartheta} K_{-a}^*(u, t)du dt \\ &\stackrel{(\text{A.4})}{=} e^{j\omega\tau/2} \int_{-\infty}^{\infty} x(t)e^{-j\omega t} \int_{-\infty}^{\infty} x_a^*(u - \tau \cos \vartheta)e^{-j\tau^2/2 \sin \vartheta \cos \vartheta + ju\tau \sin \vartheta} K_a(u, t)du dt \\ &= e^{j\omega\tau/2} \int_{-\infty}^{\infty} \int_{-\infty}^{\infty} x(t)e^{-j\omega t} x_a^*(u - \tau \cos \vartheta)e^{-j\tau^2/2 \sin \vartheta \cos \vartheta + ju\tau \sin \vartheta} K_a(u, t)dt du \\ &= e^{j\omega\tau/2} \int_{-\infty}^{\infty} x_a^*(u - \tau \cos \vartheta)e^{-j\tau^2/2 \sin \vartheta \cos \vartheta + ju\tau \sin \vartheta} \int_{-\infty}^{\infty} x(t)e^{-j\omega t} K_a(u, t)dt du \\ &\stackrel{(\text{A.5})}{=} e^{j\omega\tau/2} \int_{-\infty}^{\infty} x_a^*(u - \tau \cos \vartheta)e^{-j\tau^2/2 \sin \vartheta \cos \vartheta + ju\tau \sin \vartheta} \int_{-\infty}^{\infty} x(t)e^{-j\omega t} K_a(t, u)dt du \\ &\stackrel{(\text{A.3})}{=} e^{j\omega\tau/2} \int_{-\infty}^{\infty} x_a^*(u - \tau \cos \vartheta)e^{-j\tau^2/2 \sin \vartheta \cos \vartheta + ju\tau \sin \vartheta} \\ &\quad x_a(u + \omega \sin \vartheta)e^{-j\omega^2/2 \sin \vartheta \cos \vartheta - ju\omega \cos \vartheta} du \end{aligned}$$

$$\begin{aligned}
&= e^{j\omega\tau/2} \int_{-\infty}^{\infty} x_a(u + \omega \sin \vartheta) x_a^*(u - \tau \cos \vartheta) \\
&\quad e^{-j(\tau^2/2 + \omega^2/2) \sin \vartheta \cos \vartheta + ju(\tau \sin \vartheta - \omega \cos \vartheta)} du \\
&\stackrel{(A.10)}{=} e^{j\omega\tau/2} \int_{-\infty}^{\infty} x_a(u) x_a^*(u - \omega \sin \vartheta - \tau \cos \vartheta) \\
&\quad e^{-j(\tau^2/2 + \omega^2/2) \sin \vartheta \cos \vartheta + j(u - \omega \sin \vartheta)(\tau \sin \vartheta - \omega \cos \vartheta)} du \\
&= e^{j\omega\tau/2} \int_{-\infty}^{\infty} x_a(u) x_a^*(u - \omega \sin \vartheta - \tau \cos \vartheta) \\
&\quad e^{j(\omega^2/2 - \tau^2/2) \sin \vartheta \cos \vartheta + ju(\tau \sin \vartheta - \omega \cos \vartheta) - \omega\tau \sin^2 \vartheta} du \\
&\stackrel{(A.11)}{=} e^{j\omega\tau/2} \int_{-\infty}^{\infty} x_a(u) x_a^*(u - d) e^{j(\omega^2/2 - \tau^2/2) \sin \vartheta \cos \vartheta - ju\nu - \omega\tau \sin^2 \vartheta} du \\
&= e^{j\omega\tau/2} \int_{-\infty}^{\infty} x_a(u) x_a^*(u - d) e^{jd\nu/2 + \omega\tau/2(\sin^2 \vartheta - \cos^2 \vartheta) - ju\nu - \omega\tau \sin^2 \vartheta} du \\
&= e^{j\omega\tau/2} \int_{-\infty}^{\infty} x_a(u) x_a^*(u - d) e^{jd\nu/2 - \omega\tau/2 - ju\nu} du \\
&= e^{jd\nu/2} \int_{-\infty}^{\infty} x_a(u) x_a^*(u - d) e^{-ju\nu} du \tag{A.8}
\end{aligned}$$

where the substituting relationships are given as:

$$t \triangleq t - \tau/2 \tag{A.9}$$

$$u \triangleq u - \omega \sin a \tag{A.10}$$

$$d = \omega \sin \vartheta + \tau \cos \vartheta \quad \text{and} \quad \nu = \omega \cos \vartheta - \tau \sin \vartheta \tag{A.11}$$

It should be pointed that by substituting the integrating variables in (A.9) and (A.10) the limits of the integrals do not change. Observing (A.8) it can be easily extracted that the right-hand side of the equation simplifies to AF of  $x_a$  for the variables  $d$  and  $\nu$ , i.e. :

$$\mathcal{A}(\tau, \omega)\{x(t)\} = \mathcal{A}(d, \nu)\{x_a(u)\} \tag{A.12}$$

As it can be seen (A.12) the AF of  $x$  expressed as a function of the delay  $\tau$  and the phase modulation  $\omega$  related to the Doppler shift is equal to the AF of  $x_a$  expressed as a function of variables  $d$  and  $\nu$  given in (A.11). This relationship shows that the AF of  $x_a$ , coincides with the AF of  $x$  if we take into account the rotation that corresponds to the fact that we are using different axes. This indicates that essentially the AF of  $x_a$  is the AF of  $x$  rotated by an angle  $\vartheta$  (Almeida, 1994).

# Appendix B

## B.1 Definition of Time Delay, Time Scale and Frequency Shift Matrix

In this section the  $M \times M$  matrix  $\mathbf{a}_{j,i}$  is defined to account for the time delay, time scale and frequency shift experienced by the baseband signal  $s_i$  due to the distance and relative motion in the  $i$ -th transmitter,  $q$ -th scatter,  $j$ -th receiver system.

First let us consider that the signal experiences only a frequency shift  $f$ . The frequency shift matrix  $\mathbf{a}_{j,i}^{(f)}$  can be described as a  $M \times M$  diagonal matrix populated by the discrete samples of  $e^{j2\pi ft}$ . Furthermore, let us consider that the signal experiences only a delay of  $m_\tau$  samples. The time shift matrix  $\mathbf{a}_{j,i}^{(\tau)}$  can be described as:

$$\mathbf{a}_{j,i}^{(\tau)} = \begin{bmatrix} \mathbf{0}_{m_\tau} & \mathbf{0}_{M-m_\tau} \\ \mathbf{I}_{M-m_\tau} & \mathbf{0}_{m_\tau} \end{bmatrix} \quad (\text{B.1})$$

where  $\mathbf{0}_\ell$  denotes a  $\ell \times \ell$  square matrix populated by zeros. Moreover, let us now consider that the signal only experiences a time scale of a factor  $\alpha$ . The time shift matrix  $\mathbf{a}_{j,i}^{(\alpha)}$  can be described as:

$$\mathbf{a}_{j,i}^{(\alpha)} = \lfloor \alpha M \rfloor \begin{bmatrix} \mathbf{o}_{\lfloor \alpha \rfloor - 1} & 1 & \mathbf{o}_{M - \lfloor \alpha \rfloor} \\ \mathbf{o}_{\lfloor 2\alpha \rfloor - 1} & 1 & \mathbf{o}_{M - \lfloor 2\alpha \rfloor} \\ \vdots & \vdots & \vdots \\ \mathbf{o}_{\lfloor M\alpha \rfloor - 1} & 1 & \mathbf{o}_{M - \lfloor M\alpha \rfloor} \end{bmatrix} \quad (\text{B.2})$$

where  $\mathbf{o}_\ell$  denotes a  $1 \times \ell$  column matrix populated by zeros and  $\lfloor \cdot \rfloor$  indicates the floor function giving the largest integer less than or equal to input. We can now

describe the total time delay, time scale and frequency shift matrix as:

$$\mathbf{a}_{j,i} = \mathbf{a}_{j,i}^{(\alpha)} \times \mathbf{a}_{j,i}^{(\tau)} \times \mathbf{a}_{j,i}^{(f)} \quad (\text{B.3})$$

## B.2 Phase Integral and Sinc function Relation Proof

In this part the approximation of the phase integral being close to 0 is examined. As it can be seen the integral of a complex exponential can be described by a cardinal sine or sinc function:

$$\begin{aligned} \int_{-1/2}^{1/2} e^{j2\pi\beta m} dm &= \frac{1}{j\pi\beta} e^{j\beta m} \Big|_{-1/2}^{1/2} = \frac{1}{j2\pi\beta} (e^{j\pi\beta} - e^{-j\pi\beta}) \\ &= \frac{1}{\pi\beta} \sin(\pi\beta) = \text{sinc}(\pi\beta) \end{aligned} \quad (\text{B.4})$$

It is known the  $\text{sinc}(\pi\beta)$  will have its first zero at  $|\beta| = 1$  and will continue to decrease its absolute value as  $|\beta|$  increases. It is therefore reasonable to approximate the output of the integral to 0 for  $|\beta| > 1$ .

## B.3 Inverse Corelation Matix Proof

In this part the proof of the matrix  $\mathbf{R}_\theta^{-1}$  in (6.71) being the inverse of the covariance matrix  $\mathbf{R}_\theta$  in (6.69) is provided. In this section the index  $\theta$  will be ignored for better illustration.

By definition the inverse of the matrix  $R_\theta$  should satisfy the condition  $\mathbf{R}_\theta \mathbf{R}_\theta^{-1} = \mathbf{I}_{MN_{\mathcal{R}}}$ . Following the multiplication of the two matrices is provided

step-by-step:

$$\begin{aligned}
\mathbf{R}\mathbf{R}^{-1} &= \left(\mathbf{Y}\mathbf{C}\mathbf{Y}^\dagger + \sigma_n^2 \mathbf{I}_{MN\mathcal{R}}\right) \frac{1}{\sigma_n^2} \left(\mathbf{I}_{MN\mathcal{R}} - \mathbf{Y}\mathbf{C}[\mathbf{Y}^\dagger\mathbf{Y}\mathbf{C} + \sigma_n^2 \mathbf{I}_{N\mathcal{T}N\mathcal{R}}]^{-1}\mathbf{Y}^\dagger\right) \\
&= \frac{1}{\sigma_n^2} \mathbf{Y}\mathbf{C}\mathbf{Y}^\dagger + \mathbf{I}_{MN\mathcal{R}} - \frac{1}{\sigma_n^2} \mathbf{Y}\mathbf{C}\mathbf{Y}^\dagger\mathbf{Y}\mathbf{C}[\mathbf{Y}^\dagger\mathbf{Y}\mathbf{C} + \sigma_n^2 \mathbf{I}_{N\mathcal{T}N\mathcal{R}}]^{-1}\mathbf{Y}^\dagger \\
&\quad - \mathbf{Y}\mathbf{C}[\mathbf{Y}^\dagger\mathbf{Y}\mathbf{C} + \sigma_n^2 \mathbf{I}_{N\mathcal{T}N\mathcal{R}}]^{-1}\mathbf{Y}^\dagger \\
&= \mathbf{I}_{MN\mathcal{R}} + \frac{1}{\sigma_n^2} \mathbf{Y}\mathbf{C} \left(\mathbf{I}_{N\mathcal{T}N\mathcal{R}} - \mathbf{Y}^\dagger\mathbf{Y}\mathbf{C}[\mathbf{Y}^\dagger\mathbf{Y}\mathbf{C} + \sigma_n^2 \mathbf{I}_{N\mathcal{T}N\mathcal{R}}]^{-1}\right. \\
&\quad \left. - \sigma_n^2[\mathbf{Y}^\dagger\mathbf{Y}\mathbf{C} + \sigma_n^2 \mathbf{I}_{N\mathcal{T}N\mathcal{R}}]^{-1}\right) \mathbf{Y}^\dagger \\
&= \mathbf{I}_{MN\mathcal{R}} + \frac{1}{\sigma_n^2} \mathbf{Y}\mathbf{C} \left(\mathbf{Y}^\dagger\mathbf{Y}\mathbf{C} + \sigma_n^2 \mathbf{I}_{N\mathcal{T}N\mathcal{R}} - \mathbf{Y}^\dagger\mathbf{Y}\mathbf{C} - \sigma_n^2 \mathbf{I}_{N\mathcal{T}N\mathcal{R}}\right) \\
&\quad \times [\mathbf{Y}^\dagger\mathbf{Y}\mathbf{C} + \sigma_n^2 \mathbf{I}_{N\mathcal{T}N\mathcal{R}}]^{-1} \mathbf{Y}^\dagger \\
&= \mathbf{I}_{MN\mathcal{R}} + \frac{1}{\sigma_n^2} \mathbf{Y}\mathbf{C} \left(\mathbf{0}_{N\mathcal{T}N\mathcal{R}}\right) [\mathbf{Y}^\dagger\mathbf{Y}\mathbf{C} + \sigma_n^2 \mathbf{I}_{N\mathcal{T}N\mathcal{R}}]^{-1} \mathbf{Y}^\dagger = \mathbf{I}_{MN\mathcal{R}} \quad (\text{B.5})
\end{aligned}$$

Additively it is proven that the matrix  $[\mathbf{Y}^\dagger\mathbf{Y}\mathbf{C} + \sigma_n^2 \mathbf{I}_{N\mathcal{T}N\mathcal{R}}]$  is positive definite and hence is also invertible since:

$$\begin{aligned}
&\det(\mathbf{Y}^\dagger\mathbf{Y}\mathbf{C} + \sigma_n^2 \mathbf{I}_{N\mathcal{T}N\mathcal{R}}) = \\
&\det(\mathbf{Y}^\dagger\mathbf{Y}\mathbf{H}\mathbf{H}^\dagger + \sigma_n^2 \mathbf{I}_{N\mathcal{T}N\mathcal{R}}) = \\
&\det(\mathbf{H}^\dagger\mathbf{Y}^\dagger\mathbf{Y}\mathbf{H} + \sigma_n^2 \mathbf{I}_{N\mathcal{T}N\mathcal{R}}) = \\
&\det((\mathbf{Y}\mathbf{H})^\dagger(\mathbf{Y}\mathbf{H}) + \sigma_n^2 \mathbf{I}_{N\mathcal{Q}N\mathcal{R}}) = \\
&\det(\mathbf{U}\mathbf{\Lambda}\mathbf{U}^\dagger + \sigma_n^2 \mathbf{I}_{N\mathcal{T}N\mathcal{R}}) = \\
&\det(\mathbf{U}(\mathbf{\Lambda} + \sigma_n^2 \mathbf{I}_{N\mathcal{A}})\mathbf{U}^\dagger) = \prod (\Lambda_{m,m} + \sigma_n^2) > 0 \quad (\text{B.6})
\end{aligned}$$

where  $\mathbf{U}$  and  $\mathbf{\Lambda}$  are the eigenvector and eigenvalue matrices of the positive semi-definite covariance matrix  $[(\mathbf{Y}\mathbf{H})^\dagger(\mathbf{Y}\mathbf{H})]$ . The inequality in (B.6) holds as  $\Lambda_{m,m} \geq 0$  and  $\sigma_n^2 > 0$ .

## B.4 Proof of Lower Limits

In this part the minimum values for the of the third and fifth terms in (6.77) and the maximum value of the fourth term are examined. In this section the index  $\theta$  will be ignored for better illustration.

Starting from the third term, first let us consider the eigenvalue decomposition of the matrices inside the trace:

$$\begin{aligned}
& \text{tr} \left\{ \Phi \mathbf{C} [\Phi \mathbf{C} + \sigma_n^2 \mathbf{I}_{N_{\mathcal{T}} N_{\mathcal{R}}}]^{-1} \right\} = \\
& \text{tr} \left\{ \mathbf{U} \mathbf{\Lambda} \mathbf{U}^{-1} [\mathbf{U} \mathbf{\Lambda} \mathbf{U}^{-1} + \sigma_n^2 \mathbf{I}_{N_{\mathcal{T}} N_{\mathcal{R}}}]^{-1} \right\} = \\
& \text{tr} \left\{ \mathbf{U} \mathbf{\Lambda} \mathbf{U}^{-1} [\mathbf{U} (\mathbf{\Lambda} + \sigma_n^2 \mathbf{I}_{N_{\mathcal{T}} N_{\mathcal{R}}}) \mathbf{U}^{-1}]^{-1} \right\} = \\
& \text{tr} \left\{ \mathbf{\Lambda} [\mathbf{\Lambda} + \sigma_n^2 \mathbf{I}_{N_{\mathcal{T}} N_{\mathcal{R}}}]^{-1} \right\} = \sum \left( \frac{\mathbf{\Lambda}_{m,m}}{\mathbf{\Lambda}_{m,m} + \sigma_n^2} \right) \tag{B.7}
\end{aligned}$$

where  $\mathbf{U}$  and  $\mathbf{\Lambda}$  are the eigenvector and eigenvalue matrices so  $\Phi \mathbf{C} = \mathbf{U} \mathbf{\Lambda} \mathbf{U}^{-1}$ . It can be easily shown that:

$$\sum \left( \frac{\mathbf{\Lambda}_{m,m}}{\mathbf{\Lambda}_{m,m} + \sigma_n^2} \right) \geq \frac{\sum \mathbf{\Lambda}_{m,m}}{\max(\mathbf{\Lambda}_{m,m}) + \sigma_n^2} \tag{B.8}$$

Moreover since all the eigenvalues are positive we have:

$$\text{tr} \{ \Phi \mathbf{C} \} \geq \max(\mathbf{\Lambda}_{m,m}) \tag{B.9}$$

and therefore the following inequality holds:

$$\text{tr} \left\{ \frac{\Phi \mathbf{C}}{\Phi \mathbf{C} + \sigma_n^2 \mathbf{I}_{N_{\mathcal{T}} N_{\mathcal{R}}}} \right\} \geq \frac{\text{tr} \{ \Phi \mathbf{C} \}}{\text{tr} \{ \Phi \mathbf{C} \} + \sigma_n^2} \tag{B.10}$$

Examining the positive logarithmic determinant it can be shown that:

$$\ln \left| \Phi \mathbf{C} / \sigma_n^2 + \mathbf{I}_{N_{\mathcal{T}} N_{\mathcal{R}}} \right| = \ln \prod \left( \mathbf{\Lambda}(m, m) / \sigma_n^2 + 1 \right) \tag{B.11}$$

Using the arithmetic mean - geometric mean inequality (AM-GM) it can be easily shown that:

$$\ln \left| \Phi \mathbf{C} / \sigma_n^2 + \mathbf{I}_{N_{\mathcal{T}} N_{\mathcal{R}}} \right| \leq N_{\mathcal{R}} N_{\mathcal{T}} \ln \left( \frac{\text{tr} \{ \Phi \mathbf{C} \}}{N_{\mathcal{R}} N_{\mathcal{T}} \sigma_n^2} + 1 \right) \tag{B.12}$$

From the upper-bound of the natural logarithm  $\ln(m) \leq m - 1, m > 0$  we have:

$$\ln \left| \Phi \mathbf{C} / \sigma_n^2 + \mathbf{I}_{N_{\mathcal{T}} N_{\mathcal{R}}} \right| \leq \text{tr} \{ \Phi \mathbf{C} \} / \sigma_n^2 \tag{B.13}$$

Finally to extract the lower bound of the negative logarithmic term we can use the natural logarithm lower bound  $\ln(m) \geq 1/m - 1, m > 0$ . It can be also

easily seen that:

$$\ln \left| \Phi \mathbf{C} / \sigma_n^2 + \mathbf{I}_{N_{\mathcal{T}} N_{\mathcal{R}}} \right| \geq 1 - \frac{1}{\prod (\Lambda_{m,m} + 1)} \quad (\text{B.14})$$

Since  $\Lambda_{m,m} \geq 0$  it can be extracted that:

$$-\ln \left| \Phi \mathbf{C} / \sigma_n^2 + \mathbf{I}_{N_{\mathcal{T}} N_{\mathcal{R}}} \right| \leq 0 \quad (\text{B.15})$$

# References

- Abad, R. J., Ierkic, M. H., and Ortiz-Rivera, E. I. (2016). Basic understanding of cognitive radar. In *2016 IEEE ANDESCON*, pages 1–4.
- Abramovich, Y. I. and Frazer, G. J. (2008). Bounds on the Volume and Height Distributions for the MIMO Radar Ambiguity Function. *IEEE Signal Processing Letters*, 15:505–508.
- Alieva, T., Lopez, V., Agullo-Lopez, F., and Almeida, L. (1994). The fractional Fourier transform in optical propagation problems. *Journal of modern optics*, 41(5):1037–1044.
- Allen, R. L. and Mills, D. (2003). *TimeFrequency Signal Transforms*, pages 712–801. Wiley-IEEE Press.
- Almeida, L. B. (1994). The fractional Fourier Transform and time-frequency representations. *IEEE Transactions on Signal Processing*, 42(11):3084–3091.
- Amein, A. and Soraghan, J. J. (2005). A new chirp scaling algorithm based on the fractional Fourier transform. *IEEE Signal Processing Letters*, 12(10):705–708.
- Amirmazlaghani, M. and Amindavar, H. (2009). Modeling and Denoising Wigner-Ville Distribution. In *2009 IEEE 13th Digital Signal Processing Workshop and 5th IEEE Signal Processing Education Workshop*, pages 530–534.
- Asghari, M., Clemente, C., Jalali, B., and Soraghan, J. (2014). Synthetic aperture radar image compression using discrete Anamorphic Stretch Transform. In *Signal and Information Processing (GlobalSIP), 2014 IEEE Global Conference on*, pages 345–349.
- Asghari, M. and Jalali, B. (2013). Anamorphic time stretch transform and its application to analog bandwidth compression. In *Global Conference on Signal and Information Processing (GlobalSIP), 2013 IEEE*, pages 1013–1016.
- Asghari, M. H. and Jalali, B. (2014). Physics-inspired image edge detection. In *2014 IEEE Global Conference on Signal and Information Processing (GlobalSIP)*, pages 293–296.
- Asghari, M. H. and Jalali, B. (2015). Edge Detection in Digital Images Using Dispersive Phase Stretch Transform. *International journal of biomedical imaging*, 2015. The ‘Barbara Test image’ was sourced from Marco Schmidt’s standard test images database and is widely held to have been originally adapted by Allen Gersho, 1993. A version of the original test image can be retrieved from the University of Wisconsin-Madison subject to any terms & conditions and copyright law <https://homepages.cae.wisc.edu/ece533/images/>.

- Ashri, R. M., Shaban, H. A., and El-Nasr, M. A. (2016). BER of FRFT-based OFDM system for underwater wireless communication. In *2016 33rd National Radio Science Conference (NRSC)*, pages 266–273.
- Attia, E. H. and Abend, K. (1991). An experimental demonstration of a distributed array radar. In *Antennas and Propagation Society Symposium 1991 Digest*, pages 1720–1723 vol.3.
- Aubry, A., Carotenuto, V., Maio, A. D., Farina, A., and Pallotta, L. (2016). Optimization theory-based radar waveform design for spectrally dense environments. *IEEE Aerospace and Electronic Systems Magazine*, 31(12):14–25.
- Baker, C. J., Griffiths, H. D., and Papoutsis, I. (2005). Passive coherent location radar systems. Part 2: waveform properties. *IEE Proceedings - Radar, Sonar and Navigation*, 152(3):160–168.
- Balanis, C. A. (2016). *Antenna theory: analysis and design*. John Wiley & Sons.
- Baraniuk, R. and Steeghs, P. (2007). Compressive Radar Imaging. In *2007 IEEE Radar Conference*, pages 128–133.
- Baselice, F., Ferraioli, G., and Reale, D. (2014). Edge Detection Using Real and Imaginary Decomposition of SAR Data. *IEEE Transactions on Geoscience and Remote Sensing*, 52(7):3833–3842.
- Bechter, J., Rameez, M., and Waldschmidt, C. (2017). Analytical and Experimental Investigations on Mitigation of Interference in a DBF MIMO Radar. *IEEE Transactions on Microwave Theory and Techniques*, PP(99):1–8.
- Beide, W. (2001). The nature of bistatic and multistatic radar. In *2001 CIE International Conference on Radar Proceedings (Cat No.01TH8559)*, pages 882–884.
- Bell, K. L., Baker, C. J., Smith, G. E., Johnson, J. T., and Rangaswamy, M. (2015a). Cognitive Radar Framework for Target Detection and Tracking. *IEEE Journal of Selected Topics in Signal Processing*, 9(8):1427–1439.
- Bell, K. L., Johnson, J. T., Smith, G. E., Baker, C. J., and Rangaswamy, M. (2015b). Cognitive radar for target tracking using a software defined radar system. In *2015 IEEE Radar Conference (RadarCon)*, pages 1394–1399.
- Berger, C. R., Wang, Z., Huang, J., and Zhou, S. (2010). Application of compressive sensing to sparse channel estimation. *IEEE Communications Magazine*, 48(11):164–174.
- Bhatnagar, G. and Wu, Q. M. J. (2014). Biometric Inspired Multimedia Encryption Based on Dual Parameter Fractional Fourier Transform. *IEEE Transactions on Systems, Man, and Cybernetics: Systems*, 44(9):1234–1247.
- Bliss, D. and Forsythe, K. (2003). Multiple-input multiple-output (MIMO) radar and imaging: degrees of freedom and resolution. In *Signals, Systems and Computers, 2004. Conference Record of the Thirty-Seventh Asilomar Conference on*, volume 1, pages 54–59. IEEE.

- Blum, R. S. (1999). Distributed detection for diversity reception of fading signals in noise. *IEEE Transactions on Information Theory*, 45(1):158–164.
- Blum, R. S., Kassam, S. A., and Poor, H. V. (1997). Distributed detection with multiple sensors II. Advanced topics. *Proceedings of the IEEE*, 85(1):64–79.
- Blunt, S. D., Cook, M. R., and Stiles, J. (2010). Embedding information into radar emissions via waveform implementation. In *Waveform Diversity and Design Conference (WDD), 2010 International*, pages 000195–000199. IEEE.
- Blunt, S. D. and Mokole, E. L. (2016). Overview of radar waveform diversity. *IEEE Aerospace and Electronic Systems Magazine*, 31(11):2–42.
- Boashash, B. (2015). *Time-frequency signal analysis and processing: a comprehensive reference*. Academic Press.
- Boultadakis, G., Skrapas, K., and Frangos, P. (2004). Time-frequency analysis of radar signals. *RTO SET Symposium on Target Identification and Recognition Using RF Systems*, 80:7–1.
- Brigham, E. O. and Brigham, E. O. (1974). *The fast Fourier transform*, volume 7. Prentice-Hall Englewood Cliffs, NJ.
- Bruniquel, J. and Lopes, A. (1997). Multi-variate optimal speckle reduction in SAR imagery. *International journal of remote sensing*, 18(3):603–627.
- Budisin, S. (2010). Decimation Generator of Zadoff-Chu Sequences. In Carlet, C. and Pott, A., editors, *Sequences and Their Applications - SETA 2010, 6th International Conference*, pages 30–40. Springer Berlin Heidelberg.
- Bultheel, A. and Sulbaran, H. E. M. (2004). Computation of the fractional Fourier transform. *Applied and Computational Harmonic Analysis*, 16(3):182–202.
- Candès, E. J. and Wakin, M. B. (2008). An introduction to compressive sampling. *IEEE signal processing magazine*, 25(2):21–30.
- Canny, J. F. (1983). Finding Edges and Lines in Images. Technical report, DTIC Document.
- Carrara, W., Goodman, R., and Majewski, R. (1995). *Spotlight Synthetic Aperture Radar: Signal Processing Algorithms*. Artech House remote sensing library. Artech House.
- Chandra, S. S. and Sahu, P. K. (2015). Alternate FRFT structure in inline module in DWDM fiber optic communication system. In *2015 International Conference on Microwave, Optical and Communication Engineering (ICMOCE)*, pages 37–40.
- Chen, H., Chen, Y., Yang, Z., and Li, X. (2012). Extended ambiguity function for bistatic MIMO radar. *Systems Engineering and Electronics, Journal of*, 23(2):195–200.
- Chen, H., Ta, S., and Sun, B. (2015a). Cooperative Game Approach to Power Allocation for Target Tracking in Distributed MIMO Radar Sensor Networks. *IEEE Sensors Journal*, 15(10):5423–5432.

- Chen, S., Zhang, S., Zhao, H., and Chen, Y. (2015b). A New Chirp Scaling Algorithm for Highly Squinted Missile-Borne SAR Based on FrFT. *IEEE Journal of Selected Topics in Applied Earth Observations and Remote Sensing*, 8(8):3977–3987.
- Chernyak, V. S. (1998). *Fundamentals of multisite radar systems: multistatic radars and multistatic radar systems*. CRC Press.
- Cisco, C. V. N. I. (2016). Global Mobile Data Traffic Forecast Update, 2015–2020 White Paper, 2016.
- Clemente, C., Ilioudis, C., Gaglione, D., Thompson, K., Weiss, S., Proudler, I., and Soraghan, J. (2014a). Reuse of Fractional Waveform Libraries for MIMO Radar and Electronic Countermeasures. In *6th International Symposium on Communications, Control, and Signal Processing (ISCCSP 2014)*, Athens, Greece.
- Clemente, C., Parry, T., Galston, G., Hammond, P., Berry, C., Ilioudis, C., Gaglione, D., and Soraghan, J. J. (2015). GNSS based passive bistatic radar for micro-Doppler based classification of helicopters: Experimental validation. In *2015 IEEE Radar Conference (RadarCon)*, pages 1104–1108.
- Clemente, C., Shorokhov, I., Proudler, I., and Soraghan, J. J. (2014b). Radar waveform libraries using fractional fourier transform. In *2014 IEEE Radar Conference*, pages 0855–0858.
- Clemente, C. and Soraghan, J. J. (2010a). Fractional Range Doppler Algorithm for SAR imaging. In *The 7th European Radar Conference*, pages 248–251.
- Clemente, C. and Soraghan, J. J. (2010b). Fractional RDA and enhanced FrCSA for SAR imaging. In *Sensor Signal Processing for Defence (SSPD 2010)*, pages 1–5.
- Clemente, C. and Soraghan, J. J. (2010c). Range Doppler SAR processing using the Fractional Fourier Transform. In *11-th International Radar Symposium*, pages 1–4.
- Cochran, D., Suvorova, S., Howard, S. D., and Moran, B. (2009). Waveform Libraries. *IEEE Signal Processing Magazine*, 26(1):12–21.
- Cohen, M. N. (1991). An overview of high range resolution radar techniques. In *Telesystems Conference, 1991. Proceedings. Vol. 1., NTC'91., National*, pages 107–115. IEEE.
- Corporation, M. (2007). RADARSAT-2 Dataset. <http://mdacorporation.com/geospatial/international/satellites/RADARSAT-2>, Accessed at: 2017-01-17.
- Costas, J. P. (1984). A study of a class of detection waveforms having nearly ideal range—Doppler ambiguity properties. *Proceedings of the IEEE*, 72(8):996–1009.
- Cripps, S., C. (2002). *Advanced techniques in RF power amplifier design*. Artech House.

- Cui, D. (2009). Dual digital watermarking algorithm for image based on fractional Fourier transform. In *Web Mining and Web-based Application, 2009. WMWA '09. Second Pacific-Asia Conference on*, pages 51–54. IEEE.
- Cui, G., Li, H., and Rangaswamy, M. (2014). MIMO Radar Waveform Design With Constant Modulus and Similarity Constraints. *Signal Processing, IEEE Transactions on*, 62(2):343–353.
- Cumming, I. G. and Wong, F. H. (2005). Digital processing of synthetic aperture radar data. *Artech house*, 1(2):3.
- Curlander, J. C. and McDonough, R. N. (1991). *Synthetic aperture radar*. John Wiley & Sons New York, NY, USA.
- Cusmario, A. (2004). Cryptographic method using modified fractional Fourier transform kernel. US Patent 6,718,038.
- Dawood, M. and Narayanan, R. M. (2003). Generalised wideband ambiguity function of a coherent ultrawideband random noise radar. *IEE Proceedings - Radar, Sonar and Navigation*, 150(5):379–386.
- Derham, T., Doughty, S., Baker, C., and Woodbridge, K. (2010). Ambiguity Functions for Spatially Coherent and Incoherent Multistatic Radar. *Aerospace and Electronic Systems, IEEE Transactions on*, 46(1):230–245.
- Djurovic, I., Stankovic, S., and Pitas, I. (2001). Digital watermarking in the fractional Fourier transformation domain. *Journal of Network and Computer Applications*, 24(2):167–173.
- Durak, L. and Aldirmaz, S. (2010). Adaptive fractional Fourier domain filtering. *Signal Processing*, 90(4):1188–1196.
- Elachi, C. and Van Zyl, J. J. (2006). *Introduction to the physics and techniques of remote sensing*, volume 28. John Wiley & Sons.
- Euzière, J., Guinvarc’h, R., Lesturgie, M., Uguen, B., and Gillard, R. (2014). Dual function radar communication Time-modulated array. In *2014 International Radar Conference*, pages 1–4.
- Euzière, J., Guinvarc’h, R., Hinojosa, I., Uguen, B., and Gillard, R. (2015). Time Modulated Array for dual function radar and communication. In *2015 IEEE International Symposium on Antennas and Propagation USNC/URSI National Radio Science Meeting*, pages 806–807.
- Fang, C., Zishu, H., Hongming, L., and Jun, L. (2008). The parameter setting problem of signal OFDM-LFM for MIMO radar. In *2008 International Conference on Communications, Circuits and Systems*, pages 876–880.
- Fetterer, F. M., Gineris, D., and Kwok, R. (1994). Sea ice type maps from Alaska Synthetic Aperture Radar Facility imagery: an assessment. *Journal of Geophysical Research: Oceans*, 99(C11):22443–22458.
- Fienup, J. R. (1982). Phase retrieval algorithms: a comparison. *Applied optics*, 21(15):2758–2769.

- Firdausy, K. and Oktoeberza, K. W. (2016). Segmentation of optic disc using dispersive phase stretch transform. In *2016 6th International Annual Engineering Seminar (InAES)*, pages 154–158.
- Fishler, E., Haimovich, A., Blum, R., Cimini, L., Chizhik, D., and Valenzuela, R. (2006). Spatial diversity in radars-models and detection performance. *Signal Processing, IEEE Transactions on*, 54(3):823–838.
- Franceschetti, G. and Lanari, R. (1999). *Synthetic aperture radar processing*. CRC press.
- Frank, R., Zadoff, S., and Heimiller, R. (1962). Phase shift pulse codes with good periodic correlation properties (Corresp.). *Information Theory, IRE Transactions on*, 8(6):381–382.
- Gaglione, D., Clemente, C., Ilioudis, C. V., Persico, A. R., Proudler, I. K., and Soraghan, J. J. (2016a). Fractional fourier based waveform for a joint radar-communication system. In *2016 IEEE Radar Conference (RadarConf)*, pages 1–6.
- Gaglione, D., Clemente, C., Persico, A. R., Ilioudis, C. V., Proudler, I. K., and Soraghan, J. J. (2016b). Fractional Fourier Transform Based Co-Radar Waveform: Experimental Validation. In *2016 Sensor Signal Processing for Defence (SSPD)*, pages 1–5.
- Gao, H., Wang, J., Jiang, C., and Zhang, X. (2014a). Antenna allocation in MIMO radar with widely separated antennas for multi-target detection. *Sensors*, 14(11):20165–20187.
- Gao, H., Wang, J., and Zhang, X. (2014b). Resource allocation in MIMO radar with widely separated antennas for multi-target detection. In *2014 International Radar Conference*, pages 1–6.
- Gerchberg, R., W. and Saxton, W., O. (1972). A practical algorithm for the determination of the phase from image and diffraction plane pictures. In *Optik* 35, pages 237–246.
- Gini, F., De Maio, A., and Patton, L. (2012). *Waveform Design and Diversity for Advanced Radar Systems*. IET radar, sonar and navigation series. Institution of Engineering and Technology.
- Godrich, H., Haimovich, A., and Blum, R. (2010). Target Localization Accuracy Gain in MIMO Radar-Based Systems. *Information Theory, IEEE Transactions on*, 56(6):2783–2803.
- Godrich, H., Petropulu, A. P., and Poor, H. V. (2011). Power Allocation Strategies for Target Localization in Distributed Multiple-Radar Architectures. *IEEE Transactions on Signal Processing*, 59(7):3226–3240.
- Goncalves, P. and Baraniuk, R. G. (1998). Pseudo affine Wigner distributions: definition and kernel formulation. *IEEE Transactions on Signal Processing*, 46(6):1505–1516.

- Goodman, J. W. (1976). Some fundamental properties of speckle. *JOSA*, 66(11):1145–1150.
- Gorji, A., Tharmarasa, R., and Kirubarajan, T. (2013). Widely Separated MIMO versus Multistatic Radars for Target Localization and Tracking. *Aerospace and Electronic Systems, IEEE Transactions on*, 49(4):2179–2194.
- Gorji, A. A., Tharmarasa, R., and Kirubarajan, T. (2014). Optimal Antenna Allocation in MIMO Radars with Collocated Antennas. *IEEE Transactions on Aerospace and Electronic Systems*, 50(1):542–558.
- Griffiths, H. D. and Baker, C. J. (2005). Passive coherent location radar systems. Part 1: performance prediction. *IEE Proceedings - Radar, Sonar and Navigation*, 152(3):153–159.
- Guetein-Holzer, J., Kirschner, A., Speck, C., and Detlefsen, J. (2014). Comparison of motion compensation methods applied to a TDM FMCW MIMO radar system. In *2014 International Radar Conference*, pages 1–6.
- Haimovich, A., Blum, R., and Cimini, L. (2008). MIMO Radar with Widely Separated Antennas. *Signal Processing Magazine, IEEE*, 25(1):116–129.
- Hartenstein, H. and Laberteaux, L. P. (2008). A tutorial survey on vehicular ad hoc networks. *IEEE Communications Magazine*, 46(6):164–171.
- Hassanien, A., Amin, M. G., Zhang, Y. D., and Ahmad, F. (2015a). A dual function radar-communications system using sidelobe control and waveform diversity. In *2015 IEEE Radar Conference (RadarCon)*, pages 1260–1263.
- Hassanien, A., Amin, M. G., Zhang, Y. D., and Ahmad, F. (2015b). Dual-function radar-communications using phase-rotational invariance. In *2015 23rd European Signal Processing Conference (EUSIPCO)*, pages 1346–1350.
- Hassanien, A., Amin, M. G., Zhang, Y. D., and Ahmad, F. (2016). Signaling strategies for dual-function radar communications: an overview. *IEEE Aerospace and Electronic Systems Magazine*, 31(10):36–45.
- Hassanien, A. and Vorobyov, S. A. (2010). Phased-MIMO Radar: A Tradeoff Between Phased-Array and MIMO Radars. *IEEE Transactions on Signal Processing*, 58(6):3137–3151.
- Haykin, S. (2006). Cognitive radar: a way of the future. *IEEE Signal Processing Magazine*, 23(1):30–40.
- Hayvaci, H. T. and Tavli, B. (2014). Spectrum sharing in radar and wireless communication systems: A review. In *2014 International Conference on Electromagnetics in Advanced Applications (ICEAA)*, pages 810–813.
- Hazarika, D., Nath, V. K., and Bhuyan, M. (2015). A lapped transform domain enhanced lee filter with edge detection for speckle noise reduction in SAR images. In *2015 IEEE 2nd International Conference on Recent Trends in Information Systems (ReTIS)*, pages 243–248.

- He, Q. and Blum, R. S. (2014). The Significant Gains From Optimally Processed Multiple Signals of Opportunity and Multiple Receive Stations in Passive Radar. *IEEE Signal Processing Letters*, 21(2):180–184.
- He, Q., Lehmann, N. H., Blum, R. S., and Haimovich, A. M. (2010). MIMO Radar Moving Target Detection in Homogeneous Clutter. *IEEE Transactions on Aerospace and Electronic Systems*, 46(3):1290–1301.
- Heinzel, G., Rüdiger, A., and Schilling, R. (2002). Spectrum and spectral density estimation by the Discrete Fourier transform (DFT), including a comprehensive list of window functions and some new at-top windows.
- Hervet, E., Fjortoft, R., Marthon, P., and Lopes, A. (1998). Comparison of wavelet-based and statistical speckle filters. In *Remote Sensing*, pages 43–54. International Society for Optics and Photonics.
- Hlawatsch, F. and Boudreaux-Bartels, G. F. (1992). Linear and quadratic time-frequency signal representations. *IEEE Signal Processing Magazine*, 9(2):21–67.
- Hlawatsch, F., Manickam, T. G., Urbanke, R. L., and Jones, W. (1995). Smoothed pseudo-Wigner distribution, Choi-Williams distribution, and cone-kernel representation: Ambiguity-domain analysis and experimental comparison. *Signal Processing*, 43(2):149 – 168.
- Holyer, R. J. and Peckinpugh, S. H. (1989). Edge detection applied to satellite imagery of the oceans. *IEEE Transactions on Geoscience and Remote Sensing*, 27(1):46–56.
- Hubaux, J. P., Capkun, S., and Luo, J. (2004). The security and privacy of smart vehicles. *IEEE Security Privacy*, 2(3):49–55.
- Hussain, M. G. M. (2016). Principles of MIMO radar based on ultrawideband throb signals. In *2016 International Conference on Electromagnetics in Advanced Applications (ICEAA)*, pages 878–881.
- Ilioudis, C., Clemente, C., Proudler, I., and Soraghan, J. (2014). Constant Envelope Fractional Fourier Transform based Radar Waveforms Detection and Localization Performance in DMRS. In *Sensor Signal Processing for Defence Conference 2014 (SSPD 2014)*, Edinburgh, UK, pages 1–6.
- Ilioudis, C. V., Clemente, C., Asghari, M. H., Jalali, B., and Soraghan, J. J. (2015a). Edge detection in SAR images using Phase Stretch Transform. In *2nd IET International Conference on Intelligent Signal Processing 2015 (ISP)*, pages 1–5.
- Ilioudis, C. V., Clemente, C., Proudler, I., and Soraghan, J. (2016a). Ambiguity function for distributed MIMO radar systems. In *2016 IEEE Radar Conference (RadarConf)*, pages 1–6.
- Ilioudis, C. V., Clemente, C., Proudler, I., and Soraghan, J. (2016b). MIMO Radar Ambiguity Functions: A Case Study. In *11th IMA International Conference on Mathematics in Signal Processing*, pages 1–5.

- Ilioudis, C. V., Clemente, C., Proudler, I., and Soraghan, J. J. (2015b). Performance analysis of fractional waveform libraries in MIMO radar scenario. In *2015 IEEE Radar Conference (RadarCon)*, pages 1119–1124.
- Jagadesh, T. and Rani, R. J. (2016). A novel speckle noise reduction in biomedical images using PCA and wavelet transform. In *2016 International Conference on Wireless Communications, Signal Processing and Networking (WiSPNET)*, pages 1335–1340.
- Jensen, J. R. (1986). Introductory digital image processing: a remote sensing perspective. Technical report, Univ. of South Carolina, Columbus.
- Jiang, L., Ling, X., Geng, J., and Cheng, Y. (2015). SAR image edge detection based on fuzzy theory and information fusion. In *IET International Radar Conference 2015*, pages 1–7.
- Kadambe, S. and Boudreaux-Bartels, G. F. (1992). A comparison of the existence of ‘cross terms’ in the Wigner distribution and the squared magnitude of the wavelet transform and the short-time Fourier transform. *IEEE Transactions on Signal Processing*, 40(10):2498–2517.
- Khan, W., Qureshi, I. M., and Sultan, K. (2014). Ambiguity Function of Phased-MIMO Radar With Colocated Antennas and Its Properties. *IEEE Geoscience and Remote Sensing Letters*, 11(7):1220–1224.
- Kullback, S. (1968). *Information theory and statistics*. Courier Corporation.
- Kullback, S. and Leibler, R. A. (1951). On information and sufficiency. *The annals of mathematical statistics*, 22(1):79–86.
- Kutay, M. A., Ozaktas, H. M., Arikan, O., and Onural, L. (1997). Optimal filtering in Fractional Fourier domains. *IEEE Transactions On Signal Processing*, 45(5):1129–1143.
- Le Moigne, J. and Tilton, J. C. (1995). Refining image segmentation by integration of edge and region data. *IEEE Transactions on Geoscience and Remote Sensing*, 33(3):605–615.
- Lee, J., Haralick, R., and Shapiro, L. (1987). Morphologic edge detection. *IEEE Journal on Robotics and Automation*, 3(2):142–156.
- Lee, J.-S., Jurkevich, L., Dewaele, P., Wambacq, P., and Oosterlinck, A. (1994). Speckle filtering of synthetic aperture radar images: A review. *Remote Sensing Reviews*, 8(4):313–340.
- Lehmann, N., Haimovich, A., Blum, R., and Cimini, L. (2006). High Resolution Capabilities of MIMO Radar. In *Signals, Systems and Computers, 2006. ACSSC '06. Fortieth Asilomar Conference on*, pages 25–30.
- Levanon, N. (2010). The periodic ambiguity function—Its validity and value. In *Radar Conference, 2010 IEEE*, pages 204–208. IEEE.
- Levanon, N. and Mozeson, E. (2004). *Radar Signals*. NY: JohnWiley & Sons.

- Li, H., Zhao, Y., Cheng, Z., and Feng, D. (2017). OFDM Chirp Waveform Diversity Design With Correlation Interference Suppression for MIMO Radar. *IEEE Geoscience and Remote Sensing Letters*, PP(99):1–5.
- Li, J. and Stoica, P. (2007). MIMO Radar with Colocated Antennas. *IEEE Signal Processing Magazine*, 24(5):106–114.
- Li, J. and Stoica, P. (2009). *MIMO Radar Signal Processing*. NY, USA: Wiley.
- Li, J., Stoica, P., Xu, L., and Roberts, W. (2007). On parameter identifiability of MIMO radar. *IEEE Signal Processing Letters*, 14(12):968–971.
- Li, Y., Vorobyov, S. A., and Hassanien, A. (2014a). MIMO radar capability on powerful jammers suppression. In *2014 IEEE International Conference on Acoustics, Speech and Signal Processing (ICASSP)*, pages 5277–5281.
- Li, Y., Vorobyov, S. A., and Koivunen, V. (2014b). Generalized ambiguity function for the MIMO radar with correlated waveforms. In *2014 IEEE International Conference on Acoustics, Speech and Signal Processing (ICASSP)*, pages 5302–5306.
- Li, Y., Vorobyov, S. A., and Koivunen, V. (2015). Ambiguity Function of the Transmit Beamspace-Based MIMO Radar. *IEEE Transactions on Signal Processing*, 63(17):4445–4457.
- Lin, C., Huang, C., and Su, Y. (2016). A coherent signal processing method for distributed radar system. In *2016 Progress in Electromagnetic Research Symposium (PIERS)*, pages 2226–2230.
- Liu, B. (2009). Orthogonal Discrete Frequency-Coding Waveform Set Design with Minimized Autocorrelation Sidelobes. *IEEE Transactions on Aerospace and Electronic Systems*, 45(4):1650–1657.
- Liu, J., Ding, Z., Zhao, L., Dong, F., and Liu, D. (2014a). An Adaptive SAR Image Speckle Reduction Algorithm Based on Wavelet Transform and Partial Differential Equations. In *EUSAR 2014; 10th European Conference on Synthetic Aperture Radar*, pages 1–4.
- Liu, T., Cao, N., Mao, M., Wang, F., and Du, Y. (2014b). Waveform design and optimization for OFDM radar signal based on fractional Fourier transform. In *The 2014 2nd International Conference on Systems and Informatics (ICSAI 2014)*, pages 724–729.
- Lopes, A., Touzi, R., and Nezry, E. (1990). Adaptive speckle filters and scene heterogeneity. *IEEE Transactions on Geoscience and Remote Sensing*, 28(6):992–1000.
- Lush, D. C. and Hudson, D. A. (1991). Ambiguity function analysis of wideband radars. In *Radar Conference, 1991., Proceedings of the 1991 IEEE National*, pages 16–20.
- Ma, B., Chen, H., Sun, B., and Xiao, H. (2014). A joint scheme of antenna selection and power allocation for localization in MIMO radar sensor networks. In *2014 12th International Conference on Signal Processing (ICSP)*, pages 2226–2229.

- Mahafza, B. R. (2002). *Radar systems analysis and design using MATLAB*. CRC press.
- Maio, A. D. and Lops, M. (2007). Design Principles of MIMO Radar Detectors. *IEEE Transactions on Aerospace and Electronic Systems*, 43(3):886–898.
- Majumder, U., Bell, M., and Rangaswamy, M. (2013). A novel approach for designing diversity radar waveforms that are orthogonal on both transmit and receive. In *Radar Conference (RADAR), 2013 IEEE*, pages 1–6.
- Mansourpour, M., Rajabi, M., and Blais, J. (2006). Effects and performance of speckle noise reduction filters on active radar and SAR images. In *Proc. ISPRS*, pages 14–16.
- Mao, C., Liu, M., Liang, J., and Zhao, G. (2015). Performance for MIMO-RSN with different power allocation methods. In *2015 IEEE International Conference on Communication Workshop (ICCW)*, pages 2540–2544.
- Marr, D. and Hildreth, E. (1980). Theory of edge detection. *Proceedings of the Royal Society of London B: Biological Sciences*, 207(1167):187–217.
- Martone, M. (2001). A multicarrier system based on the fractional Fourier transform for time-frequency-selective channels. *IEEE Transactions on Communications*, 49(6):1011–1020.
- Massonnet, D. and Souyris, J.-C. (2008). *Imaging with synthetic aperture radar*. CRC Press.
- MathWorks (2013). Communications System Toolbox Support Package for RTL-SDR Radio. Available at <http://www.mathworks.co.uk/hardware-support/files/sdr-rtl-users-guide.pdf>.
- MathWorks (2017a). Image Processing Toolbox. <http://uk.mathworks.com/help/images/ref/edge.html>, Accessed at: 2017-01-17.
- MathWorks (2017b). Morphological operations on binary images. <http://uk.mathworks.com/help/images/ref/bwmorph.html>, Accessed at: 2017-01-17.
- MathWorks (2017c). Morphological operations on binary images. <http://uk.mathworks.com/help/images/ref/bwperim.html>, Accessed at: 2017-01-17.
- Meenakshi, A. and Punitham, V. (2011). Performance of speckle noise reduction filters on active radar and sar images. *Gopalax-International Journal of Technology and Engineering System (IJTES)*, (1):112–114.
- Mehany, W., Jiao, L., and Zhang, X. (2015). Design discrete frequency coding waveform based OFDM for MIMO-SAR. *International Journal of Information and Electronics Engineering*, 5(2):126.
- Melvin, W. L. and Scheer, J. A. (2014). *Principles of Modern Radar Volume III-Radar Applications*. SciTech Publishing.
- Mendlovic, D. and Ozaktas, H. M. (1993). Fractional Fourier Transforms and their optical implementation: I. *Journal of the Optical Society of America A*, 10(9):1875–1881.

- Meng, C., Xu, J., Peng, S., Yang, J., Wang, X., and Peng, Y. (2013). Suppress cross-correlation noise of same frequency coding orthogonal signals in MIMO-SAR. In *IET International Radar Conference 2013*, pages 1–6.
- Milligan, T. A. (2005). *Modern antenna design*. John Wiley & Sons.
- Mohan, R. R., Mridula, S., and Mohanan, P. (2016). Speckle noise reduction in images using Wiener filtering and adaptive Wavelet thresholding. In *2016 IEEE Region 10 Conference (TENCON)*, pages 2860–2863.
- Molisch, A. F. (2007). *Wireless communications*. John Wiley & Sons.
- Namias, V. (1980). The fractional order Fourier transform and its application to quantum mechanics. *Journal of Institute of Mathematics and its Applications*, pages 241–265.
- Nathanson, F. E., Reilly, J. P., and Cohen, M. N. (1991). Radar design principles-Signal processing and the Environment. *NASA STI/Recon Technical Report A*, 91.
- NooElec (2013). Data sheet:NESDR-Mini-RTL. Available at <http://www.nooelec.com/store/sdr/sdr-receivers/nesdr-mini-rtl2832-r820t.html>.
- North, H. and Yu, O. (2001). An edge-preserving filter for imagery corrupted with multiplicative noise. *Photogrammetric engineering and remote sensing*, 67(1):57–64.
- Nysaeter, A. and Iwe, H. (2016). Antenna processing optimization for a colocated MIMO radar. In *2016 IEEE Radar Conference (RadarConf)*, pages 1–5.
- Oliver, C. and Quegan, S. (2004). *Understanding synthetic aperture radar images*. SciTech Publishing.
- Ozaktas, H. M., Zalevsky, Z., and Kutay, M. A. (2001). *The Fractional Fourier Transform with applications in Optics and Signal Processing*. John Wiley & Sons Ltd, UK.
- Patel, V. M., Easley, G. R., Jr., D. M. H., and Chellappa, R. (2010). Compressed Synthetic Aperture Radar. *IEEE Journal of Selected Topics in Signal Processing*, 4(2):244–254.
- Pei, S.-C. and Hsue, W.-L. (2006). The multiple-parameter discrete fractional Fourier transform. *IEEE Signal Processing Letters*, 13(6):329–332.
- Pelich, R., Longépé, N., Mercies, G., Hajduch, G., and Garello, R. (2015). Refocusing of ship signatures and Azimuth speed estimation based on FRFT and SAR SLC imagery. In *2015 IEEE International Geoscience and Remote Sensing Symposium (IGARSS)*, pages 3699–3702.
- Persico, A. R., Clemente, C., Gaglione, D., Ilioudis, C., Cao, J., Pallotta, L., Maio, A. D., Proudler, I., and Soraghan, J. J. (2017). On Model, Algorithms and Experiment for Micro-Doppler based Recognition of Ballistic Targets. *IEEE Transactions on Aerospace and Electronic Systems*, PP(99):1–1.

- Persico, A. R., Clemente, C., Ilioudis, C., Gaglione, D., Cao, J., and Soraghan, J. (2015). Micro-Doppler Based Recognition of Ballistic Targets Using 2D Gabor Filters. In *2015 Sensor Signal Processing for Defence (SSPD)*, pages 1–5.
- Pikula, S. and Beneš, P. (2014). A new method for interference reduction in the smoothed pseudo Wigner-Ville distribution. In *Proceedings of 8th International Conference on Sensing Technology*, pages 599–603.
- Pillai, S., Li, K. Y., and Beyer, H. (2009). Reconstruction of constant envelope signals with given Fourier transform magnitude. In *Radar Conference, 2009 IEEE*, pages 1–4.
- Podder, P. and Hasan, M. M. (2016). A meta study of reduction of speckle noise adopting different filtering techniques. In *2016 3rd International Conference on Electrical Engineering and Information Communication Technology (ICEEICT)*, pages 1–6.
- Poularikas, A. D. (2010). *Transforms and applications handbook*. CRC press.
- Prasad, P. S., Rao, B. P., and Chandrasekhar, P. (2013). Enhanced Edge Detection Technique for SAR Images. *International Journal of Computer Applications*, 77(1):6–10.
- Radmard, M., Chitgarha, M., Nazari Majd, M., and Nayebi, M. (2014). Ambiguity function of MIMO radar with widely separated antennas. In *Radar Symposium (IRS), 2014 15th International*, pages 1–5.
- Radmard, M., Majd, M. N., Chitgarha, M. M., Karbasi, S. M., and Nayebi, M. M. (2015). MIMO ambiguity function optimization through waveform design. In *2015 16th International Radar Symposium (IRS)*, pages 333–338.
- Rambach, K., Vogel, M., and Yang, B. (2014). Optimal time division multiplexing schemes for DOA estimation of a moving target using a colocated MIMO radar. In *2014 IEEE International Symposium on Signal Processing and Information Technology (ISSPIT)*, pages 000108–000113.
- Rambach, K. and Yang, B. (2013). Colocated MIMO radar: Cramer-Rao bound and optimal time division multiplexing for DOA estimation of moving targets. In *2013 IEEE International Conference on Acoustics, Speech and Signal Processing*, pages 4006–4010.
- Ran, Q., Zhang, H., Zhang, J., Tan, L., and Ma, J. (2009). Deficiencies of the cryptography based on multiple-parameter fractional Fourier transform. *Optics letters*, 34(11):1729–1731.
- Reddy, B. R. et al. (2012). Performance analysis of MIMO radar waveform using accelerated particle swarm optimization algorithm. *arXiv preprint arXiv:1209.4015*.
- Ren, H., Ren, A., and Li, Z. (2016). A new strategy for the suppression of cross-terms in pseudo Wigner–Ville distribution. *Signal, Image and Video Processing*, 10(1):139–144.

- Rendas, M. and Moura, J. (1998). Ambiguity in radar and sonar. *Signal Processing, IEEE Transactions on*, 46(2):294–305.
- Richards, M. A. (2005). *Fundamentals of radar signal processing*. Tata McGraw-Hill Education.
- Richards, M. A. (2006). Time and Frequency Domain Windowing OF LFM Pulses.
- Richards, M. A., Scheer, J. A., Holm, W. A., Beckley, B., Mark, P., Richards, A., et al. (2010). *Principles of Modern Radar Volume I-Basic Principles*. Citeseer.
- Rihaczek, A. W. (1996). Principles of high-resolution radar. *Norwood, MA: Artech House, 1996*.
- San Antonio, G., Fuhrmann, D., and Robey, F. (2007). MIMO Radar Ambiguity Functions. *Selected Topics in Signal Processing, IEEE Journal of*, 1(1):167–177.
- Santra, A., Jadia, K., and Srinivasan, R., A. G. (2013). Generation Of Modulus Constraint Signal In Adaptive Radar Waveform. In *9th International Radar Symposium India 2013 (IRSI-13)*.
- Scarborough, S. M., Gorham, L., Minardi, M. J., Majumder, U. K., Judge, M. G., Moore, L., Novak, L., Jaroszewski, S., Spoldi, L., and Pieramico, A. (2010). A challenge problem for SAR change detection and data compression. In *SPIE Defense, Security, and Sensing*, pages 76990U–76990U. International Society for Optics and Photonics.
- Sharabati, W. K. and Xi, B. (2016). Fast local polynomial regression approach for speckle noise removal. In *2016 23rd International Conference on Pattern Recognition (ICPR)*, pages 3198–3203.
- Shen, D., Zhou, Y., Liu, X., and Zhang, L. (2014). Chaotic Discrete Frequency Coding Waveform Design for MIMO Radar. In *2014 IEEE International Conference on Computer and Information Technology*, pages 111–117.
- Shen, J. and Castan, S. (1992). An optimal linear operator for step edge detection. *CVGIP: Graphical Models and Image Processing*, 54(2):112–133.
- Sibul, L. H. and Titlebaum, E. L. (1981). Volume Properties for the Wideband Ambiguity Function. *IEEE Transactions on Aerospace and Electronic Systems*, AES-17(1):83–87.
- Singh, A. K. and Saxena, R. (2013). DFRFT: A Classified Review of Recent Methods with Its Application. *Journal of Engineering*, 2013.
- Singh, P. and Shree, R. (2016). Analysis and effects of speckle noise in SAR images. In *2016 2nd International Conference on Advances in Computing, Communication, Automation (ICACCA) (Fall)*, pages 1–5.
- Skolnik, M. I. (1970). Radar handbook.
- Smith, G. E., Cammenga, Z., Mitchell, A., Bell, K. L., Johnson, J., Rangaswamy, M., and Baker, C. (2016). Experiments with cognitive radar. *IEEE Aerospace and Electronic Systems Magazine*, 31(12):34–46.

- Stankovic, L. (1994). A method for time-frequency analysis. *IEEE Transactions on Signal Processing*, 42(1):225–229.
- Stutzman, W. L. and Thiele, G. A. (2012). *Antenna theory and design*. John Wiley & Sons.
- Sun, H.-B., Liu, G.-S., Gu, H., and Su, W.-M. (2002). Application of the fractional Fourier transform to moving target detection in airborne SAR. *IEEE Transactions on Aerospace and Electronic Systems*, 38(4):1416–1424.
- Suthar, M., Mahjoubfar, A., Seals, K., Lee, E. W., and Jalaii, B. (2016). Diagnostic tool for pneumothorax. In *2016 IEEE Photonics Society Summer Topical Meeting Series (SUM)*, pages 218–219.
- The Keithley Instruments, I. M. (2008). Data sheet: Keithley 2920-RF Vector Signal Generator. Available at [https://d3fdwrtpsindh7j.cloudfront.net/Docs/datasheet/kei\\_2920.pdf](https://d3fdwrtpsindh7j.cloudfront.net/Docs/datasheet/kei_2920.pdf).
- Touzi, R., Lopes, A., and Bousquet, P. (1988). A statistical and geometrical edge detector for SAR images. *Geoscience and Remote Sensing, IEEE Transactions on*, 26(6):764–773.
- Tsao, T., Slamani, M., Varshney, P., Weiner, D., Schwarzlander, H., and Borek, S. (1997). Ambiguity function for a bistatic radar. *IEEE Transactions on Aerospace and Electronic Systems*, 33(3):1041–1051.
- Ulaby, F. T., Moore, R. K., and Fung, A. K. (1981). Microwave remote sensing: Active and passive. volume 1-microwave remote sensing fundamentals and radiometry.
- Urkowitz, H., Hauer, C. A., and Koval, J. F. (1962). Generalized Resolution in Radar Systems. *Proceedings of the IRE*, 50(10):2093–2105.
- Van Loan, C. (1992). *Computational frameworks for the fast Fourier transform*, volume 10. Siam.
- Viswanathan, R. and Varshney, P. K. (1997). Distributed detection with multiple sensors Part I. Fundamentals. *Proceedings of the IEEE*, 85(1):54–63.
- Wang, J. (1993). LINDA—a system for automated linear feature detection and analysis. *Canadian Journal of Remote Sensing*, 19(1):009–021.
- Wang, T., Huan, H., Tao, R., and Wang, Y. (2016a). Security-Coded OFDM System Based on Multiorder Fractional Fourier Transform. *IEEE Communications Letters*, 20(12):2474–2477.
- Wang, W., Xu, H., and Liu, X. (2011). Edge detection of SAR images based on edge localization with optical images. In *2011 3rd International Asia-Pacific Conference on Synthetic Aperture Radar (APSAR)*, pages 1–4.
- Wang, W. Q. (2015a). Large Time-Bandwidth Product MIMO Radar Waveform Design Based on Chirp Rate Diversity. *IEEE Sensors Journal*, 15(2):1027–1034.

- Wang, W. Q. (2015b). MIMO SAR OFDM Chirp Waveform Diversity Design With Random Matrix Modulation. *IEEE Transactions on Geoscience and Remote Sensing*, 53(3):1615–1625.
- Wang, Z., Wang, W. Q., and Xiong, J. (2016b). Cognitive target tracking using FDA radar for increased SINR performance. In *2016 IEEE Radar Conference (RadarConf)*, pages 1–4.
- Wehner, D. R. (1987). High resolution radar. *Norwood, MA, Artech House, Inc., 1987, 484 p.*
- Wei, Q. R., Feng, D. Z., and Xie, H. (2016). Edge Detector of SAR Images Using Crater-Shaped Window With Edge Compensation Strategy. *IEEE Geoscience and Remote Sensing Letters*, 13(1):38–42.
- Wen-kun, G., Dang-wei, W., Xiao-yan, M., Dai-kun, Z., and Yao, W. (2016). Distributed OFDM-MIMO radar track-before-detect based on second order target state model. In *2016 IEEE Information Technology, Networking, Electronic and Automation Control Conference*, pages 667–671.
- Wicks, M. and Mokole, E. (2011). *Principles of waveform diversity and design*. The Institution of Engineering and Technology.
- Woodward, P. (1953). *Probability and Information Theory: With Applications to Radar*. Number v. 3 in Electronics and Waves. Elsevier Science and Technology.
- Xing, M., Wu, R., Li, Y., and Bao, Z. (2009). New ISAR imaging algorithm based on modified Wigner-Ville distribution. *IET Radar, Sonar Navigation*, 3(1):70–80.
- Yan, H., Shen, G., Zetik, R., Hirsch, O., and Thoma, R. S. (2013). Ultra-Wideband MIMO Ambiguity Function and Its Factorability. *IEEE Transactions on Geoscience and Remote Sensing*, 51(1):504–519.
- Yang, Y. and Blum, R. S. (2007). MIMO radar waveform design based on mutual information and minimum mean-square error estimation. *IEEE Transactions on Aerospace and Electronic Systems*, 43(1):330–343.
- Yetik, İ. Ş., Kutay, M. A., and Ozaktas, H. M. (2001). Image representation and compression with the fractional Fourier transform. *Optics communications*, 197(4):275–278.
- Yong-Hua, X., Xiu-You, L., Yan-Li, S., and Jian, G. (2015). Discontinuous spectra orthogonal discrete frequency-coding waveform set design for MIMO sky-wave radar. In *IET International Radar Conference 2015*, pages 1–7.
- Youssef, A. M. (2008). On the security of a cryptosystem based on multiple-parameters discrete fractional Fourier transform. *IEEE Signal Processing Letters*, 15:77–78.
- Yu, F., Zhang, Z., and Xu, M. (2006). A digital watermarking algorithm for image based on fractional Fourier transform. In *Industrial Electronics and Applications, 2006 1ST IEEE Conference on*, pages 1–5. IEEE.

- 
- Yu, Y. and Acton, S. T. (2002). Speckle reducing anisotropic diffusion. *IEEE Transactions on Image Processing*, 11(11):1260–1270.
- Zhang, X., Wang, K., Gao, Y., and Liu, X. (2016). Optimal waveform design oriented toward cognitive radar in fractional Fourier domain. In *2016 IEEE Radar Conference (RadarConf)*, pages 1–5.
- Zhou, S., Liu, H., and Su, H. Z. H. (2016). Doppler sensitivity of MIMO radar waveforms. *IEEE Transactions on Aerospace and Electronic Systems*, 52(5):2091–2110.